A Comparative Study on Applications of Surfactant-free Metal Chalcogenides

A Thesis Submitted for the Degree of

DOCTOR OF PHILOSOPHY

By

ANJU JOSEPH



School of Chemistry
University of Hyderabad
Institution of Eminence
Hyderabad- 500046
Telangana, India

July 2023

DEDICATED TO

Jørly Sir

Papa, Amma, Anu, Vijay

Arun

DECLARATION

I hereby declare that the matter embodied in the thesis entitled "A Comparative Study on Applications of Surfactant-free Metal Chalcogenides" is the result of investigations carried out by me in the School of Chemistry, University of Hyderabad, India under the supervision of Prof. K.Muralidharan.

I also confirm that this thesis is free from plagiarism. In keeping with the general practice of reporting scientific investigations, acknowledgements have been made wherever the work described is based on the finding of other investigators.

Anju Joseph

K. MURALIDHARAN
Professor
School of Chemistry
University of Hyderabad
Hyderabad - 500 046.

Reg. no. 17CHPH33



This is to certify that the thesis entitled "A Comparative Study on Applications of Surfactant-free Metal Chalcogenides" submitted by Anju Joseph bearing registration number 17CHPH33 in partial fulfillment of the requirements for award of the Doctor of Philosophy (Ph.D.) is a bonafide work carried out by him under my supervisionand guidance in the School of Chemistry, University of Hyderabad. This thesis is free from plagiarism and has not been submitted previously in part or in full to this or any other University or Institution for award of any degree or diploma. Further, the student has ten publications before submission of the thesis for adjudication and has produced evidences for the same in the form of reprints.

Parts of this thesis has been

- A. Published in the following four publications:
- 1. Anju Joseph, Srinivas Billakanti, Manzoor Ahmad Pandit, Sajmina Khatun, Aravind K. Rengan, Krishnamurthi Muralidharan, Impact of bandgap tuning on ZnS for degradation of environmental pollutants and disinfection. *Environ Sci. Pollut. Res.* **2022**, 29, 56863-56875. (Chapter 2)
- 2. Anju Joseph, Sajmina Khatun, Dasari Sai Hemanth Kumar, Aravind K. Rengan, and Krishnamurthi Muralidharan. Insight into the Effect of Stabilizers on Anticancer and Antibacterial Activity of AgBiS₂ Nanomaterial. *Chem. Eur. J.* **2023**, e202203796. (Chapter 4)
- B. Presented in the following conferences:
- 1. Poster presentation at "CHEMFEST-2019" Annual in-house Symposium of School of Chemistry, University of Hyderabad.
- 2. Poster and Oral presentation at "CHEMFEST-2021" Annual in-house symposium of School of Chemistry, University of Hyderabad.
- 3. Poster presentation in **29th CRSI National Symposium in Chemistry (NCS-29)**, 7-9 July 2022at IISER, Mohali.
- 4. Poster presentation in "International Conference on Chemistry and Applications of Soft Materials (CASM 2022)", 25-27 July 2022 at CSIR- NIIST, Thiruvananthapuram.

Further, the student has passed the following courses towards the fulfillment of coursework requirement for Ph.D.:

Sl.No.	Course No.	Title of the Course	Credits	Pass/Fail
1.	CY801	Research Proposal	4	Pass
2.	CY802	Chemistry Pedagogi	4	Pass
3.	CY805	Instrumental Methods-A	4	Pass
4.	CY806	Instrumental Methods-B	4	Pass

Prof. K.Muralidharan

Dean

(Supervisor)

24/07/2023

.K. MURALIDHARAN
Professor
School of Chemistry
University of Hyderabad
Hyderabad - 500 046.

Achi M

Contral University

ij

CONTENTS

DECLARATION	i
CERTIFICATE	ii
TABLE OF CONTENTS	iii
ACKNOWLEDGEMENTS	ix
LIST OF SCHEMES	xv
LIST OF FIGURES	xvi
LIST OF TABLES	xxi
ACRONYMS	xxii
SYNOPSIS	XXV
CHAPTER – 1	
INTRODUCTION	
1.1. Evolution of nanotechnology	3
1.2. Classification of Nanomaterials	4
1.3. Methods for preparation of nanoparticle	5
1.4. Different Methods of Synthesis of Metal Chalcogenide nanoparticles	7
1.4.1. Hydrothermal method	7
1.4.2. Sol-gel method	9
1.4.3. Precipitation method	11
1.4.4. Microwave method	12
1.4.5. Chemical Vapour Deposition method (C.V.D)	14
1.4.6. Electrochemical deposition method	15
1.5. Properties of Metal Chalcogenide nanoparticles	16
1.5.1. Surface area	17
1.5.2. Magnetic behaviour	17
1.5.3. Quantum effects	17

1.5.4. Optical property	18
1.6. Applications of Transition metal chalcogenide nanoparticles	
1.6.1. Photocatalysis	19
1.6.2. Anticancer activity	21
1.6.3. Antibacterial Activity	23
1.6.4. Chemical Oxygen Demand (COD)	27
1.6.5. Non-enzymatic glucose sensing	30
1.6.5.1. Mechanism of non-enzymatic glucose sensing	32
1.7. Scope of Thesis	35
1.7.1. Definition of problem	35
1.7.2. Aim of current work	36
1.8. References	38
CHAPTER – 2	
Impact of bandgap tuning on ZnS for degradation of environmonal pollutants and disinfection	nental
2.1. Introduction	58
2.2 Experimental	60
2.2.1. Materials required	60
2.2.2. Preparation of ZnS by HMDS-assisted method	60
2.2.3. Preparation of metal doping of ZnS (sf-m-ZnS)	61
2.2.4. Instrumentation	61
2.2.5. Photocatalytic degradation of organic dyes	62
2.2.6. Antibacterial activity test	62
2.3. Results and discussion	63
2.3.1. Preparation and characterisation of ZnS and metal doped ZnS	63

2.3.2. Effect of doping on morphology and optical property	
2.3.3. Effect of metal doping on photochemical degradation of	
dyes using zinc sulphides	68
2.3.4. The retarding effect of capping agents on photocatalysis	77
2.3.5. Antibacterial activity of metal doped zinc sulphides	78
2.4. Conclusion	80
2.5. References	81
CHAPTER – 3	
Study on the effect of the presence of capping agents on nanoc	atalysts on
the reduction of Chemical Oxygen Demand (COD) of water	r bodies
3.1. Introduction	90
3.2. Experimental	91
3.2.1. Materials required	91
3.2.2. Preparation of sf-SnS ₂ by HMDS-assisted method	91
3.2.3. Preparation of PEG-SnS ₂	91
3.2.4. Preparation of sf- AgBiS ₂ by HMDS-assisted method	91
3.2.5. Preparation of OLA/OA- AgBiS ₂	92
3.2.6. Photocatalytic degradation studies	92
3.2.7. Chemical Oxygen Demand measurement (COD)	92
3.3. Results and Discussion	93
3.3.1. Preparation and Characterisation	93
3.3.2. Photocatalytic degradation studies	98
3.3.3. Chemical Oxygen Demand	99
3.4. Conclusion	101
3.5. References	102
Annexure I	106

CHAPTER – 4

Insight into the effect of stabilizers on Anticancer and Antibacterial activity $of \ Ag Bi S_2 \ nanomaterial$

4.1. Introduction	109
4.2. Experimental	
4.2.1. Materials required	110
4.2.2. Cell lines and maintenance	111
4.2.3. Preparation of sf-AgBiS ₂ nanoparticle	111
4.2.4. Preparation of PEG-AgBiS2 nanoparticle	111
4.2.5. Bacterial sample preparation	111
4.2.6. Photothermal Transduction Efficacy	111
4.2.7. DCFDA analysis for ROS generation	111
4.2.8. Biocompatibility studies	112
4.2.9. Cell-killing activity	112
4.2.10. In-vitro 3D tumor spheroids	112
4.2.11. Antibacterial study	113
4.2.12. Statistical analysis	113
4.3 Results and Discussion	
4.3.1. Preparation and Characterisation	114
4.3.2. Photothermal Effect	118
4.3.3. In-vitro biocompatibility	121
4.3.4. In-vitro cytotoxicity in 2D and 3D cell culture	122
4.3.5. Reactive Oxygen Species (ROS) Analysis	125
4.3.6. Antibacterial activity	127
4.4. Conclusion	129
4.5. References	

CHAPTER – 5

Synthesis of surfactant free NiSe₂, CoSe₂ and NiSe₂/CoSe₂ for non-enzymatic glucose sensing

5.1. Introduction	139
5.2. Experimental	140
5.2.1. Materials required	140
5.2.2. Preparation of Selenide solution	140
5.2.3. Preparation of sf-NiSe ₂ , sf-CoSe ₂ and sf-NiSe ₂ /CoSe ₂ composite	
by HMDS-assisted method	140
5.2.4. Electrochemical measurements	141
5.3. Results and Discussion	141
5.3.1. Preparation and characterisation of sf-NiSe ₂ , sf-CoSe ₂ and	
sf-NiSe ₂ /CoSe ₂	141
5.3.2 Surface area of sf-NiSe2, sf-CoSe2 and sf-NiSe2/CoSe2 composite	
materials	144
5.3.3. Electrochemical non-enzymatic detection of glucose using	
sf-NiSe2, sf-CoSe2 and sf-NiSe2/CoSe2	145
5.3.4. Glucose sensing via chronoamperometric using sf-NiSe ₂ ,	
sf-CoSe ₂ and sf-NiSe ₂ /CoSe ₂	150
5.4. Conclusion	152
5.5. References	153

CHAPTER – 6

Summary and Conclusion

Summary and conclusion	155
List of Publications	158
Poster and Oral presentations	159

ACKNOWLEDGEMENT

My path towards a Ph.D. during the past six years has changed and moulded me by unlearning the learnt lessons. I had so many amazing encounters with people during this time, and they motivated me to pursue my interest for study further. I'm happy to take this chance to thank all of those amazing folks for their unwavering love and support throughout this journey. It was a thrilling and difficult time in my life, but I was able to complete this journey because to the encouragement and support of my teachers, friends, family, and others.

I would like to express my gratitude to my supervisor, **Prof. K. Muralidharan** who made the work possible providing me the space and time to complete it without being under any time constraints. He have not denied my request in trying new things and showed me his concern whenever I was in need. I also appreciate his patience, assistance, support and wise counsel in both my professional and personal lives. I owe my personal gratitude for his unrivalled support. I would express my gratitude towards my doctoral committee members **Prof. V. Baskar** and **Prof. P.K. Panda** for their constant support and ideas throughout my research career. I extend my gratitude to present and former deans of School of Chemistry for their support in various occasions. I acknowledge non-teaching and technical staffs for their help and cooperation in executing my research work. Especially, Sunil anna, Dr. Durga Prasad for FESEM, Rajesh bhaiyya for TEM measurements. I sincerely thank University Grants Commission – Junior Research Fellowship (UGC-JRF), New Delhi for fellowship. I acknowledge the financial assistance and equipment resources provided by the Department of Science and Technology, New Delhi, through the FIST and PURSE programmes, and the University Grants Commission, New Delhi, through the CAS and UPE programmes. I also express my gratitude to School of Physics for the PXRD and TEM studies of my samples.

I would like to thank and owe my personal appreciation to **Dr. Aravind .K. Rengan**, Associate Professor, Department of Biomedical Engineering, IIT Hyderabad for accepting my request on collaboration and providing all facilities needed for the project. Sajmina Khatun for the tremendous support and hard work in making my second work a reality. I don't know how to express my gratitude towards the hardship in making that project a success.

A debt of gratitude for my whole life is owned by my **Jerly Sir**, "the walking encyclopaedia" (as he is called by everyone who knows him) who always have the answer for any doubts his student asks and does wonders in each and every students life with his guidance, love and yes of course his scolding. The one who has helped shape who I am today. The teacher who taught

me how to study and made me realise there is sweetness of eternity in scoring high percentage in academic. Thank you for teaching me how to take the essence of knowledge from every book we read. The one and only one person who always hold my back whenever I am in need of. The first one who have opened the vast world of Chemistry, from which I was inspired about "Nanoworld", during his science classes where I came to know about everything from Lycurgus cup to water and dirt repellent cloth (work of one among his students) and later to the specific targeting nature of nanoparticle for medical applications like Cancer. Thank you for building the curiosity in me in my eight standard and help me set my career path in early stages of my life (as I believe). He was always there whenever I felt discomfort and depressed and incomplete, just to make me feel comfort either by giving a glance of him, and lending a shoulder to cry. The door of his home was always opened for me as it is to all his students. Also thank you for teaching me how to enjoy life rather than to be a book worm. How to love nature and how to develop hobbies painting, photography, singing, reading. I am not able to adequately express him in words even though I am his student along for the past years from my eighth standard onwards. I would like to pick a simple word to describe him though, "THE PERFECT TEACHER". I would extend my gratitude to his daughter, Anna, my sister and his wife Deena mam, as I call her Dodo. Thank you Anna for always sensing whenever I'm in the stage of self-doubting. Thank you for the conversations we had as if you got a telepathic message in my miserable. Thank you for boosting me and help me revalue myself. Thank you for the department tour of S. N. School of Hyderabad University and late night talks.

I feel very much thankful and proud about my parents, Mr. P. P. Joseph and Ms. K.K. Priyamma, who are my pillars. Thank you for making me an independent girl from childhood onwards and always allowed me to do what I intend or need to do with my life even though your plan was different. Thank you for always being there for me in every situations which helped me to face the problems I came through in my life. Thank you for sensing my sadness and loneliness in my voice tone, especially Amma, who have always tried to convince me and encourage me all the ways you can. Thank you for making me attracted to studies, travels etc. Also for the advices to explore new things as she does till date. Thank you for supporting my dreams throughout. Thank you Papa and Amma who have walked a long path to make our life and future safe, happy and secure. Thank you for helping me realise my aspirations and battling against the families, neighbour aunties, the society, etc. for me. I am myself because of the struggles you faced. Next is my sister, Anu, my second mother. Thank you for always being there for me whenever I was in need of a mother, a sister, a friend, whom I can tell anything

about everything. My first chemistry teacher and it's because of you I got introduced to the simplicity of chemistry. Thank you for introducing me to Jerly sir's class when I was at the age of thirteen. Thank you for teaching how to search a topic in a book, giving me the books rather than just spoon feeding me, which cherished my interest in chemistry. Thank you for being with me with Dachu to make me comfortable whenever I felt depressed keeping your work aside. The most important person next is my Dachu, my nephew, but literally my photocopy, my son. I always have the privilege to call him mine. Thank you for comforting me whenever I get lost, with your call, toys, small talks about your chickens, ducks, elephants, rhymes etc. Your presence have given me therapy for me in my whole Ph.D. journey. As we often remark, children exhibit the most innocent behaviours, which instantly heal the mind.

Like such, a very special person in my life who is innocent and caring like a father and who have always been my best friend ever, my husband, Vijay. I express my gratitude for being in my life constantly for the past 17 years without any change. You are one of the best things happened in my entire life. Thank you for being there for me discarding your own dreams as a researcher as he is one among the finest researcher I've ever known (who has worked under Prof. K. George Thomas, IISER, Thiruvananthapuram), holding my back, and supporting every decisions I make in my life. Thank you for always flying to me whenever I am depressed and lost. Thank you for being with me whenever I was in need as well as a good son for my parents now. Thank you for giving me the confidence to believe myself.

I would love to thank all the blessings given by some very special persons in my life even though they are not physically present around me. Apachan, Eliyamma, Ammachi amma, Velyanka, Kalamma, my buddy-bro Arun, Jeena and Chris. The pure souls whom always wished good for me from inner heart. Arun was a special friend with brotherly love and who would always try to confront me through his messages even when he was in palliative care. He is one among the special gem person that only some people get as a friend.

I was fortune enough to have good friends around me even though I was an introvert. Now I take the space to express my gratitude to my friends, my strength. Starting from Andrea, one with the purest heart, I am obliged for being a best friend and a best human being from L.K.G. I am so grateful to have Remya, Addu, Fabi, Cli, Safa, who have been a part of my life from plus one as the most mischievous and notorious gang whom does not allow to sacrifice studies at any cost. Thanking you for making me laugh just over a video call (always quoting the whitener story). Especially when joined with your kids Keith, Kiara and Meghna. I owe my

gratitude to Abey, Sandu, Sheffi, Jesti, who were friends initially in plus one became family gradually. They always help me to ease of my heart whenever I felt discomfort.

It would be inappropriate without mentioning three names who made my life at University of Hyderabad memorable. Dr. Rameesa P.M (Remi), Dr. Archana G.R (Archu), the ones who hooked up first through Dr. Jeladhara (Jelu) another crazy and sweet one. Thank you for teaching me how to take life in a simple way and being there for me always, with the passion for 'FOOD', which we discovered in our first journey to Maula Ali (my first outing and a special one) and lately to Gokarna, making the moments always memorable. Thank you for the outings to mushroom rock, sofa rock, white rock and check dam whenever I felt depressed and became numb. I acknowledge you for always being with me whenever I went through a selfdoubting stage and emotional damage. I couldn't have done this without you. You made my days memorable and blissful in university. Especially, with the Saturday movie nights, the badminton practices, the food preparation at night 2:30 am, etc. Another special person I would like to mention is Reshma with a good heart, and always a smile on her face and tastiest food in her hand. I extend my gratitude to Vipula, Anu, Ritesh, Salman, Abin, Pooja, Lakshmi, Subbu, Kummu and Vivek for their timely advices, concern, care, love and affection they have shown from the day I was introduced to them. Thank you for taking care of me whenever I was in need especially in hospitals.

I'd like to thank other family members Sreejith (sheeth), my brother, who always try to make me comfort with the situation sarcastically, which sometimes work though. Acchu, my cousin sister, the secret keeper who always make a call and make sure that I am okay. My younger brothers, Kannan, Aacchu, Gim, Ashly, Amrutha, Chanja, Manikkutty for their care and timely concern and sometimes meaningful words when I was in need of.

I thank my family to which I'm married to, for always supporting me to follow my dreams and accomplish them. I express my sincere gratitude to Retheesh chettan my brother, my role model from my childhood. Thank you for showing how to set up my life goals and to accomplish heights. I learnt how to dream and how to stick towards the dream from you. Thank you for making me comfortable with the family when I was introduced initially. I extend my gratitude to Vinny, my sister, for always giving me meaningful and wise advices whenever I'm confused. Thank you for your amazing 'kittunny' tricks that works miraculously. I also thank Nilakkutty, for always having a great smile. Thank you Nilakkutty for your Japanese lessons (as she taught

'Arigato'). Achan and Amma for your support, love and care you are giving me since the day I was introduced to the family. Thank you for the support you are giving me to achieve higher.

My P.G. friends Abi, Nithin, Divya, Surya, Amno, Teenu (who has been with me since day care), Jayasree, Linda and Nibin chettan (senior), Ummachan chettan (lab assistant) for tthe timely support in my journey. Thank you Abil bro for being proud of me than I am. I remember my teachers Dr. Cyriac Mathew for his belief in me and my passion to be in research field, his guidance and support till date and his valuable suggestions as a supervisor during my P.G. project. Dr. Jude Martin and Dr. Nelson (who is no more) for their care and love shown. I extend my gratitude to my teachers in St. Teresa's College, Usha mam, Anu mam, Geetha mam, Jaya mam, for training me to be systematic in studies and built a habit of studying dayto-day lessons daily. Thank you for building the confidence in me as a student. I'd thank Chandrakala miss for the love she have shown to us students and lab training given by her. Also, I would like to thank the teachers in U.C. College, Aluva and Cochin College, Cochin, S.M.T, Chelakkara (especially Sunitha mam) for the meaningful advices and help while working with them. I'd like to thank my sweet students Shifana and Smruthy for the constant support, love, concern and care shown. I'd thank my school, St. Mary's A. I. G. H. S. S, Fortkochi, where I was taught of everything including manners, the way to talk, the pronunciation, how to behave etc.

I extend my gratitude thank Dr. Joshy Joseph from NIIST, Thiruvananthapuram for the guidance and care he is giving me till date without an ego. Vinayak Chettan, Deepu chettan, Vindhya chechi, Remya chechi, Sajna, Vijitha, Arungopi chettan, Sreejith chettan, Mathews chettan from NIIST for the advices and help when I was at NIIST. Temi chechi for her continuous support and concern as an elder sister.

I'd like to thank special persons like, Jenis for the love and care and occasional calls which kept my tensions aside at least for some time and Saju for your support and joviality when I was going through my hard situations.

I extend my gratitude to Anjana chechi (former lab member), the only person I've seen without any ego, for being along with me throughout in my difficult situations in personal and professional life till date from the day I was introduced to her. I am out of words about her immense support in each and every situations in my life. The life here would have been difficult without you. I express my gratitude to Dr. Soumya, for giving me room to stay, for being a dancing partner, and for the small talks. Also I extend my respect to Rahulettan for the

charming and peaceful face shown whenever I have approached him, Mani anna, for the guidance in the early stages of my research journey and for the lessons about small things to be taken care of while in lab, Srinu anna for the guidance and support, Manzoor bhaiyya, and Venky anna for their concern. I'd like to thank my current lab mates Hemanth bro, Vinay bro, for the support, care and help in every difficult situations, Prachuritha and Kumari for the care you have given me especially in the hospital. Ramkrishna, Chandrika for making a friendly lab atmosphere. Also the project student, Subuhan for his concern and care and advices. A special thanks to Anjali and Mishab for burning the midnight oil during my final days of submission. I am also grateful to Ahsan Zohaib, without whom my third project would not have been occurred.

I'd thank my batch mates Shyam, Ishfaq, Intzar, Isha, Noorul, Smruthy, Navneetha, and my seniors, Dr. Senthil Nathan, Dr. Divya Madhuri, Dr. Showkat for their valuable suggestions and advices. Dr. Apurba Dey, for the MnCl₂ he has given even though it's costly.

I went through a difficult phase around the end of my Ph.D. time that I had never encountered before in my life. It was a challenging time for me financially, mentally, and physically. The COVID-19 pandemic also altered the balance of life. I'm grateful to everyone who was with me at the time, encouraged and understood me, and helped me get through the stressful situation. I'll never forget how you made me laugh, comforted me in my sadness, and celebrated my happiness.

Finally, I'd like to thank the most important person, that is myself for believing in me, not giving up and holding altogether even though I was hard on myself.

If I overlooked somebody, please accept my apologies. I would like to convey my sincere gratitude to everyone who has been a part of my life and has assisted me in some way.

ANJU JOSEPH

List of Schemes

1.34.	General reaction mechanism of HMDS-assisted synthesis of nanomaterial	36
2.1.	Formation of zinc sulphide via HMDS-assisted reaction	63
2.2.	Schematic illustration of energy band mechanism of photocatalysis.	77
3.1.	Preparation of sf-SnS ₂ using HMDS-assisted synthetic method	94
3.2.	Preparation of PEG-SnS ₂ using HMDS-assisted synthetic method	94
3.3.	Preparation of sf-AgBiS ₂ using HMDS-assisted synthetic method	94
3.4.	Preparation of OLA/OA-AgBiS ₂ using literature method	94
4.1.	Preparation of sf-AgBiS ₂ and PEG-AgBiS ₂ using HMDS method	115
5.1.	Preparation of sf-NiSe ₂ , sf-CoSe ₂	141
5.2.	Preparation of sf-NiSe ₂ /CoSe ₂ composite.	142

List of Figures

1.1.	Lycurgus cup	3
1.2.	Classification of nanomaterials	5
1.3.	Bottom up approach and Top down approach	6
1.4.	IBM symbol and Quantum Coral	6
1.5.	Possible mechanism of Photocatalytic degradation of pollutants	19
1.6.	Mechanism of anticancer activity by nanoparticle	23
1.7.	Experimental set up for glucose sensing	32
1.8.	Activated Chemisorption Model for electrocatalytic glucose oxidation	33
1.9.	Incipient Hydrous Oxide Adatom Mediator (IHOAM) model for glucose	
	Oxidation	34
2.1.	Schematic representation of interaction of surfactant free and stabilized	
	Nanoparticles	59
2.2.	PXRD patterns of ZnS and metal doped ZnS nanoparticles	64
2.3.	FESEM images and average particle size distribution of ZnS and	
	metal doped ZnS nanoparticles	65
2.4.	TEM and SAED patterns of ZnS and metal doped ZnS nanoparticles	65
2.5.	EDS elemental mapping of ZnS and metal doped ZnS nanoparticles	66
2.6.	Bandgap calculations of ZnS and metal doped ZnS nanoparticles	67
2.7.	DRS spectra of ZnS and metal doped ZnS nanoparticles	67
2.8.	Photodegradation of Rhodamine B dye solution for ZnS and	
	metal doped ZnS nanoparticles	68
2.9.	Photodegradation of Methylene blue dye solution for ZnS and	
	metal doped ZnS nanoparticles	69

2.10.	(C/C_0) and $In(C/C_0)$ vs Time for degradation of Rhodamine B dye	
	solution by ZnS and Cd-ZnS nanoparticles	7 0
2.11.	(C/C_0) and $ln(C/C_0)$ vs Time for degradation of Methylene blue dye	
	solution by ZnS and Cd-ZnS nanoparticles	7 0
2.12.	C/C_0 vs Time for Rhodamine B and Methylene blue dye solution for	
	Cu-ZnS, Ni-ZnS, Bi-ZnS, Mn-ZnS nanoparticles	7 0
2.13.	$ln(C/C_0)$ vs time for degradation of Rhodamine B dye for Cu-ZnS,	
	Ni-ZnS, Bi-ZnS, Mn- ZnS nanoparticles	71
2.14.	$ln(C/C_0)$ vs time for degradation of Methylene blue dye for Cu-ZnS,	
	Ni-ZnS, Bi-ZnS, Mn- ZnS nanoparticles	71
2.15.	Controlled experiments performed for Rhodamine B and Methylene	
	blue dye solutions	72
2.16.	FESEM images of nanoflakes after fifth cycle for ZnS, and metal	
	doped ZnS nanoparticles	72
2.17.	Plot of lifetime of for ZnS, and metal doped ZnS nanoparticles	73
2.18.	Degradation cycle of Rhodamine B dye solution for ZnS, and metal	
	doped ZnS nanoparticles	75
2.19.	Degradation cycle of Methylene blue dye solution for ZnS, and metal	
	doped ZnS nanoparticles	75
2.20.	Agar-agar plates showing the zone of inhibition test results for ZnS,	
	and metal doped ZnS for 12 h and 24 h	7 8
2.21.	Antibacterial activities of ZnS, and metal doped ZnS for 12 h	7 9
2.22.	Antibacterial activities of ZnS, and metal doped ZnS for 24 h	79

3.1.	PXRD pattern of sf-SnS ₂ , PEG-SnS ₂ , sf-AgBiS ₂ and OLA/OA-AgBiS ₂	
	nanoparticles	95
3.2.	FT-IR Spectra of sf-SnS ₂ , PEG-SnS ₂ , sf-AgBiS ₂ , and OLA/OA-AgBiS ₂	
	nanoparticles	95
3.3.	FESEM image, TEM images, and SAED pattern of sf-SnS ₂ , PEG-SnS ₂ ,	
	sf-AgBiS ₂ , and OLA/OA-AgBiS ₂ nanoparticles	96
3.4.	EDS elemental mapping of sf-SnS ₂ , PEG-SnS ₂ , sf-AgBiS ₂ , and	
	OLA/OA-AgBiS ₂ nanoparticles	97
3.5.	Calculated band gap of sf-SnS ₂ , PEG-SnS ₂ , sf-AgBiS ₂ , and	
	OLA/OA-AgBiS ₂ nanoparticles	98
3.6.	Photodegradation of Rhodamine B dye solution using sf-SnS ₂ ,	
	PEG-SnS ₂ , sf-AgBiS ₂ , OLA/OA-AgBiS ₂ under sunlight for 2 h.	99
3.7.	Illustration of difference in number of active sites for capping agent free	
	nanoparticles and nanoparticles with capping agent	100
4.1.	PXRD pattern of sf-AgBiS ₂ and PEG-AgBiS ₂ nanoparticles	115
4.2.	FTIR spectra of sf-AgBiS ₂ and hexamethyldisilazane (HMDS),	
	PEG-AgBiS ₂ and polyethylene glycol (PEG)	116
4.3.	Absorption coefficient of sf-AgBiS ₂ and PEG-AgBiS ₂ nanoparticles	117
4.4.	FESEM image, TEM image, High resolution TEM image, and SAED	
	pattern of sf-AgBiS ₂ and PEG-AgBiS ₂ nanoparticles	117
4.5.	Average particle size of sf-AgBiS ₂ and PEG-AgBiS ₂ nanoparticles	117
4.6.	Photothermal transduction efficiency thermal images and graph of	
	control (water), sf-AgBiS ₂ , and PEG- AgBiS ₂ nanoparticles	119

4.7.	Thermal stability images and graph of control (water), sf-AgBiS ₂ ,	
	and PEG- AgBiS ₂ nanoparticles	121
4.8.	Biocompatibility of sf -AgBiS $_2$ and PEG-AgBiS $_2$ nanoparticles	122
4.9.	NIR laser mediated cell cytotoxicity of sf-AgBiS ₂ and PEG-AgBiS ₂	
	nanoparticles in HeLa cell line	123
4.10.	In vitro NIR-laser-mediated cell cytotoxicity of sf-AgBiS2 and	
	PEG-AgBiS ₂ by the live/dead assay	124
4.11.	<i>In-vitro</i> cell killing efficacy of sf-AgBiS ₂ and PEG-AgBiS ₂ against	
	3D tumor spheroids without NIR irradiation	124
4.12.	Schematic illustration of cell killing mechanism in Photothermal therapy	125
4.13.	Schematic diagram showing the possible interaction of sf-AgBiS ₂	
	and PEG-AgBiS ₂ with bacteria or cell	126
4.14.	DCFDA analysis for Reactive Oxygen Species (ROS) generation of	
	$sf-AgBiS_2$ and $PEG-AgBiS_2$ nanoparticles (\pm NIR radiation)	127
4.15.	Antibacterial activity by disk diffusion method by PEG-AgBiS ₂	
	and sf-AgBiS ₂ nanoparticles	128
4.16.	Antibacterial activity of sf-AgBiS ₂ and PEG-AgBiS ₂ nanoparticles by	
	MTT assay	129
4.17.	Antibacterial activity of sf-AgBiS $_2$ and PEG-AgBiS $_2$ (\pm NIR radiation)	129
5.1.	PXRD pattern of sf-NiSe ₂ , sf-CoSe ₂ , sf-NiSe ₂ /CoSe ₂ nanoparticles	142
5.2.	FE-SEM, TEM image and SAED pattern of sf-NiSe ₂ , sf-CoSe ₂ ,	
	sf-NiSe ₂ /CoSe ₂ nanoparticles	143
5.3.	EDS elemental mapping of sf-NiSe ₂ , sf-CoSe ₂ , sf-NiSe ₂ /CoSe ₂	
	nanoparticles	144
5.4.	Bandgap calculations of sf-NiSe ₂ , sf-CoSe ₂ , sf-NiSe ₂ /CoSe ₂ nanoparticles	144

5.5.	Nitrogen adsorption—desorption curves and BJH pore size distribution	
	plot of sf-NiSe ₂ , sf-CoSe ₂ , sf-NiSe ₂ /CoSe ₂ nanoparticles	145
5.6.	Cyclic voltammograms and EIS spectra of sf-NiSe ₂ , sf-CoSe ₂ ,	
	sf-NiSe ₂ /CoSe ₂ nanoparticles	146
5.7.	Cyclic voltammograms of sf-NiSe ₂ , sf-CoSe ₂ , sf-NiSe ₂ /CoSe ₂ , before	
	and after 0.1 mM glucose addition	147
5.8.	Cyclic voltammograms at different scan rate and peak current	
	versus scan rate of sf-NiSe ₂ , sf-CoSe ₂ , and sf-NiSe ₂ /CoSe ₂	148
5.9.	Cyclic voltammograms at different glucose concentration and peak	
	current versus concentration of sf-NiSe ₂ , sf-CoSe ₂ , and sf-NiSe ₂ /CoSe ₂	149
5.10.	Cyclic Voltammogram of sf-NiSe ₂ , sf-CoSe ₂ and sf-NiSe ₂ /CoSe ₂	
	electrodes for 200 cycles	151
5.11.	Chronoamperometric response, calibration plot, and response time	
	of sf-NiSe ₂ , sf-CoSe ₂ , and sf-NiSe ₂ /CoSe ₂ for successive glucose addition	152
5.12 .	Amperometric response of sf-NiSe ₂ , sf-CoSe ₂ and sf-NiSe ₂ /CoSe ₂	
	electrodes for interference studies	150

List of Tables

1.1.	Applications of nanomaterials.	18
2.1.	Bandgap and rate constant determined for the photocatalytic degradation	74
2.2.	Photocatalytic performances of ZnS and metal doped ZnS-based	
	photocatalysts for the waste water treatment	76
3.1.	COD value of Rhodamine B solution before and after photocatalytic	
	degradation of dye	100
4.1.	Photothermal transduction temperature for control (water), sf-AgBiS ₂	
	and PEG-AgBiS ₂	120
4.2.	Cell viability of sf-AgBiS2 and PEG-AgBiS2 against HeLa cells	123
5.1.	Limit of detection and Sensitivity of sf-NiSe2, sf-CoSe2, and	
	sf-NiSe ₂ /CoSe ₂	149

List of Acronyms

NPs Nanoparticles

RhB Rhodamine B

MB Methylene Blue

HMDS Hexamethyldisilazane

EG Ethylene glycol

PEG Polyethylene glycol

PMMA Polymethylmethacrylate

CTAB Cetyltrimethyl ammonium bromide

OLA Oleylamine

OA Oleic Acid

TGA Thioglycolic acid

SDS Sodium dodecyl sulphate

TA Thioacetamide

EDTA Ethylenediamine tetra acetic acid

TOP Tri-n-octylphosphine

TOPO Tri-n-octylphosphine oxide

TMC Transition metal chalcogenides

CVD Chemical Vapour deposition

ALD Atomic Layer Deposition

LED Light Emitting Diode

PTT Photothermal Therapy

LSPR Local Surface Plasma Resonance

NIR Near Infra-red Radiation

ROS Reactive Oxygen Species

DNA Deoxyribonucleic acid

RNA Ribonucleic acid

FAS Ferrous Ammonium Sulphate

GOx Glucose oxidase

GDH Glucose dehydrogenase

FAD Flavin Adenine Dinucleotide

PQQ Pyrroloquinoline quinone

TOC Total Organic Carbon

COD Chemical Oxygen Demand

BOD Biological Oxygen Demand

FIA Flow Injection Analysis

EIS Electrochemical Impedance Spectroscopy

CV Cyclic Voltammetry

LSV Linear Sweep Voltammetry

DCFDA 2'-7'-Dichlorodihydrofluorescein diacetate

FDA Fluorescein diacetate

PI Propium Iodide

MTT 3-(4,5-Dimethylthiazol-2-yl)-2,5-diphenyltetrazolium bromide

DMSO Dimethyl sulfoxide

PBS Phosphate buffered saline

FBA Fetal bovine serum

LB Lysogeny broth

CFU Colony-forming unit

DMEM Dulbecco's Modified Eagle Medium

PXRD Powder X-ray diffraction

SEM Scanning Electron Microscopy

TEM Transmission Electron Microscopy

HRTEM High Resolution Transmission Electron Microscopy

SAED Selected Area Electron Diffraction

FT-IR Fourier Transmission Infra-red spectroscopy

JCPDS Joint committee on powder diffraction standards

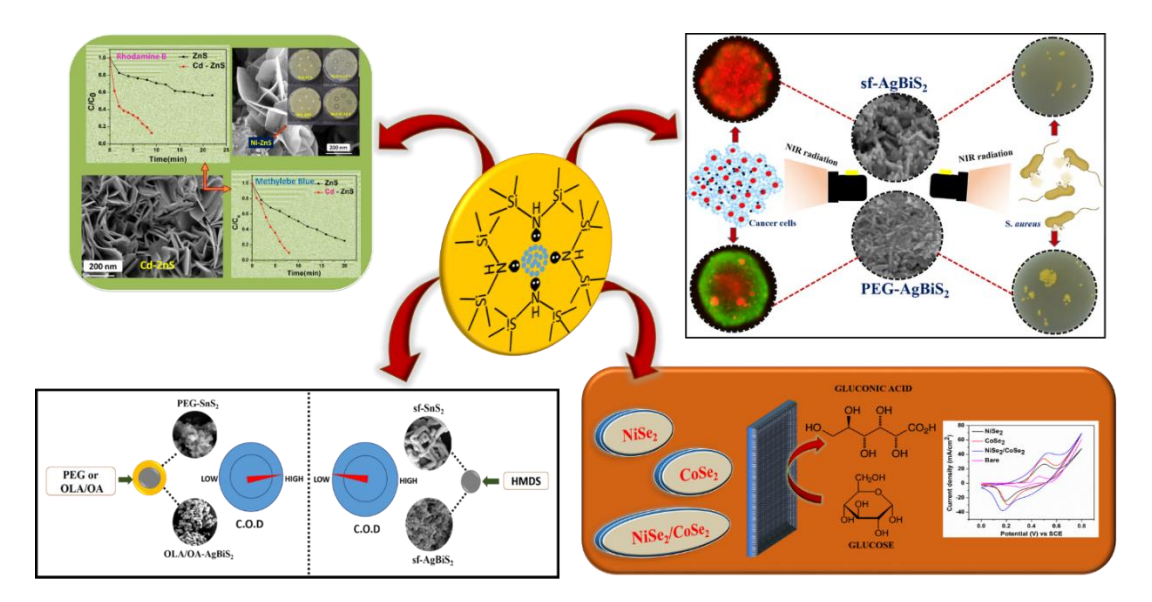
UV-Vis Ultraviolet-visible spectroscopy

SYNOPSIS

The thesis entitled "A Comparative Study on Application of Surfactant-free Metal Chalcogenides" comprises of five chapters.

Chapter 1: Introduction

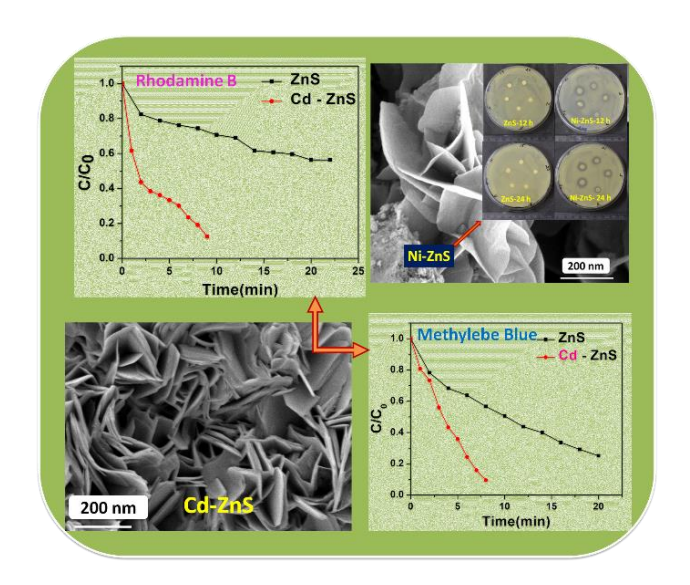
A literature review on nanomaterials, including their definition, classification, methods of synthesis, and uses, is included in the introductory chapter. The advantages and disadvantages of various techniques for producing nanomaterials are reviewed. The approach created in our lab, known as the hexamethyldisilazane (HMDS) assisted method, has been described. The benefits of this novel method are compared with those of others documented in the literature. In addition, discussions on their various characteristics, such as catalytic, optical, and magnetic, are included. There are discussions on several viable applications for environmental remediation, biomedical and glucose sensing applications. The effects of surfactant usage on catalytic characteristics have been examined.



Chapter 2: Impact of bandgap tuning on ZnS for degradation of environmental pollutants and disinfection

The materials with many uses are desirable due to their usefulness and industrial manufacturing. We have developed ZnS (sf-ZnS) and metal-doped ZnS nanoflakes (sf-m-ZnS; where m = Cu, Ni, Cd, Bi, or Mn) and compared their activity with bandgap tuning to achieve the required property for diverse applications. Without the use of surfactants, polymers, or template molecules, we synthesized these compounds using hexamethyldisilazane (HMDS), and we characterized them using a variety of methods. These materials' photocatalytic and

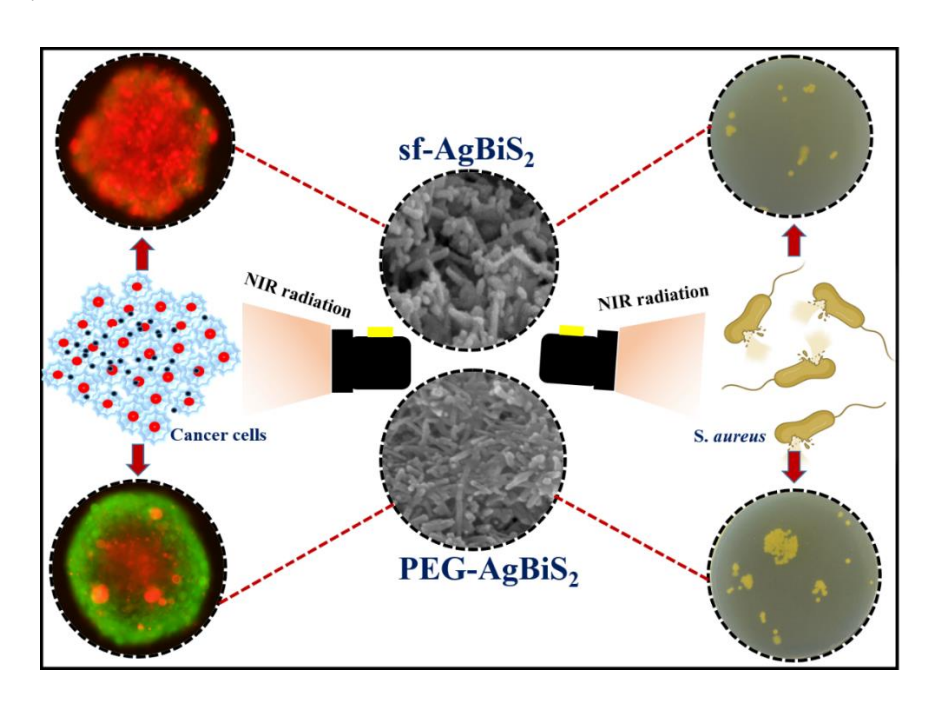
antibacterial properties have demonstrated their dual usefulness. We have shown how doping has an impact on the expansion of the absorption band into the visible spectrum and the improvement of photocatalytic activity under sunlight. When it came to all the materials synthesized, sf-Cd-ZnS excelled as a photocatalyst for the degradation of two organic contaminants in water, Rhodamine B (RhB) and Methylene blue (MB). The Zone of Inhibition technique was used to assess the antibacterial activity of sf-ZnS and sf-m-ZnS against Grampositive bacteria, namely *Staphylococcus aureus* (S. *aureus*), with sf-Ni-ZnS displaying the highest activity. This increased activity of synthesized materials can be attributed to the free surface of the nanoparticles, which allowed for close contact between the inorganic semiconductor material and organic and biomolecules. By tuning the bandgap of the materials and enabling close contact between the materials and substrates, we have thereby shown how characteristics may be changed. Metal-doped ZnS made using our approach demonstrated photocatalytic activity and antibacterial activity, highlighting their potential for environmental remediation, especially water purification.



Chapter 3: Insight into the Effect of Stabilizers on Anticancer and Antibacterial Activity of AgBiS₂ Nanomaterial

The near-infrared (NIR) light-absorbing AgBiS₂ nanoparticles can be excited by single-wavelength light, which is the primary characteristic of a photo responsive platform. Long-chain organic surfactants or polymers are invariably needed for the chemical production of nanomaterials in order to stabilize them in the nano regime. These stabilizing compounds prevent nanomaterials from interacting with biological cells. In order to investigate the impact of stabilizers, we created AgBiS₂ nanoparticles with and without polymer coatings (sf-AgBiS₂)

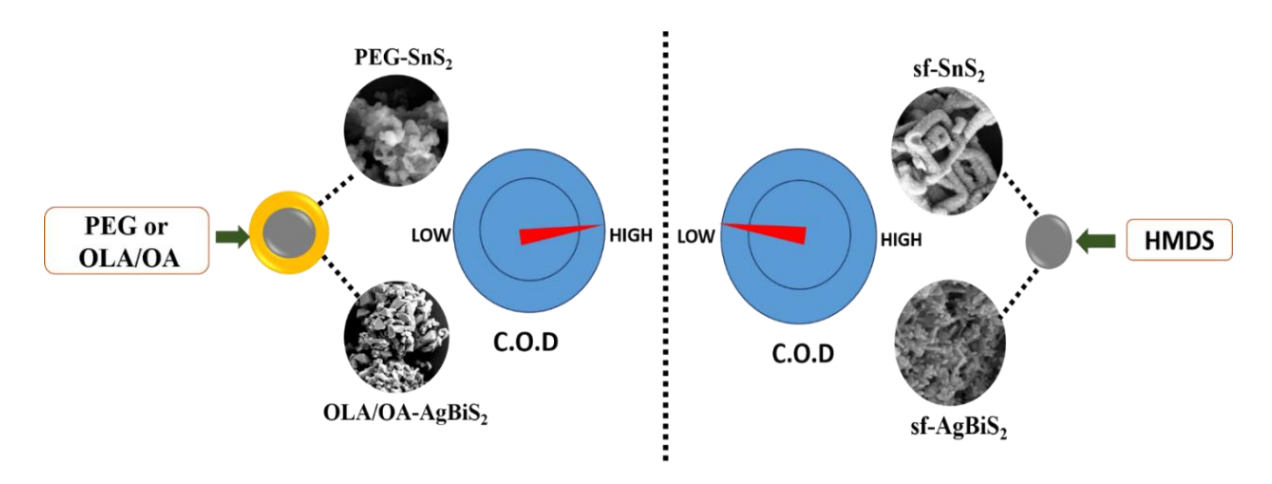
and PEG-AgBiS₂) and tested their NIR-mediated anticancer and antibacterial activities. In comparison to PEG-AgBiS₂, sf-AgBiS₂ demonstrated superior cytotoxicity against HeLa cells and live 3-D tumour spheroids and shown superior antibacterial activity against Gram-positive *Staphylococcus aureus* (S. *aureus*) in both the presence and absence of NIR radiation. The outcomes of photothermal treatment (PTT) demonstrated that sf-AgBiS₂ has the capacity to successfully ablate tumours by achieving 53.3 °C under NIR illumination. The significance of synthesizing stabilizer-free nanoparticles to create secure and potent PTT agents is illustrated by this work.



Chapter 4: Study on the effect of the presence of capping agents on nanocatalysts on the reduction of Chemical Oxygen Demand (C.O.D.) of water bodies

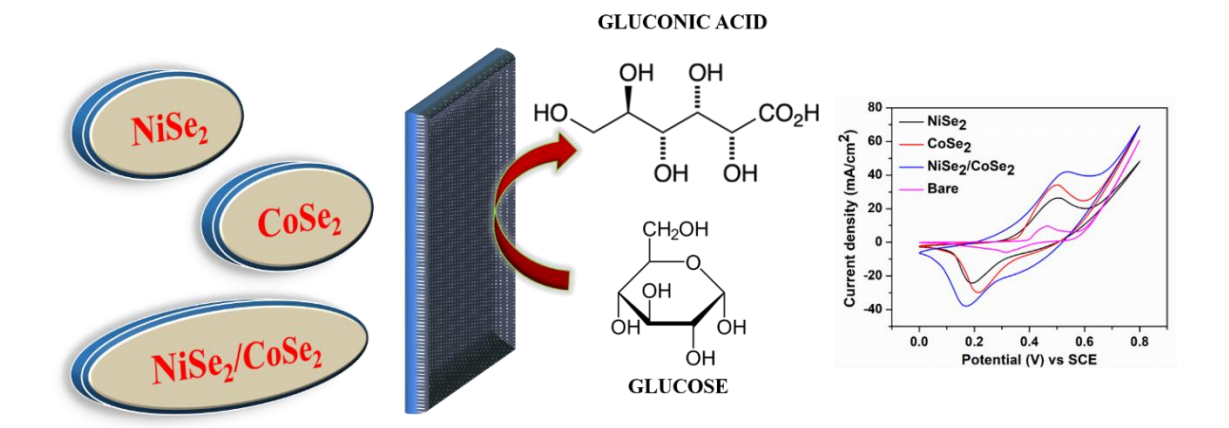
Chemical Oxygen Demand (C.O.D.) is critical parameter government agencies define to determine water quality. Various organic surfactant molecules are used as capping agents while producing nanomaterials to use as catalysts. To evaluate the impact of capping agent on nanocatalysts on water purification, nanoparticles with capping agent (PEG-SnS₂, OLA/OA-AgBiS₂) and without capping agent (sf-AgBiS₂, sf-SnS₂) were synthesized. The as-produced nanoparticles were examined using X-ray diffraction, scanning electron microscopy, transmission electron microscopy, absorption spectroscopy, and infrared spectroscopy to investigate their structural and optical features. The photodegradation of Rhodamine B (RhB) dye solution utilizing the nanoparticles was studied to assess the efficiency of the materials. C.O.D. of dye-contaminated water was measured before and after adding nanocatalysts. Interestingly, the materials without capping agents (sf-SnS₂ and sf-AgBiS₂) demonstrated

higher degradation of Rhodamine B dye solution and exhibited the lowest C.O.D. value. This higher activity can be attributed to the availability of free active sites on capping agent-free materials. We have therefore underlined the significance of the hexamethyldisilazane (HMDS) - assisted approach demonstrating increased activity.



Chapter 5: Synthesis of surfactant free NiSe₂, CoSe₂ and NiSe₂/CoSe₂ for Non-Enzymatic Glucose Sensing

In this part of the thesis, we discussed the synthesis of surfactant-free binary selenides, NiSe₂, CoSe₂ and their composite NiSe₂/CoSe₂ using the HMDS-assisted method. The structural and morphological characterization was determined using X-ray diffraction, UV-Visible spectroscopy, Scanning Electron Microscopy (S.E.M.), and Transmission Electron Microscope (T.E.M.). We examined the glucose oxidation capabilities of synthesized materials. The role of these materials in non-enzymatic glucose sensing is investigated. The results showed that the synthetic materials are effective and sensitive for the non-enzymatic electrochemical detection of glucose. When compared to individual materials, NiSe₂/CoSe₂ composite had a more significant electrochemical response with a limit of detection of 0.0588 mM, good sensitivity of 0.0576 mAmM⁻¹cm⁻², and a rapid response time of 0.603 s, as well as long-term stability and good anti-interference capabilities. This study demonstrated the possible utility of NiSe₂/CoSe₂ composite material as a practical glucose detector.



List of Publications

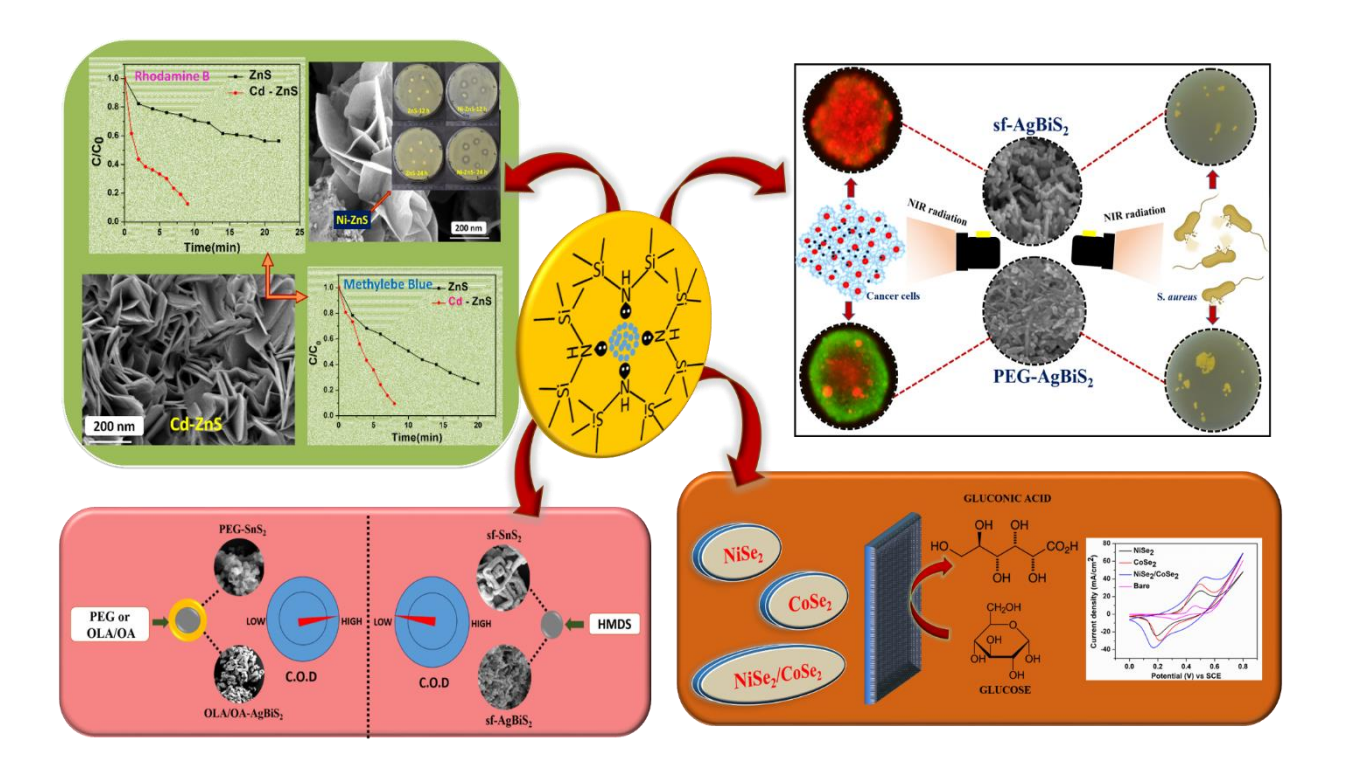
- 1. Impact of bandgap tuning on ZnS for degradation of environmental pollutants and disinfection. **Anju Joseph**, Srinivas Billakanti, Manzoor Ahmad Pandit, Sajmina Khatun, Aravind K Rengan, and Krishnamurthi Muralidharan. *Environ. Sci. Pollut. Res.*, **2022**, 29, 56863-56875.
- 2. Insight into the Effect of Stabilizers on Anticancer and Antibacterial Activity of AgBiS₂ Nanomaterial. Anju Joseph, Sajmina Khatun, Dasarai Sai Hemanth Kumar, Aravind K Rengan, and Krishnamurthi Muralidharan. *Chem. Eur. J.*, **2023**, p.e202203796.

Conferences Attended

- 1. Presented Poster entitled as "Effective degradation of organic molecules and increased antibacterial activity by bandgap tuning of ZnS" in 29th CRSI National Symposium in Chemistry (NCS-29), 7-9 July 2022 at IISER, Mohali.
- 2. Presented Poster entitled as "Bandgap Tuning on ZnS for Effective Degradation of Organic Pollutants and Antibacterial Activity" in "International Conference on Chemistry and Applications of Soft Materials (CASM 2022)", 25-27 July 2022 at CSIR-NIIST, Thiruvananthapuram.
- 3. Presented Poster entitled as "Bandgap Tuning on ZnS for Effective Degradation of Organic Pollutants and Antibacterial Activity" at CHEMFEST-2019 Annual in-house Symposium of School of Chemistry, 22-23 February at University of Hyderabad.
- 4. Presented Poster and delivered Oral talk entitled as "Impact of Bandgap tuning on ZnS for Degradation of Environmental Pollutants and Disinfection" at CHEMFEST-2022, Annual in-house symposium of School of Chemistry, 19-20 March at University of Hyderabad.

Chapter 1

Introduction



Abstract

A literature review on nanomaterials, including their definition, classification, methods of synthesis, and uses, is included in the introductory chapter. The advantages and disadvantages of various techniques for producing nanomaterials are reviewed. The approach created in our lab, known as the hexamethyldisilazane (HMDS) assisted method, has been described. The benefits of this novel method are compared with those of others documented in the literature. In addition, discussions on their various characteristics, such as catalytic, optical, and magnetic, are included. There are discussions on several viable applications for environmental remediation, biomedical and glucose sensing applications. The effects of surfactant usage on catalytic characteristics have been examined.

1.1. Evolution of nanotechnology

Nano, a Greek word with the meaning "dwarf" used to denote a 10⁻⁹ m particle dimension, had introduced the world to an alternate world of opportunities and solutions to the problems in the current world. These exhibit different properties from their bulk [1]. Reducing the particle size to the nano size shows idiosyncratic properties which are not exhibited by bulk particles [2]. The surface-to-volume ratio of a nanoparticle is greater than that of coarse particle or atom. This distinct property increases the surface reactivity of nanoparticles, which depends on size. The growing interest in their application in various fields, such as energy, medicine and nutrition can be attributed to the exceptional properties of nanoparticles [3]. Nanomaterials can be produced using two generally classified approaches: bottom-up and top-down. There are different physical and chemical methods for their synthesis, such as electrodeposition, pyrolysis, solvent, one-pot, microwave, hydrothermal, and pulverisation methods [4, 5, 6].



Figure 1.1. Lycurgus cup appearing green when light is lit from front and red when light is passed through rear.

Nanomaterials were used from C.E fourth century in the Roman era. They were used mainly to impart colour and beauty to the utensils. The most popular Lycurgus cup (figure 1.1) used in this era was a combination of Gold and Silver nanoparticles. Due to this, it appeared as green and was seen as red when the light passed through it. Later, this technique was used to impart colour to the windows of churches. The purple of Cassius or Gold sol, a colloidal solution of Gold nanoparticle, was used with a misconception for curing disease. Since then, alchemists have given significant attention to these particles for their future evolution. Primarily the alchemists performed experiments to produce gold from low-cost metals, which

paved the way for the development of a branch of chemistry called nanochemistry. Richard Feynman opened the door to the world of nanotechnology with his famous statement, "There is plenty of room at the bottom," during his speech on December 29, 1959, at the annual meeting of the American Physical Society. But the word nanotechnology was initially formulated by Norio Taniguchi. The studies of Erick Drexler published in 1984 about molecular nanotechnology enticed many young scientists to this area [4].

Nanotechnology has flourished to its extreme now and offers longevity for human beings. The implementation of nanotechnology in different fields is constantly increasing worldwide. At present, prime focus of researchers is on metal nanoparticles, nanostructures and nanomaterial synthesis due to their remarkable properties and usefulness in catalysis, preparation of polymer composites, diagnosis and treatment of diseases, sensor technology and optoelectronic devices [7-12]. Scientists, with the help of nanotechnology, are developing new methods to recycle polluted water. In the last few years, there have been nanomedicines for cancer, which is a threatening disease to human beings. Nowadays, nanomedicine is a widespread word and technology and is practiced in super specialty hospitals. They are also used in various areas, especially environmental rejuvenation and biomedical fields.

1.2. Classification of Nanomaterials

According to the chemical composition, four types of nanomaterials are present, such as inorganic-based nanomaterials like Cu, Cd, Ni-Fe, ZnO, etc, which have proven their worth in applications such as energy storage, catalysis, water splitting, etc. [1, 13]. The second type is carbon-based nanomaterials like graphene, fullerenes, and carbon nanotubes. They find applications in bioimaging, drug delivery, energy storage, photocatalysis, etc. [14]. Thirdly, organic-based nanomaterials like liposomes and porphyrin. They occupy the fields of molecular imaging, food preservation, oral disease treatment, etc. [1, 15]. And finally, composite-based nanomaterials like polymer composites and hybrid perovskites. They have the upper hand over in the fields like sensing, musculoskeletal tissue regeneration, antimicrobial applications, etc. [1, 16]. Pokropivny and Skorokhod classified nanomaterials based on dimensions (figure 1.2). The 0-D is commonly the quantum dot where the quantum confinement is visible. 1-D mainly comprises nanowires and nanorods, which have only length as their dimension. 2-D particles comprise nanosheets and nanoplates, which have length and thickness as dimensions. 3-D particles like nanocubes have all three dimensions [1, 17].

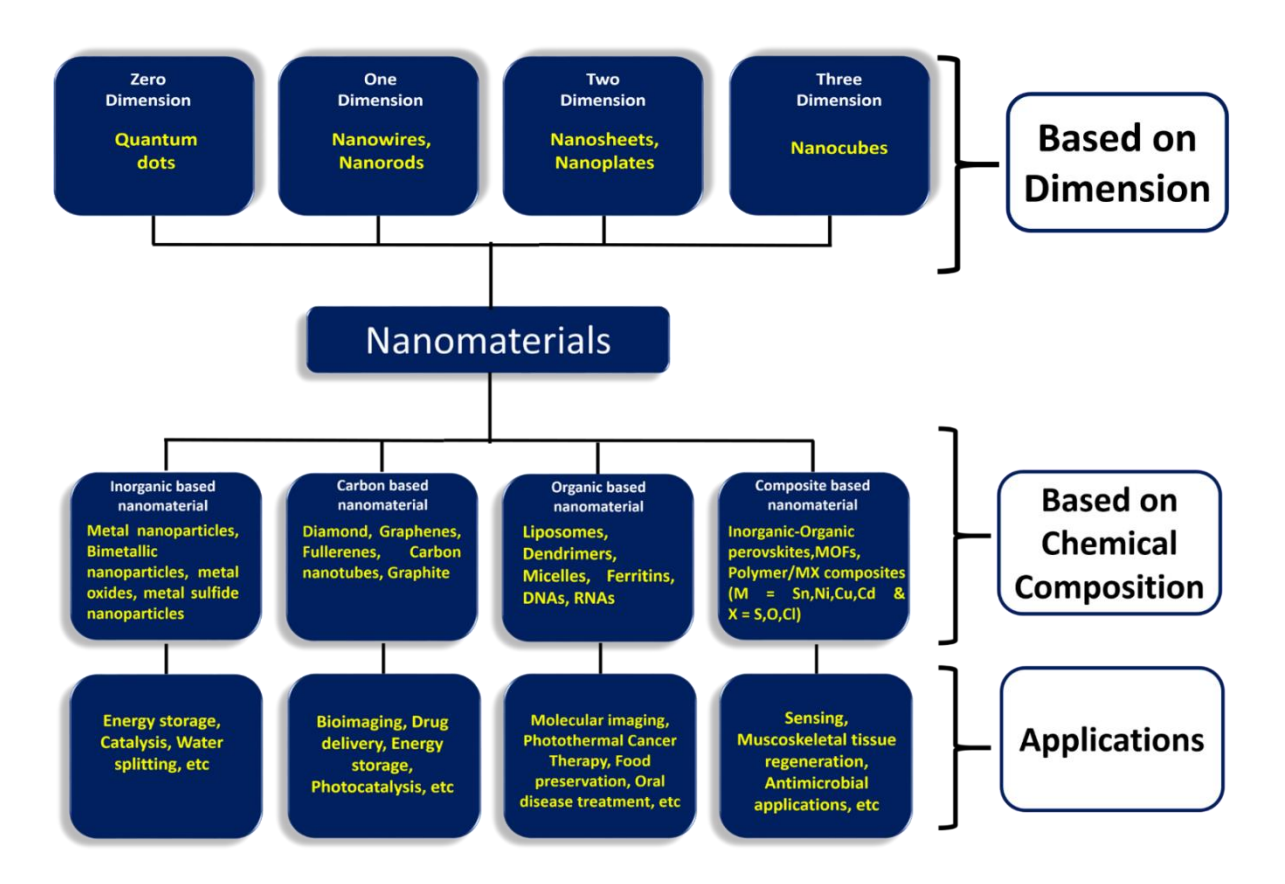


Figure 1.2. Classification of nanomaterials

1.3. Methods for preparation of nanoparticle

Nanoparticles are prepared using two methods in general.

(a) Bottom-up method and (b) Top-down method

a) Bottom-up method

As the name suggests, the nanoparticles are made from their constituent atoms in this method. While delving into history, the Scanning Tunneling Microscope (STM), invented in 1993, was not only used for taking pictures of atoms; they have been used to move and arrange atoms from one place to another to build up nanoparticles. In 1990, IBM scientists Don Eigler and his coworkers made the IBM symbol (figure. 1.4. A) from thirty-five Xe atoms, which was the first example of a typical bottom-up method. Later in 1993, with the help of the same manner, they created quantum coral (figure. 1.4. B) using forty-eight Fe atoms. They are delightful examples of bottom-up methods. The bottom-up approach usually has advantages like simplicity in the technique, less time, easiness in steps and explicit modulation over particle size. According to the requirements, morphology can be manipulated, making it more

acceptable than the top-down method [2, 4, 16, 18]. This method's practical application was synthesising thermoelectric materials.

b) Top-down method

In the top-down method, the bulk material is broken down into nanoparticles by chemical, physical and mechanical processes, including mechanical milling, laser and thermal ablation [19]. Even though top-down methods are simple to implement, they are not suitable for the preparation of informal-shaped particles of tiny sizes. The main issue deals with surface chemistry and physiochemical property changes in nanoparticles. Also, these methods are expensive ones which require more time and energy. Therefore, this method is rarely used [20, 21, 22].

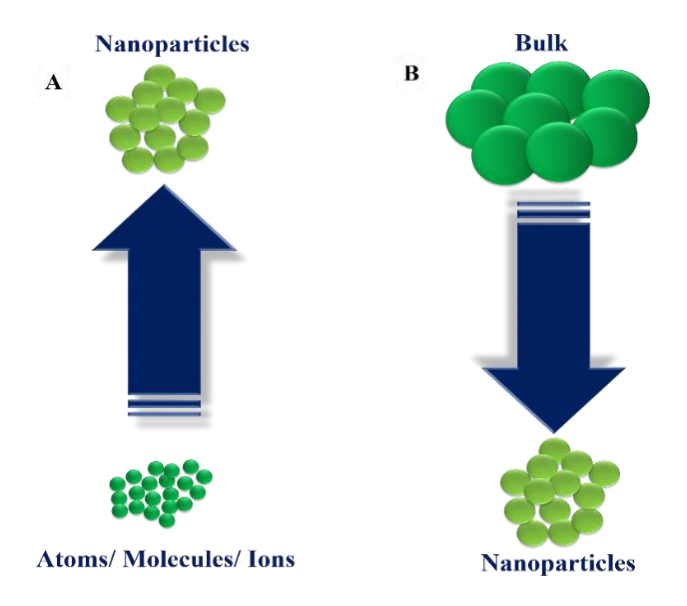


Figure 1.3. A) Bottom-up approach B) Top down approach

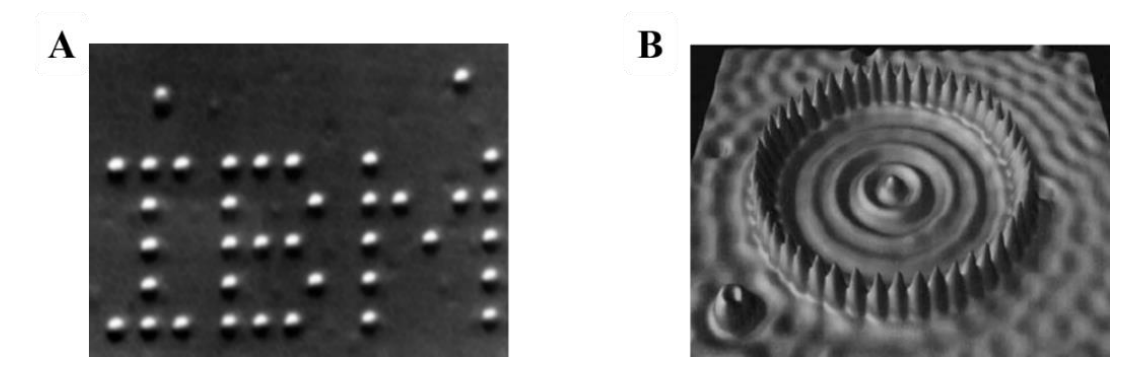


Figure 1.4. A) IBM symbol made from thirty five Xe atoms. B) Quantum Coral made from forty eight Fe atoms.

1.4. Different Methods of Synthesis of Metal Chalcogenide nanoparticles

Chalcogenides are elements of group VI A in the periodic table, starting from Oxygen to Polonium. Oxygen, Sulfur, Selenium, and Tellurium form stable compounds with metals. Transition metal chalcogenides can form various compounds depending on the number of metals present. Even though metal oxides have demonstrated exemplary performance in different areas, their usage was limited because of their wide bandgap, which led to their absorption into the UV region. In contrast, metal chalcogenides absorb in visible regions due to their narrow bandgap. In addition to being stable in both air and aqueous solution, metal chalcogenides exhibit good resistance to oxidation and strong electron/hole conductivities. The crystalline metal chalcogenide compounds are the most intriguing among the metal chalcogenides reported because they show a variety of architectural structures, extending from zero-dimensional structures to three-dimensional open frameworks. The structural diversity and physiochemical properties can be enhanced by incorporating metal ions, whereas the optical properties can be altered by varying the percentage of chalcogens [23].

Developing new nanostructured metal chalcogenides with different sizes and morphologies gave them broad applications. So, it is paramount to develop nanomaterials with controlled size and morphology [24]. Herein, a few well-known synthetic methods for producing nanomaterials are reviewed.

1.4.1. Hydrothermal method

The hydrothermal method is one of the most popular and widely utilised processes for producing nanomaterials. In hydrothermal method, nanomaterials are prepared under conditions of elevated temperature and pressure in an aqueous medium in a sealed vessel. Whereas in solvothermal method, a non-aqueous medium is employed. Microwave-assisted hydrothermal approach offers an edge over the hydrothermal and microwave processes, hence many upcoming research involves engineering nanomaterials.

Usually, hydrothermal and solvothermal methods result in highly crystalline nanomaterials with specific geometries, such as nanowires, nanorods, nanosheets, and nanospheres which results from mere change in reaction conditions. Nonetheless, it is a laborious procedure, and since the reaction occurs in a closed system, the physical state of the reaction mixture is unknown [2, 16, 24-27].

Rauf et al. synthesised zinc sulphide nanoparticles using hydrothermal method using Tween-80 as surfactant and thioglycolic acid as reducing agent at 100 °C [28].

Scheme 1.1. Synthesis of Zinc sulphide nanoparticles

Wei et al. have synthesised Europium doped zinc sulphide using hydrothermal method using oleic acid as surfactant at 210 °C [29].

$$Zn(CH_3COOH)_2.2H_2O + Na_2S + OA + Eu(CH_3COOH)_3.6H_2O \xrightarrow{210 \text{ °C}, 14 \text{ h}} Eu : ZnS$$
 $OA - Oleic acid$

Scheme 1.2. Synthesis of Europium doped Zinc sulphide nanoparticles

Manimozhi et al. have synthesised ternary silver bismuth sulphide using ethylene glycol (reducing agent) and polyethylene glycol as the surfactant at 180 °C [30].

$$AgNO_3 + Bi(NO_3)_3.5H_2O + EG + PEG + TU \xrightarrow{180 \text{ °C}, 20 \text{ h}} AgBiS_2$$

EG – Ethylene glycol, PEG – Polyethylene glycol, TU - Thiourea

Scheme 1.3. Synthesis of Silver bismuth sulphide nanoparticle

Gajendiran et al. have synthesised tin sulphide nanoparticles using sodium dodecyl sulfate as surfactant by hydrothermal method at 180 °C [31].

$$SnCl_2.5H_2O + TA + SDS \xrightarrow{180 \text{ °C}, 12 \text{ h}} SnS_2$$

TA – Thioacetamide, SDS – Sodium dodecyl sulphate

Scheme 1.4. Synthesis of Tin sulphide nanoparticle

Azam et al. have synthesised nano-sized nickel selenides by hydrothermal method at a temperature of 180 °C using hydrazine as reducing agent and cetyltrimethyl ammonium bromide (CTAB) as surfactant [32].

$$NiCl_2.6H_2O + SeCl_4 + CTAB + N_2H_4 \xrightarrow{180 \text{ °C}, 12 \text{ h}} NiSe$$

CTAB - Cetyltrimethyl ammonium bromide

Scheme 1.5. Synthesis of Nickel selenide nanoparticle

Zhang et al. have synthesised cobalt selenide nanoparticles within the temperature range of 100 $^{\circ}$ C - 170 $^{\circ}$ C with a variation of time from 24 h to 48 h through hydrothermal method using ethylenediamine tetra acetic acid (EDTA) as the surfactant [33].

$$CoCl_2.6H_2O + Se powder + NaOH + EDTA \xrightarrow{100-170 \text{ °C}} CoSe_2$$

EDTA - Ethylenediamine tetra acetic acid

Scheme 1.6. Synthesis of Cobalt selenide nanoparticle

1.4.2. Sol-gel method

The Sol-gel method is among the most commonly used methods for synthesising nanomaterials. As the name implies, it consists of a sol made by suspending solid particles in liquid and gel obtained by dissolving macromolecules in liquid. This method has many advantages, such as using low temperatures, less energy and emitting fewer pollutants. The solgel process has certain benefits, including the ability to create unusual materials like zeolites, aerogels, and ordered porous solids. Nanoparticles, nanorods, and nanotubes may be made using the sol-gel method [1, 2, 16, 34, 35]. Some of the nanoparticles prepared through the solgel process are enlisted below.

Bhattacharjee et al. have synthesised zinc sulphides nanoparticles using tetraethyl orthosilicate, zinc nitrate and thiourea in 2-propanol through sol-gel method, in which they have been successful in increasing the refractive index with annealing temperature [36].

Si(OC₂H₅)₄ + 2-propanol
$$\longrightarrow$$
 Zn(NO₃)₂.6H₂O + TU + 2-propanol \longrightarrow ZnS TU - Thiourea

Scheme 1.7. Synthesis of Zinc sulphide nanoparticle

Vijayan et al. have successfully synthesised copper doped zinc sulphides nanoparticle by varying concentrations using sol-gel method for tunable LED applications [37].

$$CuCl_2 + ZnCl_2 \xrightarrow{\text{vigorous stirring}} Na_2S.H_2O \xrightarrow{\text{pH} = 4, 12 \text{ h}} \xrightarrow{\text{calcination}} Cu:ZnS$$

Scheme 1.8. Synthesis of copper doped zinc sulphide nanoparticle

Govindan et al. have synthesised tin sulphides nanoparticles using sol-gel method. They have also prepared lanthanum doped tin sulphide and zirconium doped tin sulphide nanoparticles and have studied photocatalytic degradation of methylene blue [38].

$$SnCl_2.5H_2O + TA + CTAB + C_2H_5OH$$
 a) stirring, 3 h

b) Microwave, 160 W, 5 min

CTAB - Cetyltrimethyl ammonium bromide, TA - Thioacetamide

Scheme 1.9. Synthesis of tin sulphide nanoparticle

CTAB - Cetyltrimethyl ammonium bromide, TA - Thioacetamide

Scheme 1.10. Synthesis of lanthanum doped tin sulphide nanoparticle

TA - Thioacetamide, CTAB - Cetyltrimethyl ammonium bromide

Scheme 1.11. Synthesis of zirconium doped tin sulphide nanoparticle

Mohapatra et al. have synthesised tin sulphide/polystyrene composite using sol-gel method and measured their optical importance and studied photocatalytic efficiency using methyl red [39].

$$SnCl_2.5H_2O + TA$$
 $\xrightarrow{stirring, 30 \text{ min}}$ liquid ammonia $\xrightarrow{a) \text{ stirring, 3 h}}$ SnS_2 $TA - Thioacetamide$

Scheme 1.12. Synthesis of tin sulphide nanoparticle

Alagiri et al. have synthesised nickel oxide nanoparticles which showed super paramagnetic behaviour using sol-gel method in presence of agarose polysaccharide [40].

$$Ni(NO_3)_2.6H_2O$$
 + agarose polysaccharide + H_2O
 a) stirring, 80 °C, b) 100 °C, 4 h
 c) Calcination, 400 °C, 3 h

Scheme 1.13. Synthesis of nickel oxide nanoparticle

Mugundan et al. synthesised cobalt doped titanium dioxide nanoparticles using sol-gel method for non-linear optical study [41].

$$2\text{-propanol} + \text{Ti}(\text{OCH}(\text{CH}_3)_2)_4 \xrightarrow{\text{stirring, } 45 \text{ min}} \text{Co}(\text{NO}_3)_2.6\text{H}_2\text{O} \xrightarrow{\text{a) stirring, } 80 °C, 5 h} \text{Co}: \text{TiO}_2$$

Scheme 1.14. Synthesis of cobalt doped titanium oxide nanoparticle

1.4.3. Precipitation method

The precipitation method is a frequently used method for synthesising a variety of nanomaterials. By a series of chemical processes taking place in solution, this approach can produce homogeneous nanoparticles with small diameters. In this approach, the most frequently utilised precipitants are chlorides, hydroxides, oxalates, and carbonates. To obtain nanoparticles with proper crystal structure and morphology annealing, sintering, or calcination are performed. Nucleation is a vital stage during precipitation. During the growth phase, larger particles absorb smaller particles to lower their surface energy. Agglomeration is another option for reducing surface energy. Particle size may surpass the nanoscale if aggregation and coarsening are not controlled. However, the addition of certain stabilising or capping substances halts this growth. Capping agents are attached to the surface of the particle and generate electrostatic repulsion on its surface by chemisorbing charged species. If the repulsive forces are strong enough to stop coagulation, stable particles will be formed. Even though impurities are precipitated along with the product, their separation using filtration and washing is simple. Some of the nanoparticles prepared using this method are discussed below [1, 16, 42].

Sreedevi et al. have synthesised tin sulphide nanoparticles employing this method and proved it to be an alternative buffer [43].

TA - Thioacetamide

Scheme 1.15. Synthesis of tin sulphide nanoparticle

Remadevi et al. have synthesised Manganese doped zinc sulphide using the same method using EDAX as capping agent [44].

$$ZnSO_4 + MnSO_4 + Na_2S + EDTA \xrightarrow{stirring} Mn : ZnS$$

EDTA- Ethylenediaminetetraacetic acid

Scheme 1.16. Synthesis of manganese-doped zinc sulphides nanoparticle

Xing-Long et al. have also synthesised tin sulphide using the same method as anode materials for rechargeable Li-ion batteries [45].

$$SnCl_2 + TA + NaOH \xrightarrow{\text{stirring, } 60 °C} SnS_2$$

TA - Thioacetamide

Scheme 1.17. Synthesis of tin sulphide nanoparticle

Nakazawa et al. have synthesised silver bismuth sulphide ternary nanoparticles using oleylamine as capping agent [46].

$$Ag(OAc) + Bi(OAc)_3 + OLA \xrightarrow{\text{stirring, N}_2} Sulphur + OLA \xrightarrow{\text{stirring, 5 min}} AgBiS_2$$

OLA - Oleylamine

Scheme 1.18. Synthesis of silver bismuth sulphide nanoparticle

1.4.4. Microwave method

The microwave-based method is a simple method used recently to synthesise nanoparticles. This method has advantages over the thermal methods because of its simplicity, less time taken for the synthesis, and homogeneous heating. Polar molecules like H₂O are brought into alignment with the electric field using microwave frequency of 300 MHz to 300 GHz. The reorientation of dipolar molecules by an alternating electric field results in heat loss via friction

between the molecules. In many chemistry and materials research areas, microwave techniques are utilized to prepare metal nanoparticles from various plant-based extracts [1, 2, 42].

Zhu et al. have synthesised both cadmium sulphide and zinc sulphide using this method following the same procedure [47].

$$CdCl_2 + TA \xrightarrow{\text{Microwave irradiation, } 650 \text{ W}} CdS$$

TA - Thioacetamide

Scheme 1.19. Synthesis of cadmium sulphide nanoparticle

Yang et al. have synthesised copper, cerium and silver-doped zinc sulphide using microwave method [48].

Doping metal source: CuCl₂.2H₂O, CeCl₃.7H₂O, AgNO₃

Scheme 1.20. Synthesis of copper, cerium and silver-doped zinc sulphide nanoparticle Tipcompor et al. have synthesised silver bismuth sulphide nanoparticles with ethylene glycol as solvent using the microwave method [49].

$$Ag(OAc) + Bi(NO_3)_3.5H_2O + thiosemicarbazide + EG \xrightarrow{\qquad Microwave irradiation } AgBiS_2$$

EG - Ethylene glycol

Scheme 1.21. Synthesis of silver bismuth sulphide nanoparticle

Park et al. have synthesised tin sulphide nanoparticles using the same method to evaluate photocatalytic efficiency [50].

TA - Thioacetamide

Scheme 1.22. Synthesis of tin sulphide nanoparticle

Younas et al. have synthesised nickel selenide nanoparticles for high-performance supercapacitors using one step microwave method [51].

$$Ni(NO_3)_2.6H_2O + Na_2SeO_3 + H_2O + C_2H_5OH \xrightarrow{a) \text{ stirring, 20 min}} \xrightarrow{Microwave \text{ heating}} NiSe$$

Scheme 1.23. Synthesis of nickel selenide nanoparticle

Naveenraj et al. have synthesised nickel, copper, zinc selenides using microwave method to check their interaction with human serum albumin [52].

$$NiCl_2.6H_2O + Na_2SeO_3 + starch \xrightarrow{a) \ stirring, \ 30 \ min} \xrightarrow{b) \ N_2H_4.H_2O} \xrightarrow{Microwave \ irradiation} NiSe$$

Scheme 1.24. Synthesis of nickel selenide nanoparticle

1.4.5. Chemical Vapour Deposition method (C.V.D)

In the late 19th century, the chemical vapour deposition process was initially described and patented for the production of carbon powder pigments and carbon fibre filaments for electric lamps. This deposition involves chemical reaction of gaseous molecules containing atoms necessary for film formation. This deposition entails chemical reaction of gaseous molecules that contain atoms required for film generation. A thin film is created through a sequence of chemical interactions involving the precursor fragment, the substrate surface, and the target material, which is released as a volatile molecule and functions as a precursor. In this approach, the surface chemical reaction often produces atomic layer deposition (ALD) thin films. This method delivers different advantages, like controllability in surface morphology and high film durability. The usage of toxic, corrosive gases and the inability to deposit multi-component material deposition can be counted as disadvantages of this method. Some nanoparticles synthesised using this method are discussed below [1, 2, 16, 25].

Liu et al. have synthesised one-dimensional nanostructured zinc sulphide nanoparticles using this method [53].

$$Zn + S \xrightarrow{700-720 \text{ °C } @ 50 \text{ °C/min}} ZnS$$

Scheme 1.25. Synthesis of zinc sulphide nanoparticle

Chen et al. have synthesised two-dimensional tin sulphide nanosheet array for photoelectrochemical water splitting using chemical vapour deposition [54].

$$SnCl_4.5H_2O + S \xrightarrow{450 \text{ °C } @ 10 \text{ °C/min}} SnS_2$$

Scheme 1.26. Synthesis of tin sulphide nanoparticle

Zhou et al. have also synthesised tin sulphide nanoparticles using the same method for high performance sodium storage [55].

$$SnCl_4.5H_2O + TA \longrightarrow SnS_2$$

Scheme 1.27. Synthesis of tin sulphide nanoparticle

Masud et al. have synthesised copper selenide nanoparticles for oxygen evolution reaction using different methods, where chemical vapour deposition method is one among them [56].

$$CuSO_4 + SeO_2 \xrightarrow{700 \text{ °C, N}_2, 30 \text{ min}} Cu_2Se$$

Scheme 1.28. Synthesis of copper selenide nanoparticle

Khan et al. have synthesised cobalt doped zinc oxide nanoparticles as anodes for photoelectrochemical water splitting using chemical vapour deposition method [57].

$$Zn(OAc)_2.2H_2O + Co(OAc)_2.4H_2O + CH_3OH \xrightarrow{\hspace*{1cm} 400 \text{ }^{\circ}C, \text{ Ar, 2 h}} Co: ZnO$$

Scheme 1.29. Synthesis of cobalt doped zinc oxide nanoparticle

1.4.6. Electrochemical deposition method

The electrochemical deposition method is the simplest, quickest and most affordable method that yields nanoparticles with precise control over size and shape. This method requires an anode, a cathode for depositing the metal nanoparticles, and a reference electrode that is either Ag-AgCl or calomel. In an electrolytic bath with a metal salt, a small voltage is supplied for the appropriate amount of time, resulting in nanoparticles. This method is frequently used for various tasks, including potential step deposition, double pulse, and cyclic voltammetry. The direct attachment of nanoparticles to the substrate is a significant benefit of this method. Porus

semiconductors are usually employed using this method [2, 42]. Some nanoparticles synthesised using this method are reviewed below.

Wang et al. have synthesised nickel selenide-titanium dioxide composite using this method for the cathodic protection of stainless steel [58].

$$NiCl2.6H2O + TiO2 + SeO2 + HCl \xrightarrow{-1.5 \text{ to } 0.4 \text{ V}, 10 \text{ mV/s}} NiSe2/TiO2$$

Scheme 1.30. Synthesis of nickel selenide/titanium dioxide composite nanoparticle

Che et al. have synthesised nickel selenide nanoparticles, which could be used as counter electrode in solar cells using hydrothermal electrochemical deposition method [59].

NiCl₂.6H₂O + LiCl + Na₂SeO₃
$$\xrightarrow{-0.8 \text{ V vs Ag/AgCl}}$$
 NiSe₂

Scheme 1.31. Synthesis of nickel selenide nanoparticle

Xu et al. have synthesised zinc sulphide nanoparticles using electrochemical deposition method [60].

$$ZnCl_2 + S + DMSO \xrightarrow{6.62 \text{ mA/cm}^2} ZnS$$

Scheme 1.32. Synthesis of zinc sulphide nanoparticle

Shin et al. have synthesised manganese-iron-sulphide in nickel foam which showed good electrochemical performance using one-step electrodeposition method [61].

MnSO₄.H₂O + FeSO₄.7H₂O + TU + Ni foam
$$\frac{-1 \text{ to } 1.2 \text{ V vs SCE } 10 \text{ mV/s}}{\text{KOH, pH} = 7}$$
 Mn-Fe-S

Scheme 1.33. Synthesis of manganese-iron-sulphide nanoparticle

1.5. Properties of Metal Chalcogenide nanoparticles

In contrast to their bulk counterparts, the characteristics that matter at the nanoscale exhibit are significantly different. Due to decrease in crystallographic flaws, mechanical aspects are

noticeably better than their bulk counterparts. By adjusting the sizes and morphologies, nanomaterials with specific features and unique properties can be produced [62].

1.5.1. Surface area

The surface area of all nanomaterials is substantially higher than their bulk equivalents [62]. The high surface-to-volume ratio causes a recognizable change in the material's physiochemical characteristics, including a drop in the melting point, a rise in the bandgap, and specific features like catalytic and bacterial activity. Since chemical reactions occur at the surface, the particle's surface area substantially impacts the reaction rate. A more extensive surface area gives more room for the reactions to take place. As a result, a material with nanoscale particles demonstrated more excellent catalytic activity than the identical material in bulk [63, 64].

1.5.2. Magnetic behaviour

When an atom or molecule has an unpaired electron, it creates a magnetic field that causes it to act like a little magnet. At the nanoscale, the magnetic properties of elements can alter. A non-magnetic element can acquire magnetic properties at the nanoscale level. Because of this, magnetic nanoparticles have a variety of scientific uses. Depending on how they react to an external magnetic field, magnetic materials are categorized as diamagnetic, paramagnetic, ferromagnetic, ferrimagnetic, and antiferromagnetic [65].

1.5.3. Quantum effects

Quantum confinement is an intriguing characteristic of the material at the nanoscale. When the materials form particles of petite size, the electrons become restricted in all directions, changing the electrical energy levels from continuous to discrete until they eventually resemble atoms. Consequently, the energy difference between the valence band and conduction band widens. This finding also clarifies how these bands emerge from atoms, molecules, nanoparticles, and bulk stuff as matter progresses. The joining of several continuous energy levels of many atoms or molecules creates the bands in the bulk matter. The number of overlapping orbitals or energy levels declines, and the width of the band narrows as the particle size lowers until it reaches the nanoscale, where each particle comprises just a small number of atoms. The band gap of the nanoparticles is greater than that of the comparable bulk matter due to the transition of the electronic energy levels from continuous to discrete. The shift in absorption spectra towards the lower wavelength may readily recognize this quantum confinement effect. As a result,

choosing a material for a given application depends on the actual energy level of the valence band and conduction band and the band gap of semiconductor material. At the nanoscale, quantum effects are increasingly noticeable [66].

1.5.4. Optical property

Quantum dots have several unusual and intriguing optical features and remarkable photostability due to their quantum confinement. The localized surface plasmon associated with nanoparticles interacts with light to produce their optical characteristics. These charge density oscillations occur when nanoparticles reach a size far smaller than the wavelength of light. Surface plasmon oscillations caused by collective electron oscillations in the conduction band give colour to the materials. Remarkable performance can be found at the nanoscale level compared to bulk equivalents based on the nature of the nanomaterial [67].

1.6. Applications of Transition metal chalcogenide nanoparticles

Metal nanoparticle applications across various fields, including material science, physics, chemistry, and biology, rapidly expand globally. Stoichiometric-dependent features and size dependency of nanoparticles in their property gave researchers an idea about how to employ them in different fields. Some of them are enlisted in Table 1.

Applications	Materials	Ref.
Photocatalysts	CdS, NiS, In ₂ S ₃ , Ag ₂ S, CoS, ZnS, ZnIn ₂ S ₄	[68-70]
Water splitting	Cu ₂ S, Ni ₃ S ₂ @NiSe, Ni ₃ Te ₂ , Cu: Co ₃ Se ₄ , MoS ₂ -NiS ₂	[71]
Sensors	MoS ₂ /SnO ₂ , (Fe,Mn):CuSe, NiSe ₂ , Co ₂ Te ₃	[72-75]
Solar cells	FeSe ₂ , Cu ₂ S,CuSe, MoSe ₂ , Ni ₃ S ₄ /CoS ₂	[76-78]
Biomedical	ZnO, TiO ₂ /Au, CuO, MoS ₂ , CuS@MoS ₂ , TiSe ₂ , VS ₂ , NbTe ₂ , Ag ₂ S, CuInS/ZnS, AgBiS ₂	[79-82]
LEDs	CsPbX ₃ , MoSe ₂ /NiO, CuInS/ZnS, PbSe/Te, CdSe,InP, ZnSe	[83-85]
Super capacitors	MnSe ₂ @MoSe ₂ , MnSe/NiCo ₂ O ₄ ,Ni ₃ S ₂ /rGO, CuS/MWCNT, Bi ₂ S ₃ /MoS ₂ , WS ₂ /rGO, MoS ₂ /rGO/MoS ₂ , VS ₄ /rGO/CoS ₂	[86-90]
Photovoltaics	ZrS ₂ /Se ₂ , HfS ₂ ,Cu ₂ ZnSnS ₄ , FeS ₂ , Cu ₂ S, TaS ₂ , MoS ₂ ,CuInS ₂ , WSe ₂	[91, 92]

Table 1.1. Applications of nanomaterials

1.6.1. Photocatalysis

As the population has increased exponentially, the demand for clean water supply has also increased significantly. Thus, the shortage of clean water has led to a global water crisis. The surface water bodies alone cannot fulfil this demand. Treating wastewater can solve this crisis, as it is economical, environment friendly and abundant. Employing photocatalysts for acceleration of photoreactions has raftered in developing applications such as hydrogen production, degradation of pollutants, carbon dioxide reduction, etc. Metal oxides have been extensively used as photocatalysts in various photocatalytic applications. However, their visible-light photocatalysis is limited because of their broadband gap. Chalcogenide nanoparticles have become dominant photocatalysts due to their tunable and narrow band gap. The degradation of pollutants occurs during photocatalysis, which is a surface phenomenon. A plausible mechanism for the photocatalytic destruction of contaminants is provided in Figure 1.5 [95].

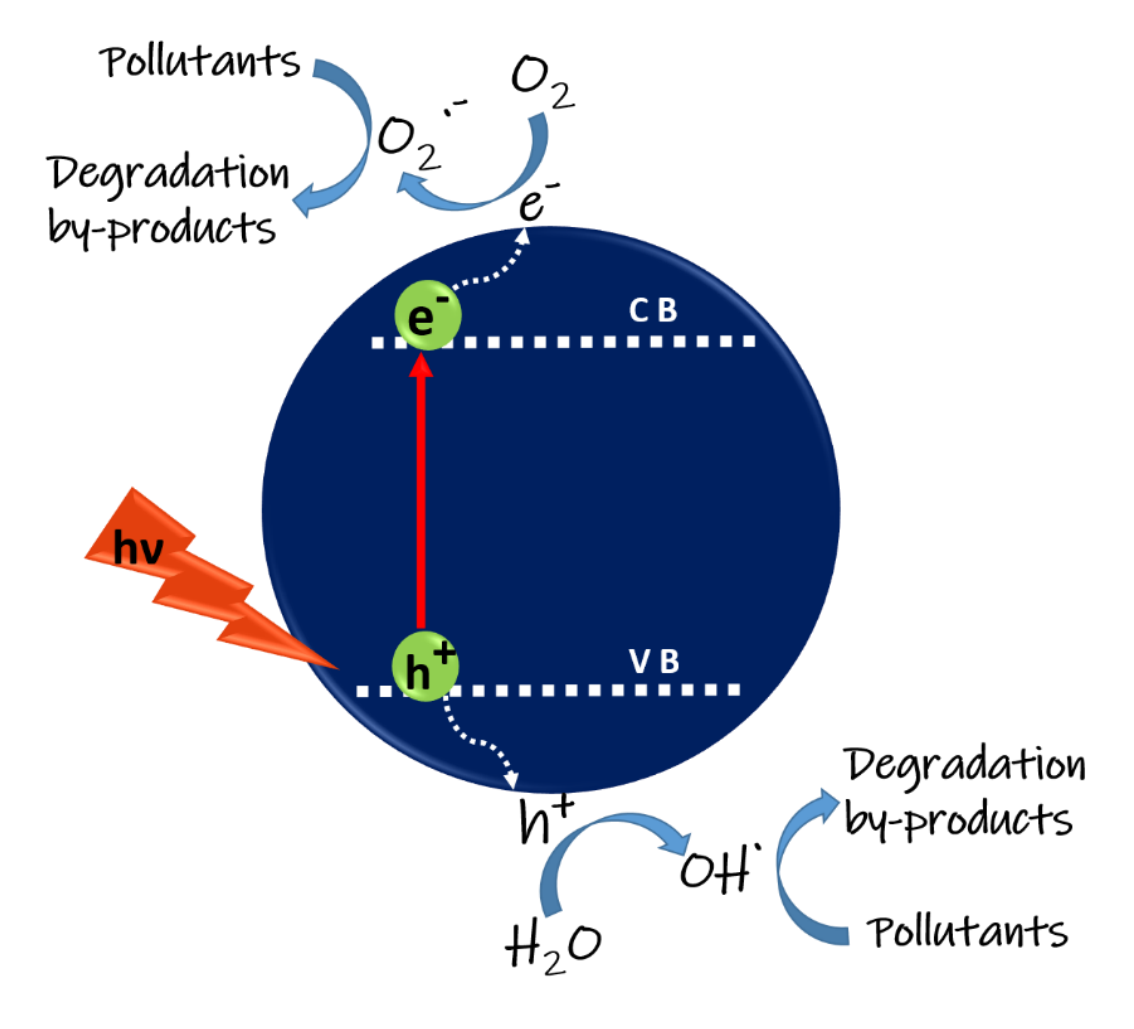


Figure 1.5. Possible mechanism of Photocatalytic degradation of pollutants

The mechanism can be explained as follows:

a) catalyst + hv
$$\longrightarrow$$
 catalyst* (electrons + holes)
b) holes + H₂O \longrightarrow OH'
c) electrons + O₂ \longrightarrow catalyst + O₂'
d) H⁺ + O₂' \longrightarrow HO₂
e) HO₂ + OH \longrightarrow H₂O₂
f) H₂O₂ \longrightarrow 2OH

Pollutants + OH \longrightarrow Degradation Products

Many metal chalcogenides have been synthesised for a broad spectrum of applications. Among which transition metal chalcogenides, mostly sulphides and selenides having variable stoichiometric compositions, distinctive crystal structures, abundant redox sites, and comparatively better electrical conductivity have allured researchers recently, even though chalcogenides of Na, K, and Li are also potential photocatalysts [93, 98, 99]. To be efficient photocatalysts, they should have large specific surface area, suitable morphology which delivers higher accessibility to exposed sites, long-term durability, narrow band gap, and anti-corrosive characteristics. Since binary, tertiary, and quaternary metal chalcogenides have exhibited these properties, they work as excellent photocatalysts [98, 100-102].

Murray et al. have synthesised the most efficient metal chalcogenide nanoparticle CdS using the organometallic precursor method using tri-n-octyl phosphine oxide (TOPO) as well as tri-n-octyl phosphine (TOP) as the capping reagents [103]. CdS have caught the attention of many researchers due to its characteristics like optimal and variable bandgaps and visible light absorption. But its limitation is mainly due to the toxicity it delivers, which led to the search for other less toxic metal chalcogenides like ZnS, ZnSe, CuS, etc. [94, 104]. Lately, transition metal dichalcogenides have established themselves in various application fields due to their remarkable properties like exceptional optical absorption, electrical conductivity, order-disorder transitions, fast charge carrier dynamics, etc. [101, 105-108].

Despite the amazing photocatalytic abilities of binary chalcogenides, higher-order chalcogenides, like ternary and quaternary metal chalcogenides, have been developed to attain favourable energy and band alignments. Due to the synergistic effects of several components, multinary metal-based chalcogenides exhibit improved photocatalytic efficiencies [94, 109,

110]. Many multinary metal-based chalcogenides and their composites are known to exist. AgBiS₂, Cu₂ZnSnS₄, CuInS₂, CuFeS₂, ZnIn₂S₄, AgFeNi₂S₄–Graphene–TiO₂, MoS₂/Cu–ZnIn₂S₄, etc. are some among them used for various applications in different fields [111-116].

1.6.2. Anticancer activity

Cancer is one of the vulnerable illnesses that has long caused major health concerns. Chemotherapy, surgical excision, and radiation therapy are traditional treatments with a low cure rate and serious adverse effects. Nanomedicines are a novel class of therapeutic agents with outstanding anti-tumour effects and few adverse effects on healthy tissues [117]. Photothermal therapy (PTT) has garnered much attention for tissue disinfection due to its better antibacterial activity, controllability, and penetrability [118]. The nanoparticles used as photothermal agents convert light into heat, termed Hyperthermia, which is greater than the physiological temperature. Due to extreme sensitivity to the heating, the malignant cells are killed due to the raised temperature. This localized heating only affects the tumour cells and does not affect nearby healthy cells [119]. PTT is a potent alternative to traditional cancer therapies because thermal effects at an appropriate level can boost intratumoral blood flow and eventually carry more oxygen into the tumour, which results in synergistic therapeutic benefits even in extremely dehydrated solid tumours.

Manikandan et al. synthesised Pt nanoparticles within the size range of 5 to 6 nm and found an increase in temperature of 9 °C, making it an excellent photothermal agent [120]. Immunohistochemical studies and histopathological examinations were performed by Elbialy et al. to study the efficiency of magnetic gold nanoparticles [121, 122].

Due to their distinct optical characteristics, transition metal chalcogenides nanoparticles can be used as imaging contrast agents and inorganic photothermal agents [123, 124]. These biocompatible nanoparticles with controllable size and composition can directly influence the production of Local Surface Plasmonic Resonance (LSPRs) and make them effective candidates for anticancer treatments. Due to the comparable size of nanomaterials with cellular components, they are excellent for monitoring molecular interactions and reactions. Also, these materials exhibit significant NIR absorbance due to unconventional LSPR. The absorbance maxima are located in the NIR region, which makes transition metal chalcogenide nanoparticles an ideal candidate for photothermal treatment (PTT). In PTT, the energy absorbed is used to generate Reactive Oxygen Species (ROS) and heat leading to hyperthermia, causing the death of cancer cells since it has less heat tolerance [122, 125-127].

CuS nanoparticles were synthesised and used in cancer imaging and photothermal therapy by Li et al. and Zhou et al. [128, 129]. Owing to low toxicity, production cost, small size and high NIR absorbing capacity CuS has attracted many. But its accumulation in the liver and spleen limited its usage further [130, 131]. Chen et al. utilized poly (acrylamide-acrylonitrile)-PEG, thermosensitive amphiphilic block copolymers modified CuS as photothermal agents and obtained a temperature rise of 18 °C [132]. MoS₂, with a layered structure, adjustable bandgap and high thermal stability, was another compound explored as a photothermal agent [122]. MoS₂ modified with hyperbranched polyglycidyl, i.e., (MoS₂—HPG) nanocomposite was synthesised by Liu et al., which exhibited 29.4% efficiency in photothermal conversion [133].

Another metal sulphide which has enticed researchers is Ag₂S, with a small bandgap [122]. Han et al. successfully ablated cancer cells using Ag₂S nanoparticles as photo immunotherapy agents. Even though Ag₂S shows less conversion efficiency compared to other compounds, less toxicity, the photothermal effect to destroy tumour cells as well as the capacity for dual-modality imaging, which offers all-inclusive imaging data than alternative methods for greater spatial resolution, higher tissue penetration and more substantial signal-to-noise ratio in the right size, makes them one among the good PTT agents [134].

Bismuth-based nanomaterials, such as Bi, Bi₂S₃, AgBiS₂, and Bi₂Se₃, are more appropriate for in vivo applications and have been attractive candidates as photothermal conversion agents since they can produce ROS when exposed to light [135, 136]. These materials are attractive due to their small band gap, high light absorption coefficient, less toxicity, affordable rates, X-ray attenuation capacity, heat dissipation rate, controllability in size and shape during synthesis, active targeting efficiency, photothermal conversion efficiency and strong Near-IR absorption [137]. Fang et al. have synthesised a non-toxic, dendrimer-stabilized Bi₂S₃ nanoparticle and found its negligible effect in haemolysis and usage in computed tomography [138]. Kinsella et al. have synthesised bismuth sulfide (Bi₂S₃) nanoparticles labelled with the cyclic nine amino acid peptide CGNKRTRGC (LyP-1) for targeting breast cancer [139].

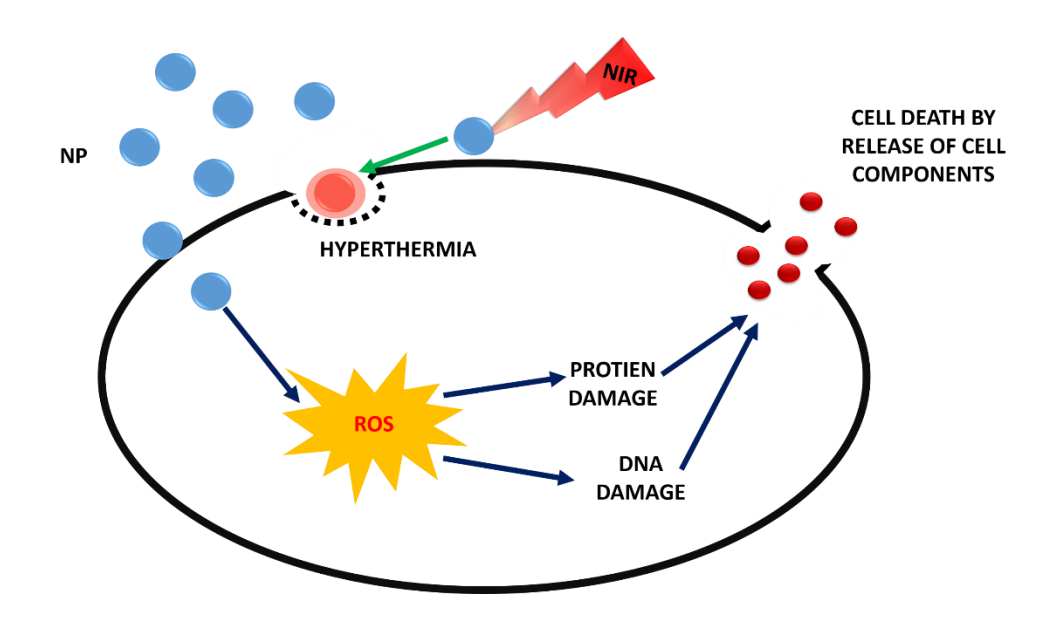


Figure 1.6. Mechanism of anticancer activity by nanoparticle.

The alloy nanoparticle AgBiS₂ offers a benefit over CT imaging and photothermal conversion efficiency in analogy with Ag₂S and Bi₂S₃ nanoparticle [140]. AgBiS₂ nanocrystals exhibit exquisite chemical stability, effective cytotoxicity against cancer cells, a relatively high absorption coefficient and high photothermal conversion efficiency with a tunable narrow energy gap [135, 141]. According to Wen et al., the production of ROS by stimulating AgBiS₂ with light at 808 nm can kill bacteria [142]. Xu et al. synthesised AgBiS₂@PVP and investigated their role in generating ROS in sonodynamic therapy and catalyzing H₂O₂ in a tumour environment [143]. Cheng et al. have synthesised AgBiS₂@DSPE-PEG2000-FA for tumour therapy, resulting in enhanced computed tomography/infrared (CT/IR) imaging, ROS generation, and photothermal and sonodynamic effects [140]. Chu et al. fabricated AgBiS₂-coated Nd³⁺-sensitized upconversion core-shell nanoparticles (UCNPs@AgBiS₂) and resulted in enhanced photothermal conversion efficiency [135]. The mechanism of anticancer activity can be illustrated as shown in Figure 1.6.

1.6.3. Antibacterial Activity

Public health is seriously threatened by bacterial pollution. Previously, it was thought that conventional antibiotics or disinfectants were the best way to kill germs. But bacteria acquired antibiotic resistance, making a novel antibacterial strategy devoid of antibiotics necessary. Based on the cell wall structure, bacteria can be classified into two. They are Gram-positive bacteria where the structure comprises Teichoic acids, a peptidoglycan layer, and a cytoplasmic membrane. Ex: Staphylococcus aureus, Streptococcus agalactiae, and Anthrax bacterium. The

unique, hydrophobic lipid bilayer present in Gram-negative bacteria offers further defence against environmental harm. The carboxylate and phosphates groups in lipopolysaccharides significantly increase the cell envelope's negative potential. Ex: E. coli, Asiatic cholera, and Salmonella enterica. These bacterial membranes are crucial for fundamental biological activities, including material transport, signal transduction, and cell-to-cell communication. Additionally, maintaining cellular homeostasis depends on the genetic materials, proteins (DNA and RNA) and organelles that make up cells. Therefore, this establishes a line of reasoning that eliminating these centres is essential to advancing the development of antibacterial tactics. The general mechanism followed for non-radiative antibacterial activity is as follows: (a) The breakage of the bacterial membrane, (b) the formation of reactive oxygen species (ROS), (c) the infiltration of the bacterial cell membrane, and (d) binding to the nucleic acid to prevent cell growth [144, 145].

According to reports, nanomaterials can directly break through cell walls, and the leaking of cytoplasmic contents is highly prone to occur. Following the destabilization of cell membranes, intracellular components, including DNA, proteins, and enzymes, become exposed to assault. Additionally, nanomaterials can affect oxidative damage, enzyme inhibition, and electrolyte imbalance and thus prevent bacteria from functioning normally, leading to cell injury or death. This results in a novel approach using nanoparticles as antibacterial agents, which have distinct physiochemical characteristics and various bactericidal routes than standard antibiotics, making them less prone to acquire resistance. Numerous noble metal compounds have been developed with strong antibacterial properties against Gram-positive and Gram-negative bacteria [79].

Sondi and Salopek-Sondi showed that Ag nanoparticles might be exploited as possible antibacterial agents [18]. They usually destroy bacterial cells by generating reactive oxygen species (ROS), radicals and ions. Ions induce the production of reactive oxygen species, in which oxygen radicals react with the cell membrane and mitochondria, resulting in their irreversible alterations and the bacterial cell's death [146-148]. Ag NPs have exceptional antibacterial characteristics, but their quick oxidation, aggregation characteristics, high cost and toxicity to humans, which can result in argyria, spasms, gastrointestinal issues, or even death, limits their usage [118, 149]. Therefore, lately, in the 1960s, transition metal oxides have been acting as antibacterial agents [150-154].

Ag₂O was the most commonly used nanoparticle as an antibacterial agent due to the electrical changes that occur when they contact bacterial membranes. These modifications are

believed to improve the reactivity of the surfaces of silver nanoparticles. Additionally, metal nanoparticles' durability in growth conditions and long-lasting effectiveness without breakdown increase their in vitro bactericidal activity. Shah et al. have successfully synthesised Ag₂O nanoparticles using Paeonia emodi (P. emodi) fresh leaves extract as a reducing agent and studied antibacterial action with Gram-negative bacteria, Escherichia coli (*E.coli*) bacterium [155]. The size dependency of Ag₂O nanoparticles in antibacterial activity was investigated by Panacek et al. Due to significant oxidation activity and exceptional hydrophilicity, using biologically inert and non-toxic, Fujishima et al. investigated TiO₂ nanoparticles as antibacterial agents [156-158].

Many researchers investigated the antibacterial activity of nanoparticles with light irradiation as these nanoparticles have high absorption characteristics. The plausible mechanism for radiative antibacterial activity is as follows: (a) The excitation of nanoparticles produces electron-hole pair and metal ions, (b) The formation of reactive oxygen species (ROS), (c) vibrational relaxation of electrons leading to hyperthermia, (d) Infiltrating the bacterial membrane by reactive oxygen species (ROS) and metal ions, (e) Increased rupture of the bacterial membrane due to hyperthermia, and (f) binding of nucleic acid to ROS and ions leads to cell death.

Chen et al. have made a composite of Fe₃O₄/TiO₂ magnetic nanoparticles to check their photo-killing efficiency [159]. Karunakaran et al. synthesised NiO-TiO₂ composite nanoparticles and compared their antibacterial activity against *E. coli* in the presence and absence of light, in which they showed increased activity within 30 minutes of light illumination. In contrast, the activity was negligible under dark conditions [157]. Other metal oxides, such as CeO₂, Fe₂O₃/Fe₃O₄, MgO, ZnO, etc., also proved their role as antibacterial agents. Still, due to their large band gap, these metal oxides can exhibit efficient antibacterial activity only under UV radiation [149].

Metal sulphides are becoming increasingly prevalent due to their nature for imitating natural minerals [160]. Even at small doses, these inorganic substances have potent antibacterial action [149, 161]. On the other hand, due to their biodegradability, safety, and biocompatibility properties, sulphur has significance for catalytic bioremediation and the production of antibacterial and anticancer chemicals. Due to well-dispersed S 3p orbits and the greater anion radius of S atoms, transition metal sulphides have a smaller band gap than transition metal oxides. So, they have an excellent capacity for utilizing solar energy due to their appropriate energy band structure, which results in strong photodynamic damage to

bacteria due to the efficient creation of ROS. Additionally, they have an excellent capacity for converting light into heat, or the photothermal effect, which opens up a second potential therapeutic application for them by effectively eradicating germs. Due to the effective surface functionalization, the method for replicating the natural antibacterial action may be easily accomplished by transition metal chalcogenides [162]. These nanoparticles may breach cell walls due to their oxidative characteristics, and they can tolerate severe processing conditions better than organic antibacterial agents [154].

Ag₂S is one such material exhibiting this property explored by the scientific community. The antimicrobial activity of Ag₂S was studied against *E. coli*, *P. aeruginosa*, *S. aureus*, and *B. thuringiensis* by Ayodhya et al. [163]. Sun et al. successfully synthesised Ag₂S/Bi₂S₃ nanocomposites to photocatalytic inactivate *E. coli* bacteria [164]. Researchers have also explored the antibacterial activity of other transition metal sulphides. Due to deeper conduction and valence bands, ZnS has become recognized as a promising biocompatible antibacterial material [146, 166]. Malarkodi et al. have synthesised and studied the antibacterial activity of ZnS and CdS nanoparticles against oral pathogens *Streptococcus*, *S. aureus*, *Lactobacillus sp., and Candida albicans* (*C. albicans*) [166]. Ganguly et al. have synthesised ZnS and checked their antibacterial activity against twelve bacterial stains like *S.aureus* 8531, 8532, *B. subtilis* UC 564, *Sh. Flexneri* 6, *E.coli* C600, *K. pneumonia* 10031, *P.aeruginosa* 27853, *E.coli* K12 Row, *A. baumanii* 462, *Sh. sonnei* 9774, *V. cholerae* 14033 and *S. enteric* 11, in which *Sh. sonnei* 9774 was resistant to ZnS [167].

MoS₂, with stable, unique, and wide surface area due to layered structure, can connect with many biomolecules [168]. Zang et al. have successfully synthesised and used CuS@MoS₂, which showed their antibacterial activity against *E. Coli* and *S. aureus* for wound dressing [79]. More recently, ternary metal chalcogenide nanoparticles with tunable narrow bandgap, high NIR absorption, non-toxic, biocompatibility, optoelectronic, thermoelectric, and catalytic nature have received immense interest. These show the synergistic effect of both metals in one compound, accelerating its applicability in different fields. Kannan et al. have successfully tested and confirmed the antibacterial activity exhibited by Cu₂WS₄ nanoparticles with grampositive, *M. luteus*, *B. subtilis* and gram-negative, *P. aeruginosa*, *K. pneumoniae*, *E. coli*, and bacteria [169]. AgBiS₂ is one among the ternary chalcogenides which have enticed many due to their chemical stability, tunable electronic and optical properties, high photothermal conversion efficiency, earth abundance, biocompatibility, non-toxic nature, etc. [31, 135, 141]. An increased ROS production was observed by Cheng et al. for AgBiS₂ nanoparticles upon

NIR irradiation which eliminated the infection caused by *S. aureus*, making it an optimal candidate as an antibacterial agent and have proven AgBiS₂ nanoparticles to be non-toxic both in-vivo and in-vitro [82].

1.6.4. Chemical Oxygen Demand (COD)

Chemical oxygen demand (COD), Biochemical oxygen demand (BOD) and Total organic carbon (TOC), and are three frequently employed criteria to measure the oxygen demand of organic contaminants in an aqueous system. The soluble organic compounds are evaluated by TOC analysis, whereas the portion of organic matter which can be oxidised and causes eutrophication in aquatic systems is not obtained. The requirement of costly equipment also constrains its applicability. Compared to BOD analysis, COD analysis offers several benefits, including quick and straightforward experimental procedures that produce stable results. As a result, in wastewater treatment plants, COD levels are frequently utilized as the primary water quality parameter [170].

COD is a quality parameter to gauge the amount of organic and inorganic pollutants degradable by chemicals in superficial waters and wastewater. COD refers to the amount of oxygen required to oxidize contaminants in water [171]. The test allows the quantification of waste through the total amount of oxygen required to oxidize organic matter to water and CO₂ [172, 173]. With regards to the reaction time, production of secondary pollutants, cost, several innovative approaches, and convenience of operation, such as Flow Injection Analysis (FIA), the Chemiluminescence (CL) method, and radiation-aided digestion methods have been developed, which shows several benefits over traditional methods. However, applying and implementing newly developed methods for standard COD laboratory analysis is challenging. Furthermore, the new techniques can only partially reduce the use of dangerous chemicals. Further complicating matters is chloride interference, which is not normally oxidized.

Standard COD reagents like Ag⁺, Hg²⁺, Cr⁶⁺ and salts are frequently employed for reducing chloride interferences. Unfortunately, it isn't advisable to use these salts because of their hazardous impact on environment. Numerous factors, including sample matrices, frequency of routine analyses, measurement frequency, instrumentation cost, interference tolerance, analytical parameters, etc., influence the selection of an appropriate method for the determination of COD. Other experimental variables like pH, reagents, and temperature also impacts COD scores. Therefore, credible and reproducible procedures such as dichromate and permanganate methods are still used as the established protocols [170].

The dichromate method is used for evaluating the water quality in water bodies that are either moderately or deeply polluted. In contrast, the permanganate method is used for analysing surface or river water [174]. The permanganate method has some shortcomings. Many organic substances either do not convert at all or only partially convert. Further, manganese dioxide is produced when permanganate reacts with substances that it readily attacks, increasing the utilization of permanganate by organic matter. Theoretically, with increase in sulphuric acid concentration and temperature, the efficiency of oxidation should rise. In practical applications the oxidation temperature should be relatively low, about 60 °C, to prevent permanganate breakdown. Hence this situation drastically restricts the permanganate method's application as it is utilized at a far lower temperature. The stability of dichromate in boiling concentrated sulphuric acid solution at temperature less than 150 °C and its increased oxidising capacity in addition to its low cost, makes the dichromate reflux method preferable over the permanganate method [175].

The principle followed for the analysis is that the initial concentration of organic compounds in the sample is estimated from a titrimetric analysis of the oxidant still present in the sample following the refluxing digesting process. Potassium dichromate must be in excess for all organic materials to oxidize. While oxidizing organic compounds in water, potassium dichromate undergoes reduction to form Cr^{3+} . The surplus amount of potassium dichromate must be estimated to calculate the quantity of Cr^{3+} when oxidation is finished accurately. To do this, Ferrous Ammonium sulphate (FAS) is titrated against excess potassium dichromate until all extra oxidising agent has been converted to Cr^{3+} . The quantity of FAS used in the titration corresponds to the amount of excess potassium dichromate added to the sample, which indirectly gives the measure of organic content in the water sample. Usually, ferroin indicator is introduced during titration. Once the excess dichromate has completely been removed, the ferroin indicator turns reddish-brown from blue-green. The general oxidation of organic substances by potassium permanganate can be summarised as follows:

$$C_n H_a O_b N_c + dC r_2 O_7^{2-} + (8d+c) H^+ \longrightarrow nCO_2 + \frac{a+8d-3c}{2} H_2 O + cN H_4^+ + 2dC r^{3+}$$

where, $d = 2n/3 + a/6 - b/3 - c/2$

As mentioned above the excess dichromate is determined using FAS by titration method. In that:

$$6Fe^{2+} + Cr_2O_7^{2-} + 14H^+ \longrightarrow 6Fe^{3+} + 2Cr^{3+} + 7H_2O$$

In concentrated sulphuric acid, the chromyl chloride formation occurs.

$$K_2Cr_2O_7 + 4NaCl + 6H_2SO_4 = 2KHSO_4 + 4NaHSO_4 + 2CrO_2Cl_2 + 3H_2O_4$$

In the course of oxidation of organic compounds by dichromate, chloride formation occurs, whose interference is thereby attenuated by HgSO₄ and results in HgCl₂ formation. It can be shown as:

$$Cr_2O_7^{2-} + 6Cl^- + 14H^+ \longrightarrow 3Cl_2 + 2Cr^{3+} + 7H_2O$$

 $Hg^{2+} + 2Cl^- \longrightarrow HgCl_2$

Since a wide range of compounds are oxidised by potassium dichromate, this method is preferred over other traditional methods [175].

After titration, C.O.D is calculated by the formula,

C.O.D =
$$\frac{[V_B - V_S] \times N \times 8 \times 1000}{V_S}$$
 mg/L,

where, N = normality of ferrous ammonium sulphate (FAS),

V_B = volume (ml) of ferrous ammonium sulphate used for blank titration,

 V_S = volume (ml) of ferrous ammonium sulphate used for sample titration,

8 = milli equivalent weight of oxygen.

Higher the C.O.D value, higher the contaminants in water sample.

Abdel Messih et al. have synthesised ZnO@SiO2 nanoparticles for photocatalytic degradation of methylene blue, and to determine the efficiency of the catalyst, they have performed COD analysis [176]. Zhao et al. have explored the potential of diphenylanthrazoline compounds against methylene blue by measuring the COD after degradation of dye, in which they found 2,8-Bis(4-triphenylamino)-4,6- diphenyl-1,9-anthrazoline compound with highest efficiency and lowest COD value [177]. Gajbiye has synthesised ZnO nanoparticles and studied the impact of modulating the parameters like loading of catalyst, concentration and temperature of dye solution, and pH of the medium on photocatalytic degradation of methylene blue and confirmed their efficiency by reporting lower COD value [178]. A comparative study on photocatalytic degradation of Rhodamine B using bare and PEG-caped ZnO nanoparticles were performed and the potency of UV shielding of PEG-capped ZnO with the support of COD measurement was confirmed by Sudha et al. [172]. Borhade et al. compared photocatalytic

degradation of methylene blue dye solution by PbO and Ni-doped PbO nanoparticles, and the mineralization of dye was confirmed with COD measurement [179]. Sari et al. have synthesised TiO₂ nanoparticles to study the influence of irradiation time and catalytic concentration on photocatalytic degradation of the dye, Procion red and confirmed the results using COD analysis [180]. Sahoo et al. have taken one step ahead by studying the photodegradation of methylene blue solution and real textile wastewater using Ag-doped TiO₂ nanoparticles. They confirmed the extent of mineralization by COD analysis in different time intervals [181].

1.6.5. Non-enzymatic glucose sensing

A sensor is a tool that captures a substance's chemical, biological, or physical changes and transforms them to quantifiable signals. A sensor contains three essential components: a transducer, a sensitive detector, and a signal processor. The signal processor gathers, amplifies, and displays while the transducer creates a matching signal. A sensitive detector primarily responds selectively to the particular analyte. An electrochemical sensor is a type of sensor that produces an electrical signal in response to changes in the target material. The traditional three-electrode system is employed in electrical analysis and detection. Carbon, metal oxide, and metal are used to create the working electrode. For analysis and better selectivity, electrodes are coated with functional nanomaterials. Cyclic and square wave voltammetry are generally used electrochemical techniques to identify the target molecules successfully.

Glucose, the primary source of energy, is one of the most common polysaccharides in nature. People's health might suffer from hypoglycemia as well as hyperglycaemia. People with hypoglycemia will experience hunger, palpitations, or even pass out, whereas those with hyperglycaemia have a slightly higher chance of developing diabetes. Additionally, one of the metrics to gauge a fruit or vegetable's quality and serve as a guide for farming is the evaluation of its glucose content. It is clear from the description above that accurate, quick, easy, and real-time glucose testing is crucial for clinical diagnosis, the food sector, and other industries [182].

Diabetes is a dangerous chronic illness that significantly contributes to disability and mortality. Therefore, it is crucial to assess and manage glucose levels. Electrochemical and analytical detection methods are the two techniques used to detect glucose. Electrochemical detection methods are superior to analytical techniques like optical, chromatographic, colourimetric, and others because of their low cost, high sensitivity, accuracy, portability, and ease of manufacture. The electrochemical methods for detecting glucose rely on the catalytic activity of an enzyme that has been immobilized, where the primary requirement is the enzyme

has to regenerate rapidly and methodically [183, 184]. There are two types of electrochemical glucose sensors.

- a) Enzymatic glucose sensor The first enzymatic glucose sensor invented by Clark and Lysons had drawbacks due to its sensitivity towards temperature, pH, humidity, chemicals, high cost, and limited stability. In this class of sensors, glucose dehydrogenase (GDH) and glucose oxidase (GOx) are the enzymes used commonly. While GOx is more stable than other enzymes and highly selective for glucose molecules, it promptly becomes inactive above pH 8 or below pH 2. At higher temperatures, it can suffer irreparable damage. Surfactants, such as sodium-dodecyl sulphate at low pH and hexadecyltrimethyl ammonium bromide at high pH, have a sensitive effect on it. The sensors based on GOx can be significantly impacted by exposure to fluctuating humidity. GDH, with a higher activity than GOx, is more often utilized with pyrroloquinoline quinone (PQQ) and adenine dinucleotide (FAD). Maltose and galactose, however, can influence blood glucose monitors that employ GDH-PQQ. In contrast, GDH-FAD is not sensitive to oxygen and maltose, whereas they are responsive to a different sugar with comparable activity to glucose, that is, xylose. According to reports, GDH systems exhibit inaccuracy in the observed glucose level because they react differently to maltose and xylose than GOx systems [185].
- **b)** Non-enzymatic glucose sensor These fourth-generation glucose sensors use nanostructured metals and metal oxides as electrodes to directly electro-oxidize glucose, resulting in significant electrocatalytic activity towards glucose. These are preferred over enzymatic glucose sensors due to simple manufacturing, excellent chemical and thermal stability, repeatability, and cheap cost.

For electrochemical glucose sensing, the three-electrode system, consisting of (i) counter electrode (CE), (ii) reference electrode (RE) and (iii) working electrode (WE), is often used to perform the electrochemical approach for the measurement of glucose concentration. The first circuit, made up of the WE and the CE, is utilized to measure current and potential accurately. The second circuit, on the other hand, is for the loop of measuring the potential between the WE and the RE. The experimental setup is shown in Figure 1.7.

Reference Electrode (RE) Calomel Electrode Pt wire Electrolyte (Alkaline solution)

Figure 1.7. Experimental setup for glucose sensing.

Many electrochemical methods, such as amperometry, electrochemical impedance spectroscopy (EIS), linear sweep voltammetry (LSV), cyclic voltammetry (CV), etc., are frequently used to find and quantify the glucose in the electrolyte. The CV is typically used in investigations of glucose sensors to characterise the glucose-sensing materials and to investigate the responses at WE by electroactive materials. Since impedence measures the effectiveness of electron transfer, EIS is another simple way to evaluate the conduct of materials as sensing electrodes. A constant electric potential is applied and corresponding current response is evaluated as a function of time in amperometric measurements. They are often used for evaluating the performances and gaining information on the rapid response of glucose-sensing materials. First, the sensitivity can be studied by continually adding glucose to the electrochemical setup while maintaining the potential at WE constant. Second, the selectivity of sensing material is analyzed by adding glucose along with interfering molecules into the electrochemical cell [186].

1.6.5.1. Mechanism of non-enzymatic glucose sensing

The occurrence of electrochemical oxidation processes of glucose by electroactive materials leading to the passage of electrons, which is then detected by an external circuit, is the basic concept of glucose sensing. The mechanism for non-enzymatic glucose sensing can be explained using two concepts: a) Activated Chemisorption Model, which is the first model

proposed by Pletcher in 1984 (figure 1.8) and b) Incipient Hydrous Oxide Adatom Mediator Model (IHOAM), which is the second model, proposed by Bruke and his co-workers in 1994 (figure 1.9). According to Activated Chemisorption Model, the mechanism of electrochemical glucose oxidation is as follows [185, 186]:

- a) Glucose adsorption on the surface of electroactive material.
- b) Simultaneous weak bond formation between adsorbed glucose and electroactive material and abstraction of hydrogen connected to hemiacetal carbon.
- c) Simultaneous weak bond formation between both hemiacetal carbon and abstracted hydrogen to the electrode surface and bond breakage between hemiacetal carbon and hydrogen.
- d) Desorption of dehydrogenated glucose molecule.

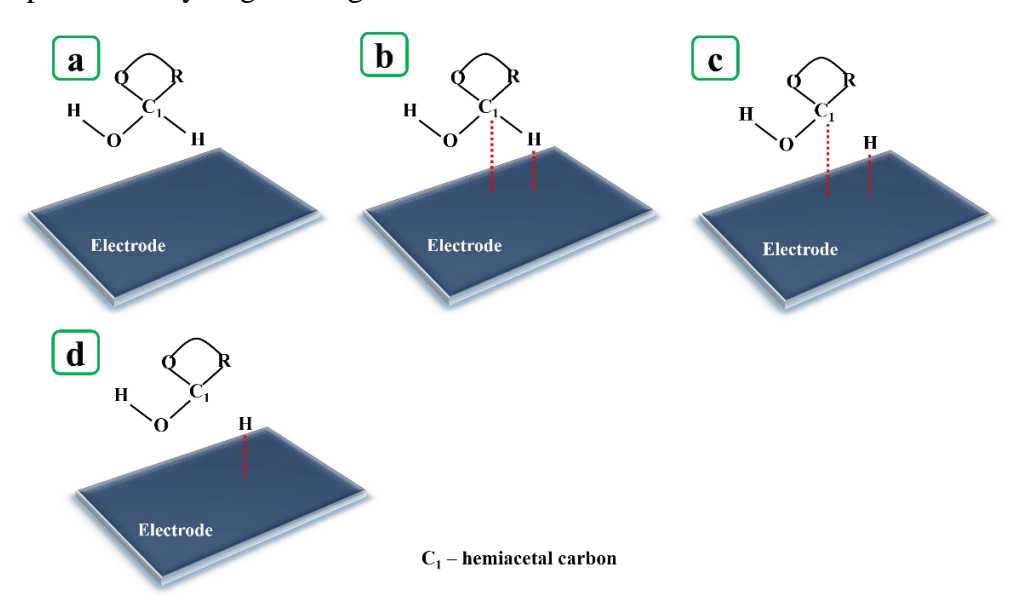


Figure 1.8. Mechanism of electrocatalytic oxidation of glucose according to Activated Chemisorption Model.

According to the Incipient Hydrous Oxide Adatom Mediator Model, the electrochemical glucose oxidation can be explained as follows:

- a) An incipient hydrous oxide (M-OH) is formed when hydroxide ion present in the electrolyte gets adsorbed onto the material surface.
- b) The hydrous oxide formed oxidise glucose to gluconolactone, which can be further oxidised to Gluconic acid in presence of OH ion and get reduced to metallic state.

Gluconic acid

Figure 1.9. Mechanism of electrocatalytic oxidation of glucose according to Incipient Hydrous Oxide Adatom Mediator (IHOAM) model.

Attempts are being made to develop non-enzymatic glucose sensors inorder to address the shortcomings mentioned above of conventional enzymatic sensors. Numerous metals, like Au, Pd, and Pt, along with oxides, sulphides, and selenides of Ni, Zn, Ti, Fe, Cu and Co, bimetallic complexes, carbon compounds, and polymers have been studied for their ability to oxidize glucose. Ye et al. have compared the electrocatalytic activity of controlled monometallic Pd nanocubes and uncontrolled polyhedral Pd nanoparticles [187]. Cu/reduced graphene oxide was synthesised and employed as a glucose sensor by Phetsang et al. Arif et al. have synthesised Ag@TiO₂@MOF (ZIF-65) and applied it for glucose sensing [188].

The materials such as NiO hollow spheres, CuO nanowires, Pd nanocubes, Fe₂O₃ nanowire arrays, NiO-Ag nanofibers AgNPs/CuO nanofibers, and Au@Cu₂O core-shell structure possess the potential to improve certain performance characteristics, including long-term stability, selectivity and detection sensitivity [186]. Similarly, employing NiSe₂ is a good option for electron transfer-assisted sensing applications due to its distinctive electrochemical, optical and physical characteristics, including excellent surface-to-volume ratio, narrow bandgap, high mobility of charge carriers, inherent electrical conductivity, and resistance to chloride poisoning [188, 189]. CoSe₂ is also a valuable material for sensing applications owing to its quick electron transfer capability [190, 191].

1.7. Scope of Thesis

1.7.1. Definition of problem

Capping agents are organic moieties employed during the production of nanoparticles to prevent nanoparticles from aggregation and precipitation. They also control their growth, possibly introducing surface functionalization and stability. Stabilizers, passivating agents and protective agents are some of the characteristic names for these organic surfactant compounds. These compounds are essential for building nanoparticles because they preserve the surfaces, regulate particle size and development rate, and make the particles soluble in various solvents. The capping agent must have enough mass to avoid agglomeration and be tiny enough to passivate the surface. Balancing these two necessities makes an ideal capping agent.

The capping agents generally consist of a head group with elements having a lone pair of electrons which helps in the passivation of the surface of nanoparticles, and a tail group with a long alkyl chain which gives the materials their solubility. Different modes of capping are observed during synthesis. (1) Passivation, in which passivating agents like polymers and organic molecules form a thin insulating protection layer. (2) Stabilization, by supplying electrostatic and/or steric repulsions between the particles, the stabilizing agent inhibits the aggregation of nanoparticles in the reaction media. (3) Functionalization, in which capping is done by organic polymer, with inorganic salts and compounds having heteroatoms, to attain specific activity or selectivity according to the applications.

The close contact among the particles decides the characteristics of the materials. A detailed examination of every synthetic technique previously described reveals the addition of some organic or polymeric molecules to regulate the particle size during the synthesis of nanoparticles. These organic molecules serve as a capping for the particles, and they are not fully eliminated after the process. These non-active components, or residual substances, cause an inorganic-organic interference. These inorganic-organic interfaces created by capping agents affect the characteristics of these materials. Examples include:

- It prevents interfacial electron transfer.
- They are lowering charge mobility.
- Blocking active spots on the surface of materials impacts their catalytic capabilities.

• Since they are difficult to detach from nanoparticles, their non-biodegradable nature might add to their toxicity when used in biomedical applications.

Earlier, our group developed a surfactant-free method to create colloidal nanocrystals to get around the issue of undesired organic moieties. For this purpose, we used hexamethyldisilazane (HMDS), which served dual functions by acting as a stabilizing agent and a reductant. In addition, it also served a primary function as a reaction medium. In the reaction, metal chlorides were selected as metal precursors due to their solubility in HMDS, whereas sulphur, selenium and thiourea were employed as chalcogenide sources. The generation of trimethylsilyl groups drove the reaction. We have also determined the formation of polymeric [SN(SiMe₃)]x as an intermediate in this reaction. This polymeric intermediate helped prevent the aggregation of nanoparticles during the reaction. Many nanoparticles like CuS, Ni₃S₄, Bi₂S₃, CdS, In₂S₃, and CuS/CdS were synthesised successfully using the HMDS-assisted method. When those materials were subjected to various applications, they fared better as catalysts or photo-responsive substances [192]. The general mechanism of the hexamethyldisilazane (HMDS)–assisted method can be illustrated as shown in the scheme below.

$$nMX + (NH_2)_2CS/S/Se \xrightarrow{\mathbf{Reflux}} \mathbf{P}_{S} = \mathbf{P}_{S$$

$$= - \frac{1}{\sqrt{\frac{8}{8}}} - \frac{1}{\sqrt{\frac{1}{8}}}$$

Scheme 1.34. General reaction mechanism of HMDS-assisted synthesis of nanomaterial

1.7.2. Aim of current work

In our current work, we have successfully synthesised several binary, ternary metal chalcogenides as well as composites with excellent catalytic characteristics utilising the HMDS-assisted synthetic technique. No further stabilizers are needed because HMDS served

as the only reaction medium, stabilising agent, and reductant in each reaction. We were able to remove any unreacted HMDS and precursor contaminants from our reaction mixtures by washing the components with organic solvents and applying a vacuum after the reactions.

In the current work, we are successful in producing a variety of highly crystalline and high purity grade nanomaterials, including ZnS, Transition metal doped ZnS (M: ZnS) where M = Cu, Ni, Cd, Bi, Mn, AgBiS₂, with and without polyethylene glycol and oleic acid / oleylamine as surfactants. We have also produced SnS₂ with and without polyethylene glycol, NiSe₂, CoSe₂ and their composite NiSe₂/CoSe₂. We observed that the HMDS-assisted method produced nanomaterials with improved characteristics compared with materials with organic capping agents. In this thesis, we provided photocatalytic dye degradation (RhB, MB), anticancer and antibacterial activity, and non-enzymatic glucose sensing, all catalysed by surfactant-free nanomaterials. A detailed study of the effect of bare surfaces on nanoparticles in different fields of applications is examined and described in the thesis.

1.8. References

- 1. Roy, A. and Bhattacharya, J. Nanotechnology in industrial wastewater treatment. *IWA Publishing*. **2015**.
- 2. Jamkhande, P.G., Ghule, N.W., Bamer, A.H. and Kalaskar, M.G. Metal nanoparticles synthesis: An overview on methods of preparation, advantages and disadvantages, and applications. *J Drug Deliv Sci Technol.* **2019**, 53, 101174.
- 3. Chandra, R., Chawla, A.K. and Ayyub, P. Optical and structural properties of sputter-deposited nanocrystalline Cu₂O films: Effect of sputtering gas. *J. Nanosci. Nanotechnol.* **2006**, 6, 1119-1123.
- 4. Bayda, S., Adeel, M., Tuccinardi, T., Cordani, M. and Rizzolio, F. The history of nanoscience and nanotechnology: from chemical–physical applications to nanomedicine. *Molecules*. **2019**, 25, 112.
- 5. Pacioni, N.L., Borsarelli, C.D., Rey, V. and Veglia, A.V. Synthetic routes for the preparation of silver nanoparticles: A mechanistic perspective. *Silver nanoparticle applications: In the fabrication and design of medical and biosensing devices*. **2015**, 13-46.
- 6. Rajput, N. Methods of preparation of nanoparticles-a review. *Int J Adv Eng Sci Appl.* **2015**, 7, 1806-1811.
- 7. Narayanan, R. and El-Sayed, M.A. Shape-dependent catalytic activity of platinum nanoparticles in colloidal solution. *Nano Lett.* **2004**, 4, 1343-1348.
- 8. Moura, D., Souza, M.T., Liverani, L., Rella, G., Luz, G.M., Mano, J.F. and Boccaccini, A.R. Development of a bioactive glass-polymer composite for wound healing applications. *Mater. Sci. Eng. C.* **2017**, 76, 224-232.
- 9. Banerjee, K., Das, S., Choudhury, P., Ghosh, S., Baral, R. and Choudhuri, S.K. A novel approach of synthesising and evaluating the anticancer potential of silver oxide nanoparticles in vitro. *Chemotherapy*. **2017**, 62, 279-289.
- 10. Gomez-Romero, P. Hybrid organic—inorganic materials—in search of synergic activity. *Adv. Mater.* **2001**, 13,163-174.
- 11. Shaikh, S.F., Mane, R.S., Min, B.K., Hwang, Y.J. and Joo, O.S. D-sorbitol-induced phase control of TiO₂ nanoparticles and its application for dye-sensitized solar cells. *Sci. Rep.* **2016**, 6, 20103.
- 12. Gracias, D.H., Tien, J., Breen, T.L., Hsu, C. and Whitesides, G.M. Forming electrical networks in three dimensions by self-assembly. *Science*. **2000**, 289, 1170-1172.

- 13. Choi, Y. and Lee, S.Y. Biosynthesis of inorganic nanomaterials using microbial cells and bacteriophages. *Nat. Rev. Chem.* **2020**, 4, 638-656.
- 14. Khan, I., Saeed, K. and Khan, I. Nanoparticles: Properties, applications and toxicities. *Arab. J. Chem.* **2019**, 12, 908-931.
- 15. Virlan, M.J.R., Miricescu, D., Radulescu, R., Sabliov, C.M., Totan, A., Calenic, B. and Greabu, M. Organic nanomaterials and their applications in the treatment of oral diseases. *Molecules*. **2016**, *2*, 207.
- Abid, N., Khan, A.M., Shujait, S., Chaudhary, K., Ikram, M., Imran, M., Haider, J., Khan, M., Khan, Q. and Maqbool, M. Synthesis of nanomaterials using various top-down and bottom-up approaches, influencing factors, advantages, and disadvantages: A review. *Adv. Colloid Interface Sci.* 2022, 300, 102597.
- 17. Zhu, W., Cheng, Y., Wang, C., Pinna, N. and Lu, X. Transition metal sulfides meet electrospinning: versatile synthesis, distinct properties and prospective applications. *Nanoscale*. **2021**, 13, 9112-9146.
- 18. Pradeep, T. *Textbook of nanoscience and nanotechnology*. **2012**, McGraw-Hill Education.
- 19. Meyers, M.A., Mishra, A. and Benson, D.J. Mechanical properties of nanocrystalline materials. *Prog. Mater. Sci.* **2006**, 51, 427-556.
- 20. Nadagouda, M.N., Speth, T.F. and Varma, R.S. Microwave-assisted green synthesis of silver nanostructures. *Acc. Chem. Res.* **2011**, 44, 469-478.
- 21. Tavakoli, A., Sohrabi, M. and Kargari, A. A review of methods for synthesis of nanostructured metals with emphasis on iron compounds. *Chem. Pap.* **2007**, 61,151-170.
- 22. Tsuzuki, T. and McCormick, P.G. Mechanochemical synthesis of nanoparticles. *J. Mater. Sci.* **2004**, 39, 5143-5146.
- 23. Nie, L. and Zhang, Q. Recent progress in crystalline metal chalcogenides as efficient photocatalysts for organic pollutant degradation. *Inorg. Chem. Front.* **2017**, 4, 1953-1962.
- Gao, M.R., Xu, Y.F., Jiang, J. and Yu, S.H. Nanostructured metal chalcogenides: synthesis, modification, and applications in energy conversion and storage devices. *Chem Soc Rev.* 2013, 42, 2986-3017.
- 25. Dharmalingam, P., Palani, G., Apsari, R., Kannan, K., Lakkaboyana, S.K., Venkateswarlu, K., Kumar, V. and Ali, Y. Synthesis of metal oxides/sulfides-based nanocomposites and their environmental applications: A review. *Mater. Today Sustain.* **2022**, 20, 100232.
- 26. Zhao, X., An, Q. and Cai, J. Recent Progress in the Transition Metal Sulfide/Phosphide for Cancer Theranostic Applications. *Cancer Insight*. **2022**, 1, 52-75.

- Presutti, D., Agarwal, T., Zarepour, A., Celikkin, N., Hooshmand, S., Nayak, C., Ghomi, M., Zarrabi, A., Costantini, M., Behera, B. and Maiti, T.K. Transition metal dichalcogenides (TMDC)-based nanozymes for biosensing and therapeutic applications. *Materials*. 2022, 15, 337.
- 28. Rauf, M., Shah, S.S., Shah, S.K., Shah, S.N.A., Haq, T.U., Shah, J., Ullah, A., Ahmad, T., Khan, Y., Aziz, M.A. and Hayat, K. Facile hydrothermal synthesis of zinc sulfide nanowires for high-performance asymmetric supercapacitor. *J. Saudi Chem. Soc.* **2022**, 26,101514.
- 29. Wei, Z., Lu, Y., Zhao, J., Zhao, S., Wang, R., Fu, N., Li, X., Guan, L. and Teng, F. Synthesis and luminescent modulation of ZnS crystallite by a hydrothermal method. *ACS Omega*. **2018**, 3,137-143.
- 30. Manimozhi, T., Archana, J., Navaneethan, M. and Ramamurthi, K. Shape-controlled synthesis of AgBiS₂ nano-/microstructures using PEG-assisted facile solvothermal method and their functional properties. *Appl. Surf. Sci.* **2019**, 487, 664-673.
- 31. Gajendiran, J. and Rajendran, V. Synthesis of SnS₂ nanoparticles by a surfactant-mediated hydrothermal method and their characterization. *Adv. Nat. Sci.: Nanosci. Nanotechnol.* **2011**, 2, 015001.
- 32. Sobhani, A., Davar, F. and Salavati-Niasari, M. Synthesis and characterization of hexagonal nano-sized nickel selenide by simple hydrothermal method assisted by CTAB. *Appl. Surf. Sci.* **2011**, 257, 7982-7987.
- 33. Zhang, W., Yang, Z., Liu, J., Hui, Z., Yu, W., Qian, Y., Zhou, G. and Yang, L. A hydrothermal synthesis of orthorhombic nanocrystalline cobalt diselenide CoSe₂. *Mater. Res. Bull.* **2000**, 35, 2403-2408.
- 34. Owens, G.J., Singh, R.K., Foroutan, F., Alqaysi, M., Han, C.M., Mahapatra, C., Kim, H.W. and Knowles, J.C. Sol–gel based materials for biomedical applications. *Prog. Mater. Sci.* **2016**, 77, 1-79.
- 35. Pandey, S. and Mishra, S.B. Sol–gel derived organic–inorganic hybrid materials: synthesis, characterizations and applications. *J Solgel Sci Technol*. 2011, 59, 73-94.
- 36. Bhattacharjee, B., Ganguli, D., Chaudhuri, S. and Pal, A.K. Synthesis and optical characterization of sol–gel derived zinc sulphide nanoparticles confined in amorphous silica thin films. *Mater. Chem. Phys.* **2003**, 78, 372-379.
- 37. Vijayan, S., Umadevi, G., Mariappan, R., Narayanan, M., Narayanamoorthy, B. and Kandasamy, S. High luminescence efficiency of Copper doped Zinc Sulfide (Cu: ZnS) nanoparticles towards LED applications. *Mater. Today Proc.***2020**.

- 38. Govindan, V., Kashinath, L., Joseph Daniel, D. and Sankaranarayanan, K. Sol-gel mediated microwave synthesis of pure, La and Zr doped SnS₂ nanoflowers an efficient photocatalyst for the degradation of methylene blue. *J. Mater. Sci.: Mater. Electron.* **2019**, 30, 7963-7973.
- 39. Mohapatraa, R., Kaundala, J.B. and Goswamia, Y.C. Synthesis of optically important transparent SnS₂/PS composites films through chemical route and their photocatalytic applications. *J. Ovonic Res.* **2022**, 18, 343-355.
- 40. Alagiri, M., Ponnusamy, S. and Muthamizhchelvan, C. Synthesis and characterization of NiO nanoparticles by sol–gel method. *J. Mater. Sci.: Mater. Electron.* **2012**, 23, 728-732.
- 41. Mugundan, S., Rajamannan, B., Viruthagiri, G., Shanmugam, N., Gobi, R. and Praveen, P. Synthesis and characterization of undoped and cobalt-doped TiO₂ nanoparticles via sol–gel technique. *Appl. Nanosci.* **2015**, *5*, 449-456.
- 42. El-Khawaga, A.M., Zidan, A. and Abd El-Mageed, A.I. Preparation methods of different nanomaterials for various potential applications: A Review. *J. Mol. Struct.* **2023**, 1281, 135148.
- 43. Gedi, S., Alhammadi, S., Noh, J., Minnam Reddy, V.R., Park, H., Rabie, A.M., Shim, J.J., Kang, D. and Kim, W.K. SnS₂ nanoparticles and thin film for application as an adsorbent and photovoltaic buffer. *Nanomaterials*. **2022**, 12, 282.
- 44. Rema Devi, B.S., Raveendran, R. and Vaidyan, A.V. Synthesis and characterization of Mn²+-doped ZnS nanoparticles. *Pramana J. Phys.* **2007**, 68, 679-687.
- 45. Gou, X.L., Chen, J. and Shen, P.W. Synthesis, characterization and application of SnS_X (x= 1, 2) nanoparticles. *Mater. Chem. Phys.* **2005**, 93, 557-566.
- 46. Nakazawa, T., Kim, D., Oshima, Y., Sato, H., Park, J. and Kim, H. Synthesis and application of AgBiS₂ and Ag₂S nanoinks for the production of IR photodetectors. *ACS Omega.* **2021**, 6, 20710-20718.
- 47. Zhu, J., Zhou, M., Xu, J. and Liao, X. Preparation of CdS and ZnS nanoparticles using microwave irradiation. *Mater. Lett.* **2001**, 47, 25-29.
- 48. Yang, H., Huang, C., Su, X. and Tang, A. Microwave-assisted synthesis and luminescent properties of pure and doped ZnS nanoparticles. *J. Alloys Compd.* **2005**, 402, 274-277.
- 49. Tipcompor, N., Thongtem, S. and Thongtem, T. Transformation of cubic AgBiS2 from nanoparticles to nanostructured flowers by a microwave-refluxing method. *Ceram. Int.* **2013**, 39, S383-S387.

- 50. Park, S., Park, J., Selvaraj, R. and Kim, Y. Facile microwave-assisted synthesis of SnS₂ nanoparticles for visible-light responsive photocatalyst. *J Ind Eng Chem.* **2015**, 31, 269-275.
- 51. Younas, W., Naveed, M., Cao, C., Zhu, Y., Du, C., Ma, X., Mushtaq, N., Tahir, M. and Naeem, M. Facile one-step microwave-assisted method to synthesise nickel selenide nanosheets for high-performance hybrid supercapacitor. *J. Colloid Sci.* **2022**, 608, 1005-1014.
- 52. Naveenraj, S., Mangalaraja, R.V., Krasulyaa, O., Syed, A., Ameen, F. and Anandan, S. A general microwave synthesis of metal (Ni, Cu, Zn) selenide nanoparticles and their competitive interaction with human serum albumin. *New J. Chem.* **2018**, 42, 5759-5766.
- 53. Liu, J.Z., Yan, P.X., Yue, G.H., Kong, L.B., Zhuo, R.F. and Qu, D.M. Synthesis of doped ZnS one-dimensional nanostructures via chemical vapor deposition. *Mater. Lett.* **2006**, 60, 3471-3476.
- 54. Chen, L., Liu, E., Teng, F., Zhang, T., Feng, J., Kou, Y., Sun, Q., Fan, J., Hu, X. and Miao, H. Two-dimensional SnS2 nanosheets arrays as photoelectrode by low temperature CVD method for efficient photoelectrochemical water splitting. Appl. Surf. Sci. 2019, 467, 698-707.
- 55. Zhou, P., Wang, X., Guan, W., Zhang, D., Fang, L. and Jiang, Y. SnS₂ nanowall arrays toward high-performance sodium storage. *ACS Appl. Mater. Interfaces.* **2017**, 9, 6979-6987.
- Masud, J., Liyanage, W.P., Cao, X., Saxena, A. and Nath, M. Copper selenides as high-efficiency electrocatalysts for oxygen evolution reaction. ACS Appl. Energy Mater. 2018, 1, 4075-4083.
- 57. Khan, H.R., Aamir, M., Malik, M.A., Tahir, A.A., Akram, B., Murtaza, G., Choudhary, M.A. and Akhtar, J. Chemically vaporized cobalt incorporated wurtzite as photoanodes for efficient photoelectrochemical water splitting. Mater. Sci. Semicond. Process. 2019, 101, 223-229.
- 58. Wang, X.T., Wei, Q.Y., Li, J.R., Li, H., Zhang, Q.X. and Ge, S.S. Preparation of NiSe2/TiO2 nanocomposite for photocathodic protection of stainless steel. *Mater. Lett.* **2016**, 185, 443-446.
- 59. Che, H., Liu, X., Gao, Y., Liu, J. and Cao, Z. Hydrothermal electrochemical deposition synthesis NiSe₂ as efficient counter electrode materials for dye-sensitized solar cells. *J. Alloys Compd.* **2017**, 705, 645-651.

- 60. Xu, X.J., Fei, G.T., Yu, W.H., Wang, X.W., Chen, L. and Zhang, L.D. Preparation and formation mechanism of ZnS semiconductor nanowires made by the electrochemical deposition method. *Nanotechnology*. **2005**, 17, 426-429.
- 61. Shin, J.C., Yang, H.K., Lee, J.S., Lee, J.H., Kang, M.G. and Kwon, E. Fabrication and Development of Binder-Free Mn–Fe–S Mixed Metal Sulfide Loaded Ni-Foam as Electrode for the Asymmetric Coin Cell Supercapacitor Device. *Nanomaterials*. **2022**, 12, 3193.
- 62. Baig, N., Kammakakam, I. and Falath, W. Nanomaterials: A review of synthesis methods, properties, recent progress, and challenges. *Materials Advances*. **2021**, 2, 1821-1871.
- a) Kubo, R. Electronic properties of metallic fine particles. I. J. Phys. Soc. Jpn. 1962, 17, 975-986. b) Ghosh, S.K. and Pal, T. Interparticle coupling effect on the surface plasmon resonance of gold nanoparticles: from theory to applications. Chem. Rev. 2007, 107, 4797-4862. c) Daniel, M.C. and Astruc, D. Gold nanoparticles: assembly, supramolecular chemistry, quantum-size-related properties, and applications toward biology, catalysis, and nanotechnology. Chem. Rev. 2004, 104, 293-346.
- a) Buffat, P. and Borel, J.P. Size effect on the melting temperature of gold particles. *Phys. Rev. A.* **1976**. 13, 2287- 2298. b) Jiang, Q., Shi, H.X. and Zhao, M., 1999. Melting thermodynamics of organic nanocrystals. *J. Chem. Phys.* **1999**, 111, 2176-2180. c) Nanda, K.K., Sahu, S.N. and Behera, S.N. Liquid-drop model for the size-dependent melting of low-dimensional systems. *Phys. Rev. A.* **2002**, 66, 013208 013216.
- a) Jeong, U., Teng, X., Wang, Y., Yang, H. and Xia, Y. Superparamagnetic colloids: controlled synthesis and niche applications. *Adv. Mater.* **2007**, 19, 33-60. b) Dormann, J.L. and Fiorani, D. Magnetic properties of fine particles. *Elsevier.* **2012**. c) Silva, F.G., Depeyrot, J., Campos, A.F., Aquino, R., Fiorani, D. and Peddis, D. Structural and magnetic properties of spinel ferrite nanoparticles. *J. Nanosci. Nanotechnol.* **2019**, 19, 4888-4902.
- a) Yu, H., Li, J., Loomis, R.A., Wang, L.W. and Buhro, W.E. Two-versus three-dimensional quantum confinement in indium phosphide wires and dots. *Nat. Mater.*2003, 2, 517-520. b) Yu, H., Li, J., Loomis, R.A., Gibbons, P.C., Wang, L.W. and Buhro, W.E. Cadmium selenide quantum wires and the transition from 3D to 2D confinement. *J. Am. Chem. Soc.* 2003, 125, 16168-16169.
- 67. Kelly, K.L., Coronado, E., Zhao, L.L. and Schatz, G.C. The optical properties of metal nanoparticles: the influence of size, shape, and dielectric environment. *J. Phys. Chem. B.* **2003**, 107, 668-677.

- 68. Lim, W.Y., Hong, M. and Ho, G.W. In situ photo-assisted deposition and photocatalysis of ZnIn₂S₄/transition metal chalcogenides for enhanced degradation and hydrogen evolution under visible light. *Dalton Trans.* **2016**, 45, 552-560.
- 69. Pathania, D., Gupta, D., Ala'a, H., Sharma, G., Kumar, A., Naushad, M., Ahamad, T. and Alshehri, S.M. Photocatalytic degradation of highly toxic dyes using chitosan-g-poly (acrylamide)/ZnS in presence of solar irradiation. *J. Photochem. Photobiol.* A. **2016**, 329, 61-68.
- 70. Kapinus, E.I., Viktorova, T.I. and Khalyavka, T.A. Photocatalytic activity of nanoparticles of metal sulfides in the degradation of organic dyes. *Theor. Exp. Chem.* **2006**, 42, 282-286.
- 71. Liu, Y., Guo, Y., Liu, Y., Wei, Z., Wang, K. and Shi, Z. A Mini Review on Transition Metal Chalcogenides for Electrocatalytic Water Splitting: Bridging Material Design and Practical Application. *Energy Fuels.* **2023**, 37, 2608-2630.
- 72. Han, Y., Ma, Y., Liu, Y., Xu, S., Chen, X., Zeng, M., Hu, N., Su, Y., Zhou, Z. and Yang, Z. Construction of MoS₂/SnO₂ heterostructures for sensitive NO₂ detection at room temperature. *Appl.Surf. Sci.* 2019, 493, 613-619.
- 73. Masrat, S., Poolla, R., Dipak, P. and Zaman, M.B. Rapid hydrothermal synthesis of highly crystalline transition metal (Mn & Fe) doped CuSe nanostructures: applications in wastewater treatment and room temperature gas sensing. *Surf. Interfaces.* **2021**, 23, 100973.
- 74. Mani, S., Ramaraj, S., Chen, S.M., Dinesh, B. and Chen, T.W. Two-dimensional metal chalcogenides analogous NiSe₂ nanosheets and its efficient electrocatalytic performance towards glucose sensing. *J. Colloid Sci.* **2017**, 507, 378-385.
- 75. Kumbhakar, P., Sha, M.S., Tiwary, C.S., Muthalif, A.G., Al-Maadeed, S. and Sadasivuni, K.K. An efficient transition metal chalcogenide sensor for monitoring respiratory alkalosis. *Biotech.* **2023**, 13, 109.
- 76. Liu, F., Zhu, J., Hu, L., Zhang, B., Yao, J., Nazeeruddin, M.K., Grätzel, M. and Dai, S. Low-temperature, solution-deposited metal chalcogenide films as highly efficient counter electrodes for sensitized solar cells. *J. Mater. Chem. A.* **2015**, 3, 6315-6323.
- 77. Santhosh, S., Rajasekar, R., Gobinath, V.K., Moganapriya, C. and Sri, A.M. Utilisation of transition metal chalcogenide MoSe₂ as promising antireflective coating for achieving intensified light traption. *Chalcogenide Lett.* **2021**, 18, 327-337.
- 78. Hariharan, G., Dharani, A.P., Moorthi, N.S.V. and Saravanan, K.K. Design and fabrication of mixed phase transition metal chalcogenide hybrid composite (M= Ni & Co) for Pt-free

- efficient dye-sensitized solar cell applications. *J. Mater. Sci. Mater. Electron.* **2023**, 34, 188.
- 79. Tang, Y., Qin, Z., Yin, S. and Sun, H. Transition metal oxide and chalcogenide-based nanomaterials for antibacterial activities: an overview. *Nanoscale*. **2021**, 13, 6373-6388.
- 80. Zhou, X., Sun, H. and Bai, X. Two-dimensional transition metal dichalcogenides: synthesis, biomedical applications and biosafety evaluation. Front. Bioeng. Biotechnol. **2020**, 8, 236.
- 81. Fu, Q., Zhu, R., Song, J., Yang, H. and Chen, X. Photoacoustic imaging: contrast agents and their biomedical applications. *Advanced Materials*. **2019**, 31, 1805875.
- 82. Cheng, J., Wang, W., Xu, X., Lin, Z., Xie, C., Zhang, Y., Zhang, T., Li, L., Lu, Y. and Li, Q. AgBiS₂ nanoparticles with synergistic photodynamic and bioimaging properties for enhanced malignant tumor phototherapy. Mater. Sci. Eng. C. **2020**, 107, 110324.
- 83. Ding, H., Liu, W., Zheng, Y., Li, C., Jiang, H. and Wang, X. Transition metal halide-doped, highly stable all-inorganic perovskite nanocrystals for fabrication of white light-emitting diodes. *J. Mater. Chem. C.* **2019**, 7, 1690-1695.
- 84. Wang, C., Kang, Z., Zheng, Z., Zhang, Y., Zhang, L., Su, J., Zhang, Z., Liu, N., Li, L. and Gao, Y. Monolayer MoSe₂/NiO van der Waals heterostructures for infrared light-emitting diodes. *J. Mater. Chem. C.* **2019**, 7, 13613-13621.
- 85. Wang, L., Guan, Z. and Tang, A. Multinary copper-based chalcogenide semiconductor nanocrystals: synthesis and applications in light-emitting diodes and bioimaging. *J Nanopart Res*, **2020**, 22, 1-20.
- 86. Vidhya, M.S., Yuvakkumar, R., Kumar, P.S., Ravi, G. and Velauthapillai, D. Hydrothermal Synthesis of Flower Like MnSe₂@ MoSe₂ Electrode for Supercapacitor Applications. *Top Catal.* 2022, 65, 615-622.
- 87. Raman, V., Chinnadurai, D., Rajmohan, R., Chebrolu, V.T., Rajangam, V. and Kim, H.J. Transition metal chalcogenide based MnSe heterostructured with NiCo₂O₄ as a new high performance electrode material for capacitive energy storage. *New J. Chem.* **2019**, 43, 12630-12640.
- 88. Sahoo, S., Pazhamalai, P., Krishnamoorthy, K. and Kim, S.J. Hydrothermally prepared α-MnSe nanoparticles as a new pseudocapacitive electrode material for supercapacitor. *Electrochim. Acta.* **2018**, 268, 403-410.
- 89. Theerthagiri, J., Karuppasamy, K., Durai, G., Rana, A.U.H.S., Arunachalam, P., Sangeetha, K., Kuppusami, P. and Kim, H.S. Recent advances in metal chalcogenides (MX; X= S, Se)

- nanostructures for electrochemical supercapacitor applications: a brief review. *Nanomater*. **2018**, 8, 256.
- 90. Dahiya, Y., Hariram, M., Kumar, M., Jain, A. and Sarkar, D. Modified transition metal chalcogenides for high performance supercapacitors: Current trends and emerging opportunities. *Coord. Chem. Rev.* **2022**, 451, 214265.
- 91. Matthews, P.D., McNaughter, P.D., Lewis, D.J. and O'Brien, P. Shining a light on transition metal chalcogenides for sustainable photovoltaics. *Chem. Sci.* **2017**, 8, 4177-4187.
- 92. Roy, S., Hu, Z., Kais, S. and Bermel, P. Enhancement of Photovoltaic Current through Dark States in Donor-Acceptor Pairs of Tungsten-Based Transition Metal Di-Chalcogenides. *Adv. Funct. Mater.* **2021**, 31, 2100387.
- 93. Wang, S. Solvothermal synthesis of porous SnS₂ nanotubes with higher adsorption and photocatalytic activity. *Surf. Sci.* **2019**, 690, 121469.
- 94. Munonde, T.S. and Nomngongo, P.N. Review on Metal Chalcogenides and Metal Chalcogenide-Based Nanocomposites in Photocatalytic Applications. *Chemistry Africa*. **2023**, 1-17.
- 95. Liu, Y., Geng, P., Wang, J., Yang, Z., Lu, H., Hai, J., Lu, Z., Fan, D. and Li, M. In-situ ion-exchange synthesis Ag₂S modified SnS₂ nanosheets toward highly photocurrent response and photocatalytic activity. *J. Colloid Sci.* **2018**, 512, 784-791.
- 96. Chen, M.M., Xue, H.G. and Guo, S.P. Multinary metal chalcogenides with tetrahedral structures for second-order nonlinear optical, photocatalytic, and photovoltaic applications. *Coord. Chem. Rev.* **2018**, 368,115-133.
- 97. Regulacio, M.D. and Han, M.Y. Multinary I-III-VI₂ and I₂-II-IV-VI₄ semiconductor nanostructures for photocatalytic applications. *Acc. Chem. Res.* **2016**, 49, 511-519.
- 98. Khan, M.M. Chalcogenide-based nanomaterials as photocatalysts. *Elsevier*. **2021**.
- 99. Yuan, H., Kong, L., Li, T. and Zhang, Q. A review of transition metal chalcogenide/graphene nanocomposites for energy storage and conversion. *Chin. Chem. Lett.* **2017**, 28, 2180-2194.
- 100. Ifires, M., Hadjersi, T., Chegroune, R., Lamrani, S., Moulai, F., Mebarki, M. and Manseri, A. One-step electrodeposition of superhydrophobic NiO-Co(OH)₂ urchin-like structures on Si nanowires as photocatalyst for RhB degradation under visible light. *J. Alloys Compd.* 2019, 774, 908-917.
- 101. Xu, K., Wang, L., Xu, X., Dou, S.X., Hao, W. and Du, Y. Two dimensional bismuth-based layered materials for energy-related applications. *Energy Storage Mater.* **2019**, 19, 446-463.

- 102. Qadir, A., Le, T.K., Malik, M., Min-Dianey, K.A.A., Saeed, I., Yu, Y., Choi, J.R. and Pham, P.V. Representative 2D-material-based nanocomposites and their emerging applications: a review. *RSC Adv.* **2021**, 11, 23860-23880.
- 103. Murray, C., Norris, D.J. and Bawendi, M.G., 1993. Synthesis and characterization of nearly monodisperse CdE (E= sulfur, selenium, tellurium) semiconductor nanocrystallites. *J. Am. Chem. Soc.* **1993**, 115, 8706-8715.
- 104. Xiang, X., Wang, L., Zhang, J., Cheng, B., Yu, J. and Macyk, W. Cadmium Chalcogenide (CdS, CdSe, CdTe) Quantum Dots for Solar-to-Fuel Conversion. *Adv. Photonic. Res.* **2022**, 3, 2200065.
- 105. Bouroushian, M. Electrochemistry of metal chalcogenides. *Springer Science & Business Media*. **2010**.
- 106. Zhu, J., Wu, J., Sun, Y., Huang, J., Xia, Y., Wang, H., Wang, H., Wang, Y., Yi, Q. and Zou, G.Thickness-dependent bandgap tunable molybdenum disulfide films for optoelectronics. *RSC Adv.* **2016**, 6, 110604-110609.
- 107. Wei, Z., Li, B., Xia, C., Cui, Y., He, J., Xia, J.B. and Li, J. Various structures of 2D transition-metal dichalcogenides and their applications. *Small Methods*, **2018**, 2, 1800094.
- 108. Thomas, N., Mathew, S., Nair, K.M., O'Dowd, K., Forouzandeh, P., Goswami, A., McGranaghan, G. and Pillai, S.C. 2D MoS₂: structure, mechanisms, and photocatalytic applications. *Mater. Today Sustain.* **2021**, 13, 100073.
- 109. Yang, X. and Wang, D. Photocatalysis: from fundamental principles to materials and applications. *ACS Appl Energy Mater.* **2018**, 1, 6657–6693.
- 110. Rahman, A. and Khan, M.M. Chalcogenides as photocatalysts. *New J. Chem.* **2021**, 45, 19622-19635.
- 111. Hernández-Ramírez, A. and Medina-Ramírez. Photocatalytic semiconductors. *Springer International*. **2016**, 58-67.
- 112. Nefzi, C., Askri, B., Dabaki, Y. and Kamoun-Turki, N. Synthesis of new promising quaternary Cu₂InSnS₄ absorber layer: physical behaviors, wettability and photocatalysis applications. *J. Alloys Compd.* **2022**, 898, 162771.
- da Silveira Salla, J., Dotto, G.L., Hotza, D., Landers, R., da Boit Martinello, K. and Foletto, E.L. Enhanced catalytic performance of CuFeS₂ chalcogenide prepared by microwave-assisted route for photo-Fenton oxidation of emerging pollutant in water. *J. Environ. Chem. Eng.* **2020**, 8, 104077.

- 114. Bai, X. and Li, J. Photocatalytic hydrogen generation over porous ZnIn₂S₄ microspheres synthesised via a CPBr-assisted hydrothermal method. *Mater. Res. Bull.* **2011**, 46, 1028-1034.
- 115. Yuan, Y.J., Chen, D., Zhong, J., Yang, L.X., Wang, J., Liu, M.J., Tu, W.G., Yu, Z.T. and Zou, Z.G. Interface engineering of a noble-metal-free 2D–2D MoS₂/Cu-ZnIn₂S₄ photocatalyst for enhanced photocatalytic H₂ production. *J. Mater. Chem. A*, **2017**, 5, 15771-15779.
- Otgonbayar, Z. and Oh, W.C. Photo-electrochemical reduction of CO₂ to Methanol on Quaternary chalcogenide loaded Graphene-TiO₂ ternary nanocomposite fabricated via Pechini method. *J Inorg Organomet Polym Mater.* **2022**, 32, 2910-2927.
- 117. Li, Y. and Chen, G. Upconversion Nanoparticles for Cancer Therapy. *Adv. Nano Biomed. Res.* **2022**, 2, 2200092.
- 118. Maleki, A., He, J., Bochani, S., Nosrati, V., Shahbazi, M.A. and Guo, B. Multifunctional photoactive hydrogels for wound healing acceleration. *ACS Nano.* **2021**, 15, 18895-18930.
- 119. Maddela, N.R., Chakraborty, S. and Prasad, R. Nanotechnology for advances in medical microbiology. *Springer*. **2021**.
- 120. Manikandan, M., Hasan, N. and Wu, H.F. Platinum nanoparticles for the photothermal treatment of Neuro 2A cancer cells. *Biomaterials*. **2013**, 34, 5833-5842.
- 121. Elbialy, N.S., Fathy, M.M., Reem, A.W., Darwesh, R., Abdel-Dayem, U.A., Aldhahri, M., Noorwali, A. and Al-Ghamdi, A.A. Multifunctional magnetic-gold nanoparticles for efficient combined targeted drug delivery and interstitial photothermal therapy. *Int. J. Pharm.* **2019**, 554, 256–263.
- Wei, W., Zhang, X., Zhang, S., Wei, G. and Su, Z. Biomedical and bioactive engineered nanomaterials for targeted tumor photothermal therapy: A review. *Mater. Sci. Eng. C.* **2019**, 104, 109891.
- 123. Jin, Y., Jia, C., Huang, S.W., O'donnell, M. and Gao, X. Multifunctional nanoparticles as coupled contrast agents. *Nat. Commun.* **2010**, 1, 41.
- 124. Li, W. and Chen, X. Gold nanoparticles for photoacoustic imaging. *Nanomedicine*. **2015**, 10, 299-320.
- 125. Luther, J.M., Jain, P.K., Ewers, T. and Alivisatos, A.P. Localized surface plasmon resonances arising from free carriers in doped quantum dots. *Nat. Mater.* **2011**, 10, 361-366.
- 126. Xie, Y., Carbone, L., Nobile, C., Grillo, V., D'Agostino, S., Della Sala, F., Giannini, C., Altamura, D., Oelsner, C., Kryschi, C. and Cozzoli, P.D. Metallic-like stoichiometric

- copper sulfide nanocrystals: phase-and shape-selective synthesis, near-infrared surface plasmon resonance properties, and their modeling. *ACS Nano.* **2013**, 7, 7352-7369.
- 127. Nieves, L.M., Mossburg, K., Hsu, J.C., Maidment, A.D. and Cormode, D.P. Silver chalcogenide nanoparticles: a review of their biomedical applications. *Nanoscale*. **2021**, 13, 19306-19323.
- 128. Li, Y., Lu, W., Huang, Q., Li, C. and Chen, W. Copper sulfide nanoparticles for photothermal ablation of tumor cells. *Nanomedicine*. **2010**, 5, 1161-1171.
- 129. Zhou, M., Tian, M. and Li, C. Copper-based nanomaterials for cancer imaging and therapy. *Bioconjug. Chem.* **2016**, 27, 1188–1199.
- 130. Feng, W., Nie, W., Cheng, Y., Zhou, X., Chen, L., Qiu, K., Chen, Z., Zhu, M. and He, C. In vitro and in vivo toxicity studies of copper sulfide nanoplates for potential photothermal applications. *Nanomedicine*. **2015**, 11, 901–912.
- 131. Zhou, M., Li, J., Liang, S., Sood, A.K., Liang, D. and Li, C. CuS nanodots with ultrahigh efficient renal clearance for positron emission tomography imaging and image-guided photothermal therapy. ACS Nano. 2015, 9, 7085-7096.
- 132. Chen, G., Ma, B., Wang, Y., Xie, R., Li, C., Dou, K. and Gong, S. CuS-based theranostic micelles for NIR-controlled combination chemotherapy and photoacoustic imaging. *ACS Appl. Mater. Interfaces.* **2017**, 9, 41700-41711.
- Wang, K., Chen, Q., Xue, W., Li, S. and Liu, Z. Combined chemo-photothermal antitumor therapy using molybdenum disulfide modified with hyperbranched polyglycidyl. *ACS Biomater. Sci. Eng.* **2017**, 3, 2325-2335.
- 134. Han, R., Xiao, Y., Yang, Q., Pan, M., Hao, Y., He, X., Peng, J. and Qian, Z. Ag₂S nanoparticle-mediated multiple ablations reinvigorates the immune response for enhanced cancer photo-immunotherapy. *Biomaterials*. **2021**, 264, 120451.
- 135. Chu, Z., Tian, T., Tao, Z., Yang, J., Chen, B., Chen, H., Wang, W., Yin, P., Xia, X., Wang, H. and Qian, H. Upconversion nanoparticles@AgBiS₂ core-shell nanoparticles with cancer-cell-specific cytotoxicity for combined photothermal and photodynamic therapy of cancers. *Bioact. Mater.* **2022**, 17, 71-80.
- 136. Badrigilan, S., Choupani, J., Khanbabaei, H., Hoseini-Ghahfarokhi, M., Webster, T.J. and Tayebi, L. Bismuth-based nanomaterials: Recent advances in tumor targeting and synergistic cancer therapy techniques. *Adv. Healthc. Mater.* **2020**, 9, 1901695.
- 137. Shahbazi, M.A., Faghfouri, L., Ferreira, M.P., Figueiredo, P., Maleki, H., Sefat, F., Hirvonen, J. and Santos. H.A. The versatile biomedical applications of bismuth-based

- nanoparticles and composites: therapeutic, diagnostic, biosensing, and regenerative properties. *Chem. Soc. Rev.* **2020**, 49, 1253-1321.
- 138. Fang, Y., Peng, C., Guo, R., Zheng, L., Qin, J., Zhou, B., Shen, M., Lu, X., Zhang, G. and Shi, X. Dendrimer-stabilized bismuth sulfide nanoparticles: synthesis, characterization, and potential computed tomography imaging applications. *Analyst.* **2013**, 138, 3172-3180.
- 139. Kinsella, J.M., Jimenez, R.E., Karmali, P.P., Rush, A.M., Kotamraju, V.R., Gianneschi, N.C., Ruoslahti, E., Stupack, D. and Sailor, M.J. X-ray computed tomography imaging of breast cancer by using targeted peptide-labeled bismuth sulfide nanoparticles. *Angew. Chem., Int. Ed.* **2011**, 50, 12308-12311.
- 140. Cheng, K., Zhang, R.Y., Yang, X.Q., Zhang, X.S., Zhang, F., An, J., Wang, Z.Y., Dong, Y., Liu, B., Zhao, Y.D. and Liu, T.C. One-for-all nanoplatform for synergistic mild cascade-potentiated ultrasound therapy induced with targeting imaging-guided photothermal therapy. *ACS Appl. Mater. Interfaces.* **2020**, 12, 40052-40066.
- 141. Chen, B., Zhang, C., Wang, W., Chu, Z., Zha, Z., He, X., Zhou, W., Liu, T., Wang, H. and Qian, H. Ultrastable AgBiS₂ hollow nanospheres with cancer cell-specific cytotoxicity for multimodal tumor therapy. *ACS Nano*. **2020**, 14, 14919-14928.
- 142. Wen, S., Wu, T., Long, H., Ke, L., Deng, S., Huang, L., Zhang, J. and Tan, S. Mechanism insight into rapid photodriven sterilization based on silver bismuth sulfide quantum dots. *ACS Appl. Mater. Interfaces.* **2021**, 13, 21979-21993.
- 143. Xu, Q., Wu, J., Feng, Y., Hu, H., Mo, Z., Xu, Z., Li, H. and Yang, S. Raspberry-like AgBiS₂@PVP nanoparticles for enhanced sonodynamic and chemodynamic cancer therapy. *J. Mater. Chem. B.* **2022**, 10, 8514-8524.
- 144. Rajendiran, K., Zhao, Z., Pei, D.S. and Fu, A. Antimicrobial activity and mechanism of functionalized quantum dots. *Polymers*. **2019**, 11, 1670.
- 145. Wang, L., Hu, C. and Shao, L. The antimicrobial activity of nanoparticles: present situation and prospects for the future. *Int J Nanomedicine*. **2017**, 12, 1227-1249.
- 146. Karimi, M., Sadeghi, E., Bigdeli, S.K. and Zahedifar, M. Synthesis, feasibility study of production of singlet oxygen and hydroxyl radical and performance in antibacterial activity of ZnS: Eu QDs. *J. compos. compd.* **2022**, 4, 77-82.
- 147. Khan, S.T. and Malik, A. Engineered nanomaterials for water decontamination and purification: From lab to products. *J. Hazard. Mater.* **2019**, 363, 295–308.
- 148. Zhang, W., Xiao, B. and Fang, T. Chemical transformation of silver nanoparticles in aquatic environments: Mechanism, morphology and toxicity. *Chemosphere*. 2019, 191, 324-334.

- Han, H., Yang, J., Li, X., Qi, Y., Yang, Z., Han, Z., Jiang, Y., Stenzel, M., Li, H., Yin, Y., Du, Y., Liu, J., and Wang, F. Shining light on transition metal sulfides: New choices as highly efficient antibacterial agents. *Nano Res.* 2021, 14, 2512–2534.
- 150. Djurišić, A.B., Leung, Y.H. and Ng, A.M.C. Strategies for improving the efficiency of semiconductor metal oxide photocatalysis. *Mater. Horiz.* **2014**, 1, 400-410.
- 151. Kasinathan, K., Kennedy, J., Elayaperumal, M., Henini, M. and Malik, M. Photodegradation of organic pollutants RhB dye using UV simulated sunlight on ceria based TiO₂ nanomaterials for antibacterial applications. *Sci. Rep.* **2016**, 6, 38064.
- 152. Wang, Z., Zhu, W., Qiu, Y., Yi, X., von dem Bussche, A., Kane, A., Gao, H., Koski, K. and Hurt, R. Biological and environmental interactions of emerging two-dimensional nanomaterials. *Chem. Soc. Rev.* **2016**, 45, 1750–1780.
- 153. He, X., Yang, D.P., Zhang, X., Liu, M., Kang, Z., Lin, C., Jia, N. and Luque, R. Waste eggshell membrane-templated CuO-ZnO nanocomposites with enhanced adsorption, catalysis and antibacterial properties for water purification. *Chem. Eng. J.* **2019**, 369, 621–633.
- 154. Feng, Y., Marusak, K.E., You, L. and Zauscher, S. Biosynthetic transition metal chalcogenide semiconductor nanoparticles: progress in synthesis, property control and applications. *Curr. Opin. Colloid Interface Sci.* **2018**, 38, 190–203.
- 155. Shah, A., Haq, S., Rehman, W., Waseem, M., Shoukat, S. and Rehman, M.U. Photocatalytic and antibacterial activities of paeonia emodi mediated silver oxide nanoparticles. *Mater. Res. Express.* **2019**, 6, 045045.
- 156. Fujishima, A. and Zhang, X. Titanium dioxide photocatalysis: present situation and future approaches. *C. R. Chimie*. **2006**, 9, 750–760.
- 157. Allahverdiyev, A.M., Abamor, E.S., Bagirova, M. and Rafailovich, M. Antimicrobial effects of TiO₂ and Ag₂O nanoparticles against drug-resistant bacteria and leishmania parasites. *Future Microbiol.* **2011**, 6, 933–940.
- 158. Zaleska, A. Doped-TiO₂: a review. *Recent Pat. Eng.* **2008**, 2, 157-164.
- 159. Chen, W.J. and Chen, Y.C. Fe₃O₄/TiO₂ core/shell magnetic nanoparticle-based photokilling of pathogenic bacteria. *Nanomedicine*. **2010**, 5, 1585–1593
- Baláž, M., Tkáčiková, L.U., Stahorský, M., Casas-Luna, M., Dutková, E., Čelko, L., Kováčová, M., Achimovičová, M. and Baláž, P. Ternary and Quaternary Nanocrystalline Cu-Based Sulfides as Perspective Antibacterial Materials Mechanochemically Synthesised in a Scalable Fashion. ACS Omega. 2022, 7, 27164–27171.

- 161. Haider, S., Shar, S.S., Shakir, I. and Agboola, P.O. Design of NiS/CNTs nanocomposites for visible light driven catalysis and antibacterial activity studies. *Ceram. Int.* **2021**, 47, 34269-34277.
- Rabaan, A.A., Bukhamsin, R., AlSaihati, H., Alshamrani, S.A., AlSihati, J., Al-Afghani, H.M., Alsubki, R.A., Abuzaid, A.A., Al-Abdulhadi, S., Aldawood, Y. and Alsaleh, A.A. Recent Trends and Developments in Multifunctional Nanoparticles for Cancer Theranostics. *Molecules*. 2022, 27, 8659.
- 163. Ayodhya, D. and Veerabhadram, G. Green synthesis, characterization, photocatalytic, fluorescence and antimicrobial activities of Cochlospermum gossypium capped Ag₂S nanoparticles. *J. Photochem. Photobiol. B, Biol.* **2016**, 157, 57-69.
- 164. Sun, B., Qiao, Z., Shang, K., Fan, H. and Ai, S. Facile synthesis of silver sulfide/bismuth sulfide nanocomposites for photocatalytic inactivation of Escherichia coli under solar light irradiation. *Mater. Lett.* **2013**, 91, 142-145.
- 165. Panthi, G., Ranjit, R., Khadka, S., Gyawali, K.R., Kim, H.Y. and Park, M. Characterization and antibacterial activity of rice grain-shaped ZnS nanoparticles immobilized inside the polymer electrospun nanofibers. *Adv. Compos. Mater.* **2020**, *3*, 8-15.
- 166. Malarkodi, C., Rajeshkumar, S., Paulkumar, K., Vanaja, M., Gnanajobitha, G. and Annadurai, G. Biosynthesis and antimicrobial activity of semiconductor nanoparticles against oral pathogens. *Bioinorg. Chem. Appl.* **2014**, 2014, 1–10.
- 167. Ganguly, S., Das, S. and Dastidar, S.G. Distinct antimicrobial effects of synthesised ZnS nanoparticles against twelve pathogenic bacterial strains. *Open Science Repository Chemistry*, **2013**, e70081948.
- 168. Kasinathan, K., Murugesan, B., Pandian, N., Mahalingam, S., Selvaraj, B. and Marimuthu, K. Synthesis of biogenic chitosan-functionalized 2D layered MoS₂ hybrid nanocomposite and its performance in pharmaceutical applications: in-vitro antibacterial and anticancer activity. *Int. J. Biol. Macromol.* 2020, 149, 1019-1033.
- 169. Kannan, S., Vinitha, P., Mohanraj, K. and Sivakumar, G. Antibacterial studies of novel Cu₂WS₄ ternary chalcogenide synthesised by hydrothermal process. *J Solid State Chem.* **2018**, 258, 376–382.
- 170. Ma, J. Determination of chemical oxygen demand in aqueous samples with non-electrochemical methods. *Trends Environ. Anal. Chem.* **2017**, 14, 37-43.
- 171. Nóbrega, E.T.D., de Oliveira, I.T.G., Viana, A.D., da Silva Gasparotto, L.H. and Moraes, E.P. A low-cost sensor based on silver nanoparticles for determining chemical oxygen demand in wastewater via image processing analysis. *Anal. Methods.* **2019**, 11, 5577-5583.

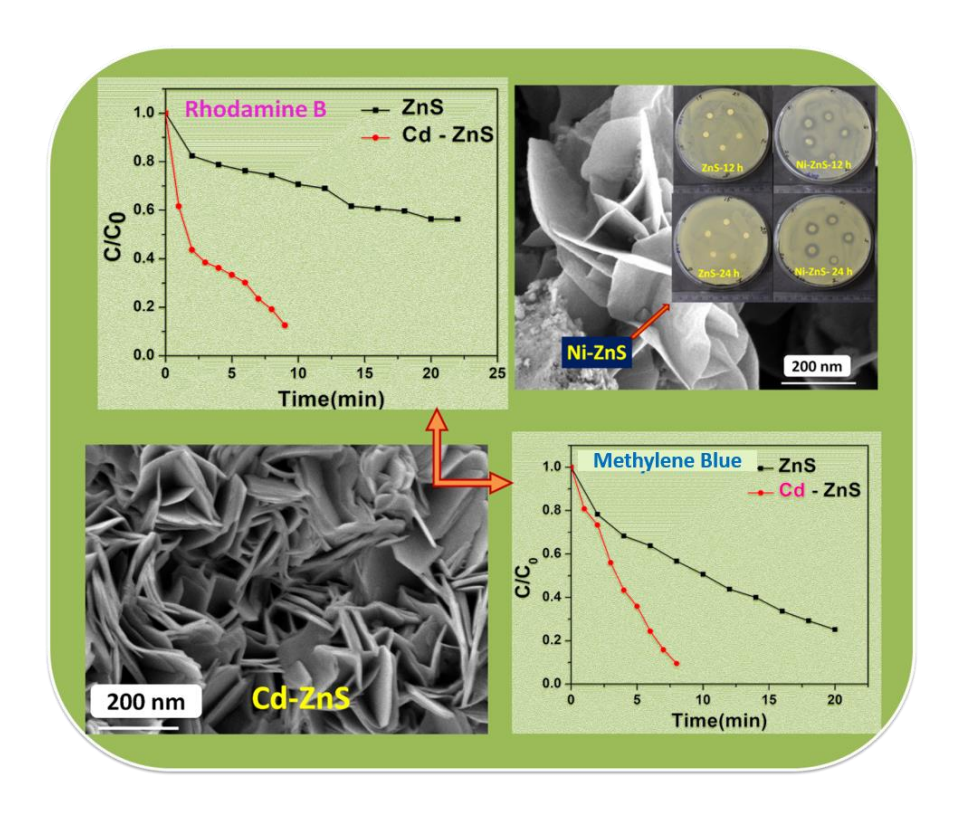
- 172. Sudha, M., Senthilkumar, S., Hariharan, R., Suganthi, A. and Rajarajan, M. Synthesis, characterization and study of photocatalytic activity of surface modified ZnO nanoparticles by PEG capping. *J Sol-Gel Sci Technol.* **2013**, 65, 301–310.
- 173. Sanad, M.F., Shalan, A.E., Bazid, S.M. and Abdelbasir, S.M. Pollutant degradation of different organic dyes using the photocatalytic activity of ZnO@ZnS nanocomposite materials. *J. Environ. Chem. Eng.* **2018**, 6, 3981-3990.
- 174. Li, J., Luo, G., He, L., Xu, J. and Lyu, J. Analytical approaches for determining chemical oxygen demand in water bodies: a review. *Crit Rev Anal Chem.* **2018**, 48, 47-65.
- 175. Geerdink, R.B., van den Hurk, R.S. and Epema, O.J. Chemical oxygen demand: Historical perspectives and future challenges. *Anal. Chim. Acta.* **2017**, 961, 1-11.
- 176. Abdel Messih, M.F., Shalan, A.E., Sanad, M.F. and Ahmed, M.A. Facile approach to prepare ZnO@SiO₂ nanomaterials for photocatalytic degradation of some organic pollutant models. *J Mater Sci Mater Electron.* **2019**, 30, 14291-14299.
- 177. Zhao, T., Liu, R., Lu, J., Zhu, X., Zhu, X., Lu, K. and Zhu, H. Photocatalytic degradation of methylene blue solution by diphenylanthrazoline compounds. *J Phys Org Chem.* **2017**, 30, e3712.
- 178. Gajbhiye, S.B. Photocatalytic degradation study of methylene blue solutions and its application to dye industry effluent. *Int. J. Mod. Eng. Res.* **2012**, 2, 1204-1208.
- 179. Borhade, A.V., Tope, D.R. and Uphade, B.K. An efficient photocatalytic degradation of methyl blue dye by using synthesised PbO nanoparticles. *E-J. Chem.* **2012**, 9, 705-715.
- 180. Sari, M.I., Agustina, T.E., Melwita, E. and Aprianti, T. November. Color and COD degradation in photocatalytic process of procion red by using TiO₂ catalyst under solar irradiation. In *AIP Conference Proceedings AIP Publishing LLC*. **2017**, 1903, 040017.
- 181. Sahoo, C., Gupta, A.K. and Sasidharan Pillai, I.M., Photocatalytic degradation of methylene blue dye from aqueous solution using silver ion-doped TiO₂ and its application to the degradation of real textile wastewater. *J. Environ. Sci. Health A.* **2012**, 47, 1428-1438.
- Wei, M., Qiao, Y., Zhao, H., Liang, J., Li, T., Luo, Y., Lu, S., Shi, X., Lu, W. and Sun, X. Electrochemical non-enzymatic glucose sensors: Recent progress and perspectives. *Chem. Commun.* **2020**, 56, 14553-14569.
- 183. Venkadesh, A., Mathiyarasu, J., Dave, S. and Radhakrishnan, S. Amine mediated synthesis of nickel oxide nanoparticles and their superior electrochemical sensing performance for glucose detection. *Inorg. Chem. Commun.* **2021**, 131, 108779.

- Phetsang, S., Kidkhunthod, P., Chanlek, N., Jakmunee, J., Mungkornasawakul, P. and Ounnunkad, K. Copper/reduced graphene oxide film modified electrode for non-enzymatic glucose sensing application. *Sci.Rep.* **2021**, 11, 9302.
- 185. Hwang, D.W., Lee, S., Seo, M. and Chung, T.D. Recent advances in electrochemical non-enzymatic glucose sensors—a review. *Anal. Chim. Acta.* **2018**, 1033, 1-34.
- 186. Chiu, W.T., Chang, T.F.M., Sone, M., Hosoda, H., Tixier-Mita, A. and Toshiyoshi, H. Developments of the Electroactive Materials for Non-Enzymatic Glucose Sensing and Their Mechanisms. *Electrochem*, **2021**, 2, 347-389.
- 187. Ye, J.S., Chen, C.W. and Lee, C.L. Pd nanocube as non-enzymatic glucose sensor. *Sens. Actuators B Chem.* **2015**, 208, 569-574.
- 188. Arif, D., Hussain, Z., Sohail, M., Liaqat, M.A., Khan, M.A. and Noor, T. A non-enzymatic electrochemical sensor for glucose detection based on Ag@ TiO₂@ metal-organic framework (ZIF-67) nanocomposite. *Front. Chem.* **2020**, 8, 573510.
- 189. Veeralingam, S. and Badhulika, S. Two-dimensional metallic NiSe₂ nanoclusters—based low-cost, flexible, amperometric sensor for detection of neurological drug carbamazepine in human sweat samples. *Front. Chem.* **2020**, 8, 337.
- 190. Wang, L., Li, S., Zhang, X. and Huang, Y. CoSe₂ hollow microspheres with superior oxidase-like activity for ultrasensitive colorimetric biosensing. *Talanta*, **2020**, 216, 121009.
- 191. He, B. and Yan, X. Ultrasensitive electrochemical aptasensor based on CoSe₂/AuNRs and 3D structured DNA-PtNi@ Co-MOF networks for the detection of zearalenone. *Sens. Actuators B Chem.* **2020**, 306, 127558.
- Kumar, B.G. and Muralidharan, K. Hexamethyldisilazane-assisted synthesis of indium sulfide nanoparticles. *J. Mater. Chem*, 2011, 21, 11271-11275. b) Kumar, B.G. and Muralidharan, K. Organic-Free Self-Assembled Copper Sulfide Microflowers. *Eur. J. Inorg. Chem.* 2013, 12, 2102-2108. c) Kumar, B.G. and Muralidharan, K. S4N4 as an intermediate in Ag₂S nanoparticle synthesis. *RSC Adv.* 2014, 4, 28219-28224. d) Kumar, B.G., Srinivas, B., Prasad, M.D. and Muralidharan, K. Ag/Ag₂S heterodimers: tailoring the metal–semiconductor interface in a single nanoparticle. *J Nanopart Res.* 2015, 17, 1-11.
 e) Srinivas, B., Kumar, B.G. and Muralidharan, K. Stabilizer free copper sulphide nanostructures for rapid photocatalytic decomposition of Rhodamine B. *J Mol Catal A Chem.* 2015, 410, 8-18. f) Billakanti, S., Baskaran, G.K. and Muralidharan, K. Recyclable Ni₃S₄ nanocatalyst for hydrogenation of nitroarenes. *ChemistrySelect.* 2017, 2, 4753-4758.
 g) Kumar, B.G., Srinivas, B. and Muralidharan, K. Photo-responsive Bi₂S₃ nanoflakes:

Synthesis and device fabrication at ambient conditions. Mater. Res. Bull. 2017, 89, 108-115. h) Billakanti, S. and Krishnamurthi, M. Facile preparation of surfactant or support material free CdS nanoparticles with enhanced photocatalytic activity. J. Environ. Chem. Eng. 2018, 6, 1250-1256. i) Srinivas, B., Pandit, M.A. and Muralidharan, K. Importance of clean surfaces on the catalyst: SnS₂ nanorings for environmental remediation. ACS Omega. 2019, 4, 14970-14980. j) Pandit, M.A., Sai Hemanth Kumar, D., Billakanti, S., Ramadoss, M. and Muralidharan, K. Chalcopyrite with magnetic and dielectric properties: an introductory catalyst for 4-nitrophenol reduction. J. Phys. Chem. C, 2020, 124, 18010-18019. k) Pandit, M.A., Billakanti, S. and Muralidharan, K. A simplistic approach for the synthesis of CuS-CdS heterostructure: A novel photo catalyst for oxidative dye degradation. J. Environ. Chem. Eng. 2020, 8, 103542. l) Pandit, M.A., Kumar, D.S.H., Ramadoss, M., Chen, Y. and Muralidharan, K. Template free-synthesis of cobalt–iron chalcogenides [Co_{0.8} Fe_{0.2} L₂, L= S, Se] and their robust bifunctional electrocatalysis for the water splitting reaction and Cr(vi) reduction. RSC Adv. 2022, 12, 7762-7772.

Chapter 2

Impact of bandgap tuning on ZnS for degradation of environmental pollutants and disinfection



Abstract

The materials showing multiple applications are appealing for their practical use and industrial production. To realize the suitable property for various applications, we have produced ZnS (sf-ZnS) and metal-doped ZnS nanoflakes (sf-m-ZnS; where m = Cu, Ni, Cd, Bi, or Mn) and correlated their activity with bandgap variation. We obtained all these materials via hexamethyldisilazane (HMDS)-assisted synthetic method without using any surfactants, polymers, or template molecules and characterised them thoroughly using various techniques. Photocatalytic, as well as antibacterial activities of these materials, shown their bifunctional utility. We have demonstrated the effect of doping and consequent extension of absorption band to the visible region and resultant improved photocatalytic activity under sunlight. Thus, the change in bandgap influenced their performance as photocatalysts. Among all materials produced, **sf-Cd-ZnS** provided superior results as a photocatalyst while degrading two organic pollutants - Rhodamine B (RhB) and Methylene blue (MB) in water. The antibacterial activity of sf-ZnS and sf-m-ZnS against Gram-positive bacteria. i.e., Staphylococcus aureus (S. aureus), was examined by the Zone of inhibition method, wherein sf-Ni-**ZnS** showed maximum activity. The enhanced activity of these ZnS materials can be attributed to the free surface of nanoparticles without any capping by organic molecules, which provided an intimate interaction of inorganic semiconductor material with organic and biomolecules. Thus, we have demonstrated modification of properties both by bandgap tuning of materials and providing the opportunity for intimate interaction of materials with substrates. The photocatalytic activity and antibacterial action of metal-doped ZnS produced by our method exhibited their potential for environmental remediation, specifically water purification.

2.1. Introduction

Rapid growth in population and industrialization have resulted in vast pollution to the environment and water, leading to a severe threat to the endurance of human beings [1, 2]. Photocatalysis is a light-driven chemical process and is a much-needed process for our society's well-being in terms of water purification, water splitting, and other photocatalytic applications. The photocatalysis process is helpful for the degradation of contaminants on the surface of the photocatalyst. There is an increasing need to control chemical and bacterial contaminations in water that originate mainly from chemical, textile, printing, plastics, papers, food, cosmetic, drugs and healthcare industries. Photocatalysts play a crucial role in the degradation of water pollutants that have fatal effects on humans. Though many methods such as coagulation, biodegradation, and photocatalysis have been used for water purification, photocatalysis is proved to be lethal for the degradation of pollutants like organic dyes (RhB and MB) [3, 4]. Several semiconductor photocatalysts such as metal oxides, metal hydroxides, sulphides, metal-free semiconductors have been used for water purification. Many of them worked well because of their high surface to volume ratio and quantum confinement effect [5, 6, 7].

After the pioneering work of using the environmentally friendly and economical process of photocatalytic splitting of water on TiO₂ electrodes by Honda and Fujishima, the focus on preparing II-VI semiconductor nanomaterials received widespread attention for their application in phosphors, electroluminescence devices, light-emitting displays and optical sensors. Among many semiconductors, zinc sulphide (ZnS) is studied extensively by researchers for [3, 5, 7-17] versatile applications in many fields like photonics, electroluminescence, nonlinear optical devices, infrared windows, and as sensors. ZnS is an II-VI semiconductor material at room temperature with a wide direct bandgap (3.5–3.8 eV), and it possesses high exciton binding energy (40 meV) and is less toxic. Therefore, it can be used in the short wavelength region (UV, blue, green) of the electromagnetic spectrum for optoelectronic applications [11]. It is also a phosphor material with electroluminescent and photoluminescent properties and shows size-dependent electrical and photoluminescent properties, which are useful in the fields of sensors, displays and lasers [5, 7, 18].

Theoretically, ZnS possess a much higher capability of photo-carrier generation than TiO₂ due to the direct bandgap. However, its wide bandgap energy restricts the absorption of the visible light reducing its usability as a photocatalyst. At the same time, the large bandgap favours it to host any metals ions. By incorporating the transition metal dopants on the ZnS

material with different loadings, it is possible to tune the absorption capacity from the UV-region to the Visible region. Therefore, many studies were directed on improving its properties by doping process where the transition metals doped ZnS are prominent [3-5, 7, 9-12, 15, 17, 19]. Since these materials have comparable surface atoms to those in the crystal lattice, their chemical and physical properties differ from bulk. In addition, luminescent centres are formed by doping ions, resulting in their luminescent property [5, 8]. The role of these dopants is to create charge carrier traps which result in enhanced photocatalytic activities [3, 17].

While acting as a photocatalyst, ZnS has also shown potent biological applicability, particularly the antibacterial activity. According to the Infectious Disease Society of America (IDSA), the threatening bacterial species exhibiting rapid growth of antibiotic resistance include *Staphylococcus aureus* (S.aureus), *Pseudomonas aeruginosa* (P. aeruginosa) and Enterobacter species. The Methicillin-resistant *Staphylococcus aureus* caused a large number of deaths worldwide [20]. Therefore, more effective antibiotics are to be developed to overcome the resistance of S.aureus. The effect of doping ZnS in its antibacterial activity against gram-positive bacteria S.aureus has also been studied and evaluated by the zone inhibition method [15, 18, 21]. These materials are popularly used in medical diagnostics since they are non-toxic, biocompatible, and biosafe [22, 23].

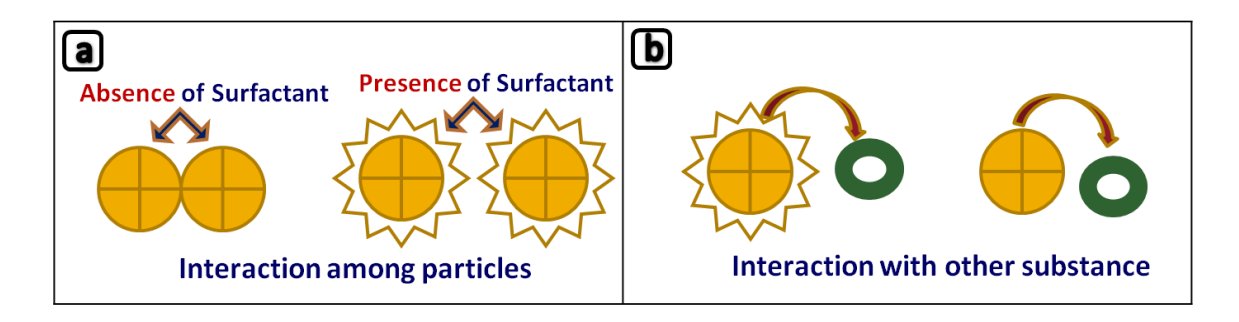


Figure 2.1. Schematic representation of interaction of surfactant free and stabilized nanoparticles

Different transition metals have been doped into ZnS through different methods of preparation for potential applications. While the unhindered mobility of charge is an essential characteristic, the toxicity of materials used is deciding factor for biological activity. The intimate contact of active catalytic materials with polluting molecules for their degradation and inhibition of bacterial growth is much needed for efficient catalytic activities. Many synthetic methods of ZnS and its doping processes involve using long-chain organic molecules as surfactants to assist in controlling the growth process of nanoparticles. These molecules form

a layer between the active materials and the substrates, such as dye needing decomposition or bacteria required to be inactivated (Figure 2.1). Sometimes these surfactant molecules may be toxic to humans and also inhibit charge mobility. There are few reports on stripping these surfactants by post-synthetic methods such as ligand exchange reactions and annulation. Though these methods are somewhat effective, they do leave some impurities, and many of them involve multistep preparation processes.

This chapter aims to tune the absorption capacity of pure zinc sulphide (UV-region) to visible-region by having transition metal ions as dopants and providing unhindered movement to the charge carriers. In this chapter, the high pure surfactant-free ZnS nanoparticles (sf-ZnS) and surfactant-free metal doped ZnS nanoparticles (sf-m-ZnS; where m = Cu, Ni, Cd, Bi, or Mn) were prepared with the tuneable bandgap, which showed excellent photocatalytic and antibacterial properties. The materials were synthesised by a simple one-pot reaction utilizing hexamethyldisilazane (HMDS) assisted synthesis method, wherein HMDS played a multi-role such as solvent and a capping agent [24, 25, 26, 27, 28]. There are no previous reports on the preparation of metal-doped ZnS using this method. The reactions yielded high pure materials without any organic molecules in their surroundings. Various analytical and spectroscopic techniques are used to characterise the **sf-ZnS** and **sf-m-ZnS** nanoparticles. The materials were tested for the photocatalytic degradation of organic dyes (RhB and MB) to explain clearly the impact of doping on ZnS nanoparticles. Besides photocatalysis, the effect of doping was studied through its action against the gram-positive bacteria- S. aureus. This chapter, therefore, provides a way of tuning the properties of wide bandgap semiconductors and their impact on the degradation of environmental pollutants and health hygiene.

2.2 Experimental

2.2.1. Materials required

Zinc chloride (ZnCl₂), thiourea, hexamethyldisilazane (HMDS), copper chloride (CuCl₂), nickel chloride (NiCl₂), cadmium chloride (CdCl₂), bismuth chloride (BiCl₂), and manganese chloride (MnCl₂) were purchased from Sigma Aldrich. All chemicals were used without any further purification.

2.2.2. Preparation of ZnS by HMDS-assisted method

Hexamethyldisilazane (HMDS)-assisted method (Scheme 2.1) was utilized to synthesise ZnS nanoparticles. Zinc chloride (200 mg, 1.4 mmol), thiourea (106 mg, 1.4 mmol) (1:1

stoichiometric ratio), and excess HMDS (5 ml) were taken in a flask, and the mixture was heated to about 140 °C for 6 h under nitrogen (flow) atmosphere. After the reaction was completed, high vacuum was applied to remove excess HMDS and other gaseous side products. The residue was washed repeatedly with distilled water and acetone. The collected product (**sf-ZnS**) was dried in an oven at 70 °C for 24 h.

2.2.3. Preparation of metal doping of ZnS (sf-m-ZnS)

To prepare metal doped ZnS, metal chloride (5% loading) was added to the reaction mixture of zinc chloride, thiourea, and HMDS. The rest of the reaction conditions and workup were similar to the one discussed for ZnS. Likewise, the other metal doped zinc sulphides (**sf-m-ZnS**; where m = Cu, Ni, Cd, Bi, or Mn) (9 mg of CuCl₂; 9 mg of NiCl₂; 14 mg of CdCl₂; 24 mg of BiCl₃; and 9 mg of MnCl₂) were also prepared following the above prescribed procedure.

2.2.4. Instrumentation

XRD patterns of sf-ZnS and sf-m-ZnS were collected at room temperature using Bruker D8 X-ray diffractometer (XRD) at a scan rate of 1 $^{\circ}$ min⁻¹ (CuK α = 1.54 Å; operating voltage = 40 kV; operating current = 30 mA) measurements with Cu K α radiation in a 2 θ range from 10 ° to 80°. The synthesised sf-ZnS and sf-m-ZnS materials were made into suspension in ethanol by sonicating for 2-3 min. The suspension was drop-casted on carbon-coated copper grids (200 mesh) for the TEM analyses. FEI Technai G2 20 STEM with a 200 kV acceleration voltage was used to capture TEM images of sf-ZnS and sf-m-ZnS particles. The morphology (FESEM) of **sf-ZnS** and **sf-m-ZnS** materials and Energy Dispersive Spectroscopy (EDS) were studied using an Ultra 55 Carl Zeiss instrument at an operating voltage of 10 kV. JASCO 5300 spectrophotometer was used to record the Fourier transform infrared (FT-IR) spectra (KBr pellet) of sf-ZnS and sf-m-ZnS materials. The optical properties of sf-ZnS and sf-m-**ZnS** materials were confirmed by studying the UV/Vis absorption spectra of samples in the solid and liquid states (for photocatalysis) using JASCO-V770 UV/Vis spectrometer, wherein barium sulphate was used as the filler. The lifetime studies were performed using MicroTime 200 resolved confocal fluorescence setup from PicoQuant equipped with an inverted microscope, a 485 nm pulsed laser source used for excitation.

2.2.5. Photocatalytic degradation of organic dyes

Rhodamine B and Methylene blue are the dyes chosen as pollutants in our study. The corresponding wavelength used for Rhodamine B and Methylene Blue are 554 nm and 663 nm respectively. Stock solutions of dyes [Rhodamine B (RhB) and Methylene blue (MB)] were prepared by adding 10 mgL⁻¹ of dye in deionized water for the study of catalytic activity. From this stock solution, 60 ml was taken in a beaker. The photocatalyst powders (Doped and undoped ZnS), 30 mg was added to the solution, and 3 ml of solution was taken in a specific interval of time. The sample was centrifuged at 2500 rpm for 5 min, and its UV-Vis spectrum was recorded to identify the degradation of dye. The observed decrease in intensity of absorption peak represented the degradation. The rate of decolourization of the solution was measured as the decrease in absorbance. The decolourization efficiency is calculated using the formula given below.

Decolorization efficiency = $\left(\frac{C_0 - C_t}{C_0}\right) \times 100$, where C_0 is amount of dye at zero time, C_t is the amount of dye at time t.

2.2.6. Antibacterial activity test

The antibacterial activity of ZnS and metal-doped ZnS has been evaluated through the Zone inhibition method in agar medium. The liquid agar medium was sterile at a temperature of 121 °C. It was poured into the petri dish, 20 ml/plate, and was allowed to solidify. Filter papers of 0.5 – 0.6 cm in diameter were cut using a sterile borer. Nanoparticle solutions with concentration 2, 5, 10, 15, 20 mg/ml were delivered to the filter paper discs leaving 5-10 min for semi- dry. As a positive-standard control, Gentamicin discs consisting of the concentration of 2, 4, 8 and 10 µl (from the stock solution of 2 mg/4 ml) were used to determine the sensitivity of microbial species. 100 µl of bacterial inoculums (1 O.D at 600 nm wavelength of staphylococcus aureus containing 8.3×108 CFU/ml) were used to spread for each solidified agar plate. The inoculated plates were incubated at 37 °C for 12 h and 24 h. To evaluate the antibacterial activity, the diameter of the inhibition zone of tested bacteria was measured in cm. After 12 h and 24 h, the inhibition zone was examined.

2.3. Results and discussion

2.3.1. Preparation and characterisation of ZnS and metal doped ZnS

We have chosen the HMDS-assisted synthetic method to produce ZnS without organic surfactants (sf-ZnS) and metal-doped ZnS (sf-m-ZnS) to obtain high pure materials. When ZnCl₂ was reacted with thiourea in an excess amount of HMDS, we obtained sf-ZnS. When the same reaction was conducted in the presence of other metal sources (Zn:metal ratio =0.95:0.05), metal-doped ZnS were obtained. The possibility of getting a series of metal-doped ZnS by systematically changing the metal sources showcased the control and the versatility of the synthetic method. Earlier, we postulated the mechanism of this HMDS-assisted reaction as occurring via the formation of a polymetric intermediate. The intermediate formation was confirmed earlier by time-dependent ³¹Si NMR spectral studies and GPC data of partially purified air and moisture sensitive intermediate. This intermediate would form on the interaction of thiourea and HMDS and then surround the metal chloride. The interaction of this intermediate with chloride would produce trimethylsilyl chloride. When we monitored the pH of the reaction every one hour, it remained around seven and did not change considerably as the reaction progressed even after six hours. This observation indicates the leaving of hydrogen gas rather than H⁺ ions from HMDS and thus rule out the formation of H₂S gas as an intermediate. Also, since pH was not increasing towards the basic, the formation of NH₃ in this reaction is ruled out. All these observations suggested that hydrogen and nitrogen from HMDS are leaving as H₂ and N₂ gases. Scheme 2.1 depicts the overall reaction. In all these reactions, HMDS played a dual role as solvent and surfactant during synthesis, but not a part of the product. Therefore, these reactions are termed HMDS-assisted reactions.

$$ZnCl_2 + SC(NH_2)_2 + excess HNSi(Me_3)_2 \rightarrow$$

$$\rightarrow [-S - N(SiMe_3) -] \cdots ZnCl_2 \rightarrow$$

$$\rightarrow ZnS + (Me_3)SiCl + N_2 + H_2$$

Scheme 2.1. Formation of zinc sulphide via HMDS-assisted reaction.

The crystalline structure and grain size are obtained from powder X-ray diffraction. The PXRD pattern (Figure 2.2) shows the Bragg's reflection peaks at 2θ of 28.68°, 47.70°, 56.47° analogous to the planes (111), (220), and (311), which are the planes of cubic phase zinc blende (ZnS) (JCPDS-05-0566) [9]. We have noticed the shift in the peak positions in the PXRD pattern of doped ZnS due to the small dissimilitude in ionic radii of doped ions [14].

However, the peak pattern remains the same for all samples, indicating no crystal structure disturbances, showing that the metal ions are inside the lattice. Also, no impurity phases were observed within the resolution limits of the diffractometer [9]. The small changes in Full width at half maximum (FWHM) are due to the changes in the radius of metal atoms doped [16].

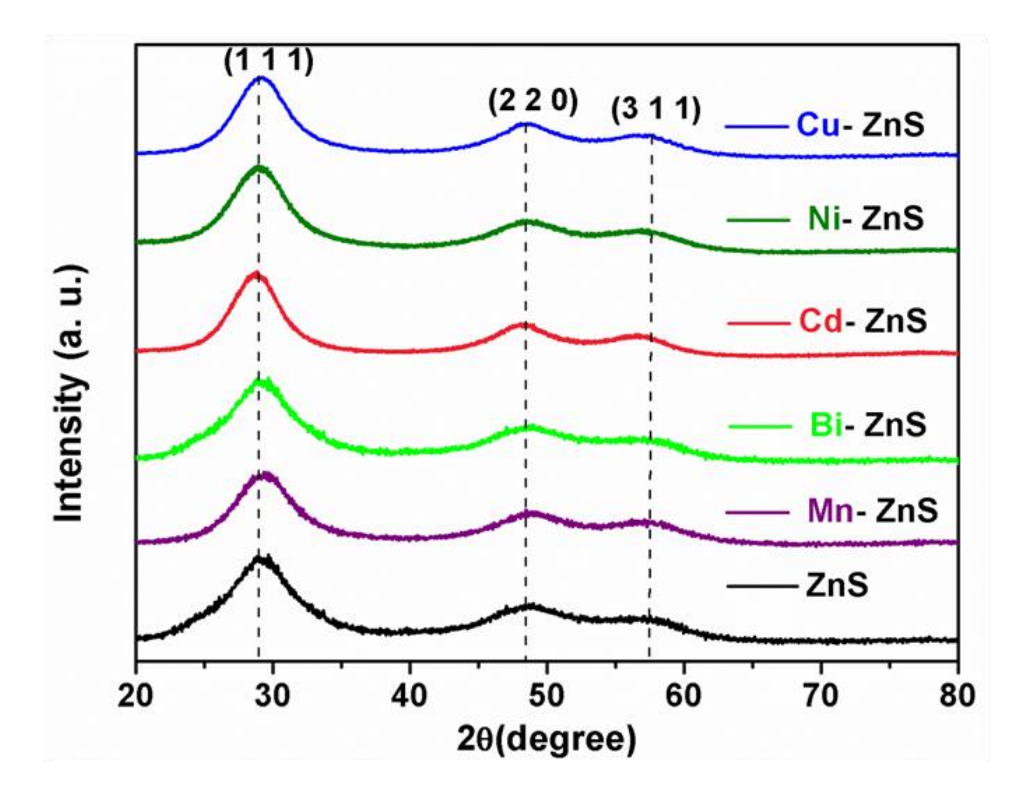


Figure 2.2. PXRD patterns of as synthesised **sf-ZnS** and **sf-m-ZnS** (m= Cu, Ni, Cd, Bi and Mn) nanoparticles.

2.3.2. Effect of doping on morphology and optical property

The effect of doping on the size and shape of ZnS nanoparticles can be observed in electron microscopic images [Figure 2.3 (SEM) and Figure 2.4 (TEM)]. The SEM and TEM images revealed that all the synthesised particles exhibited nanoflakes morphology. There was a variation in thickness of nanoflakes as seen in SEM images attributed to doping. The average particle size of nanoparticles has been calculated (Figure 2.3). The analysis revealed the average particle size as 119 nm for the **sf-ZnS**, 115 nm for the **sf-Cu-ZnS**, 124 nm for the **sf-Ni-ZnS**, 98 nm for the **sf-Cd-ZnS**, 112 nm for the **sf-Bi-ZnS** and 137 nm for the **sf-Mn-ZnS**. Recorded elemental mapping of doped and undoped samples confirmed the homogeneous distribution of doped elements in Figure 2.5. The SAED patterns (Figure 2.4-inset) shows three broad diffused rings for ZnS due to the smaller size of particles, whereas the spots in SAED pattern for the doped sample shows the crystalline nature. The three rings in the SAED pattern

are corresponding to the planes (111), (220), (311) [5, 29-34]. The PXRD pattern supports these observations as well.

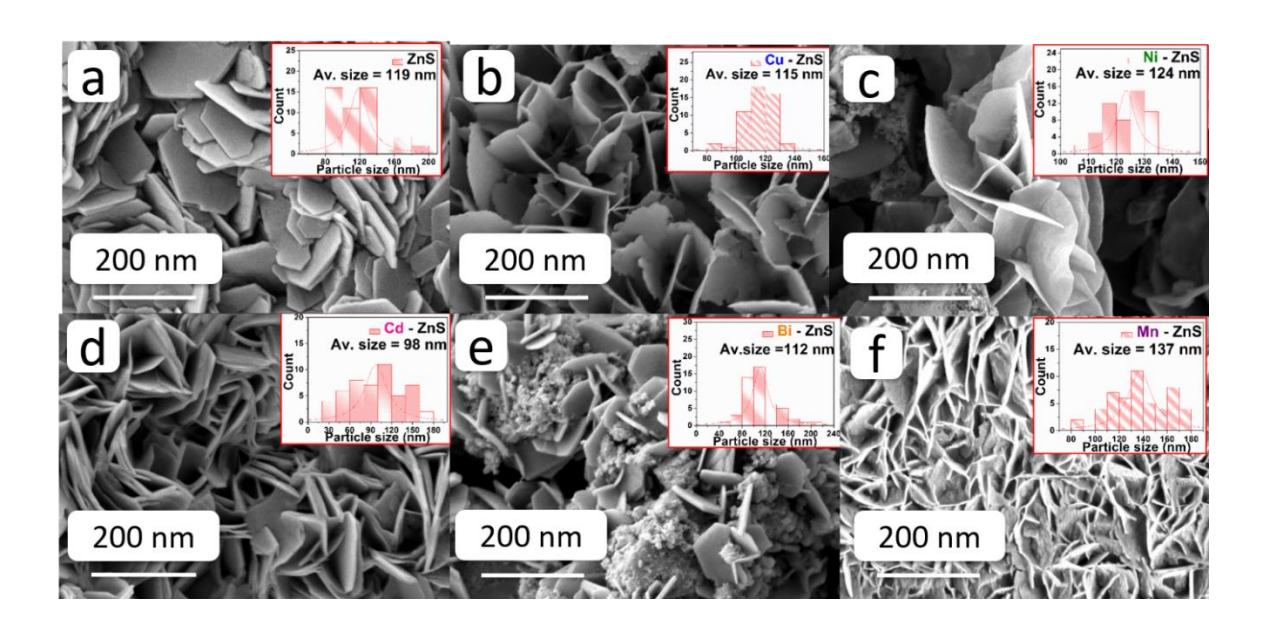


Figure 2.3. FESEM images of as synthesised surfactant free ZnS and transition metal doped ZnS nanoflakes and also presented the calculated average particle size distribution of nanoflakes (inset) (a) **sf-ZnS** (b) **sf-Cu-ZnS** (c) **sf-Ni-ZnS** (d) **sf-Cd-ZnS** (e) **sf-Bi-ZnS** and (f) **sf-Mn-ZnS**.

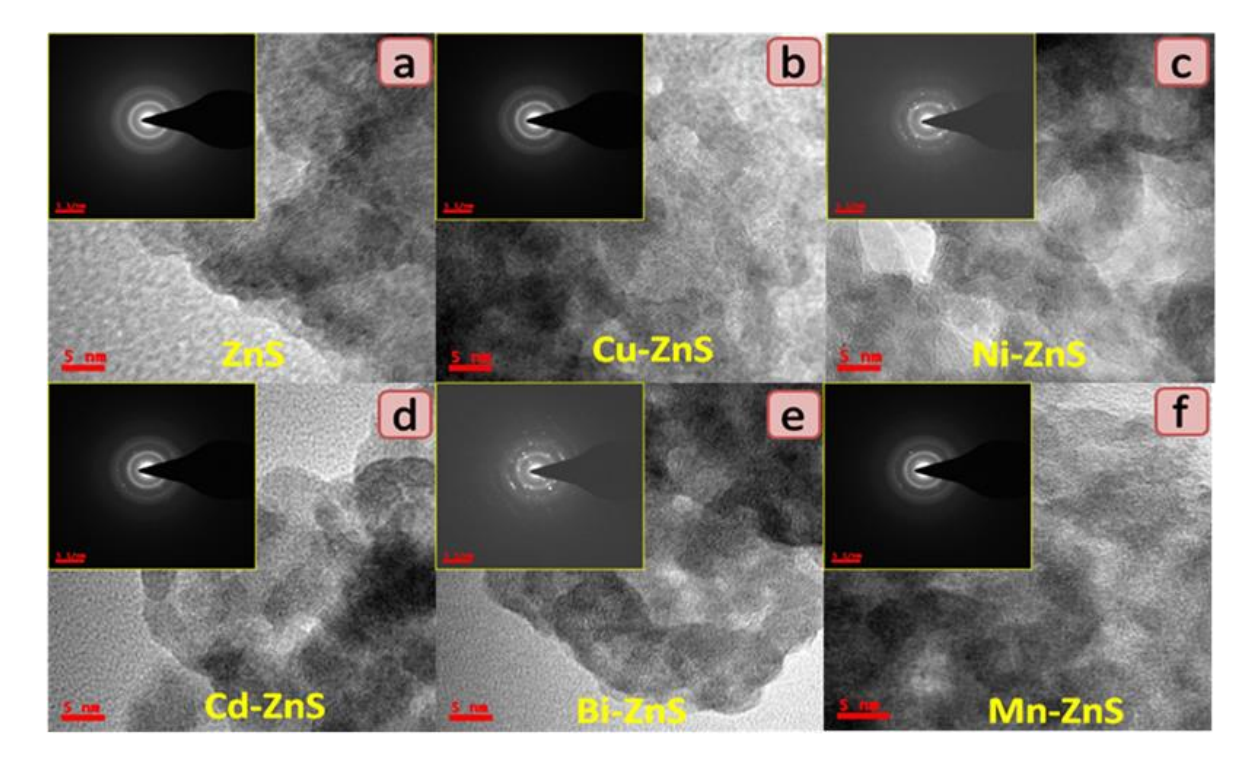


Figure 2.4. TEM and SAED patterns (inset) of (a) sf-ZnS, (b) sf-Cu-ZnS, (c) sf-Ni-ZnS, (d) sf-Cd-ZnS, (e) sf-Bi-ZnS, and (f) sf-Mn-ZnS.

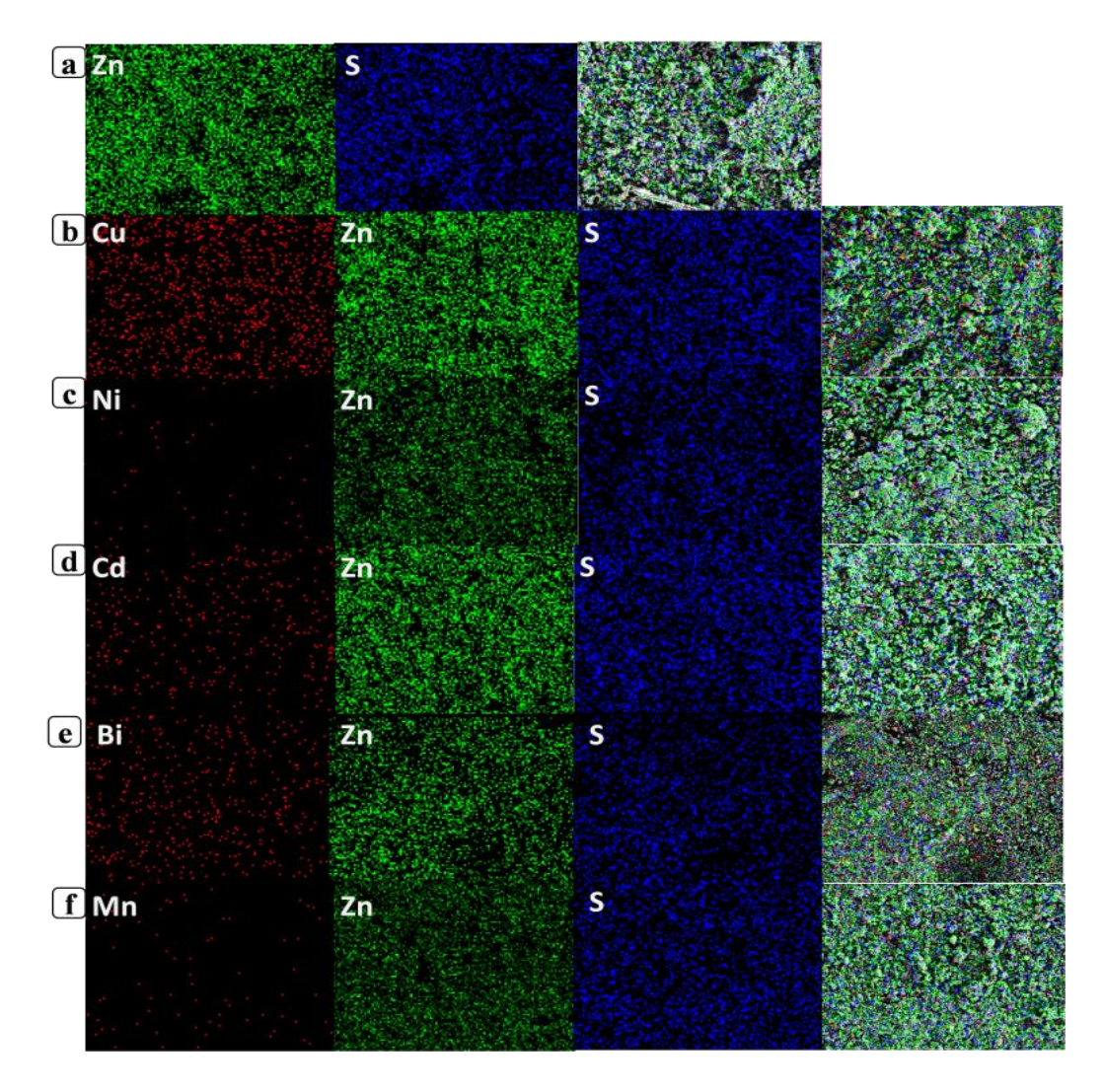


Figure 2.5. EDS elemental mapping of (a) sf-ZnS (b) sf-Cu-ZnS (c) sf-Ni-ZnS (d) sf-Cd-ZnS (e) sf-Bi-ZnS (f) sf-Mn-ZnS.

Optical properties of the synthesised **sf-ZnS** and transition metal doped **sf-ZnS** nanoflakes were examined by UV–vis spectroscopy. Solid-state spectra were recorded to understand the optical properties, which showed a broad absorption. E-gap spectra (Figure 2.6) calculated from DRS spectra (Figure 2.7) for undoped and cadmium doped zinc sulphide nanoparticles showed a blue shift in absorption after doping. For an efficient photocatalyst, the conduction band should be more negative, which zinc sulphide fulfils. However, ZnS has a wide bandgap that helps to absorb only UV light and not the visible light where doping becomes necessary. When zinc sulphide is doped with transition metal ions, there creates a dopant level that acts as an electron-hole trap site between the fundamental energy level and thus helps decrease the HOMO-LUMO gap than that of undoped zinc sulphide. While doping, an exchange interaction occurs between valence band sp electrons and localized d electrons of doped ions [16] as observed in UV-Vis spectra and bandgap spectra. Among the doped metal

ions, **sf-Cd-ZnS** has the lowest bandgap (3.441 eV), the lowest among the reported works. This observation highlights the effect of doping on ZnS nanoparticles and the efficiency of the HMDS-assisted method, which helped to synthesise capping agent-free nanoparticles with control in size. Similarly, the bandgap calculated for Cu, Ni, Bi and Mn-doped ZnS are displayed (Figure 2.7, Table 2.1) variation in their bandgap compared to pure ZnS. A fine-tuning in the bandgap resulted in the change in absorption capacitance from UV to the visible region, enhancing the overall photocatalytic activity.

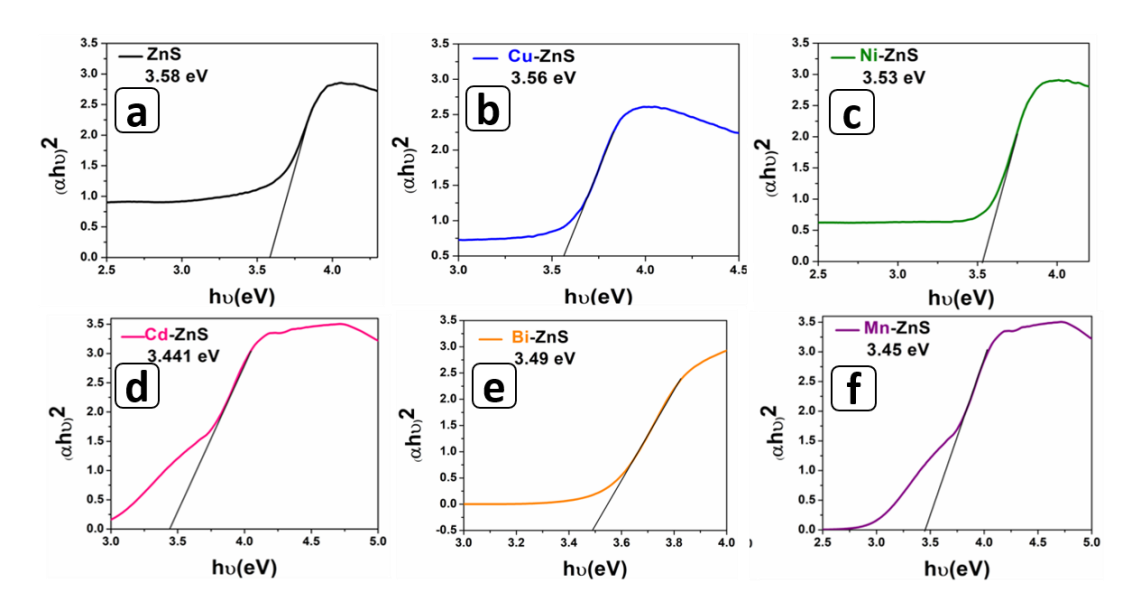


Figure 2.6. Bandgap calculations of (a) sf-ZnS (b) sf-Cu-ZnS (c) sf-Ni-ZnS (d) sf-Cd-ZnS (e) sf-Bi-ZnS (f) sf-Mn-ZnS.

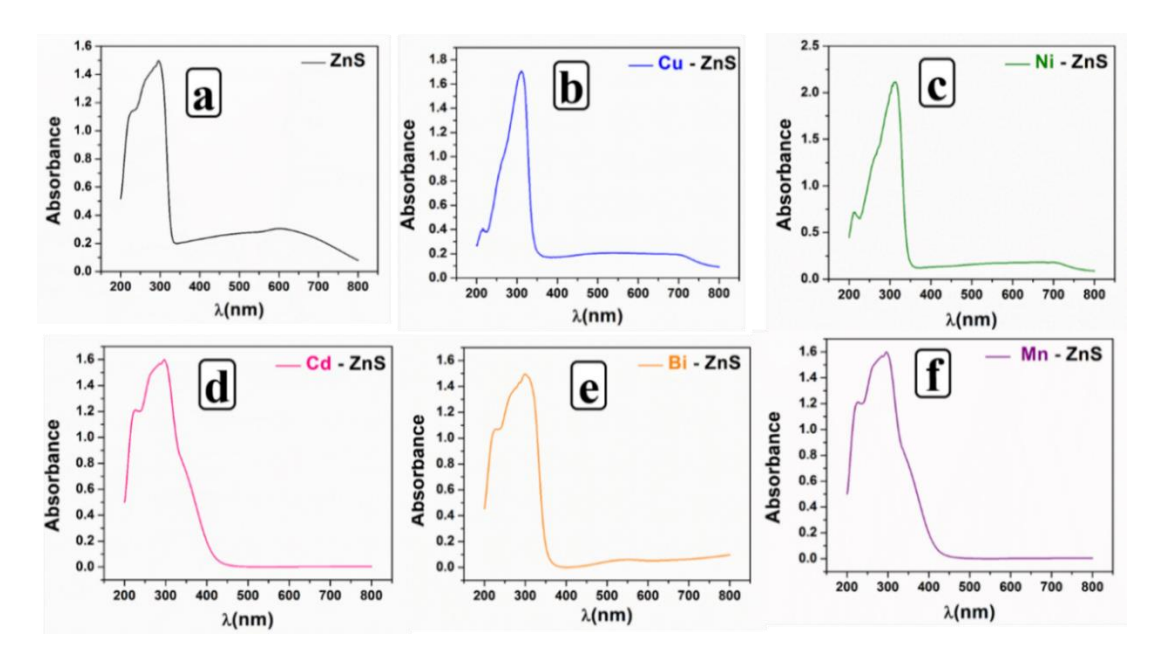


Figure 2.7. DRS spectra of (a) sf-ZnS (b) sf-Cu-ZnS (c) sf-Ni-ZnS (d) sf-Cd-ZnS (e) sf-Bi-ZnS (f) sf-Mn-ZnS.

2.3.3. Effect of metal doping on photochemical degradation of dyes using zinc sulphides

Photocatalysis is a well-established technology for environmental remediation. The doped ZnS photocatalysts exhibited excellent photocatalytic efficiencies since the high conduction band of ZnS is maintained even after doping [35]. Apart from the bandgap tuning, the HMDS-assisted method provided metal doped ZnS without any organic insulating agent at the immediate surroundings of the particles. We tested the degrading abilities of these materials by measuring the absorbance dye solutions (RhB and MB) (Figure 2.8 and 2.9) and calculating the rate constants of degradation reactions (Table 2.1).

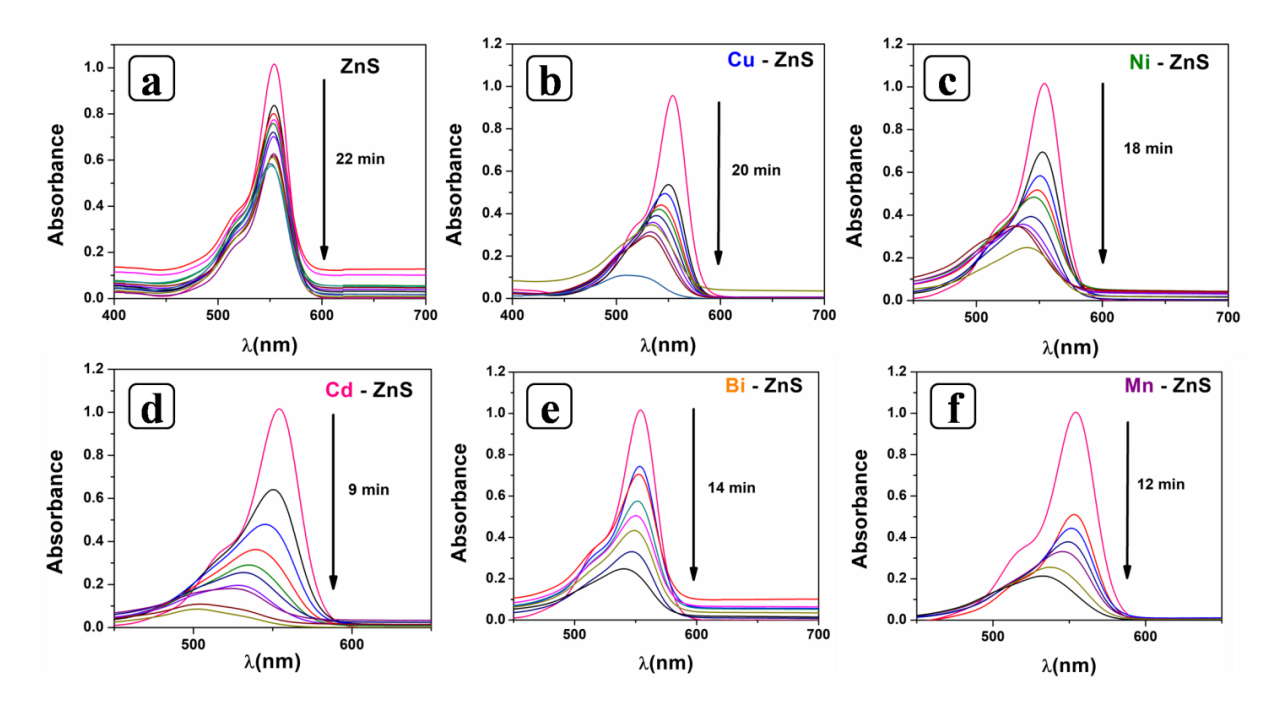


Figure 2.8. Photodegradation of Rhodamine B dye solution for (a) sf-ZnS (b) sf-Cu-ZnS (c) sf-Ni-ZnS (d) sf-Cd-ZnS (e) sf-Bi-ZnS (f) sf-Mn-ZnS.

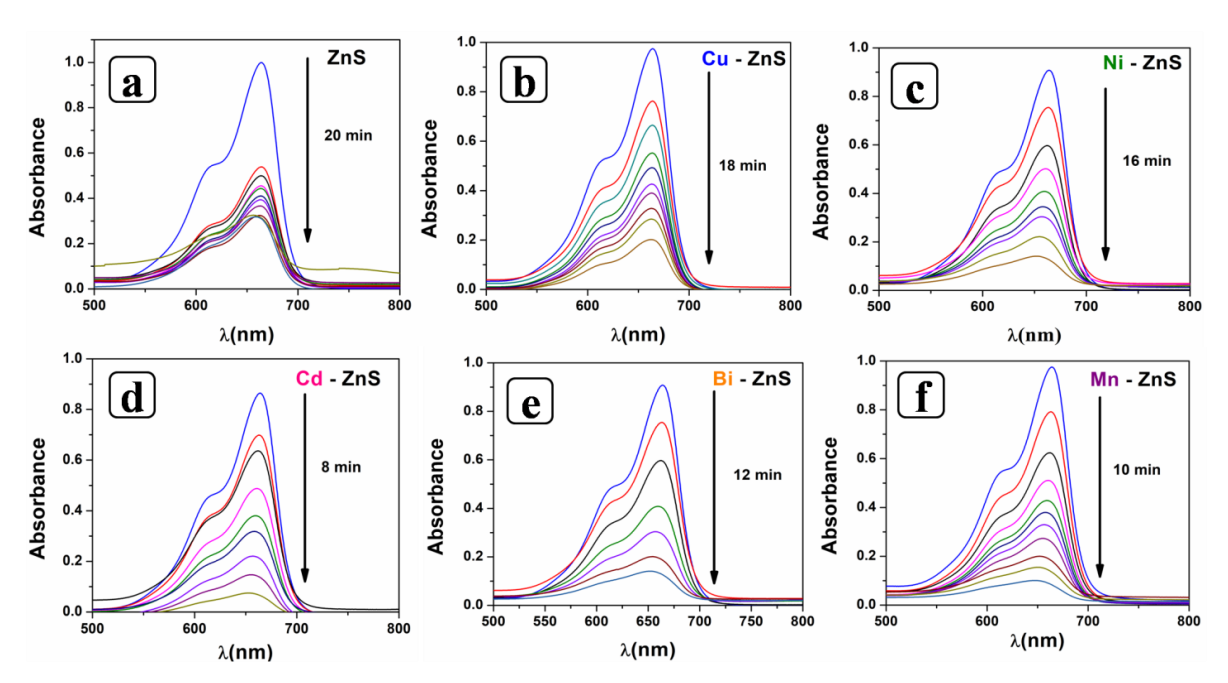


Figure 2.9. Photodegradation of Methylene blue dye solution for (a) sf-ZnS (b) sf-Cu-ZnS (c) sf-Ni-ZnS (d) sf-Cd-ZnS (e) sf-Bi-ZnS (f) sf-Mn-ZnS.

The plots of change in concentration of dyes versus time in the presence of various catalysts showed that the dye degradation followed first-order kinetics. The rate of dye degradation reaction was low $(-2.345 \times 10^{-2} \, \text{min}^{-1} \, \text{for RhB} \, \text{and} \, -6.23 \times 10^{-2} \, \text{min}^{-1} \, \text{for MB})$ when undoped ZnS nanoparticle catalyst, whereas the rate increased considerably with doping. While using **sf-Cd-ZnS** nanoparticles as the catalyst, an approximately 8-fold increase of reaction rate was observed $(-18.6 \times 10^{-2} \, \text{min}^{-1} \, \text{for RhB} \, \text{and} \, -28.23 \times 10^{-2} \, \text{min}^{-1} \, \text{for MB})$. The difference in their catalytic activity can be compared and illustrated as can be seen in Figure 2.10 and 2.11 respectively. Similarly, the catalytic activity of Cu, Ni, Bi and Mn-doped ZnS is illustrated in Figure 2.12, 2.13 and 2.14.

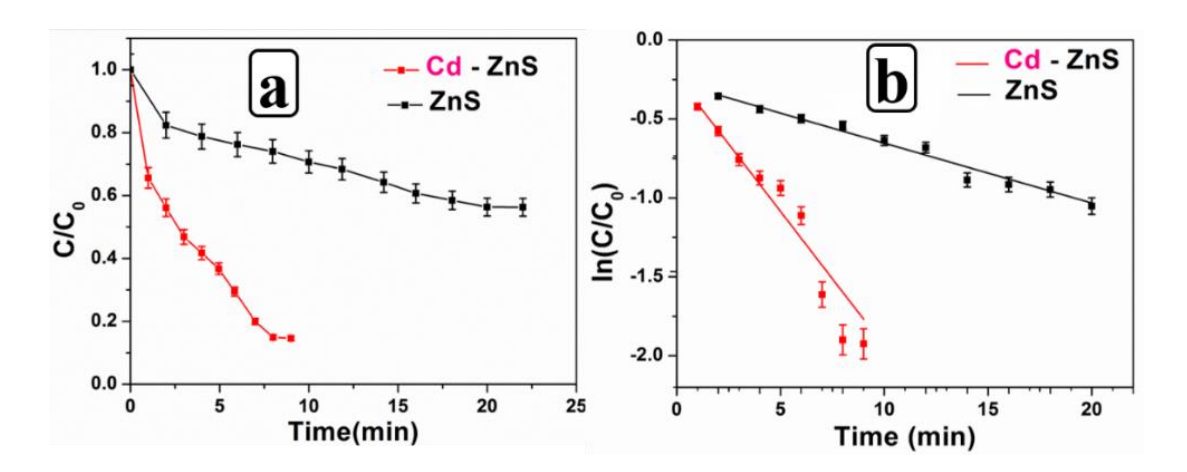


Figure 2.10. (a) (C/C_0) and (b) $ln(C/C_0)$ vs Time for degradation of Rhodamine B dye solution by **sf-ZnS** and **sf-Cd-ZnS** nanoflakes.

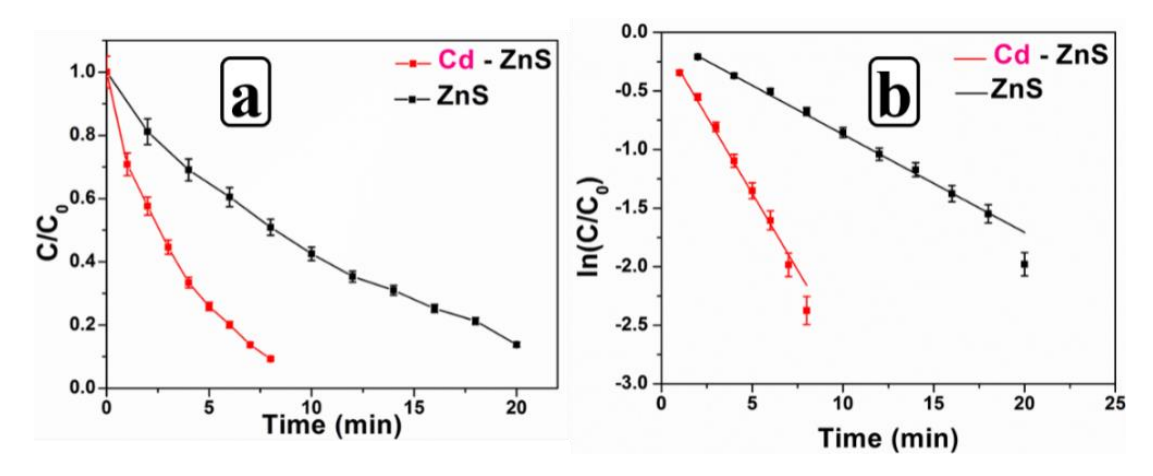


Figure 2.11. (a) (C/C_0) and (b) $ln(C/C_0)$ vs Time for degradation of Methylene blue dye solution by **sf-ZnS** and **sf-Cd-ZnS** nanoflakes.

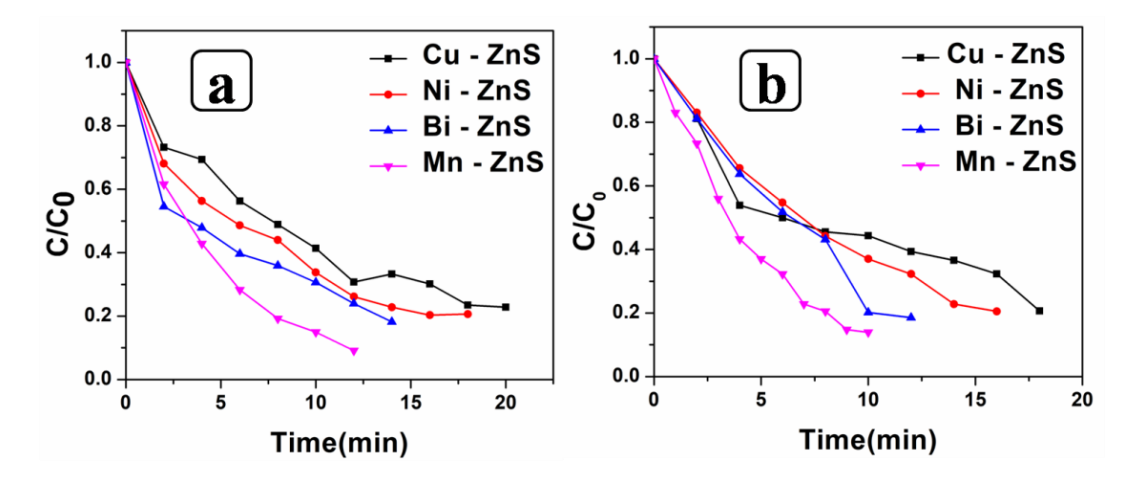


Figure 2.12. C/C₀ vs Time (min) for a) Rhodamine B and b) Methylene blue dye solution respectively for **sf-Cu-ZnS**, **sf-Ni-ZnS**, **sf-Bi-ZnS**, **sf-Mn-ZnS** nanoparticles.

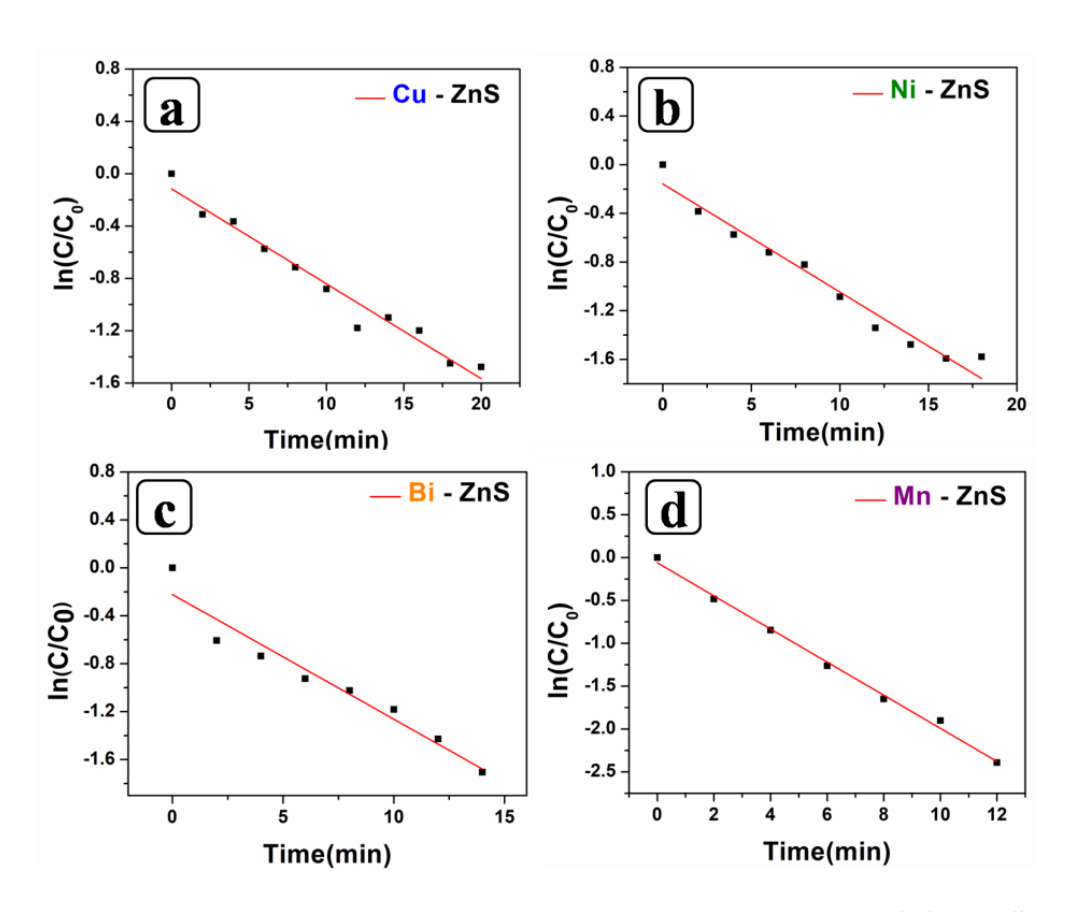


Figure 2.13. ln(C/C₀) vs time for degradation of Rhodamine B dye for(a) **sf-Cu-ZnS** (b) **sf-Ni-ZnS** (c) **sf-Bi-ZnS** (d) **sf-Mn-ZnS**.

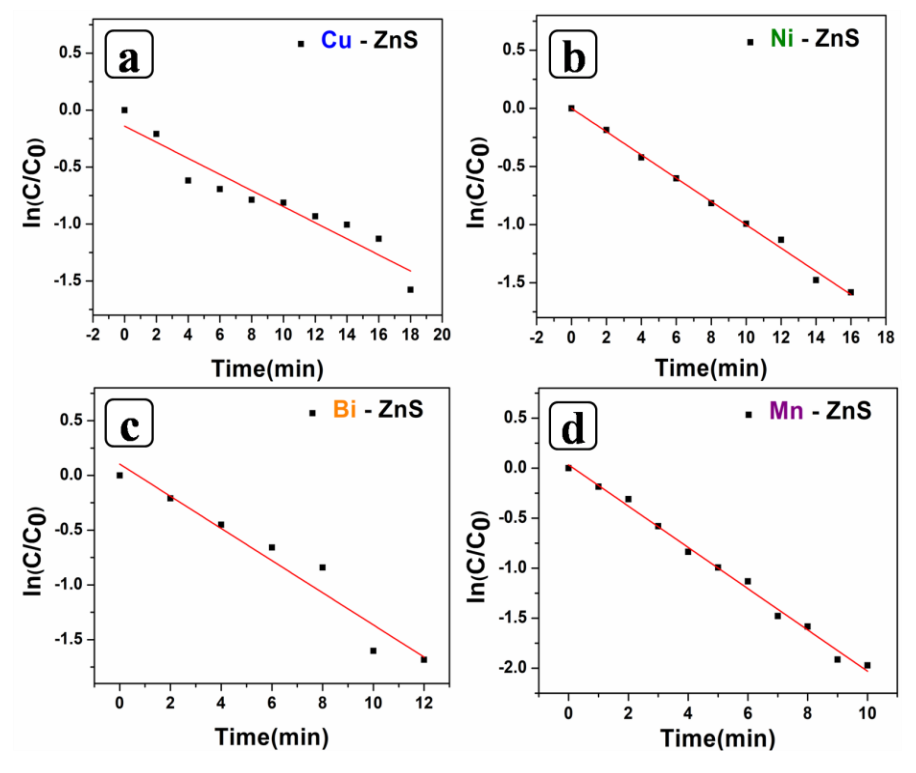


Figure 2.14. $ln(C/C_0)$ vs time for degradation of Methylene blue dye for (a) **sf-Cu-ZnS** (b) **sf-Ni-ZnS** (c) **sf-Bi-ZnS** (d) **sf-Mn-ZnS**.

We have performed few controlled experiments to highlight the importance of the photocatalysis using the least active **sf-ZnS** and highly active **sf-Cd-ZnS**. In the first reaction the degradation of dyes (Rh B and MB) was monitored in the absence of catalyst but in the presence of light (photolysis), while the second degradation reaction was conducted in the presence of catalyst in dark condition (catalysis). From the results (Figure 2.15.) it was clear that to degrade the chosen pollutants catalyst shows it efficiency only in presence of sunlight (photocatalysis).

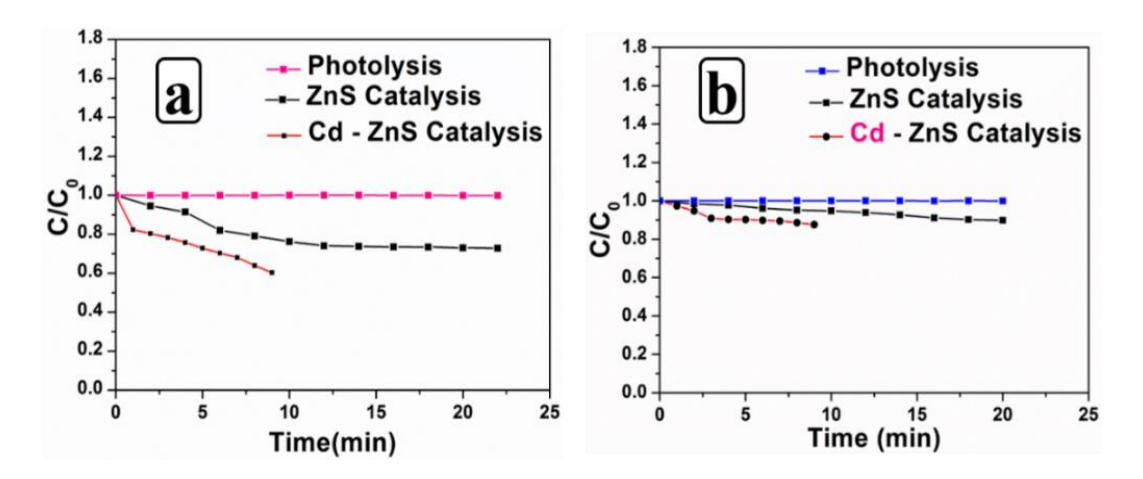


Figure 2.15. Controlled experiments performed for (a) Rhodamine B and (b) Methylene blue dye solutions.

To know the morphological stability of the used catalyst, we have performed the FESEM analysis for the recycled catalyst and noted that the morphology of catalyst has been deformed after fifth cycle, which might be the reason for the decrease in the activity (Figure 2.16).

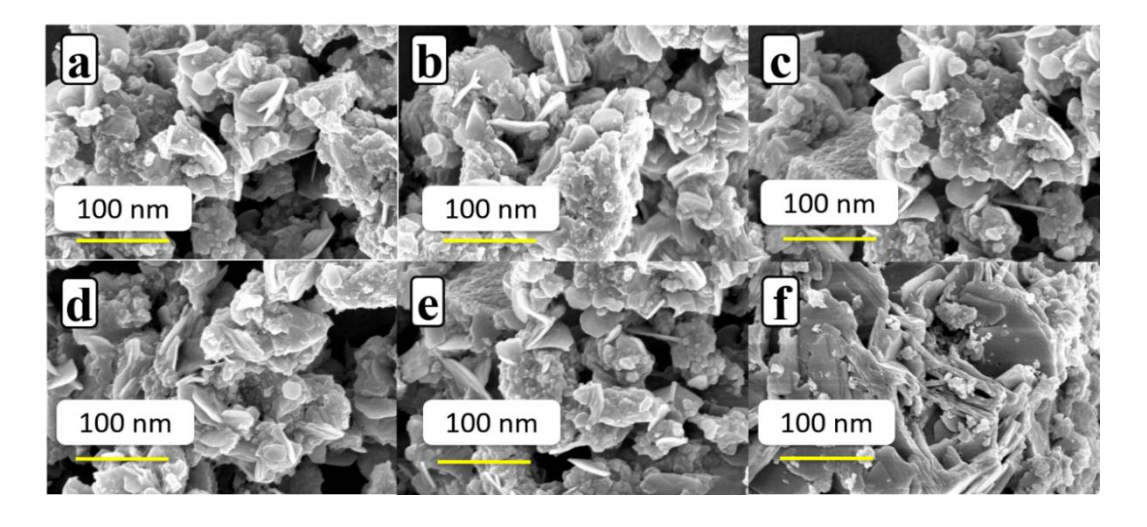


Figure 2.16. FESEM images of nanoflakes after fifth cycle for (a) sf-ZnS (b) sf-Cu-ZnS (c) sf-Ni-ZnS (d) sf-Cd-ZnS (e) sf-Bi-ZnS (f) sf-Mn-ZnS.

The metal doping creates impurity levels in the forbidden band, accommodating charge carriers and thereby increasing photocatalytic activity. Presumably, while doping with Cd, it maintained a relatively high conduction band compared to others, resulting in the best catalytic activity. The photocatalytic efficiency is related to the efficient separation of photo-induced electrons and holes. It appeared that the charge separation was effective in the case of Cd, which showed excellent catalytic behaviour. This explanation is supported by the lifetime of charge separation (Figure 2.17), where Cd doped ZnS showed a higher lifetime than other nanoparticles synthesised.

Table 2.2 depicts the comparison of literature data on the photocatalytic performances of ZnS and doped ZnS-based photocatalysts to purify wastewater. To endorse our study, the results were compared with standard TiO₂-P25 nanoparticles [36, 37]. Interestingly, **sf-Cd-ZnS** was repeatedly used, and it showed good activity even after five cycles of degradation of both RhB and MB (Figure 2.18 and 2.19 for RhB and MB respectively).

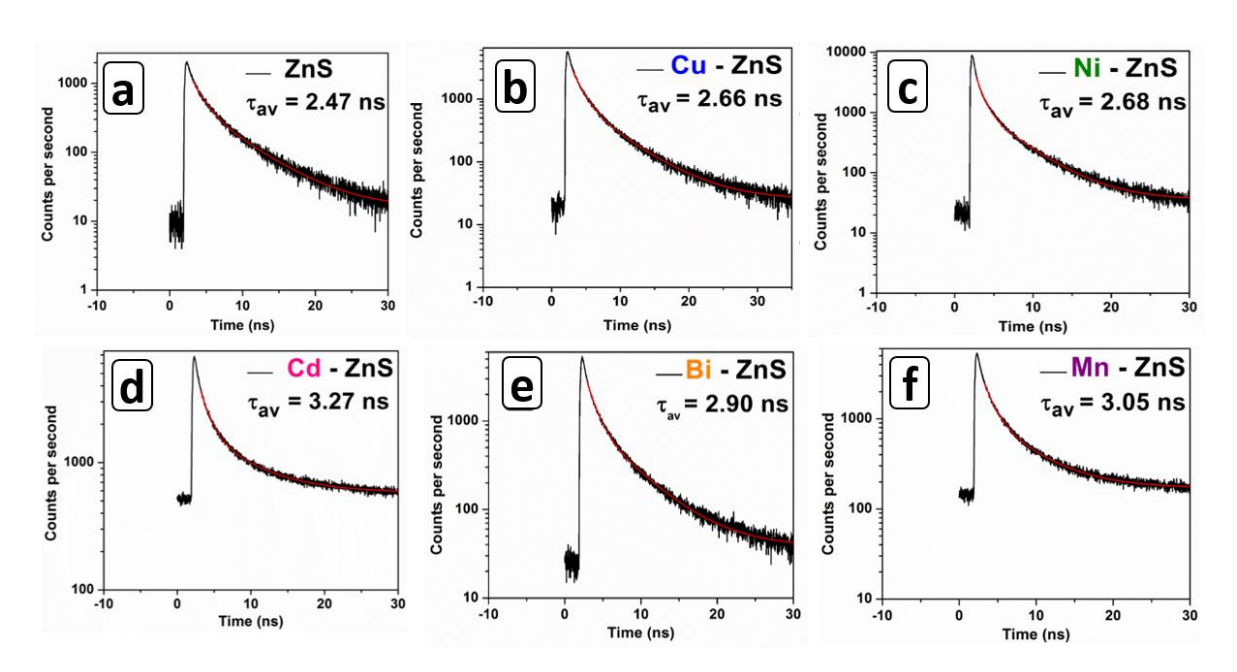


Figure 2.17. Plot of lifetime of (a) sf-ZnS (b) sf-Cu-ZnS (c) sf-Ni-ZnS (d) sf-Cd-ZnS (e) sf-Bi-ZnS (f) sf-Mn-ZnS.

Table 2.1. Bandgap and rate constant determined for the photocatalytic degradation of dyes.

Substance	Bandgap (eV)	Lifetime (ns)	Rate constant value (min ⁻¹)		
			Rhodamine B	Methylene blue	
ZnS	3.58	2.47	-2.345 ×10 ⁻²	-6.23 ×10 ⁻²	
sf-Cu-ZnS	3.56	2.66	-7.254 ×10 ⁻²	-7.066×10 ⁻²	
sf-Ni-ZnS	3.53	2.68	-8.888×10 ⁻²	-10.01 ×10 ⁻²	
sf-Cd-ZnS	3.44	3.27	-18.6×10^{-2}	-28.23 ×10 ⁻²	
sf-Bi-ZnS	3.49	2.90	-10.405 ×10 ⁻²	-14.69×10^{-2}	
sf-Mn-ZnS	3.45	3.05	-12.584 ×10 ⁻²	-20.61×10 ⁻²	

The mechanism of degradation reaction is well-known in the literature. When sunlight falls on the semiconductor, the electrons from the valence band gets excited to the conduction band. While doping with metal ions, it creates intermediate trap states decreasing the bandgap. More electrons get excited to these states since less energy is needed for the excitation of electrons [19, 32-34, 38-47] and this will increase the number of charge carriers available for dye degradation, which results in increasing photocatalytic activity [3, 17]. As soon as electrons are excited to the conduction bands or trap states, holes are created in the valence band. These holes are taken immediately by water adsorbed on the catalyst surface to undergo oxidation and produce hydroxyl radical, OH. These hydroxyl radicals so produced oxidize the organic species (dyes) adsorbed on the surface of catalysts to simpler molecules, CO₂, H₂O. The electrons in the conduction band react with oxygen to produce anionic superoxide radical species O_2^{-} , which produces hydroperoxyl radicals, which in turn leads to the formation of H_2O_2 and undergo dissociation to form OH, which degrades the organic dyes present on the surface (Scheme 2.20). In the case of Cd, this process is happening at a faster rate and thus enhances the photocatalytic activity. In contrast, there is a decrease in activity in other cases due to the recombination of charge carriers, resulting in the unavailability of charge carriers for the dye to participate in photocatalysis.

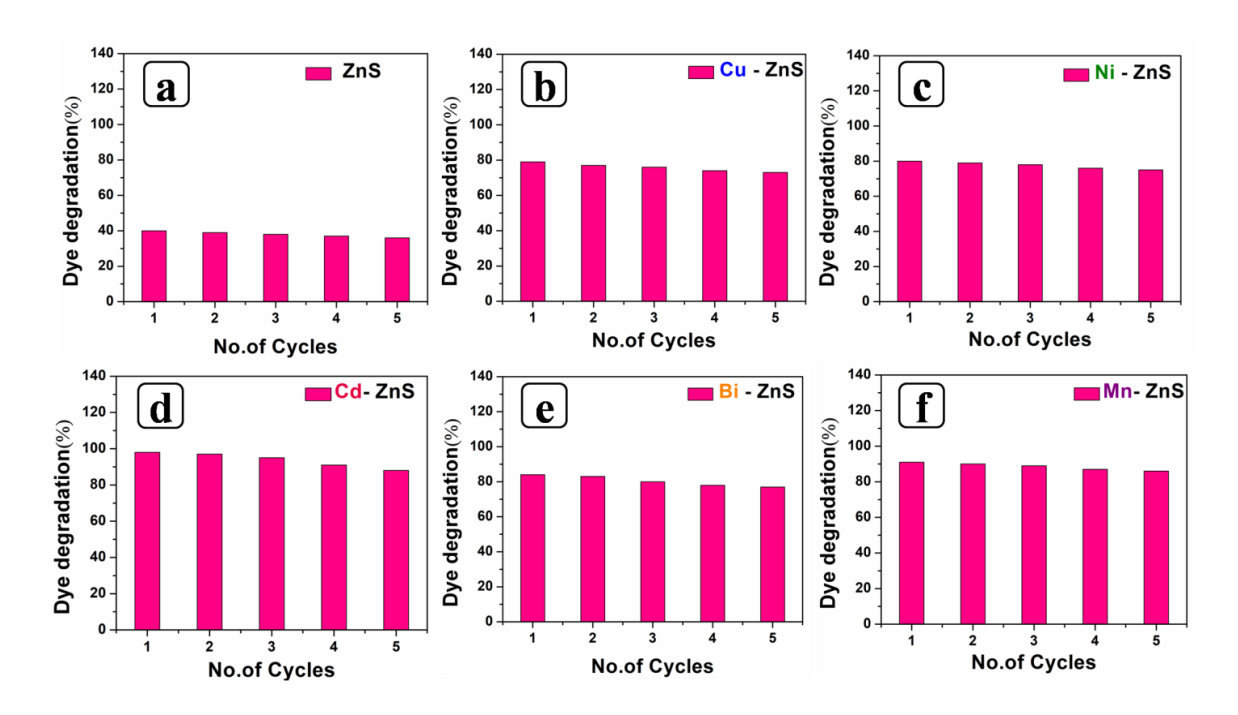


Figure 2.18. Degradation cycle of Rhodamine B dye solution for (a) sf-ZnS (b) sf-Cu-ZnS (c) sf-Ni-ZnS (d) sf-Cd-ZnS (e) sf-Bi-ZnS (f) sf-Mn-ZnS.

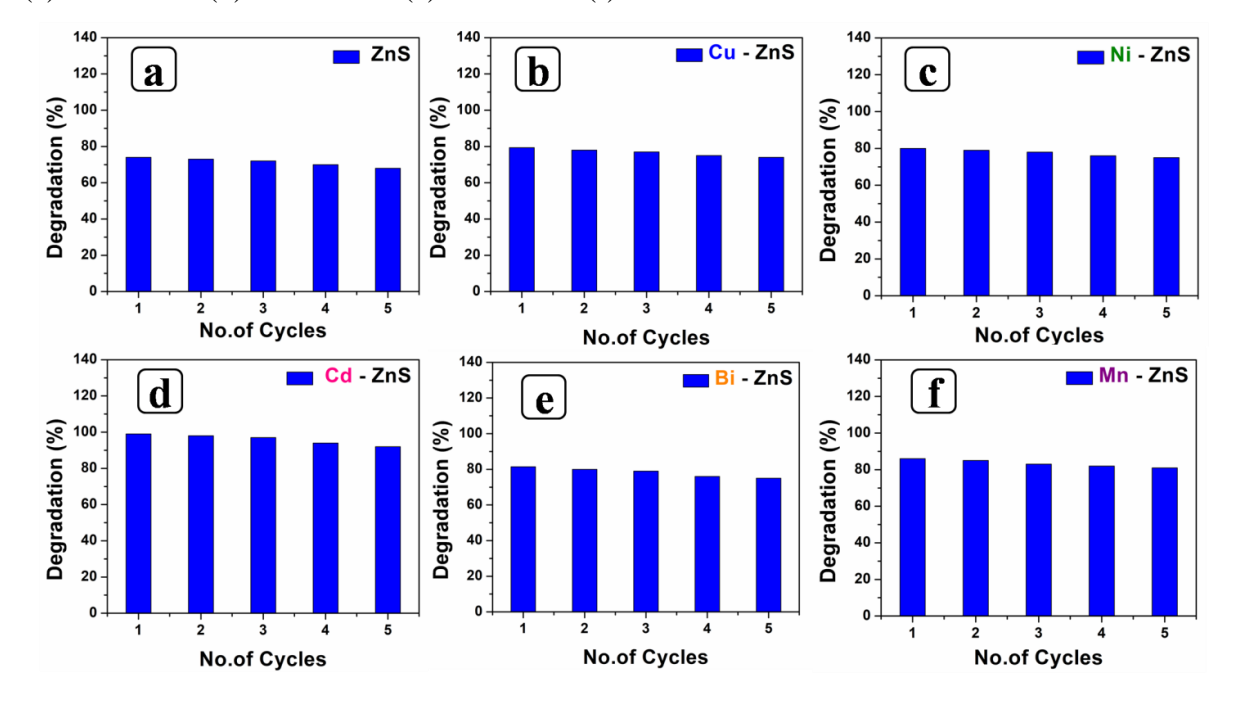
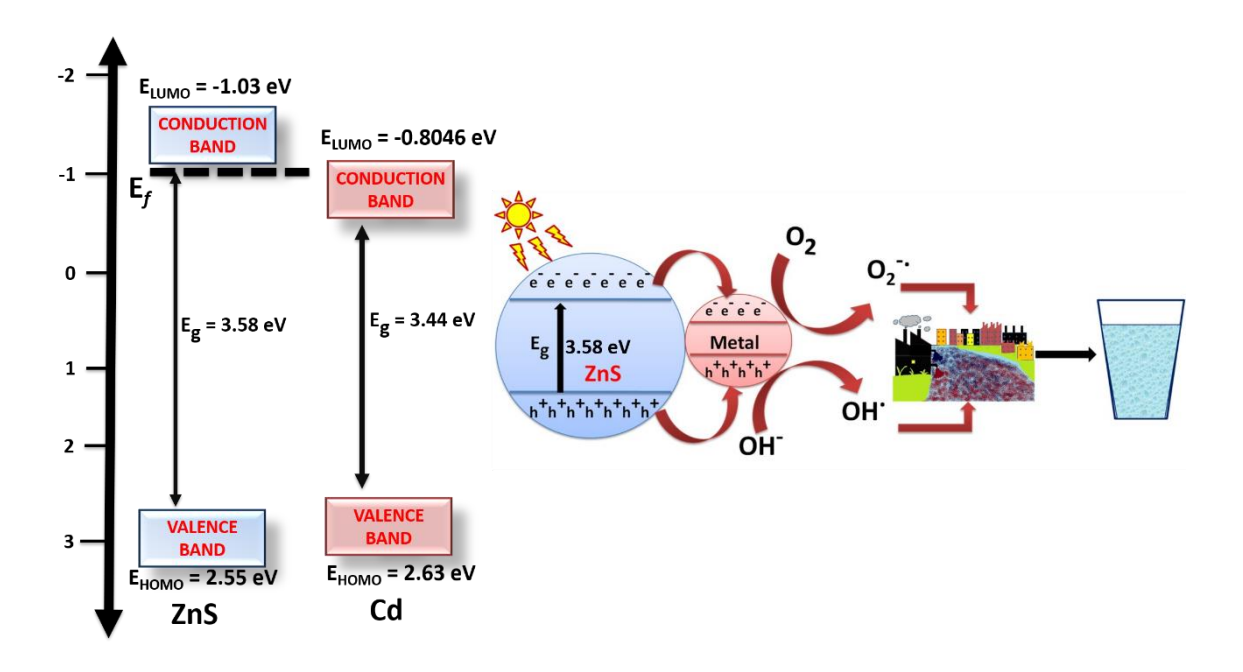


Figure 2.19. Degradation cycle of Methylene blue dye solution for (a) sf-ZnS (b) sf-Cu-ZnS (c) sf-Ni-ZnS (d) sf-Cd-ZnS (e) sf-Bi-ZnS (f) sf-Mn-ZnS.

Table 2.2. Photocatalytic performances of ZnS and metal doped ZnS-based photocatalysts for the waste water treatment.

Type of Catalyst	Pollutant concentration	Amount of catalyst	Time (min)	Efficiency (%)	References	
ZnS	RhB 10mg/L	1000mg/L	30		48	
PVP-ZnS	MB 10mg/L	100mg/L	360	65	49	
Zn _{0.2} Cd _{0.8} S	MB 10mg/L	1600mg/L	60	96	50	
ZnS	MB 10mg/L	300mg/L	60	93	51	
ZnS	RhB 10mg/L	750mg/L	210	82	52	
ZnS	RhB 20mg/L	200mg/L	180	70	53	
ZnS	MB 50mg/L	500mg/L	120	78	54	
Ni-ZnS	MB 10mg/L	500mg/L	120	52	55	
Ni-ZnS	RhB 10mg/L	500mg/L	180	87	56	
Mn-ZnS	MB 5mg/L	film in 20ml	180	99	57	
Cu-ZnS	MB 10mg/L	1000mg/L in 50ml	300	100	58	
Cu-ZnS	МВ 10μМ	250mg/L in 100ml	60	74	17	
Sn - ZnS	MB 20ppm	1000mg/L	180	93	45	
TiO ₂ - P25	RhB 5mg/L	1000mg/L	300	22	36	
TiO ₂ -P25	RhB 2.8×10^{-5} M	1600mg/L	180	96	37	
sf-ZnS	RhB 10mg/L	500mg/L	22	40	Present work	
	MB 10mg/L	500mg/L	20	74		
sf-Cd-ZnS	RhB 10mg/L	500mg/L	9	98	Present work	
	MB 10mg/L	500mg/L	8	99		



Scheme 2.2. Schematic illustration of energy band mechanism of photocatalysis by doped ZnS nanoparticles.

2.3.4. The retarding effect of capping agents on photocatalysis

The purpose of capping agents aimed for controlling the particle size in nano region, but impact, necessity and further consequences of those capping agents were decided based on targeted applications. Adverse effects of capping agents were elaborated in the introduction in Figure 2.1. The presence of capping agents decreases the communication between the particles, hinder the mobility of charge carrier. As we discussed in above sections, capping agents hide the active centers of absorption and leads to reduced surface area and simultaneously affects the catalytic activity and finally reduce device efficiency and catalyst activity.

Photocatalysis is a surface phenomenon. In this area of research, capping agents plays a major role in the photodegradation of organic dyes, since they are at interface between dye molecules and catalyst surface. A reduction of visible emission spectra was observed for ZnO nanoparticles capped with capping agents such as Polyvinylpyrrolidone (PVP), hexamine, tetraethylammoniumbromide (TEAB), tetraoctlyammoniumbromide (TOAB) and cetyltrimethylammoniumbromide (CTAB) [59, 60, 61]. In support, the increase in concentration of humic acid as capping agent on ZnO decreased the photocatalytic efficiency of the catalyst, by trapping the electron generated by excitation of photocatalyst by humic acid [62, 63]. From our group [64], endorsed the surfactant free approach over the PVP stabilized SnS₂ Nanostructures for the organic dye degradation and reduction of toxic heavy metals. The

electrons and holes created by the excitation of photocatalysts are not able to reach the surface due to the covering created by capping agent, which restricts the formation of superoxide radical anion and hydroxide radicals, which are the active species required for dye degradation. This ineptitude of active species formation decreases the photocatalytic activity of the photocatalyst.

2.3.5. Antibacterial activity of metal doped zinc sulphides

An earlier report [18] suggested that the sharp edges and corners of nanoflakes can cause breakage of the bacterial cell membrane, which releases the oxidation products to cause oxidation of protein and eventually leads to cell death [15, 65, 66]. The organic-free exposed surface of nanoflakes produced in our HMDS-assisted method could help to improve the adhesion between *Staphylococcus aureus* (S. aureus) bacteria and the nanoparticles. The antibacterial activity of ZnS and metal-doped ZnS against gram-positive S. aureus was studied by the zone of inhibition method. Figure 2.20 depicts the results of the antibacterial study at different concentrations of each nanoparticle synthesised. In these pictures of agar-agar plates, the zone of inhibition is visible around the ZnS materials. The results illustrate that as the concentration of materials increased, the zone of inhibition also increased (Figure 2.21 and 2.22) and thus, the nanoparticle synthesised was effective against gram-positive bacteria (S. aureus).

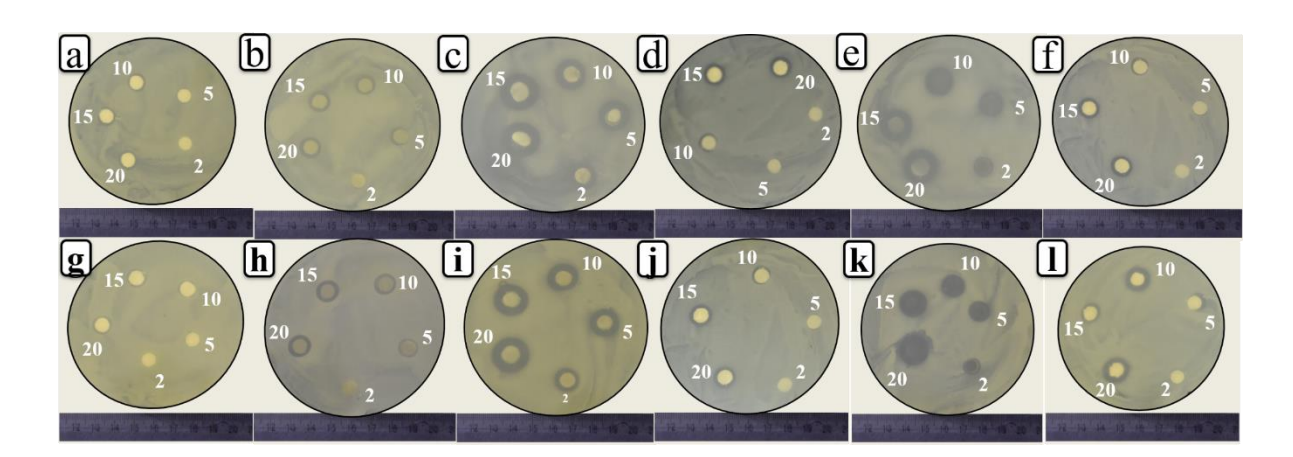


Figure 2.20 Agar–agar plates showing the zone of inhibition test results using the concentrations 2, 5, 10, 15, 20 mg/ml of (a) sf-ZnS, (b) sf-Cu-ZnS, (c) sf-Ni-ZnS, (d) sf-Cd-ZnS, (e) sf-Bi-ZnS f) sf-Mn-ZnS for 12 h and (g) sf-ZnS, (h) sf-Cu-ZnS, (i) sf-Ni-ZnS, (j) sf-Cd-ZnS, (k) sf-Bi-ZnS, (l) sf-Mn-ZnS for 24 h.

Microbial Agents	Concentration	Zone Inhibition (cm)	Microbial Agents	Concentration	Zone Inhibition (cm)	Microbial Agents	Concentration	Zone Inhibition (cm)
Control (S. <i>aureus</i>)		0	Control (S. aureus)		0	Control (S. aureus)		0
Gentamicin	2 μl 4 μl 8 μl 10 μl	0.9 ± 0.1 1.1 ± 0.1 1.4 ± 0.1 1.5 ± 0.1	Gentamicin	2 μl 4 μl 8 μl 10 μl	0.9 ± 0.0 1.3 ± 0.1 1.5 ± 0.1 1.6 ± 0.1	Gentamicin	2 μl 4 μl 8 μl 10 μl	0.9 ± 0.1 1.1 ± 0.2 1.5 ± 0.2 1.4 ± 0.2
ZnS	2 mg/ml 5 mg/ml 10 mg/ml 15 mg/ml 20 mg/ml	$\begin{array}{c} 0.4 \pm 0.1 \\ 0.5 \pm 0.1 \\ 0.7 \pm 0.1 \\ 0.8 \pm 0.1 \\ 0.8 \pm 0.1 \end{array}$	Cu doped ZnS	2 mg/ml 5 mg/ml 10 mg/ml 15 mg/ml 20 mg/ml	$0.6 \pm 0.1 \\ 0.7 \pm 0.1 \\ 0.8 \pm 0.1 \\ 0.9 \pm 0.1 \\ 0.9 \pm 0.1$	Ni doped ZnS	2 mg/ml 5 mg/ml 10 mg/ml 15 mg/ml 20 mg/ml	0.9 ± 0.1 1.2 ± 0.2 1.2 ± 0.1 1.4 ± 0.1 1.4 ± 0.1
Microbial Agents	Concentration	Zone Inhibition (cm)	Microbial Agents	Concentration	Zone Inhibition (cm)	Microbial Agents	Concentratio n	Zone Inhibition (cm)
Control (S. <i>aureus</i>)		0	Control (S. aureus)		0	Control (S. aureus)		0
Gentamicin	2 μl 4 μl 8 μl 10 μl	0.8 ± 0.2 1.1 ± 0.1 1.3 ± 0.1 1.3 ± 0.1	Gentamicin	2 μl 4 μl 8 μl 10 μl	1.0 ± 0.2 1.1 ± 0.2 1.5 ± 0.2 1.5 ± 0.2	Gentamicin	2 μl 4 μl 8 μl 10 μl	$0.9 \pm 0.1 \\ 1.1 \pm 0.1 \\ 1.2 \pm 0.2 \\ 1.3 \pm 0.1$
Cd doped ZnS	2 mg/ml 5 mg/ml 10 mg/ml 15 mg/ml 20 mg/ml	$\begin{array}{c} 0.5 \pm 0 \\ 0.5 \pm 0 \\ 0.7 \pm 0.1 \\ 0.8 \pm 0.1 \\ 0.9 \pm 0.1 \end{array}$	Bi doped ZnS	2 mg/ml 5 mg/ml 10 mg/ml 15 mg/ml 20 mg/ml	0.7 ± 0.2 0.9 ± 0.1 1.0 ± 0.1 1.2 ± 0.1 1.3 ± 0.1	Mn doped ZnS	2 mg/ml 5 mg/ml 10 mg/ml 15 mg/ml 20 mg/ml	0.5 ± 0 0.5 ± 0.1 0.6 ± 0.1 0.9 ± 0.1 0.9 ± 0.2

Figure 2.21. Antibacterial activities of **sf-ZnS**, **sf-Cu-ZnS**, **sf-Ni-ZnS**, **sf-Cd-ZnS**, **sf-Bi-ZnS**, **sf-Mn-ZnS** for 12 h

Microbial Agents	Concentration	Zone Inhibition (cm)	Microbial Agents	Concentration	Zone Inhibition (cm)	Microbial Agents	Concentration	Zone Inhibition (cm)
Control (S. aureus)		0	Control (S. aureus)		0	Control (S. aureus)		0
Gentamicin	2 μl 4 μl 8 μl 10 μl	1.2 ± 0.1 1.4 ± 0.1 1.5 ± 0.2 1.6 ± 0.2	Gentamicin	2 μl 4 μl 8 μl 10 μl	$ 1.0 \pm 0 1.4 \pm 0.1 1.5 \pm 0.2 1.3 \pm 0.1 $	Gentamicin	2 μl 4 μl 8 μl 10 μl	1.1 ± 0.1 1.3 ± 0.2 1.6 ± 0.2 1.5 ± 0.1
ZnS	2 mg/ml 5 mg/ml 10 mg/ml 15 mg/ml 20 mg/ml	$\begin{array}{c} 0.5 \pm 0.1 \\ 0.6 \pm 0.1 \\ 0.7 \pm 0.1 \\ 0.8 \pm 0.1 \\ 0.8 \pm 0.1 \end{array}$	Cu doped ZnS	2 mg/ml 5 mg/ml 10 mg/ml 15 mg/ml 20 mg/ml	0.6 ± 0 0.8 ± 0.1 0.9 ± 0.1 1.0 ± 0.1 1.0 ± 0.1	Ni doped ZnS	2 mg/ml 5 mg/ml 10 mg/ml 15 mg/ml 20 mg/ml	0.9 ± 0.1 1.2 ± 0.1 1.2 ± 0.1 1.4 ± 0.1 1.5 ± 0.1
Microbial Agents	Concentration	Zone Inhibition (cm)	Microbial Agents	Concentration	Zone Inhibition (cm)	Microbial Agents	Concentratio n	Zone Inhibition (cm)
Control (S. aureus)		0	Control (S. aureus)		0	Control (S. aureus)		0
Gentamicin	2 μl 4 μl 8 μl 10 μl	0.9 ± 0.1 1.1 ± 0.1 1.3 ± 0.1 1.4 ± 0.2	Gentamicin	2 μl 4 μl 8 μl 10 μl	1.2 ± 0.2 1.4 ± 0.2 1.5 ± 0.2 1.5 ± 0.1	Gentamicin	2 µl 4 µl 8 µl 10 µl	0.9 ± 0 1.1 ± 0.1 1.3 ± 0.1 1.5 ± 0.1
Cd doped ZnS	2 mg/ml 5 mg/ml 10 mg/ml 15 mg/ml 20 mg/ml	$\begin{array}{c} 0.5 \pm 0.1 \\ 0.5 \pm 0.1 \\ 0.6 \pm 0.1 \\ 0.8 \pm 0.1 \\ 0.8 \pm 0.1 \end{array}$	Bi doped ZnS	2 mg/ml 5 mg/ml 10 mg/ml 15 mg/ml 20 mg/ml	0.7 ± 0.2 0.9 ± 0.1 1.0 ± 0.1 1.2 ± 0.1 1.4 ± 0.1	Mn doped ZnS	2 mg/ml 5 mg/ml 10 mg/ml 15 mg/ml 20 mg/ml	0.5 ± 0.1 0.7 ± 0.2 1.0 ± 0.1 0.9 ± 0.1 1.2 ± 0.1

Figure 2.22. Antibacterial activities of sf-ZnS, sf-Cu-ZnS, sf-Ni-ZnS, sf-Cd-ZnS, sf-Bi-ZnS, sf-Mn-ZnS for 24 h.

It is clear that the metal-doped ZnS showed higher activity than the undoped ZnS. The Ni doped ZnS showed the highest activity among all doped ZnS. As explained in the existing reports, the nanoparticles like ZnS attack the cytoplasmic and extra-cytoplasmic targets when they enter through the bacterial membrane. This interaction results in the production of biologically reactive oxygen species (R.O.S) like superoxide anion (O_2^-) , hydroxyl ion (OH^-) , hydroxyl radicals (OH^+) . In addition to this, the metal ions do have an affinity towards carboxyl (-COOH), amino (-NH₂), thiol (R-SH) and imidazole $(C_3H_4N_2)$ groups present in the microbial membrane proteins, which cause a change in protein functions and nucleic acids of the targeted organism. These changes enhance the cell permeability, which in turn cause DNA damage and oxidation of protein, eventually causing cell death [15, 16, 65, 66]. The results of the present study limn the efficiency of Ni-doped ZnS as an antibacterial agent.

2.4. Conclusion

In summary, we have successfully produced surfactant-free ZnS (sf-ZnS) and metal-doped ZnS (sf-m-ZnS: m= Cu, Ni, Cd, Bi, Mn) nanoparticles using the HMDS-assisted method. The X-ray diffraction and SAED patterns confirmed the formation of the cubical phase of crystalline ZnS nanoparticles. The bandgap tuning of ZnS was achieved by doping with transition metals as confirmed through measurements of the optical property. The sf-Cd-ZnS exhibited higher photocatalytic activity among the other doped and undoped ZnS nanoparticles in degrading organic dyes (RhB and MB) under visible light. In the case of antibacterial activity, sf-Ni-ZnS showed higher activity against Gram-positive bacteria, *Staphylococcus aureus*. The absorption edge of the doped ZnS materials shifts to the lower energy region compared to pure ZnS. Simultaneously, the activity of the doped ZnS nanoparticles has increased a maximum of 8-fold for the photodegradation of organic dyes in comparison to undoped ZnS nanoparticles. Thus, this chapter highlights the impact of tuning the bandgap of wide bandgap semiconductor photocatalyst, ZnS and its application in industrial wastewater treatment and its role as an antibacterial agent.

2.5. References

- 1. Zhang, F., Li, Y.H., Li, J.Y., Tang, Z.R. and Xu, Y.J. 3D graphene-based gel photocatalysts for environmental pollutants degradation. *Environ. Pollut.* **2019**, 253, 365-376.
- 2. Ferreira-Neto, E.P., Ullah, S., Da Silva, T.C., Domeneguetti, R.R., Perissinotto, A.P., De Vicente, F.S., Rodrigues-Filho, U.P. and Ribeiro, S.J. Bacterial nanocellulose/MoS₂ hybrid aerogels as bifunctional adsorbent/photocatalyst membranes for in-flow water decontamination. *ACS Appl. Mater. Interfaces.* **2020**, 12, 41627-41643.
- 3. Habibi-Yangjeh, A., Poormohammadi-Ahandani, Z. and Pirhashemi, M. Ultrasonic-assisted method for preparation of Cu-doped ZnS nanoparticles in water as a highly efficient visible light photocatalyst. *Phys. Chem. Res.* **2014**, 2, 76-89.
- 4. Velanganni, S., Pravinraj, S., Immanuel, P. and Thiruneelakandan, R.J.P.B.C.M. Nanostructure CdS/ZnO heterojunction configuration for photocatalytic degradation of Methylene blue. *Phys. Rev. B Condens. Matter.* **2018**, 534, 56-62.
- 5. Wang, W., Chen, L., Wang, S., Xi, B., Xiong, S., Qian, Y. and Zhang, Z. Low-temperature synthesis of nearly monodisperse ZnS nanospheres using a facile solution-phase approach. *Aust. J. Chem.* **2006**, 59, 791-795.
- 6. Corrado, C., Jiang, Y., Oba, F., Kozina, M., Bridges, F. and Zhang, J.Z. Synthesis, structural, and optical properties of stable ZnS: Cu, Cl nanocrystals. *J. Phys. Chem. A.* **2009**, 113, 3830-3839.
- 7. Uekawa, N., Ouchi, M., Wen, C.M., Matsumoto, T. and Kojima, T. Synthesis of copper ion doped ZnS phosphor sols by peptization process of sulfide-citrate complex precipitates. *J. Ceram. Soc. Jpn.* **2015**, 123, 924-928.
- 8. Yang, P., Song, C., Lü, M., Zhou, G., Yang, Z., Xu, D. and Yuan, D. Photoluminescence of Cu⁺-doped and Cu²⁺-doped ZnS nanocrystallites. *J. Phys. Chem. Solids.* **2002**, 63, 639-643.
- 9. Peng, W.Q., Cong, G.W., Qu, S.C. and Wang, Z.G. Synthesis and photoluminescence of ZnS: Cu nanoparticles. *Opt. Mater.* **2006**, 29, 313-317.
- 10. Cadiş, A.I., Popovici, E.J., Bica, E., Perhaita, I., Barbu-Tudoran, L., Indrea, E. and Silaghi-Dumitrescu, L. Synthesis of manganese doped zinc sulphide nanocrystalline powders by wet-chemical synthesis route. *Dig. J. Nanomater. Biostructures.* **2011**, 6.

- 11. Kole, A.K. and Kumbhakar, P. Effect of manganese doping on the photoluminescence characteristics of chemically synthesised zinc sulfide nanoparticles. *Appl. Nanosci.* **2016**, 2, 15-23.
- 12. Ummartyotin, S., Bunnak, N., Juntaro, J., Sain, M. and Manuspiya, H. Synthesis and luminescence properties of ZnS and metal (Mn, Cu)-doped-ZnS ceramic powder. *Solid State Sci.* **2012**, 14, 299-304.
- 13. Zhang, K. and Guo, L. Metal sulphide semiconductors for photocatalytic hydrogen production. *Catal. Sci. Technol.* **2013**, 3, 1672-1690.
- 14. Sahraei, R. and Darafarin, S. Preparation of nanocrystalline Ni doped ZnS thin films by ammonia-free chemical bath deposition method and optical properties. *J. Lumin.* **2014**, 149, 170-175.
- 15. Singh, P. K., Sharma, P. K., Kumar, M., Dutta, R., Sundaram, S., & Pandey, A. C. Red luminescent manganese-doped zinc sulphide nanocrystals and their antibacterial study. *J. Mater. Chem. B.* **2014**, 2, 522–528.
- 16. Harish, S., Archana, J., Navaneethan, M., Ponnusamy, S., Singh, A., Gupta, V., Aswal, D.K., Ikeda, H. and Hayakawa, Y. Synergetic effect of CuS@ ZnS nanostructures on photocatalytic degradation of organic pollutant under visible light irradiation. *RSC Adv.* 2017, 7, 34366-34375.
- 17. Prasad, N. and Balasubramanian, K. Optical, phonon and efficient visible and infrared photocatalytic activity of Cu doped ZnS micro crystals. *Spectrochim. Acta A Mol. Biomol.* **2017**, 173, 687-694.
- Song, J., Zhang, F., Huang, Y., Keller, A.A., Tang, X., Zhang, W., Jia, W. and Santos,
 J. Highly efficient bacterial removal and disinfection by magnetic barium phosphate
 nanoflakes with embedded iron oxide nanoparticles. *Environ. Sci. Nano.* 2018, 5, 1341-1349.
- 19. Dilpazir, S., Siddiq, M. and Iqbal, A. Synthesis of zinc sulphide nanostructures by Coprecipitation: effects of doping on electro-optical properties. *Kenkyu j. nanotechnol. nanosci.* **2015**, 1, 34-9.
- 20. Qumar, U., Ikram, M., Imran, M., Haider, A., Ul-Hamid, A., Haider, J., Riaz, K.N. and Ali, S. Synergistic effect of Bi-doped exfoliated MoS₂ nanosheets on their bactericidal and dye degradation potential. *Dalton Trans.* **2020**, 49, 5362-5377.
- 21. Kumar, G.A., Naik, H.B., Viswanath, R., Gowda, I.S. and Santhosh, K.N. Tunable emission property of biotin capped Gd: ZnS nanoparticles and their antibacterial activity. *Mater. Sci. Semicond. Process.* **2017**, 58, 22-29.

- 22. Rose, A., Shunmugapriya, B., Maiyalagan, T. and Vijayakumar, T. Investigation on the electrochemical properties of hydrothermally synthesized pure and Nickel doped Zinc Sulfide microspheres for supercapacitor electrode applications. *J Mater Sci Mater Electron.* **2020**, 31, 19204-19212.
- 23. Hussain, I., Mohapatra, D., Dhakal, G., Lamiel, C., Mohamed, S.G., Sayed, M.S. and Shim, J.J. Different controlled nanostructures of Mn-doped ZnS for high-performance supercapacitor applications. *J Energy Storage*. **2020**, 32, 101767.
- 24. Srinivas, B., Kumar, B.G. and Muralidharan, K. Stabilizer free copper sulphide nanostructures for rapid photocatalytic decomposition of Rhodamine B. *J. Mol. Catal*, **2015**, 410, 8-18.
- 25. Kumar, B.G., Srinivas, B. and Muralidharan, K. Photo-responsive Bi₂S₃ nanoflakes: Synthesis and device fabrication at ambient conditions. *Mater. Res. Bull.* **2017**, 89, 108-115.
- 26. Billakanti, S. and Krishnamurthi, M. Facile preparation of surfactant or support material free CdS nanoparticles with enhanced photocatalytic activity. *J. Environ. Chem. Eng.* **2018**, 6, 1250-1256.
- 27. Pandit, M.A., Billakanti, S. and Muralidharan, K. A simplistic approach for the synthesis of CuS-CdS heterostructure: A novel photo catalyst for oxidative dye degradation. *J. Environ. Chem. Eng.* **2019**, 8, 103542.
- 28. Pandit, M.A., Sai Hemanth Kumar, D., Billakanti, S., Ramadoss, M. and Muralidharan, K. Chalcopyrite with magnetic and dielectric properties: an introductory catalyst for 4-nitrophenol reduction. *J. Phys. Chem. C.* **2020**, 124, 18010-18019.
- 29. Kuppayee, M., Nachiyar, G.V. and Ramasamy, V. Synthesis and characterisation of Cu²⁺ doped ZnS nanoparticles using TOPO and SHMP as capping agents. *Appl. Surf. Sci.* **2011**, 257, 6779-6786.
- 30. Anand, K.V., Mohan, R., Kumar, R.M., Chinnu, M.K. and Jayavel, R. Structural and optical properties of high-purity cubic phase ZnS nanoparticles prepared by thermal decomposition route for optoelectronic applications. *Proc. Indian National Sci. Acad.* **2013**, 79, 395-399.
- 31. Murugadoss, G. Luminescence properties of co-doped ZnS: Ni, Mn and ZnS: Cu, Cd nanoparticles. *J. Lumin.* **2012**, 132, 2043-2048.
- 32. Kumar, V., Rawal, I., Kumar, V. and Goyal, P.K. Efficient UV photodetectors based on Ni-doped ZnS nanoparticles prepared by facial chemical reduction method. *Phys. Rev. B Condens. Matter.* **2019**, 575, 411690.

- 33. Bindu, K.R. and Anila, E.I. Optimized synthesis temperature and doping concentration of copper in zinc sulphide nanoparticles for green emission. *Mater. Sci. Semicond. Process.* **2021**, 121, 105317.
- 34. Mostafa, M., El Nady, J., Ebrahim, S.M. and Elshaer, A.M. Synthesis, structural, and optical properties of Mn²⁺ doped ZnS quantum dots for biosensor application. *Opt. Mater.* **2021**, 112, 110732.
- 35. Michael, R.J.V., Theerthagiri, J., Madhavan, J., Umapathy, M.J. and Manoharan, P.T. Cu₂S-incorporated ZnS nanocomposites for photocatalytic hydrogen evolution. *RSC Adv.* **2015**, 5, 30175-30186.
- 36. Ren, W., Ai, Z., Jia, F., Zhang, L., Fan, X. and Zou, Z. Low temperature preparation and visible light photocatalytic activity of mesoporous carbon-doped crystalline TiO₂. *Appl. Catal.* B. **2007**, 69, 138-144.
- 37. Natarajan, T.S., Thomas, M., Natarajan, K., Bajaj, H.C. and Tayade, R.J. Study on UV-LED/TiO₂ process for degradation of Rhodamine B dye. *J. Chem. Eng.* **2011**, 169, 126-134.
- 38. Mageswari, S., Dhivya, L., Palanivel, B. and Murugan, R. Influence of bismuth doping on the structural and optical properties of ZnS thin films and nanopowders. *Phys. Scr.* **2013**, 88, 065703.
- 39. Mote, V.D., Purushotham, Y. and Dole, B.N. Structural, morphological and optical properties of Mn doped ZnS nanocrystals. *Cerâmica*, **2013**, 59, 395-400.
- 40. Kurnia, F. and Hart, J.N. Band-Gap Control of Zinc Sulfide: Towards an Efficient Visible-Light-Sensitive Photocatalyst. *ChemPhysChem*, **2015**, 16, 2397-2402.
- 41. Madkour, M., Salih, T., Al-Sagheer, F. and Bumajdad, A. Nano-heterostructured photostable Cd_xZn_{1-x}S heterojunction as a non-photocorrosive visible light active photocatalyst. *Opt. Mater. Express.* **2016**, 6, 2857-2870.
- 42. Jeyakumari, A.P., Sumathi, M., Thirumagal, N. and Kumar, M.U. Chemical precipitation synthesis of Fe, Ni, and Co doped zinc sulphide nanoparticles. *J Appl Phys.* **2017**, 1, 64-70.
- 43. Mosavi, S.M. and Kafashan, H. Physical properties of Cd-doped ZnS thin films. *Superlattices Microstruct.* **2019**, 126, 139-149.
- 44. Gbashi, K.R. and Hussein, A.K. Cu-doped ZnS coatings for optoelectronics with enhanced protection for UV radiations. *J Mater Sci Mater Electron.* **2020**, 31, 17258-17268.

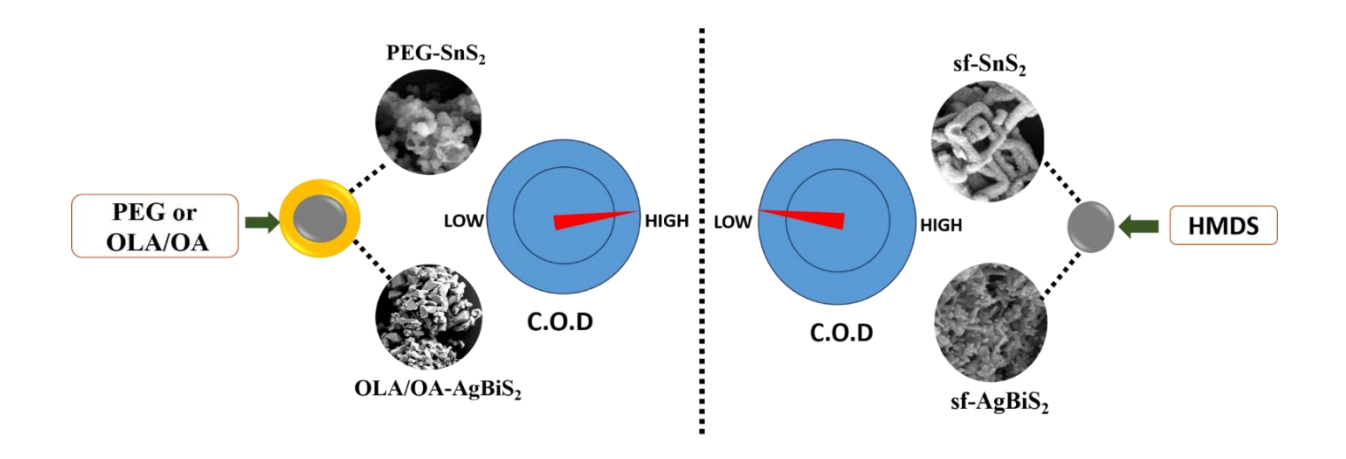
- 45. Ramki, K., RajaPriya, A., Sakthivel, P., Murugadoss, G., Thangamuthu, R. and Rajesh Kumar, M. Rapid degradation of organic dyes under sunlight using tin-doped ZnS nanoparticles. *J Mater Sci Mater Electron.* **2020**, 31, 8750-8760.
- 46. Das, P., Tantubay, K., Ghosh, R., Dam, S. and Baskey, M. Transformation of CuS/ZnS nanomaterials to an efficient visible light photocatalyst by 'photosensitizer' graphene and the potential antimicrobial activities of the nanocomposites. *Environ. Sci. Pollut. Res.* **2021**, 28, 49125-49138.
- 47. Vall, C.S., Chaik, M., Tchenka, A., Hnawi, S., Mellalou, A., Aggour, M. and Outzourhit, A. Effect of chromium percentage doping on the optical, structural, morphological and electrical properties of ZnS: Cr thin films. *Phys. E: Low-Dimens. Syst. Nanostructures.* **2021**, 130, 114694.
- 48. Luo, M., Liu, Y., Hu, J., Li, J., Liu, J. and Richards, R.M. General strategy for one-pot synthesis of metal sulfide hollow spheres with enhanced photocatalytic activity. *Appl. Catal.* B. **2012**, 125, 180-188.
- 49. Soltani, N., Saion, E., Yunus, W.M.M., Navasery, M., Bahmanrokh, G., Erfani, M., Zare, M.R. and Gharibshahi, E. Photocatalytic degradation of methylene blue under visible light using PVP-capped ZnS and CdS nanoparticles. *Sol. Energy.* **2013**, 97, 147-154.
- 50. Song, L., Zhang, S., Chen, B., Ge, J. and Jia, X. Fabrication of ternary zinc cadmium sulfide photocatalysts with highly visible-light photocatalytic activity. *Catal. Commun.* **2010**, 11, 387-390.
- 51. Zhang, S. Preparation of controlled-shape ZnS microcrystals and photocatalytic property. *Ceram. Int.* **2014**, 40, 4553-4557.
- 52. La Porta, F.D.A., Nogueira, A.E., Gracia, L., Pereira, W.S., Botelho, G., Mulinari, T.A., Andrés, J. and Longo, E. An experimental and theoretical investigation on the optical and photocatalytic properties of ZnS nanoparticles. *J. Phys. Chem. Solids.* **2017**, 103, 179-189.
- 53. Ayodhya, D. and Veerabhadram, G. Green synthesis, optical, structural, photocatalytic, fluorescence quenching and degradation studies of ZnS nanoparticles. *J. Fluoresc.* **2016**, 26, 2165-2175.
- 54. Ye, Z., Kong, L., Chen, F., Chen, Z., Lin, Y. and Liu, C. A comparative study of photocatalytic activity of ZnS photocatalyst for degradation of various dyes. *Optik*, **2018**, 164, 345-354.

- 55. Othman, A.A., Osman, M.A., Ali, M.A., Mohamed, W.S. and Ibrahim, E.M.M. Sonochemically synthesized Ni-doped ZnS nanoparticles: structural, optical, and photocatalytic properties. *J Mater Sci Mater Electron*. **2019**, 31, 1752-1767.
- 56. Zhao, W.H., Wei, Z.Q., Wu, X.J., Zhang, X.D., Zhang, L. and Xuan, W.A.N.G. Microstructure and photocatalytic activity of Ni-doped ZnS nanorods prepared by hydrothermal method. *Trans. Nonferrous Met. Soc. China.* 2019, 29, 157-164.
- 57. Kannan, S., Subiramaniyam, N.P. and Sathishkumar, M. Effect of annealing temperature and Mn doping on the structural and optical properties of ZnS thin films for enhanced photocatalytic degradation under visible light irradiation. *Inorg. Chem. Commun.* **2020**, 119, 108068.
- 58. Chauhan, R., Kumar, A. and Chaudhary, R.P. Photocatalytic degradation of methylene blue with Cu doped ZnS nanoparticles. *J. Lumin.* **2014**, 145, 6-12.
- 59. Singla, M.L. and Kumar, M. Optical characterisation of ZnO nanoparticles capped with various surfactants. *J. Lumin.* **2009**, 129, .434-438.
- 60. Sudha, M., Senthilkumar, S., Hariharan, R., Suganthi, A. and Rajarajan, M. Controlled reduction of the deleterious effects of photocatalytic activity of ZnO nanoparticles by PVA capping. *J. Sol-Gel Sci. Technol.* **2012**, 61, 14-22.
- 61. Sudha, M. and Rajarajan, M. Deactivation of photocatalytically active ZnO nanoparticle by surface capping with poly vinyl pyrrolidone. *J. Appl. Chem.* **2013**, 3, 45-53.
- 62. Cao, Z. and Zhang, Z. Deactivation of photocatalytically active ZnO nanoparticle and enhancement of its compatibility with organic compounds by surface-capping with organically modified silica. *Appl. Surf. Sci.* **2011**, 257, 4151-4158.
- 63. Chandran, P., Netha, S. and Khan, S.S. Effect of humic acid on photocatalytic activity of ZnO nanoparticles. *J. Photochem. Photobiol. B: Biol.* **2014**, 138, 155-159.
- 64. Srinivas, B., Pandit, M.A. and Muralidharan, K. Importance of clean surfaces on the catalyst: SnS₂ nanorings for environmental remediation. *ACS Omega*, **2019**, 4, 14970-14980.
- 65. Chu, Z., Zhang, S., Zhang, B., Zhang, C., Fang, C.Y., Rehor, I., Cigler, P., Chang, H.C., Lin, G., Liu, R. and Li, Q. Unambiguous observation of shape effects on cellular fate of nanoparticles. *Sci. Rep.* **2014**, 4, 4495.

66. Gnanamozhi, P., Renganathan, V., Chen, S.M., Pandiyan, V., Arockiaraj, M.A., Alharbi, N.S., Kadaikunnan, S., Khaled, J.M. and Alanzi, K.F. Influence of Nickel concentration on the photocatalytic dye degradation (methylene blue and reactive red 120) and antibacterial activity of ZnO nanoparticles. *Ceram. Int.* **2020**, 46, 18322-18330.

Chapter 3

Study on the effect of the presence of capping agents on nanocatalysts on the reduction of Chemical Oxygen Demand (COD) of water bodies



Abstract

Chemical Oxygen Demand (COD) is a critical parameter government agencies define to determine water quality. Various organic surfactant molecules are used as capping agents while producing nanomaterials to use as catalysts. To evaluate the impact of capping agent on nanocatalysts on water purification, nanoparticles with capping agent (PEG-SnS2, OLA/OA-AgBiS2) and without capping agent (sf-AgBiS2, sf-SnS2) were synthesised. The as-produced nanoparticles were examined using X-ray diffraction, scanning electron microscopy, transmission electron microscopy, absorption spectroscopy, and infrared spectroscopy to investigate their structural and optical features. The photodegradation of Rhodamine B (RhB) dye solution utilizing the nanoparticles was studied to assess the efficiency of the materials. COD of dye-contaminated water was measured before and after adding nanocatalysts. Interestingly, the materials without capping agents (sf-SnS2 and sf-AgBiS2) demonstrated higher degradation of Rhodamine B dye solution and exhibited the lowest COD value. This higher activity can be attributed to the availability of free active sites on capping agent-free materials. We have therefore underlined the significance of the hexamethyldisilazane (HMDS) - assisted approach demonstrating increased activity.

3.1. Introduction

Water pollution is one of the major problems we face nowadays. The primary cause of water pollution is the usage of stable, structured, non-degradable toxic dyes by industries like textiles, pharmaceuticals, cosmetics, plastic, etc. [1-4]. Discharging these dyes to the water bodies by the industries depletes the water quality. Rhodamine B is one of the toxic dyes released by these industries [4]. Therefore, it is essential to treat them before discharging into water bodies. Recently many researchers have focused on the photocatalytic degradation of dyes in polluted water using semiconductor nanoparticles such as TiO₂, ZnO, ZrO₂, ZnO, ZnO, CuS, CdS, CuS/CdS, and Bi₂S₃ under sunlight [3-10]. Metal sulphides have gained attention due to their excellent photocatalytic behaviour.

Various parameters are defined by Government agencies all over the world to evaluate the quality of water. Some critical parameters are; Chemical Oxygen Demand (COD), Biological Oxygen Demand (BOD), Total Organic Content (TOC), turbidity and pH of water. The COD is one of the reliable analyses, measuring oxygen required to oxidise the contaminants in water. When the water is contaminated, less light will penetrate the water body, inhibiting photosynthesis and decreasing the dissolved oxygen level. When the COD value is more, it indicates that the level of oxygen dissolved in the water for the oxidation of contaminants is less, which directly shows that the water is polluted [1, 3, 11, 12].

Various methods are available for synthesising semiconductor nanoparticles wherein complex preparation steps, elevated temperature and using different organic surfactant molecules as capping agents are involved [13-38]. However, some of these capping agents are toxic organic molecules [8, 10, 39, 40]. To eliminate these disadvantages, as discussed in the previous chapter, we have developed our hexamethyldisilazane (HMDS)- assisted one-pot synthesis method, where the process yields nanoparticles that are free from capping agents [5, 7-10, 41, 42]. Also, we have been studying the effect of organic surfactant molecules as capping agents on the surface of nanoparticles on their various properties. This chapter aims to learn how the capping agent affects the catalysts in the water purification process. Since COD is one of the critical parameters of water quality, we have monitored it to understand the effect of organic surfactant molecules as capping agents on the nanocatalysts.

For the present chapter, we have prepared surfactant-free SnS₂ (**sf-SnS₂**), polyethylene glycol coated SnS₂ (**PEG-SnS₂**), surfactant-free AgBiS₂ (**sf-AgBiS₂**), and oleylamine-oleic acid coated AgBiS₂ (**OLA/OA-AgBiS₂**) and tested for photocatalytic degradation of RhB dye

solution. The materials are characterised using analytical and spectroscopic methods. To monitor water quality after photocatalytic degradation using these materials, we measured the COD value before and after the degradation of the Rhodamine B dye solution. Herein, we highlight the role of a capping agent in decreasing catalyst efficiency in the water purification process and the advantage of using the HMDS method for synthesising surfactant-free nanoparticles as photocatalysts.

3.2. Experimental

3.2.1. Materials required

Tin(IV) chloride (SnCl_{4.5}H₂O), Silver chloride (AgCl), Bismuth chloride (BiCl₃), thiourea, Hexamethyldisilazane (HMDS), Oleylamine, Oleic acid and Polyethylene glycol-400 (PEG-400), Ag₂SO₄, HgSO₄, K₂Cr₂O₇, Ferrous ammonium sulphate, Conc. H₂SO₄, ferroin indicator, and sulphamic acid were purchased from Sigma Aldrich. Rhodamine B (RhB) from Merck. The characterisation of product synthesised was done as discussed in Chapter 2.

3.2.2. Preparation of sf-SnS₂ by HMDS-assisted method

Hexamethyldisilazane (HMDS)-assisted method, as illustrated in Scheme 3.1, was used to synthesise surfactant-free SnS_2 nanoparticles by employing a one-pot method and conventional Schlenk line methods in an inert environment. In an RB flask, surplus hexamethyldisilazane (5 ml) was added to the precursors of tin $(SnCl_4 \cdot 5H_2O = 0.200 \text{ g}, 0.57 \text{ mmol})$ and sulphur (thiourea = 0.086 g, 1.14 mmol) taken in 1:2 ratio. The mixture was heated to about 140 °C for 3 h in nitrogen atmosphere. High vacuum was used to eliminate extra HMDS and other gaseous side products once the reaction was completed. Multiple washes using distilled water and methanol were performed. The collected product (**sf-SnS**₂) was dried under vacuum at 120 °C for 3 h.

3.2.3. Preparation of PEG-SnS₂

To prepare **PEG-SnS₂**, 10 ml, PEG-400 was mixed with the reaction mixture of tin chloride, thiourea, and HMDS with the same reaction conditions as discussed above (Scheme 3.2). The product (**PEG-SnS₂**) was collected and dried under vacuum oven at 120 °C for 3 h.

3.2.4. Preparation of sf- AgBiS₂ by HMDS-assisted method

To prepare **sf-AgBiS**₂, AgCl (200 mg, 1.39 mmol), BiCl₃ (440 mg, 1.39 mmol), and thiourea (212 mg, 2.79 mmol) were taken in a double neck in 1:1:2 ratio along with excess HMDS

(Scheme 3.3). The mixture was heated to 160 °C for 6 h under nitrogen flow. Once the reaction was completed, high vaccum was applied to eliminate excess HMDS. The residue obtained was repeatedly washed with deionised water and acetone. The product was collected and dried under vacuum at 120 °C for 3 h.

3.2.5. Preparation of OLA/OA- AgBiS₂

To prepare **OLA/OA-AgBiS₂**, AgCl (200 mg, 1.39 mmol), BiCl₃ (440 mg, 1.39 mmol), and thiourea (212 mg, 2.79 mmol) were taken in a double neck in 1:1:2 ratio along with oleylamine (1 ml), oleic acid (5 ml). The mixture was heated to 120 °C for 6 h under nitrogen flow (Scheme 3.4). The gaseous side products were removed by applying high vaccum. The residue was repeatedly washed with hexane and methanol. The product was collected and dried under vacuum at 120 °C for 3 h [43].

3.2.6. Photocatalytic degradation studies

Rhodamine B (RhB) was chosen for the photodegradation studies. Stock solution was prepared by adding 10 mg per litre of dye in deionized water. 60 mL of stock solution was taken in a beaker. To the dye solution, 30 mg of photocatalyst powder (sf-SnS₂, PEG-SnS₂, sf-AgBiS₂, and OLA/OA-AgBiS₂), was added with stirring. The solution was kept for dye degradation in sunlight for 2 h. The sample was centrifuged for 5 min at 2500 rpm. To identify the deterioration of dye solution, UV-Vis absorption spectra were recorded before and after the dye degradation. The drop in intensity of absorption peak represented the degradation.

3.2.7. Chemical Oxygen Demand measurement (COD)

Water quality was analysed (monitored) by measuring the chemical oxygen demand. The COD of the dye solution before and after photocatalytic degradation was measured using the Indian standard method of titration analysis. The procedure is as follows: 0.4 g HgSO₄, which eliminates the chloride interference, was added to the R.B. flask. Before photodegradation, 20 ml of sample dye solution was pipetted into it, followed by 20 ml distilled water and 10 ml 0.1 N K₂Cr₂O₇—sulphamic acid solution. Sulphamic acid was added to eliminate nitrite interference. Then 30 ml sulphuric acid—silver sulphate reagent was added (prepared by dissolving 0.6325 g of Ag₂SO₄ in 62.5 mL conc. H₂SO₄) to accelerate the oxidation of straight-chain aliphatic and aromatic compounds. The mixture was mixed well and was allowed to cool. The above mixture was refluxed at 150 °C for 2 h. The same procedure was repeated for the dye solution after 2 h of photodegradation using sf-SnS₂, PEG-SnS₂, sf-AgBiS₂ and OLA/OA-

AgBiS₂ as catalysts. The above procedure was repeated for the blank with 20 ml DI water instead of a 20 ml sample.

After 2 h, the heating was stopped, and it was kept for cooling. It was then titrated with std. Ferrous Ammonium Sulphate (FAS) solution with ferroin as an indicator with the colour change from green to wine red as the endpoint [44]. The COD was calculated as shown in the equation below.

COD
$$(mg/L) = \frac{[V_1 - V_2] \times N \times 8 \times 1000}{V_0}$$

where,

 V_1 = Volume of FAS for blank

 V_2 = Volume of FAS for sample

N = Normality of FAS solution

 V_0 = Volume of sample taken

8 = milli equivalent weight of Oxygen

3.3. Results and discussion

3.3.1. Preparation and Characterisation

The objective of this chapter is to study the effect of the presence of the organic surfactant or polymer molecules on the surface of the nanomaterials which are used as catalysts in water purification. For this study, it is required to compare the activity of nanomaterials with and without surfactants or polymers. Therefore, we have prepared surfactant-free SnS₂ (sf-SnS₂) and AgBiS₂ (sf-AgBiS₂) and compared their activity with polyethylene glycol coated SnS₂ (PEG-SnS₂) and oleylamine-oleic acid coated AgBiS₂ (OLA/OA-AgBiS₂). The materials sf-SnS₂ and sf-AgBiS₂ were prepared using HMDS-assisted synthetic method as shown in Scheme 3.1 and 3.3, respectively, while PEG-SnS₂ and OLA/OA-AgBiS₂ were prepared using procedures similar to the reported methods in the literature (Scheme 3.2 and 3.4) [8, 43].

$$SnCl_2 + TU$$

$$1 : 2$$

$$Si_{N} Si_{N}$$

$$1 : 2$$

$$120 °C, 3 h$$

$$sf-SnS_2$$

Scheme 3.1. Preparation of sf-SnS₂ using HMDS-assisted synthetic method.

Scheme 3.2. Preparation of PEG-SnS₂ using HMDS-assisted synthetic method.

$$AgCl + BiCl3 + TU$$

$$1 : 1 : 2$$

$$Si H Si$$

$$N$$

$$Si H Si$$

$$1 : 1 : 2$$

$$160 °C, 6 h$$

Scheme 3.3. Preparation of sf-AgBiS₂ using HMDS-assisted synthetic method.

Scheme 3.4. Preparation of OLA/OA-AgBiS₂ using literature method.

Employing the HMDS-assisted method yielded pure **sf-SnS**₂ and **sf-AgBiS**₂ materials free from organic capping agents. The phase purity and crystal lattice information about these materials were obtained from their PXRD patterns. The PXRD peaks indicating the planes (100), (011), (012), (110), (111), (200), (201) in Figure 3.1a was in correlation with hexagonal SnS₂ (JCPDS data card no. 23-0677) [8]. The PXRD peaks in the figure. 3.1b depicting the planes (111), (200), (220), (311), and (222) were harmonized with the cubic phase of AgBiS₂ (JCPDS- 89-2046) [17]. No impurity phases within the resolution limits of the diffractometer were observed, indicating the purity of the samples synthesised.

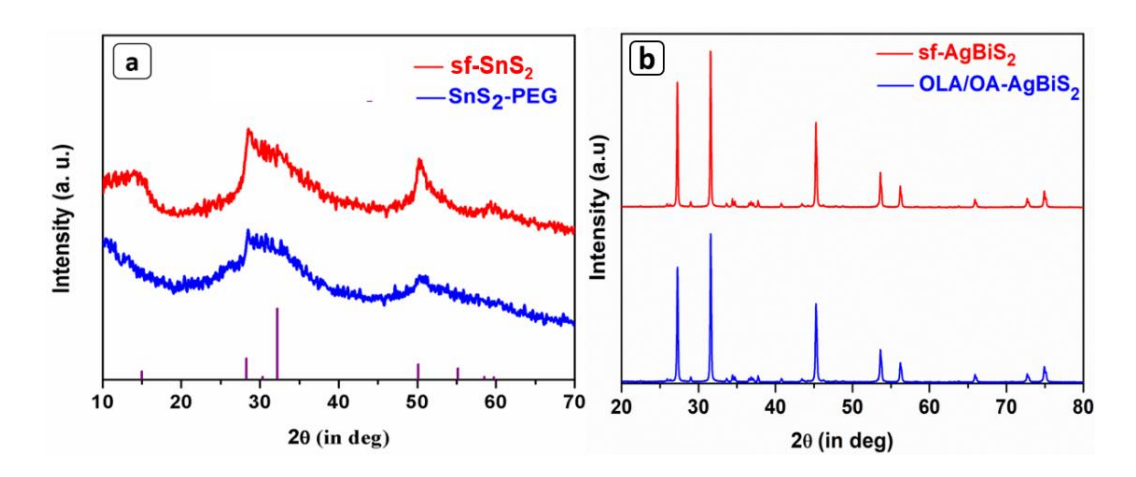


Figure 3.1. PXRD pattern of as synthesised a) sf-SnS₂ and PEG-SnS₂, b) sf-AgBiS₂ and OLA/OA-AgBiS₂ nanoparticles.

FTIR spectra of all these materials were analysed to identify the presence of organic surfactant or polymer as capping. The capping of SnS₂ by polyethylene glycol (Figure 3.2a) and AgBiS₂ by oleylamine and oleic acid (Figure 3.2b) can be witnessed in the FT-IR spectra. The absence of HMDS peaks in Figure 3.2a &Figure 3.2b indicates the capping agent-free SnS₂ and AgBiS₂ nanoparticle formation, respectively. In FTIR spectra of oleic acid/oleylamine capped AgBiS₂ nanoparticles (Figure 3.2b), small amounts of oleic acid, which is used as a solvent and capping agent during synthesis, can also be seen.

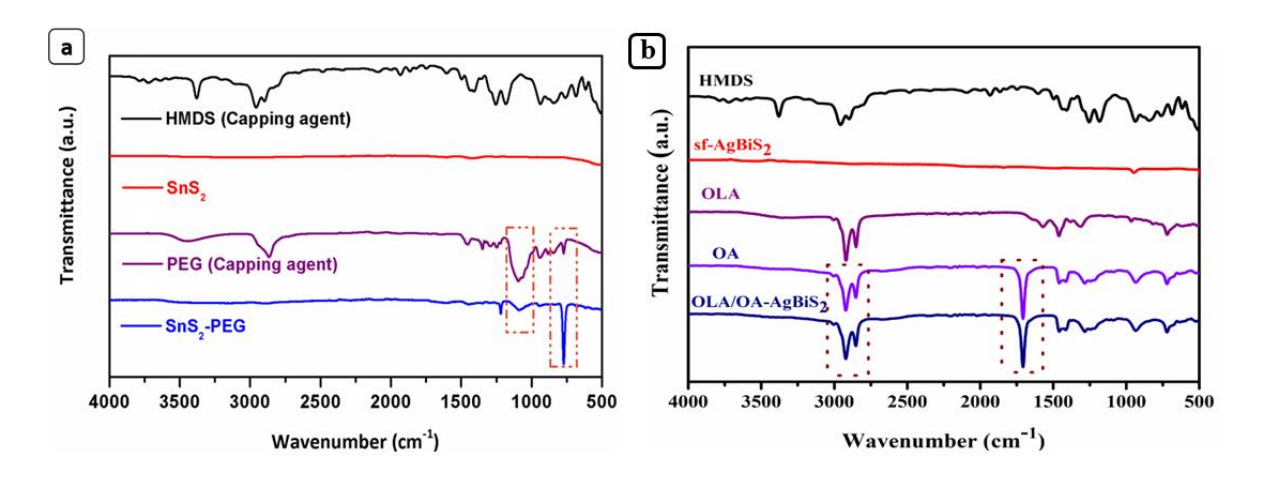


Figure 3.2. FT-IR Spectra of a) sf-SnS₂ and PEG-SnS₂ b) sf-AgBiS₂ and OLA/OA- AgBiS₂.

The morphology of the samples prepared was analysed using FESEM and TEM, which revealed the formation of nanorings of **sf-SnS**₂ and nanoflowers of **PEG-SnS**₂ as shown in figure 3.3(a-c) and 3.3(e-g) respectively. A nanorods morphology was exhibited by **sf-AgBiS**₂ and a truncated polyhedral morphology by **PEG-AgBiS**₂ in Figure 3.3(i-k) and Figure 3.3(m-o), respectively. The SAED patterns confirmed the crystalline nature of **sf-SnS**₂, **sf-AgBiS**₂,

and **PEG-AgBiS**₂ [figure 3.3(d, i, and p, respectively)]. The amorphous nature of **PEG-SnS**₂ was also shown by the SAED pattern (figure 3.3h). The elemental mapping showed the distribution of elements (figure 3.4).

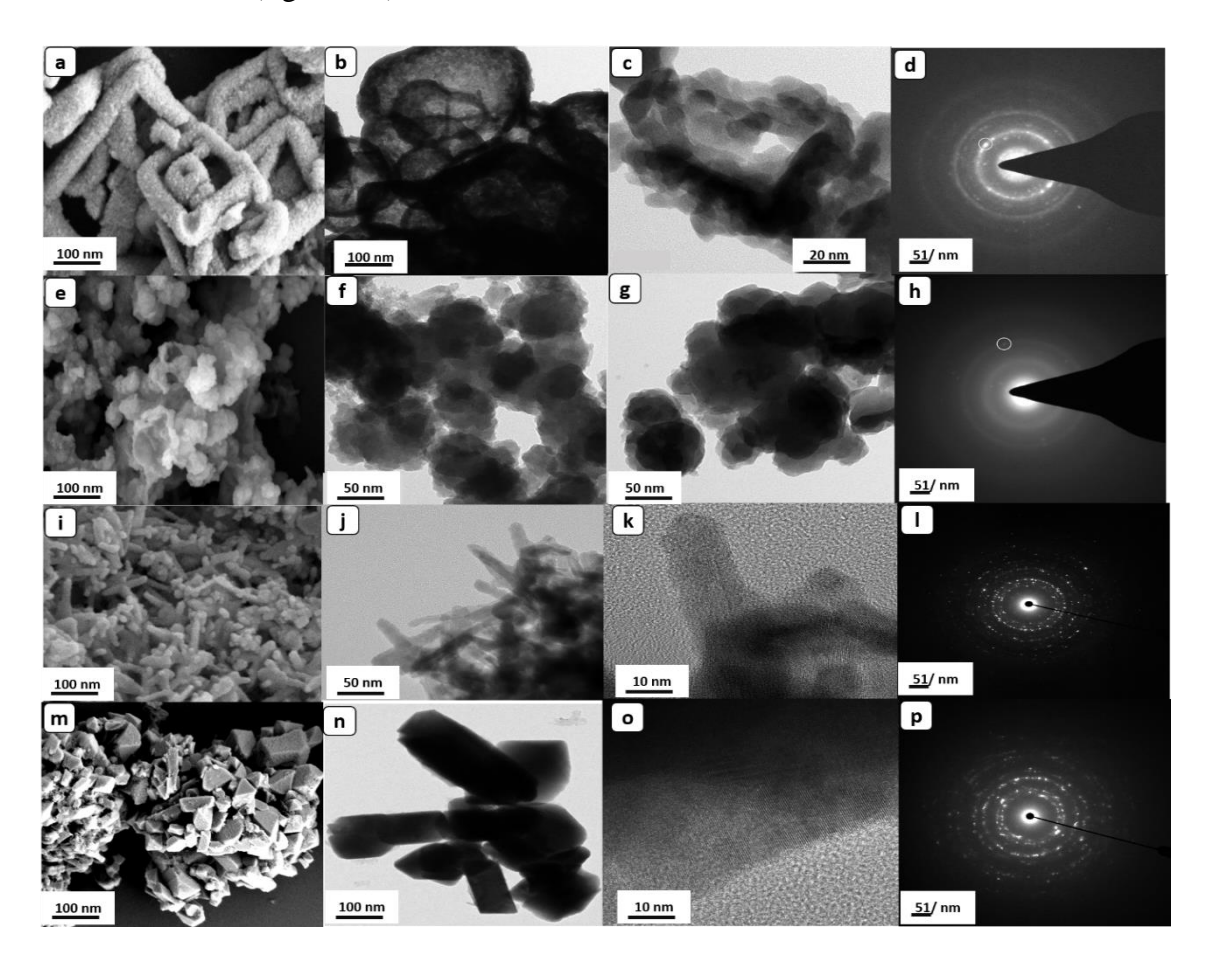


Figure 3.3. a) FESEM image, b) TEM (low resolution), c) TEM (high resolution), d) SAED pattern of **sf-SnS**₂. e) FESEM image, f) TEM (low resolution), g) TEM (high resolution), h) SAED pattern of **PEG-SnS**₂.i) FESEM image, j) TEM (low resolution), k) TEM (high resolution), l) SAED pattern of **sf-AgBiS**₂. m) FESEM image, n) TEM (low resolution), o) TEM (high resolution), p) SAED pattern of **OLA/OA-AgBiS**₂.

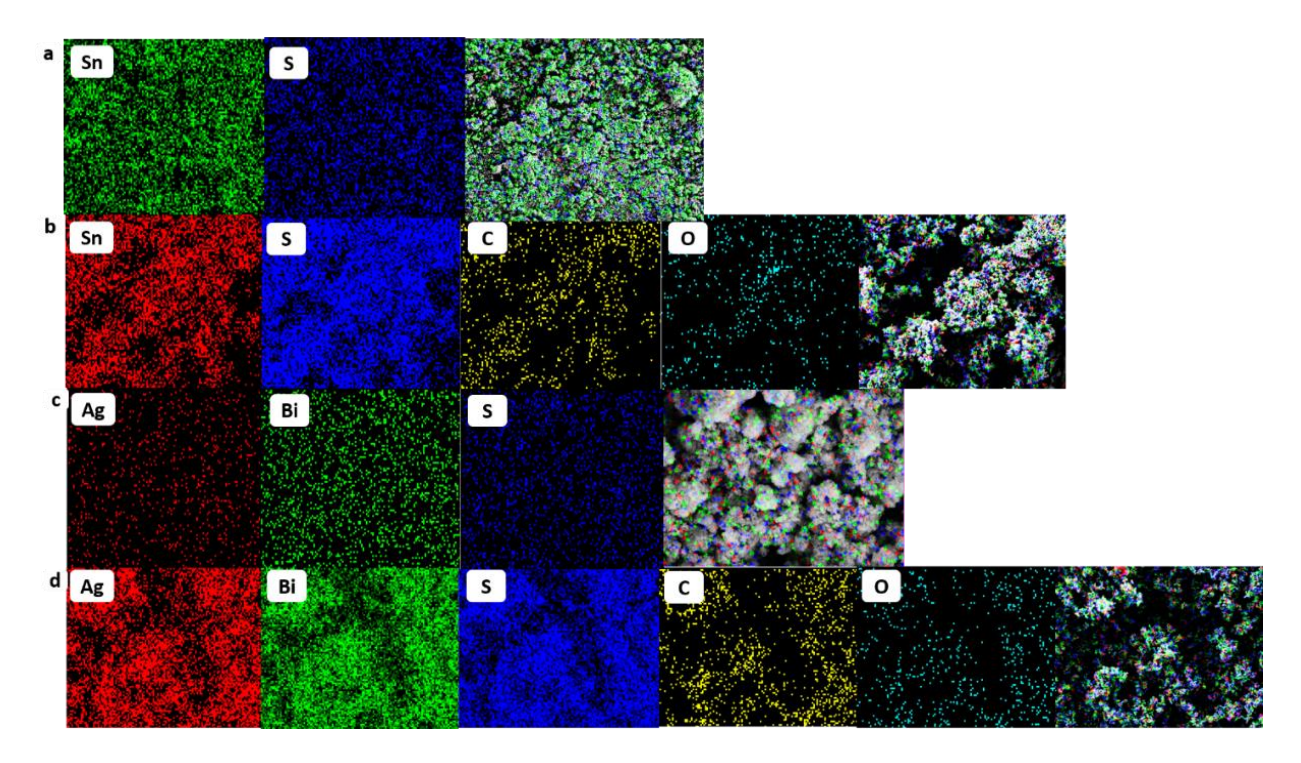


Figure 3.4. EDS elemental mapping of (a) sf-SnS₂ (b) PEG-SnS₂ (c) sf-AgBiS₂ (d) OLA/OA- AgBiS₂

The capability of materials to absorb visible light makes them good photocatalysts. The bandgap of these materials was determined from their absorption spectra using the Tauc method, as shown in Figure 3.5. The bandgaps of **sf-SnS2**, **PEG-SnS2**, **sf-AgBiS2**, and **OLA/OA-AgBiS2** are 2.45 eV, 2.55 eV, 0.76 eV and 0.92 eV, respectively. The decrease in bandgap helps the materials to absorb light in the UV as well as Visible regions. The trend in the bandgap shows that the capping agent-free nanoparticles prepared using the HMDS-assisted method showed a slight decrease in bandgap than the ones with capping agents.

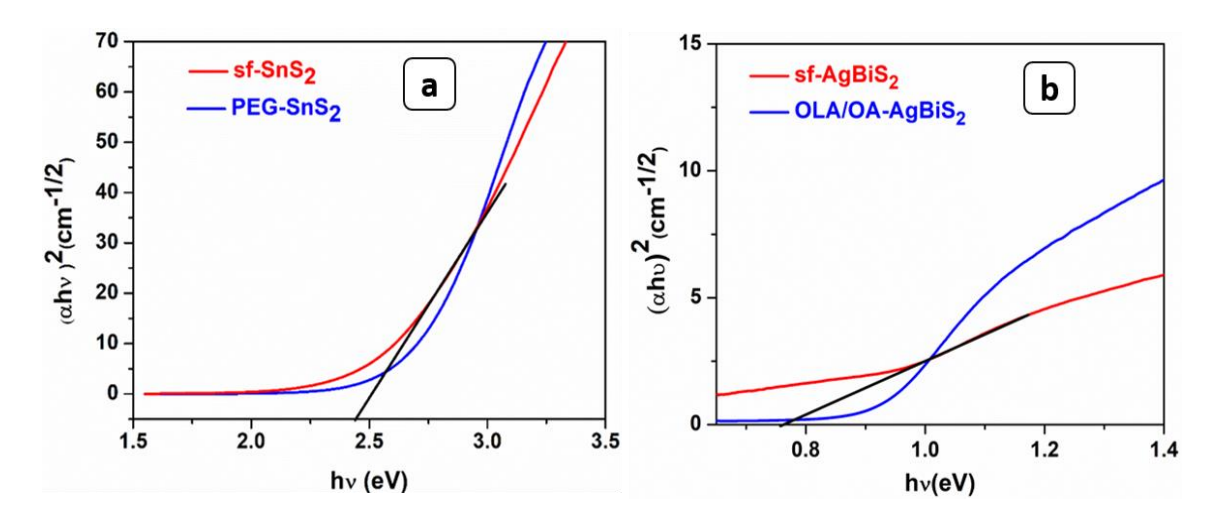


Figure 3.5. Calculated band gap of a) sf-SnS₂ and PEG-SnS₂b) sf-AgBiS₂ and OLA/OA-AgBiS₂.

3.3.2. Photocatalytic degradation studies

Free availability of the surface of the materials is important where all catalytic processes occur. The degrading efficiencies of the synthesised materials were studied by measuring the decrease in absorption of Rhodamine B (RhB) dye solution using absorption spectroscopy after sunlight irradiation for 2 h with stirring. sf-SnS2 and sf-AgBiS2 showed effective degradation of RhB dye than PEG-AgBiS₂ and OLA/OA-AgBiS₂ as depicted in figure 3.6. This observation showed that the degradation of the dye solution was hindered by the presence of capping agents on PEG-AgBiS₂ and OLA/OA-AgBiS₂. As the capping agent-free nanoparticles render more active sites, more and more dye molecules were adsorbed on the surface of nanoparticles, eventually leading to increased degradation of dye molecules. As described in the previous chapters, the dye molecules get adsorbed on the catalyst surface. During excitation, electrons in the conduction band interact with the dissolved oxygen, producing hydroxyl radicals which degrade the dye molecule. Similarly, the holes in the valence band react with the adsorbed water molecule and produce hydroxyl radical, degrading the dye molecules again [10]. When capping agents were present, these interactions were hindered, leading to less degradation of dye molecules [8, 10, 39, 40]. This study showed the importance of synthesising capping agentfree nanoparticles, which was achieved by the HMDS-assisted method.

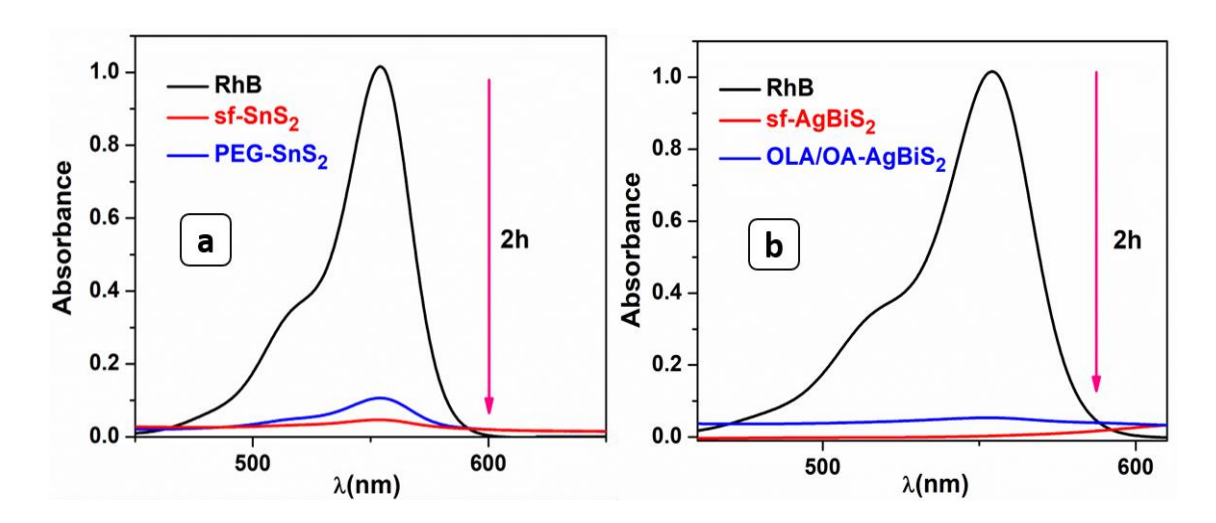


Figure 3.6. Photodegradation of Rhodamine B dye solution using a) sf-SnS₂, PEG-SnS₂ and b) sf-AgBiS₂, OLA/OA-AgBiS₂ under sunlight for 2h.

3.3.3. Chemical Oxygen Demand

Monitoring the purity of water is an essential step before using it for various purposes. Especially when water from industrial effluent and sewage in cities is treated, it is necessary to test their quality continuously. Government agencies all over the world stipulate various parameters to determine the quality of water. Some critical parameters are; Turbidity and pH of water, Chemical Oxygen Demand (COD), Biological Oxygen Demand (BOD), and Total Organic Content (TOC). The COD is a measure of oxygen required to oxidize water contaminants, indirectly indicating the amount of oxidizable pollutants in water. Therefore, it was decided to assess water quality by measuring COD.

The quality of water after dye degradation was analysed by comparing the chemical oxygen demand value before and after photodegradation of RhB dye solution using sf-SnS2, PEG-SnS2, sf-AgBiS2, and OLA/OA-AgBiS2 under sunlight with stirring for 2 h. The COD value was determined using titrimetric analysis. In this method, the pollutant was oxidized by the known amount of potassium dichromate, which is a strong oxidizing agent in a sulphuric acid medium. The excess dichromate was titrated against ferrous ammonium solution. The amount of dichromate consumed gave the amount of oxygen required to oxidize the organic matter or the pollutant dissolved in water. The higher COD value indicates the increased need for oxygen for the degradation of pollutants dissolved, i.e., more pollutant was present. The results from all titrations (averaged from 3 measurements in Annexure I) are tabulated and shown in Table 3.1.

Table 3.1. COD value of Rhodamine B solution before and after photocatalytic degradation of dye.

S.No	Sample and condition	COD value (mg/L)		
1	Pure Rhodamine B dye solution	339.70		
2	Irradiation with light, without catalysts	266.66		
3	With light + PEG-SnS ₂	188.31		
4	With light + OLA/OA-AgBiS ₂	140.74		
5	With light + sf-SnS ₂	5.00		
6	With light + sf-AgBiS ₂	3.703		

As it is clear from Table 3.1, there was a significant decrease in COD value when capping agent-free nanoparticles such as **sf-AgBiS2** and **sf-SnS2** were used for RhB degradation. The effective degradation of dye solution using capping agent-free nanoparticles can be attributed to more active sites available for the adsorption of dye molecules on the catalyst surface (Figure 3.7).

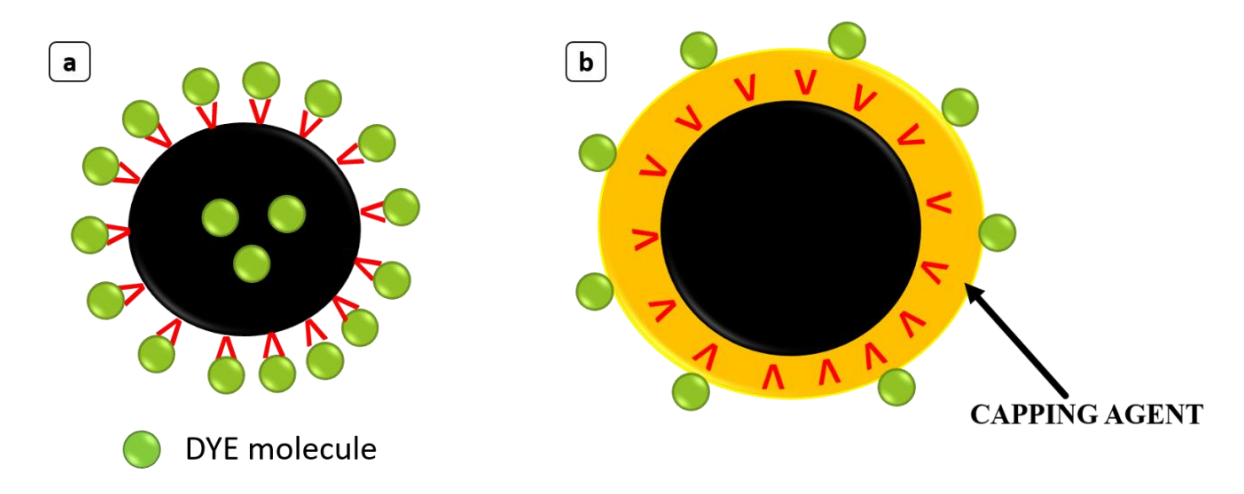


Figure 3.7. Illustration of more active sites for a) capping agent free nanoparticles and less for b) nanoparticles with capping agent for the adsorption of dye molecules.

Regardless of the nature of the capping agent, it was clear from the COD values that the presence of the capping agent hindered the absorption of sunlight for dye degradation and thereby leading to incomplete degradation of the dye solution. Here, the transmittance of electrons and holes produced by the absorption of sunlight by nanoparticles was hindered by

the capping agents surrounding the catalyst surface [10, 39, 40]. This observation demonstrated the necessity of capping agent-free nanoparticles, which can be produced by the HMDS—assisted method [5-10, 41, 42]. The presence of capping agents, which are toxic organic molecules, depletes the water quality even after degradation.

3.4. Conclusion

In this chapter, we have successfully synthesised nanoparticles with capping agents (PEG-SnS2, OLA/OA-AgBiS2) and without capping agents (sf-SnS2, sf-AgBiS2) using two different synthetic methods. The hexagonal structure of PEG-SnS2, sf-SnS2 and cubic form of OLA/OA-AgBiS2, sf-AgBiS2 was confirmed by X-ray diffraction. It was observed that surfactant-free nanoparticles such as sf-SnS2 and sf-AgBiS2 exhibited good photocatalytic behaviour against Rhodamine B dye solution under sunlight irradiation. The COD of the dye solution before and after degradation was analysed to check the efficiency of the prepared nanoparticles. The results displayed that the presence of a capping agent qualitatively decreased the efficiency of the photocatalyst. The increased activity of capping agent-free nanoparticles can be attributed to the availability of more active sites on the bare surface resulting in more significant interaction with the substrate. The present chapter thus highlights the importance of the Hexamethyldisilane (HMDS)-assisted method to synthesis capping agent-free nanoparticles as promising photocatalysts for wastewater treatment than nanoparticles with capping agents.

3.5. References

- 1. Singh, M., Kumar, P. and Bhagat, D.M. Removal of rhodamine B from aqueous solution by ZnO nanoparticles. *Int J Innov Res SciEng Technol.* **2017**, *6*,4050-4056.
- 2. Ferreira-Neto, E.P., Ullah, S., da Silva, T.C., Domeneguetti, R.R., Perissinotto, A.P., de Vicente, F.S., Rodrigues-Filho, U.P. and Ribeiro, S.J. Bacterial nanocellulose/MoS₂ hybrid aerogels as bifunctional adsorbent/photocatalyst membranes for in-flow water decontamination. *ACS Appl. Mater. Interfaces.* **2020**, 12, 41627-41643.
- 3. Sari, M.I., Agustina, T.E., Melwita, E. and Aprianti, T. November. Color and COD degradation in photocatalytic process of procion red by using TiO₂ catalyst under solar irradiation. *AIP Conf. Proc.* **2017**, 1903, 040017. AIP Publishing LLC.
- 4. Sanad, M.F., Shalan, A.E., Bazid, S.M. and Abdelbasir, S.M. Pollutant degradation of different organic dyes using the photocatalytic activity of ZnO@ ZnS nanocomposite materials. *J. Environ. Chem. Eng.* **2018**, 6, 3981-3990.
- 5. Srinivas, B., Kumar, B.G. and Muralidharan, K. Stabilizer free copper sulphide nanostructures for rapid photocatalytic decomposition of Rhodamine B. *J MolCatalA Chem.* **2015**, 410,8-18.
- 6. Kumar, B.G., Srinivas, B. and Muralidharan, K. Photo-responsive Bi₂S₃ nanoflakes: Synthesis and device fabrication at ambient conditions. *Mater. Res. Bull.* **2017**, 89, 108-115.
- 7. Billakanti, S. and Krishnamurthi, M. Facile preparation of surfactant or support material free CdS nanoparticles with enhanced photocatalytic activity. *J. Environ. Chem. Eng.* **2018**, 6, 1250-1256.
- 8. Srinivas, B., Pandit, M.A. and Muralidharan, K. Importance of clean surfaces on the catalyst: SnS₂ nanorings for environmental remediation. *ACS Omega.* **2019**, 4, 14970-14980.
- 9. Pandit, M.A., Billakanti, S. and Muralidharan, K. A simplistic approach for the synthesis of CuS-CdS heterostructure: A novel photocatalyst for oxidative dye degradation. *J. Environ. Chem. Eng.* **2020**, 8,103542.
- 10. Joseph, A., Billakanti, S., Pandit, M.A., Khatun, S., Rengan, A.K. and Muralidharan, K. Impact of bandgap tuning on ZnS for degradation of environmental pollutants and disinfection. *Environ. Sci. Pollut. Res.* **2022**, 29, 56863-56875.
- 11. Tayade, R.J., Natarajan, T.S. and Bajaj, H.C. Photocatalytic degradation of methylene blue dye using ultraviolet light emitting diodes. *Ind. Eng. Chem. Res.* **2009**, 48, 10262-10267.

- 12. Abdel Messih, M.F., Shalan, A.E., Sanad, M.F. and Ahmed, M.A. Facile approach to prepare ZnO@ SiO₂ nanomaterials for photocatalytic degradation of some organic pollutant models. *J Mater Sci Mater Electron.* **2019**, 30, 14291-14299.
- 13. Lei, P., An, R., Zheng, X., Zhang, P., Du, K., Zhang, M., Dong, L., Gao, X., Feng, J. and Zhang, H. Ultrafast synthesis of ultrasmallpolyethylenimine-protected AgBiS₂nanodots by "rookie method" for in vivo dual-modal CT/PA imaging and simultaneous photothermal therapy. *Nanoscale*. **2018**, 10,16765-16774.
- 14. Chen, B., Zhang, C., Wang, W., Chu, Z., Zha, Z., He, X., Zhou, W., Liu, T., Wang, H. and Qian, H. Ultrastable AgBiS₂ hollow nanospheres with cancer cell-specific cytotoxicity for multimodal tumor therapy. *ACS Nano*. **2020**, 14,14919-14928.
- 15. Cheng, J., Wang, W., Xu, X., Lin, Z., Xie, C., Zhang, Y., Zhang, T., Li, L., Lu, Y. and Li, Q. AgBiS₂ nanoparticles with synergistic photodynamic and bioimaging properties for enhanced malignant tumor phototherapy. *Mater. Sci. Eng. C.***2020**, 107, 110324.
- 16. Khan, M.D., Aamir, M., Sohail, M., Bhoyate, S., Hyatt, M., Gupta, R.K., Sher, M. and Revaprasadu, N. Electrochemical investigation of uncapped AgBiS₂ (schapbachite) synthesised using in situ melts of xanthate precursors. *Dalton Trans.* **2019**, 48,3714-3722.
- 17. Chen, C., Qiu, X., Ji, S., Jia, C. and Ye, C. The synthesis of monodispersed AgBiS₂ quantum dots with a giant dielectric constant. *CrystEngComm.* **2013**, 15, 7644-7648.
- 18. Wang, J., Yang, X., Hu, W., Li, B., Yan, J. and Hu, J. Synthesis of AgBiS₂ microspheres by a templating method and their catalytic polymerization of alkylsilanes. *Chemical Communications*. **2007**, 4931-4933.
- 19. Nakazawa, T., Kim, D., Oshima, Y., Sato, H., Park, J. and Kim, H. Synthesis and Application of AgBiS₂ and Ag₂S Nanoinks for the Production of IR Photodetectors. *ACS Omega.* **2021**, 6, 20710-20718.
- 20. Wen, S., Wu, T., Long, H., Ke, L., Deng, S., Huang, L., Zhang, J. and Tan, S. Mechanism insight into rapid photodriven sterilization based on silver bismuth sulfide quantum dots. *ACS Appl. Mater. Interfaces.* **2021**, 13, 21979-21993.
- 21. Paul, S., Dalal, B., Jana, R., Shit, A., Datta, A. and De, S.K. Enhanced Photophysical Properties of Bi₂S₃/AgBiS₂Nanoheterostructures Synthesised via Ag (I) Cation Exchange-Mediated Transformation of Binary Bi₂S₃. *J. Phys. Chem. C.* **2020**, 124, 12824-12833.
- 22. Ganguly, P., Mathew, S., Clarizia, L., Akande, A., Hinder, S., Breen, A. and Pillai, S.C. Theoretical and experimental investigation of visible light responsive AgBiS₂-TiO₂ heterojunctions for enhanced photocatalytic applications. *Appl. Catal.*, *B.* **2019**, 253, 401-418.

- 23. Sugarthi, S., Bakiyaraj, G., Abinaya, R., Navaneethan, M., Archana, J. and Shimomura, M. Effect of different growth temperature on the formation of ternary metal chalcogenides AgBiS₂. *Mater Sci Semicond Process.* **2020**, 107, 104781.
- 24. Wang, J., Li, L., Yu, H., Guan, F. and Wang, D. Binary–Ternary Bi₂S₃–AgBiS₂ Rod-to-Rod Transformation via Anisotropic Partial Cation Exchange Reaction. *Inorg. Chem.* **2019**, 58, 12998-13006.
- 25. Chen, D., Shen, G., Tang, K., Jiang, X., Huang, L., Jin, Y. and Qian, Y. Microwave synthesis of AgBiS₂ dendrites in aqueous solution. *Inorg. Chem. Commun.* **2003**, 6, 710-712.
- 26. Calva-Yáñez, J.C., Pérez-Valdovinos, O., Reynoso-Soto, E.A., Alvarado-Tenorio, G., Jaramillo-Quintero, O.A. and Rincón, M. Interfacial evolution of AgBiS₂ absorber layer obtained by SILAR method in hybrid solar cells. J. Phys. D: Appl. Phys. **2019**, 52, 125502.
- 27. Xiao-Xue, S.H.I., Xiu-Qi, L.I., Xiao-Ping, W.E.I. and Jian-Ping, L.I.Molecularly imprinted photoelectrochemical sensor based on AgBiS₂/Bi₂S₃ for determination of propoxur. *Chinese J. Anal. Chem.* **2020**, 48, 396-404.
- 28. Zhang, Y. C.; Du, Z. N.; Li, K. W.; Zhang, M.Size-controlled hydrothermal synthesis of SnS₂ nanoparticles with high performance in visible light-driven photocatalytic degradation of aqueous methyl orange. *Sep. Purif. Technol.***2011**, 81, 101–107.
- 29. Wei, H.; Hou, C.; Zhang, Y.; Nan, Z. Scalable low temperature in air solid phase synthesis of porous flower-like hierarchical nanostructure SnS₂ with superior performance in the adsorption and photocatalytic reduction of aqueous Cr(VI). Sep.Purif. Technol.**2017**, 189, 153–161.
- 30. Wang, S.; Peng, T.; Zhang, Y.NH₄Cl-assisted in air, low temperature synthesis of SnS₂ nanoflakes with high visible-light activated photocatalytic activity. *Mater. Lett.***2019**, 234, 361–363.
- 31. Zhang, Y. C.; Yao, L.; Zhang, G.; Dionysiou, D. D.; Li, J.; Du, X.One-step hydrothermal synthesis of high-performance visible-light driven SnS₂/SnO₂ nanoheterojunction photocatalyst for the reduction of aqueous Cr(VI). *Appl. Catal.*, *B.***2014**, 144, 730–738.
- 32. Zhang, Y. C.; Li, J.; Xu, H. Y.One-step in situ solvothermal synthesis of SnS₂/TiO₂nanocomposites with high performance in visible light-driven photocatalytic reduction of aqueous Cr(VI). *Appl. Catal.*, *B.* **2012**, 123, 18–26.
- 33. Zhang, Y.; Zhang, F.; Yang, Z.; Xue, H.; Dionysiou, D. D.Development of a new efficient visible-light-driven photocatalyst from SnS₂ and polyvinyl chloride. *J. Catal.***2016**, 344, 692–700.

- 34. Zhang, F.; Zhang, Y.; Zhang, G.; Yang, Z.; Dionysiou, D. D.; Zhu, A.Exceptional synergistic enhancement of the photocatalytic activity of SnS₂ by coupling with polyaniline and N-doped reduced graphene oxide. *Appl. Catal.*, *B.***2018**, 236, 53–6.
- 35. Ji, Y.; Zhang, H.; Ma, X.; Xu, J.; Yang, D.Single-crystalline SnS₂ nano-belts fabricated by a novel hydrothermal method. *J. Phys.: Condens. Matter.* **2003**, 15, L661–L665.
- 36. Johny, J.; Sepulveda-Guzman, S.; Krishnan, B.; Avellaneda, D.; Shaji, S.Facile and fast synthesis of SnS₂ nanoparticles by pulsed laser ablation in liquid. *Appl. Surf. Sci.***2018**, 435, 1285–1295.
- 37. Yang, Y.-B.; Dash, J. K.; Littlejohn, A. J.; Xiang, Y.; Wang, Y.; Shi, J.; Zhang, L. H.; Kisslinger, K.; Lu, T.-M.; Wang, G.-C.Large Single Crystal SnS₂ Flakes Synthesised from Co-evaporation of Sn and S. *Cryst. Growth Des.***2016**, 16, 961–973.
- 38. Ludi, B.; Olliges-Stadler, I.; Rossell, M. D.; Niederberger, M. Extension of the benzyl alcohol route to metal sulfides: "non-hydrolytic" thio sol-gel synthesis of ZnS and SnS₂. *Chem. Commun.***2011**, 47, 5280–5282.
- 39. Sudha, M. and Rajarajan, M. Deactivation of photocatalytically active ZnO nanoparticle by surface capping with poly vinyl pyrrolidone. *J. Appl. Chem.* **2013**, 3,45-53.
- 40. Sudha, M., Senthilkumar, S., Hariharan, R., Suganthi, A. and Rajarajan, M. Controlled reduction of the deleterious effects of photocatalytic activity of ZnO nanoparticles by PVA capping. *J SolgelSciTechnol*, **2012**, 61, 14-22.
- 41. Pandit, M.A., Kumar, D.S.H., Ramadoss, M., Chen, Y. and Muralidharan, K. Template free-synthesis of cobalt–iron chalcogenides [Co _{0.8} Fe _{0.2} L ₂, L= S, Se] and their robust bifunctional electrocatalysts for the water splitting reaction and Cr (vi) reduction. *RSC Adv.* **2022**, 12, 7762-7772.
- 42. Pandit, M.A., Sai Hemanth Kumar, D., Billakanti, S., Ramadoss, M. and Muralidharan, K. Chalcopyrite with magnetic and dielectric properties: an introductory catalyst for 4-nitrophenol reduction. *J. Phys. Chem.* C. **2020**, 124, 18010-18019.
- 43. Li, Q., Zheng, X., Shen, X., Ding, S., Feng, H., Wu, G. and Zhang, Y. Optimizing the Synthetic Conditions of "Green" Colloidal AgBiS₂ Nanocrystals Using a Low-Cost Sulfur Source. *Nanomater.* **2022**, 12, 3742.
- 44. Standard, I. Methods of sampling and test (physical and chemical) for water and wastewater. IS 3025, **2006**, (Part 58).

Titration of std. Ferrous ammonium sulphate (FAS) against Rhodamine B dye solution before and after degradation with and without catalysts.

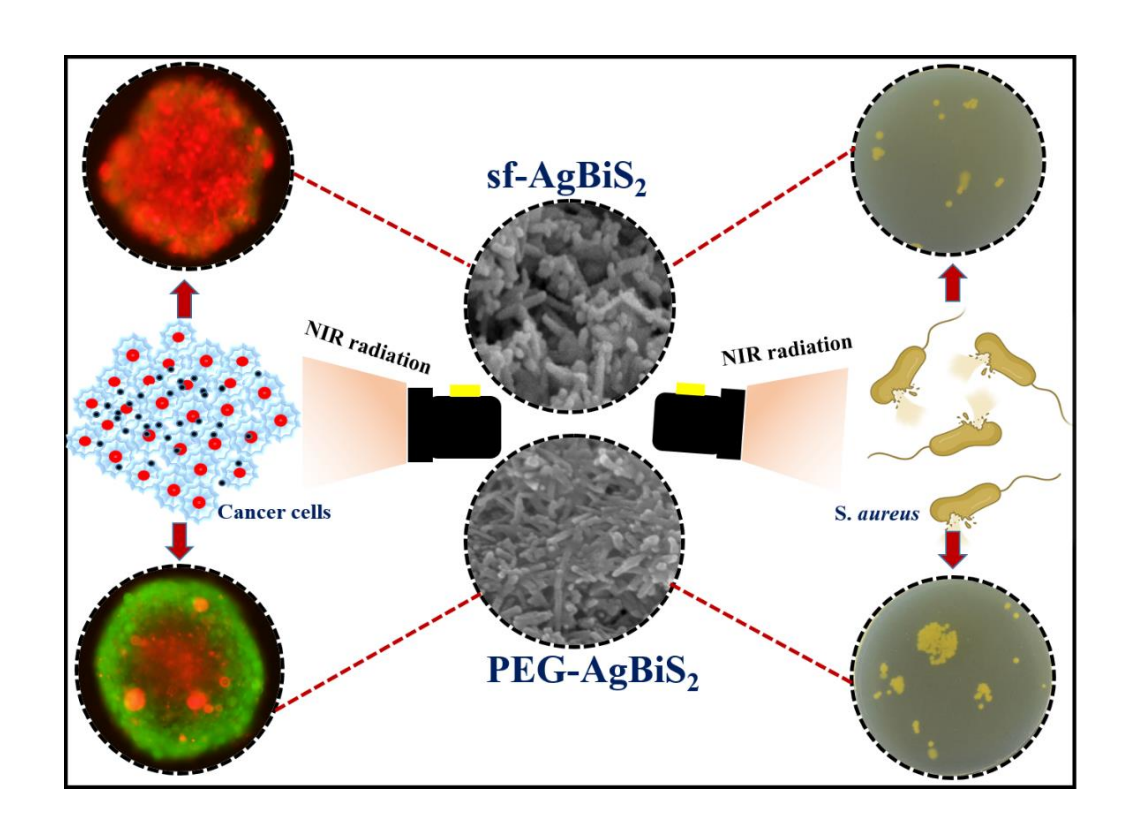
Annexure I

Sample name (Trial no.)	Normality of FAS (N)	Vol. of sample (ml)	TV-1 (ml)	TV-2 (ml)	TV-3 (ml)	Blank (ml)	COD (mg/L)
Rh B (Trial-1)	0.100	20	0.5	0.5	0.5	9.0	340
Rh B (Trial-2)	0.106	20	1.1	1.1	1.1	9.1	339.2
Rh B (Trial – 3)	0.106	20	0.5	0.5	0.5	9.0	340
Rh B + Light (Trial-1)	0.0925	20	1.9	1.9	1.9	9.1	266.4
Rh B + Light (Trial-2)	0.0925	18	2.6	2.6	2.6	9.0	263.11
Rh B+ Light (Trial-3)	0.0994	20	2.2	2.2	2.2	9.0	270.41
Rh B + PEG-SnS ₂ (Trial-1)	0.102	13	4.5	4.5	4.5	7.5	188.308
Rh B + PEG-SnS ₂ (Trial-2)	0.102	18	3.3	3.3	3.3	7.3	181.33
Rh B + PEG-SnS ₂ (Trial-3)	0.102	13	4.3	4.3	4.3	7.3	184.61
Rh B + OLA/OA- AgBiS ₂ (Trial-1)	0.100	16	7.1	7.1	7.1	9.9	140
Rh B + OLA/OA- AgBiS ₂ (Trial-2)	0.100	18	6.7	6.7	6.7	9.9	142.2
Rh B + OLA/OA- AgBiS ₂ (Trial-3)	0.0951	20	6.2	6.2	6.2	9.9	140.739
Rh B + sf-SnS ₂ (Trial-1)	0.0980	15	9.7	9.7	9.7	9.8	5.2
Rh B + sf-SnS ₂ (Trial- 2)	0.0980	16	9.8	9.8	9.8	9.9	4.9
Rh B + sf - SnS_2 (Trial-3)	0.0980	16	9.7	9.7	9.7	9.8	4.9
Rh B + sf-AgBiS ₂ (Trial-1)	0.0925	20	9.0	9.0	9.0	9.1	3.7037
Rh B + sf-AgBiS ₂ (Trial-2)	0.0925	20	8.9	8.9	8.9	9.0	3.7
Rh B + sf-AgBiS ₂ (Trial-3)	0.0925	20	8.9	8.9	8.9	9.0	3.7

^{*}TV-Titre Value, COD-Chemical Oxygen Demand

Chapter 4

Insight into the Effect of Stabilizers on Anticancer and Antibacterial Activity of AgBiS₂ Nanomaterial



Abstract

The near-infrared (NIR) light-absorbing AgBiS₂ nanoparticles can be excited by single-wavelength light, which is the primary characteristic of a photo-responsive platform. Chemical synthesis of nanomaterials inevitably requires long-chain organic surfactants or polymers to stabilize them in the nano regime. These stabilising molecules barricade the interaction of nanomaterials with biological cells. We have produced stabilizer-free (sf-AgBiS₂) and polymer-coated (PEG-AgBiS₂) nanoparticles; and assessed their NIR-mediated anticancer and antibacterial activity to evaluate the effect of stabilizers. sf-AgBiS₂ showed better antibacterial activity against Gram-positive Staphylococcus aureus (S. *aureus*) and displayed excellent cytotoxicity against HeLa cells and live 3-D tumour spheroids compared to PEG-AgBiS₂ both in presence and absence of NIR radiation. The photothermal therapy (PTT) results illustrated the tumour ablation ability of sf-AgBiS₂, which converted light into heat effectively up to 53.3 °C under NIR irradiation. This chapter demonstrates the importance of synthesising stabilizer-free nanoparticles to produce safe and highly active PTT agents.

4.1. Introduction

The organizations for disease control and prevention reported cancer as the major reason for death worldwide, with 22.5% death rate. The standard treatments practiced are surgery, chemotherapy, and radiotherapy [1]. The usage of these methods is limited due to their adverse effects on healthy cells and the immune system. Further, there exist chances of the generation of secondary cancers [2]. There are enormous efforts by scientists to develop efficient cancer treatments, among which the NIR-mediated photothermal therapy (PTT) is more attractive owing to its high specificity to tumour cells, non-invasive nature, and minimal side effects. It also helps prevent metastasis by stimulating immune-mediated abscopal phenomenon [1-8]. NIR light possesses safety advantages like temperature-controlled localized therapy, deep penetration, cancer cell cytotoxicity, and minimal damage to healthy cells.

A good photothermal agent can inhibit the growth of cancer cells effectively. In PTT, photothermal agents absorb NIR light and translate it to heat energy, killing cancer cells [1, 5]. Various researchers have introduced different photothermal agents, including noble metals like platinum (Pt), palladium (Pd), gold (Au), metal sulphides, and metal selenides. A good photothermal agent is anticipated to have high photothermal conversion efficiency and good photostability [5]. Bismuth-based materials are significantly attractive due to their broad NIR absorption, *in-vivo* and *in-vitro* photothermal effect, and low cost [1, 6]. Specifically, AgBiS₂ is known for various applications [1, 3, 6, 9-21] and, most prominently, as good photothermal agents as they are non-toxic, *in-vivo*, and *in-vitro* biocompatible [1, 6].

Many methods are available to synthesise AgBiS₂ nanoparticles, including microwave, solvothermal, and solid-state chemical reaction methods [1, 3, 6, 9-21]. These methods involve complicated preparation procedures, high temperatures, and using surfactant or polymer molecules to stabilize the particle size in nano regimes. Nanoparticles interact with various cell biopolymers in the biological environment. The physicochemical interactions between nanoparticles and proteins have a crucial impact on their potency [22-25]. The surface properties of the nanoparticles influence physical and chemical phenomena such as aggregation, an affinity for bacterial membranes, and dissolution. Therefore, it is necessary to understand the stabilizer molecule's impact on the interaction with biological cells.

The stabilizers (long-chain surfactant or polymer molecules) used during the synthesis of nanoparticles stay with particles. They can sometimes be cytotoxic to the healthy cells during treatment and encounter compatibility issues. Lao and co-workers [23] studied the effects of surface compositional and structural heterogeneity on protein adsorption on gold nanoparticles.

Wheeler and co-workers [24] discussed the engineered silver nanoparticle's mediation in protein corona formation, while Lundqvist *et al.* studied [25] the surface implications of polystyrene nanoparticles in a biological fluid. Dawson and co-workers explained, through in vitro or in vivo experiments, the key protein recognition motifs that bind with SiO₂ nanoparticles' surface when they adsorb proteins [26]. Though the surface effect has been studied to some extent by varying protein environments, a comparative study on stabilizer's effects by modifying the surface of nanoparticles on their biological activity has been largely overlooked. In order to minimize the complexity and adverse impact of surfactants, we need a simple and effective way to synthesise AgBiS₂ nanoparticles.

In this chapter, we have adapted the hexamethyldisilazane (HMDS) assisted method [27] to synthesise surfactant-free AgBiS₂ (**sf-AgBiS₂**) and polyethylene glycol decorated AgBiS₂ (**PEG-AgBiS₂**) nanoparticles. A comparative study of anticancer activity against HeLa cells using **sf-AgBiS₂** and **PEG-AgBiS₂** reveals the importance of a surfactant-free surface. In tumour treatments, the immunosuppression from chemotherapy is always accompanied by bacterial infection [6]. Since silver has been known as an antibacterial agent for years [28-32], a comparative study of the antibacterial activity of **sf-AgBiS₂** and **PEG-AgBiS₂** against clinically derived Gram-positive bacteria, S. *aureus* was also performed. In this chapter, we have highlighted the importance and advantage of using surfactant-free AgBiS₂ nanoparticles as an effective photothermal and antibacterial agent.

4.2. Experimental

4.2.1. Materials required

Silver chloride (AgCl), Bismuth chloride (BiCl₃), thiourea, hexamethyldisilazane (HMDS), and polyethyleneglycol-400 (PEG-400) were provided by Sigma Aldrich, India. The cell culture media Dulbecco's Modified Eagle Medium (DMEM), solvents like Dimethyl sulfoxide (DMSO), PBS, trypsin–EDTA, and FBS were bought from HiMedia Chemicals, India. Sartorius 0.2 µm syringe filter was bought from Carrigtwohill, Ireland. Bacterial cultured media like Luria Bertani Agar (Miller), Luria Bertani Broth (Miller), and antibiotic Gentamicin were provided by Sisco Research Laboratories (SRL) Pvt. Ltd. *Staphylococcus aureus* (MTCC 3160) was purchased from MTCC. The characterization of synthesised materials was done as discussed in Chapter 2.

4.2.2. Cell lines and maintenance

The HeLa (human cervical cancer cells, P⁷⁵) and L929 (normal mouse fibroblast cell line, P⁵³) were purchased from NCCS, Pune, India. The cells were maintained in DMEM +10% (v/v) FBS+L-glutamine+streptomycin/penicillin at 37 °C and 5% CO₂.

4.2.3. Preparation of sf-AgBiS₂ nanoparticle

Silver chloride (1.4 mmol, 200 mg), bismuth chloride (1.4 mmol, 440 mg), and thiourea (2.8 mmol, 212 mg) were taken in a 100 ml flask with an excess of hexamethyldisilazane and heated to 160 °C under nitrogen atmosphere for 6 h. Later, the mixture was allowed to be cooled down at room temperature and subjected to a high vacuum to eliminate side products and unreacted HMDS. Washed the black residue with distilled water followed by acetone, and the resulting material (sf-AgBiS₂) was dried for 24 h in an oven maintained at 60 °C.

4.2.4. Preparation of PEG-AgBiS₂ nanoparticle

To obtain **PEG-AgBiS₂**, we followed a similar protocol as mentioned above. In addition, we have added 10 ml of polyethyleneglycol-400 (PEG-400) to the above mixture. The reaction conditions and work-up procedures are the same as prescribed above.

4.2.5. Bacterial sample preparation

LB agar and LB broth were autoclaved at 120 °C for 15 min. LB agar was poured into the 100 mm cultured plates and kept for 30 min to solidify. *Staphylococcus aureus* was cultured in broth at 37 °C in a humidified atmosphere.

4.2.6. Photothermal Transduction Efficacy

The PTT efficacy of **sf-AgBiS**² and **PEG-AgBiS**² was evaluated by adding 20 µg/ml of each to 96-well plates. The 808 nm NIR laser with 650 mW power source was used to irradiate the samples for 3-10 min at separate intervals. Autoclaved miliQ was used as a control group. The temperature rise was noted by capturing thermal camera images. The NIR-laser mediated 5 on/off cycles were used to analyze the synthesised nanoparticle's photothermal stability.

4.2.7. DCFDA analysis for ROS generation

For the free radical generation analysis, HeLa cells (7×10^3 cells/well) were seeded in 96 well plates and kept in CO₂ incubator for 24 h. Next day cells were treated with 20 µg/ml **sf-AgBiS**₂ and **PEG-AgBiS**₂. Cells were loaded with 10 µM of DCFDA after treatment. After being exposed to an 808 nm NIR laser (power = 650 mW) for 3 min, fluorescence

measurements were taken before and after using a fluorescent microplate reader with Ex: 485 nm and Em: 535 nm wavelengths. An Olympus fluorescence microscopy was used to capture the images.

4.2.8. Biocompatibility studies

The biocompatibility studies have been done by MTT assay. L929 cells (7000 cells/wells) were cultured in 96-well plates providing 10% FBS containing DMEM. The next day, the media was substituted with fresh media containing 20, 40, 60, 80, and 100 μg/ml sf-AgBiS₂ and PEG-AgBiS₂ keeping for an incubation period of 24 h. Later, the media was removed, MTT solution (5 mg/ml) was added, and incubated for 3 h. The formazan crystals were dissolved using DMSO. The BIORAD Microplate Reader was used to measure the absorbance at 570 nm.

4.2.9. Cell-killing activity

The cytotoxicity of **sf-AgBiS**₂ and **PEG-AgBiS**₂ against HeLa was assessed using an MTT assay. HeLa cells (5000) were seeded in 96-well plates supplemented with DMEM, followed by 24 h incubation to attain the confluency. Media was replaced with new one containing **sf-AgBiS**₂ and **PEG-AgBiS**₂. Cells are irradiated with 808 nm NIR Laser (power = 650 mW) for 3 min and set aside for 24 h for incubation. MTT solution was added (5 mg/ml) and kept for incubation for 3 h. DMSO was used to dissolve formazan crystals, and absorbance was recorded at 570 nm by a microplate reader.

4.2.10. In-vitro 3D tumor spheroids

To observe deep tumor tissue penetration and cell-killing efficacy of **sf-AgBiS**₂ and **PEG-AgBiS**₂ in the live 3D tumor spheroids, HeLa cells $(0.3 \times 10^3 \text{ cells/ wells})$ were seeded in agarose coated 96-well plates and incubated for 5 days in an undisturbed condition inside CO₂ incubator. After that, spheroids were treated with 20 µg/ml of **sf-AgBiS**₂ and **PEG-AgBiS**₂ and irradiated with 808 nm NIR laser (power = 650 mW) for 3 min followed by further 6 h incubation. Live and dead cells were observed staining with FDA (fluorescein diacetate) and PI (propidium iodide) under fluorescence microscope.

4.2.11. Antibacterial study

Antibacterial activity of **sf-AgBiS**² and **PEG-AgBiS**² were studied by disk diffusion and MTT assay against *S. aureus*. The bacterial suspensions with concentrations of 1.5×10⁸ CFU/ml were spread on prepared agar plates. Different concentrations of **sf-AgBiS**² and **PEG-AgBiS**² (150, 250, 500, 1000, 2000 (μg/ml)) were loaded on 0.6 cm disk and placed on top of the agar plates. The plates are incubated for 24 h at 37 °C. The diameter of zone inhibition was measured by a scale. The bacterial suspensions without the treated sample were set as the control group. Gentamicin was used as the positive/standard control group.

For antibacterial MTT assay, *S. aureus* (1.5×10⁸ CFU/ml) was co-cultured with various concentrations of the **sf-AgBiS₂** and **PEG-AgBiS₂** in 96-well plates (100 μL/well) and incubated at 37 °C for 24 h. The bacterial suspensions without the **sf-AgBiS₂** and **PEG-AgBiS₂** were set as the control group. Gentamicin was used as the positive/standard control group. After 3 h incubation with MTT (5 mg/ml) followed by DMSO-formazan crystal solubilization, absorbance was recorded by a plate reader at 570 nm.

The antibacterial study of **sf-AgBiS**₂ and **PEG-AgBiS**₂ with NIR radiation was performed using an inoculum of bacterial culture S. *aureus* as per the standard institute protocols. Briefly, S. *aureus* inoculum of 1.5 x 10⁸ CFU/mL was prepared, followed by treatment with 2000 µg/mL of **sf-AgBiS**₂ and **PEG-AgBiS**₂ incubated for 4 h in two 96-well plates. One plate was further incubated without treatment (-NIR group), and the other plate was exposed to an 808 nm light using a laser (+NIR) for 10 min and incubated at 37 °C for 24 h. After the incubation period, a colony formation assay was performed. Briefly, 100 µL from the inoculum from the treated 96-well plates was spread onto MH Agar plates and untreated controls were also plated using the same procedure and incubated for 16 h at 37 °C. The difference in the number of colonies was evaluated after the incubation period.

4.2.12. Statistical analysis

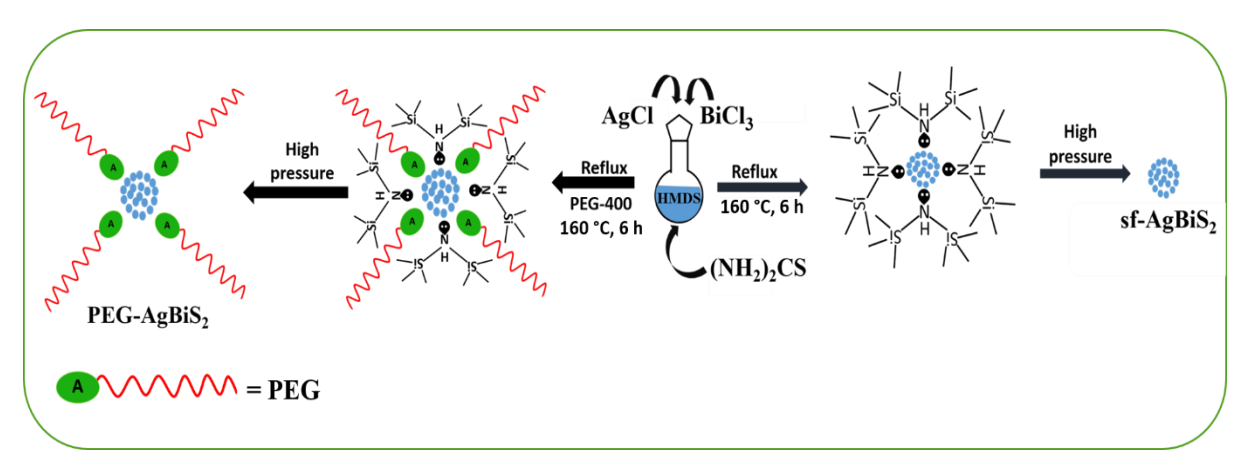
The statistical comparison between the control and treated groups was made using a one-way ANOVA test, Tukey's test (***p<0.001, **p<0.01, *p<0.05).

4.3 Results and Discussion

4.3.1. Preparation and Characterisation

Numerous attempts have been made to identify photo-responsive material for simultaneous photothermal and photodynamic therapy. Silver bismuth sulphide (AgBiS₂) is studied well for light-activated sterilization techniques as it can be excited by a single-wavelength light in the NIR region. However, many reported synthetic procedures of AgBiS₂ are tedious and inevitably require stabilizers like surfactants or polymers. In this chapter, we prepared stabilizer-free nanoparticles **sf-AgBiS₂**, and polyethylene glycol wrapped **PEG-AgBiS₂**, then compared their antibacterial and photothermal anticancer abilities. These materials were prepared successfully by a versatile hexamethyldisilazane (HMDS)-assisted synthetic method, as shown in Scheme 4.1 [27a]. In this method, thiourea reacts with HMDS to form a polymeric molecule, which then reacts with metal chloride to form metal sulphides and trimethylsilyl chloride as a by-product. The pH monitoring throughout the reaction showed no change indicating the absence of formation of both NH₃ and H₂S, and these reactions are believed to occur via the formation of S-N polymeric intermediate [27].

HMDS acts as a reducing agent, solvent, and surfactant in the synthesis by forming S-N polymeric intermediate. The advantage of this method is that all side products are volatile and can be removed simply by vacuum. Since HMDS or any intermediate in this reaction is removed after nanoparticle formation, the purity of **sf-AgBiS2** is very high. Further, the active sites on the surface of **sf-AgBiS2** are readily available for interactions resulting in higher activity in multiple applications. In comparison, many other reported methods use long-chain surfactant molecules in the synthesis, which covers the surface and prevents interactions. The presence of these surfactants mostly retards the activity of nanoparticles by forming an intermediate layer between the active surface and substrates. Some surfactants are toxic to human beings, also. This sophisticated HMDS-assisted method has been used to produce various surfactant-free metal sulphides, and those results demonstrated increased performance in terms of conductivity, photoresponsivity and catalytic activity [27, 33-38].



Scheme 4.1. Preparation of sf-AgBiS2 and PEG-AgBiS2 using HMDS method

The powder X-ray diffraction pattern of **sf-AgBiS**₂ and **PEG-AgBiS**₂ (Figure 4.1) implies the formation of cubic AgBiS₂ (JCPDS- 89-2046) [10]. The major peaks found at 27.451, 31.751, 45.531, 53.931, 56.621 and 66.281 corresponding to (111), (200), (220), (311), (222), and (400) planes of cubic AgBiS₂ respectively can be clearly observed in Figure 4.1. Both **sf-AgBiS**₂ and **PEG-AgBiS**₂ nanoparticles show the same crystal structure, which can be identified from the PXRD pattern. Moreover, the absence of Bi₂S₃ and Ag₂S peaks in PXRD shows the purity of samples prepared using HMDS assisted method. The absence of peaks in the IR spectrum (Figure 4.2. A) of **sf-AgBiS**₂ related to HMDS indicates the absence of HMDS, whereas the peaks in IR spectrum (Figure 4.2. B) corresponding to PEG in **PEG-AgBiS**₂ confirm the formation of it. As discussed in the literature, [27] the presence of surfactant or stabilizer molecules on the surface of nanoparticles receded its activity as most of their active sites were covered.

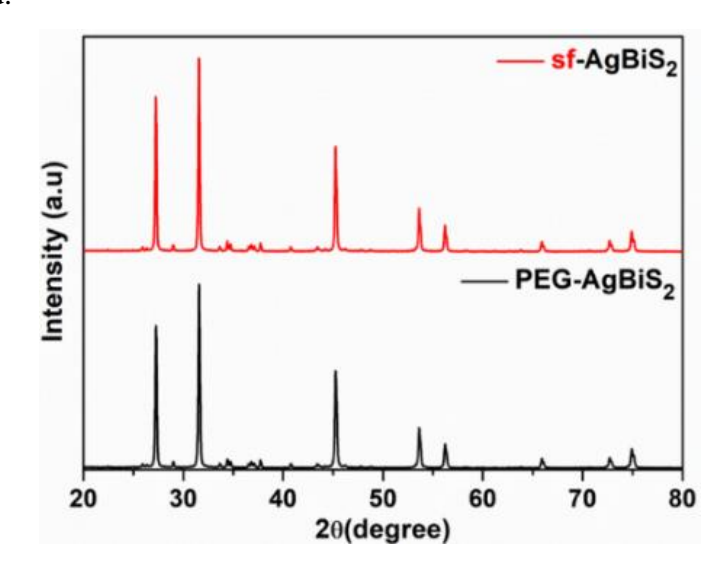


Figure 4.1. PXRD pattern of sf-AgBiS₂ and PEG-AgBiS₂ nanoparticles.

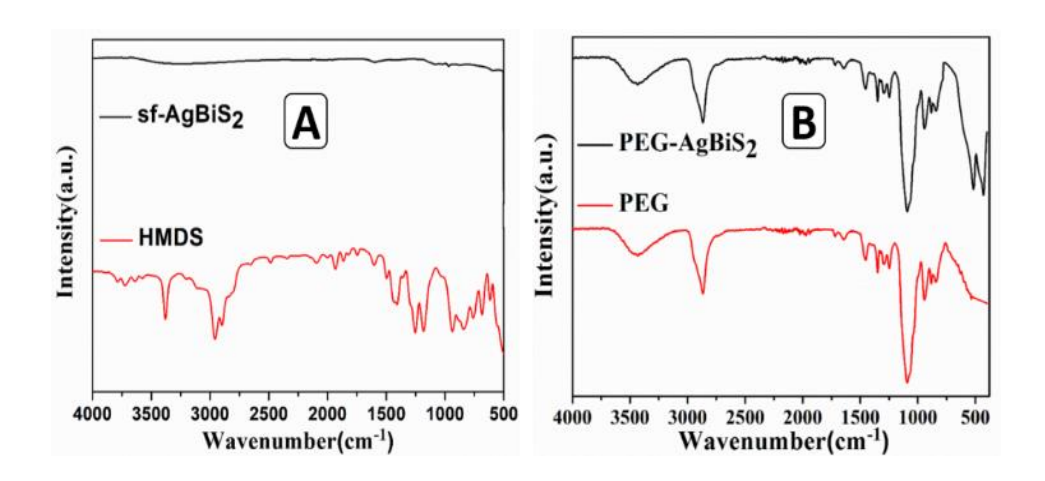


Figure 4.2. FTIR spectra. A) **sf-AgBiS**² and hexamethyldisilazane (HMDS), B) **PEG-AgBiS**² and polyethylene glycol (PEG).

The calculated absorption coefficient spectra (Figure 4.3) of AgBiS₂ show the broad and strong absorption spectra near the NIR region for both the samples indicating their utilization as PTT agents [3, 6, 39]. The SEM and TEM images (Figure 4.4) showed a nanorod-like morphology of both **sf-AgBiS**₂ and **PEG-AgBiS**₂ particles, while the SAED pattern confirmed the crystalline nature of the samples. The average particle size of **sf-AgBiS**₂ and **PEG-AgBiS**₂ nanoparticles was 16.5 nm and 19 nm, respectively (Figure 4.5). Interestingly, both **sf-AgBiS**₂ and **PEG-AgBiS**₂ exhibited similar morphology and formed an excellent dyad for a comparative study vis-à-vis presence and absence of stabilizers on the biological activity of AgBiS₂. It appears that **PEG-AgBiS**₂ was agglomerated, probably due to the adhesive nature of surfactants.

Capping agents are generally used to control the growth of particles and prevent agglomeration. The surface modification of nanoparticles is acquired using these capping agents. We have chosen PEG as a capping agent in the current study because of its biocompatibility for biomedical applications. This non-ionic, hydrophilic, low molecular weight polymer with antioxidant properties and high solubility in the buffer has a high adsorption rate. It helps the nanoparticle penetrate through the mucous membrane. PEG also helps nanoparticles from non-specific protein binding and macrophages. PEG also has antibacterial activity against various pathogens and is used in biomedical applications [40-45].

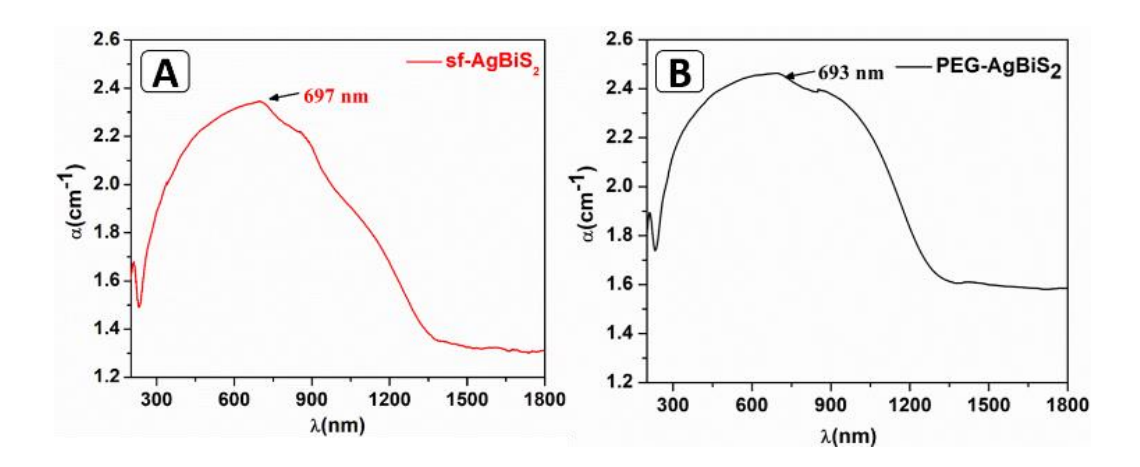


Figure 4.3. Calculated absorption coefficient of sf-AgBiS₂ and PEG-AgBiS₂ nanoparticles.

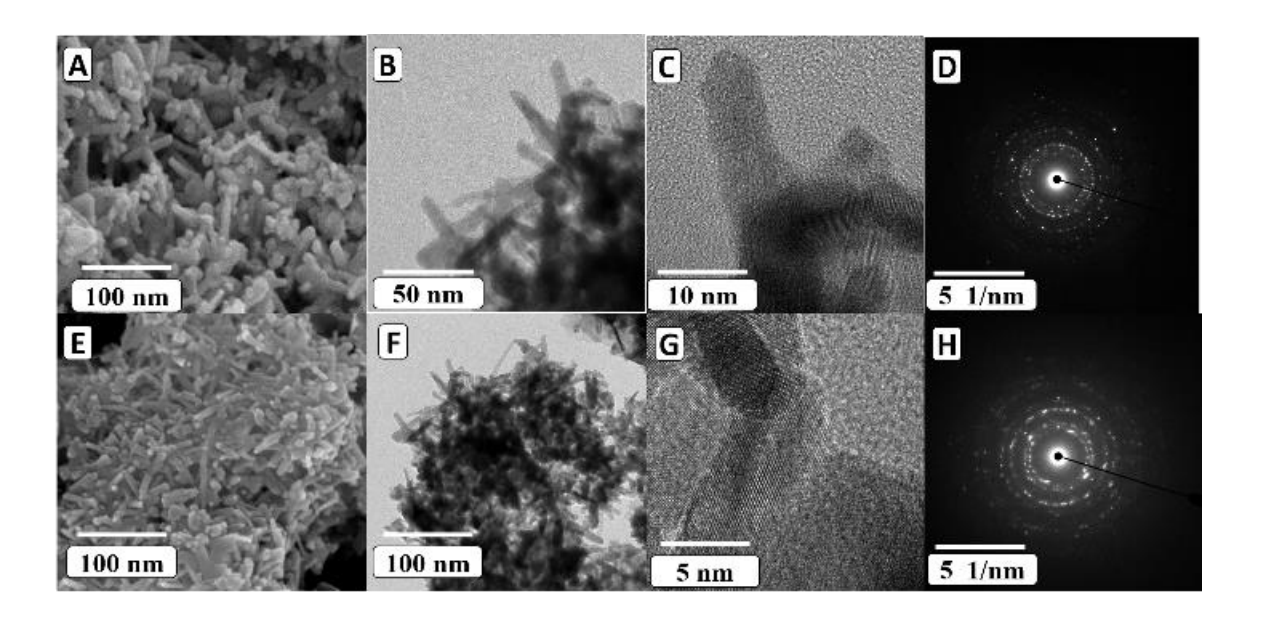


Figure 4.4. A) FESEM image, B) TEM image, C) High resolution TEM image, and D) SAED pattern of **sf-AgBiS**₂ nanoparticles. E) FESEM image, F) TEM image, G) High resolution TEM image, and H) SAED pattern of **PEG-AgBiS**₂ nanoparticles.

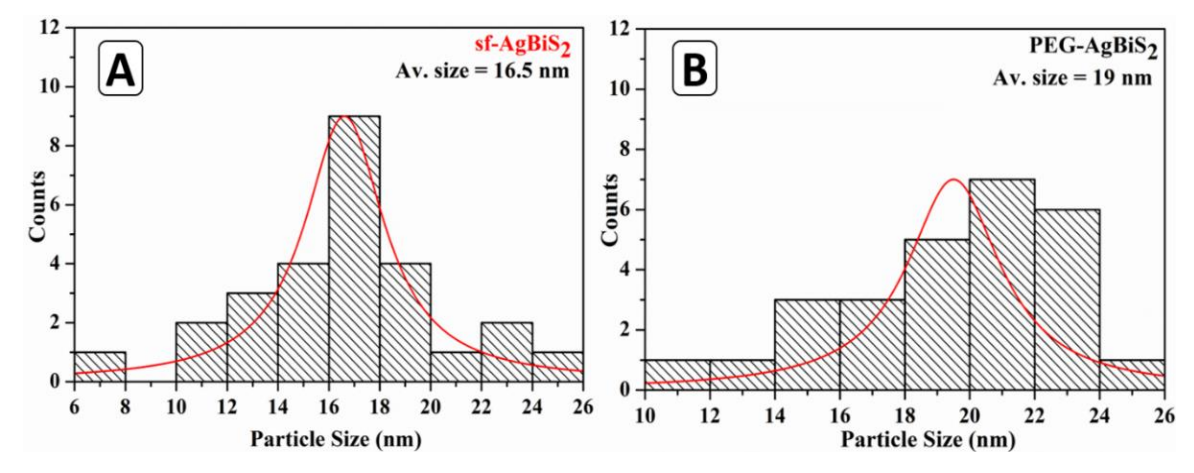


Figure 4.5. Average particle size of sf-AgBiS₂ and PEG-AgBiS₂ nanoparticles.

4.3.2. Photothermal Effect

A good PTT agent can absorb at NIR regime. They get excited when the PTT agent accumulated on cancer cells is irradiated with the external light source. The excited PTT agent undergoes vibrational relaxation through non-radiative decay, releasing the energy as heat, which is transferred to the cancer cells. The cells die when the temperature of the tissue is increased above 46 °C due to protein denaturation and plasma membrane destruction [5, 46-51]. The photothermal effect of **sf-AgBiS2** and **PEG-AgBiS2** (20 μg/ml each) was measured at various time using an 808 nm NIR laser (power = 650 mW) for 3-10 min (Figure 4.6). It was found that the temperature of **sf-AgBiS2** reached to a maximum of 53.3 °C after 10 min of radiation, and 43.9 °C with 3 min exposure was. Similarly, the maximum temperature obtained for **PEG-AgBiS2** was 44.9 °C at 10 min and 38.9 °C for 3 min exposure. The temperature of DI water (control) was only 25.9 °C (Table 4.1). The thermal stability of compounds was studied, as shown in Figure 4.7.

Generally, a temperature above 41 °C makes cell inactivation for a definite time, while a temperature above 48 °C results in irreversible cell inactivation. These results demonstrate the efficiency of **sf-AgBiS2** and **PEG-AgBiS2** as effective photothermal agents by converting NIR light to heat efficiently. Interestingly, **sf-AgBiS2** act as a more powerful photothermal agent compared with **PEG-AgBiS2** [3, 6]. The maximum temperature obtained for even 20 μ g/ml of **sf-AgBiS2** when irradiated with 808 nm NIR laser (power = 650 mW) is much higher than the earlier reported temperatures for AgBiS2 nanoparticles prepared using different methods. In many reported works, researchers have used a higher concentration of 150 μ g/ml, 1000 μ g/ml 125 μ g/ml to obtain 60 °C, 62 °C, and 49 °C, respectively, with NIR 808 radiation of 1 W for 10 min irradiation and 200 μ g/ml with 0.4 W NIR radiation to obtain 46.7 °C [1, 3, 6]. Interestingly, we can bring a temperature as high as 53.3 °C even at a lower concentration of **sf-AgBiS2**.

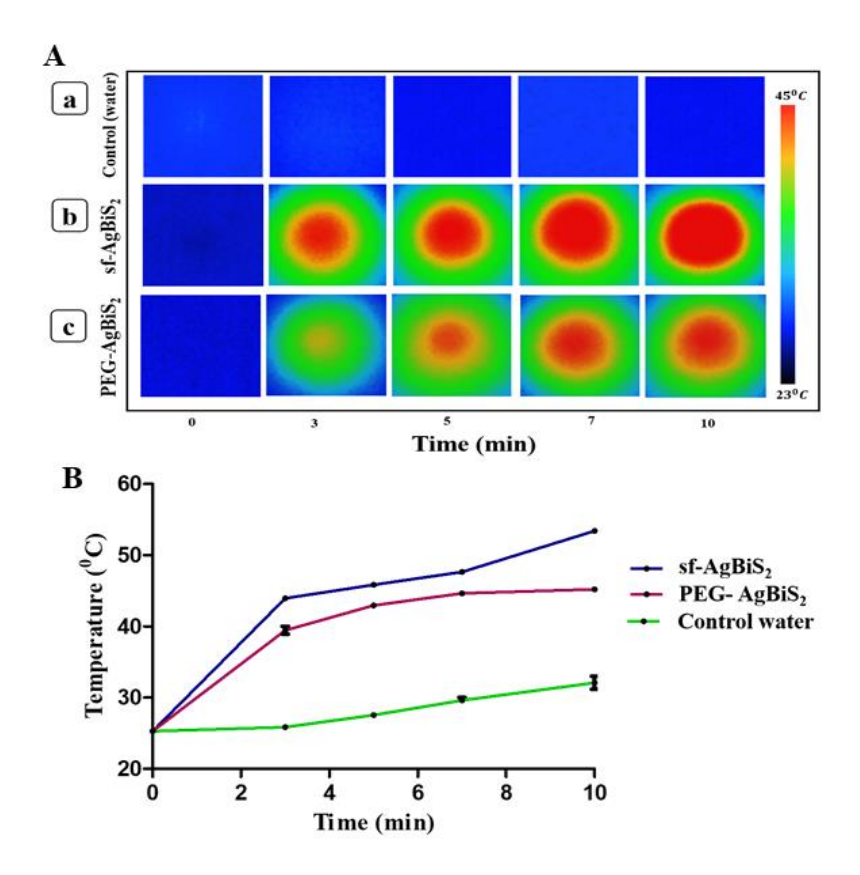


Figure 4.6. A) Photothermal transduction efficiency thermal images of (a) control (water), (b) **sf-AgBiS₂**, and (c) **PEG- AgBiS₂** nanoparticles irradiated with 808 nm NIR laser. B) PTT transduction efficiency graph of control (water), **sf-AgBiS₂** and **PEG-AgBiS₂** nanoparticles.

The difference in photothermal transduction temperature can be explained based on the low thermal conductivity of polyethylene glycol (PEG) in **PEG-AgBiS2**. In the case of **PEG-AgBiS2**, the heat generated is trapped within the nanoparticle and is not transferred to cancer cells. Whereas in the case of **sf-AgBiS2**, the heat generated is wholly transferred to the cancer cells as these nanoparticles are not covered with capping agents, making it a good PTT agent. These can also exhibit SPR, a phenomenon in which conductive free electrons resonate jointly with the incoming electromagnetic radiation, which results in increased light absorption and scattering. This observation indirectly reveals that more free surface electrons are available for **sf-AgBiS2** than **PEG-AgBiS2**, where the surface electrons are unavailable due to the coverage by the capping agent polyethylene glycol (PEG). Thus, more NIR light absorption is observed in the case of **sf-AgBiS2**, leading to higher temperature generation.

Due to their large light absorption and scattering cross section, nanorods usually give high SPR frequency. Therefore, nanorods can generally increase the temperature in tumour cells more than other morphologies. Since both sf-AgBiS₂ and PEG-AgBiS₂ exhibit nanorods

morphology, the difference in photothermal transduction temperature can be due to the absence of the capping agent in **sf-AgBiS₂**. **sf-AgBiS₂** prepared using the HMDS-assisted method is crystalline. Albeit crystalline nature, it exhibited a good PTT. It is worth mentioning that few crystalline nanoparticles reported in the literature exhibited a good PTT effect [1, 5]. These results also demonstrate the importance of HMDS-assisted method to obtain surfactant-free nanoparticles to acquire a more active photothermal agent [5, 46-51].

Table 4.1. Photothermal transduction temperatures were obtained for control (water), **sf-AgBiS**₂ and **PEG-AgBiS**₂.

Time (min)	Temperature of Control (water)	Temperature of sf-AgBiS2	Temperature of PEG-AgBiS2
0	25.4	25.1	25.2
3	25.9	43.9	38.9
5	27.6	45.8	42.9
7	28.0	47.4	44.6
10	29.0	53.3	44.9

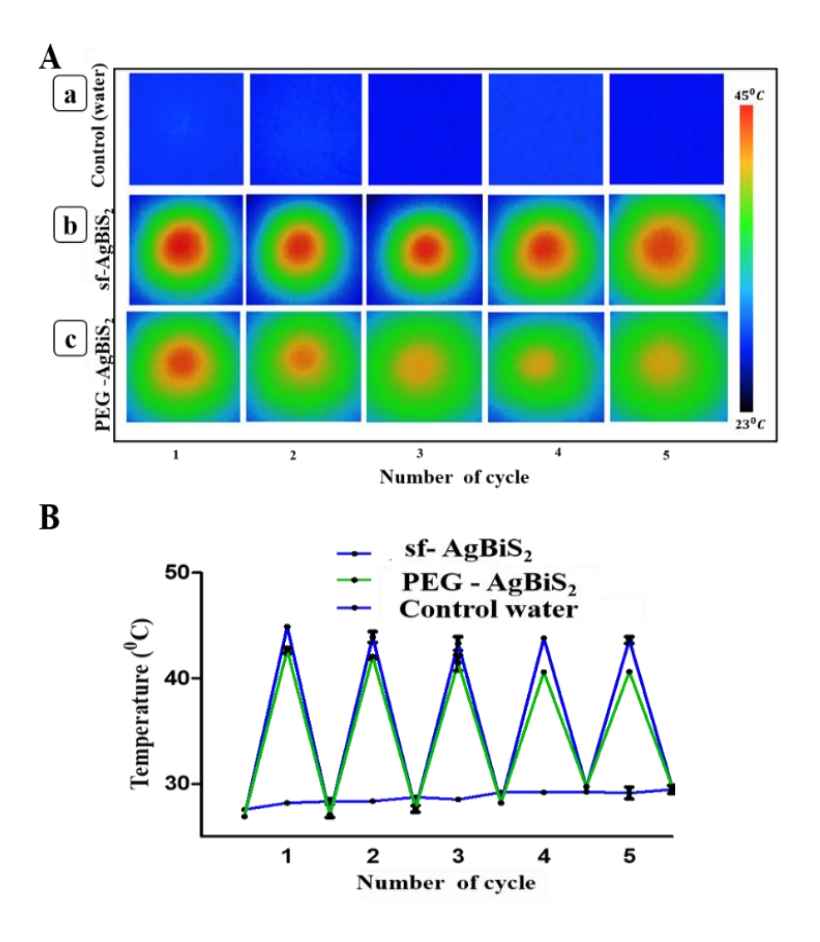


Figure 4.7. A) Thermal stability (on/ off cycle) images irradiated with an 808 nm Laser of (a) control (water), (b) **sf-AgBiS₂**, and (c) **PEG- AgBiS₂** NPs for 5 min (five cycles), B) Thermal stability (on/off cycle) graph of water, **sf- AgBiS₂** and **PEG-AgBiS₂** nanoparticles irradiated with a 808 nm laser for 5 min (five cycles).

4.3.3. *In-vitro* biocompatibility

In-vitro biocompatibility for 20, 40, 60, 80, 100 μg/ml of **sf-AgBiS**₂ and **PEG-AgBiS**₂ to normal cell line L929 was measured using MTT assay. The results (Figure 4.8) reveal that both exhibited no significant toxicity. Even at the high concentration of 100 μg/ml, **sf-AgBiS**₂ shows a cell viability of 86.29% to 71.63 ± 5% with 20, 40, 60, 80 and 100 μg/ml and **PEG-AgBiS**₂ offers a cell viability of cell viability 86.29% to 67.3 ± 3% with 20, 40, 60, 80 and 100 μg/ml. Among these, **sf-AgBiS**₂ showed slightly greater biocompatibility to normal fibroblast cell lines L929 than **PEG-AgBiS**₂. The good biocompatibility of **sf-AgBiS**₂ may attribute to their more active sites available on the surface than **PEG-AgBiS**₂, where most of the active sites are covered, resulting in less interaction with the cells [33].

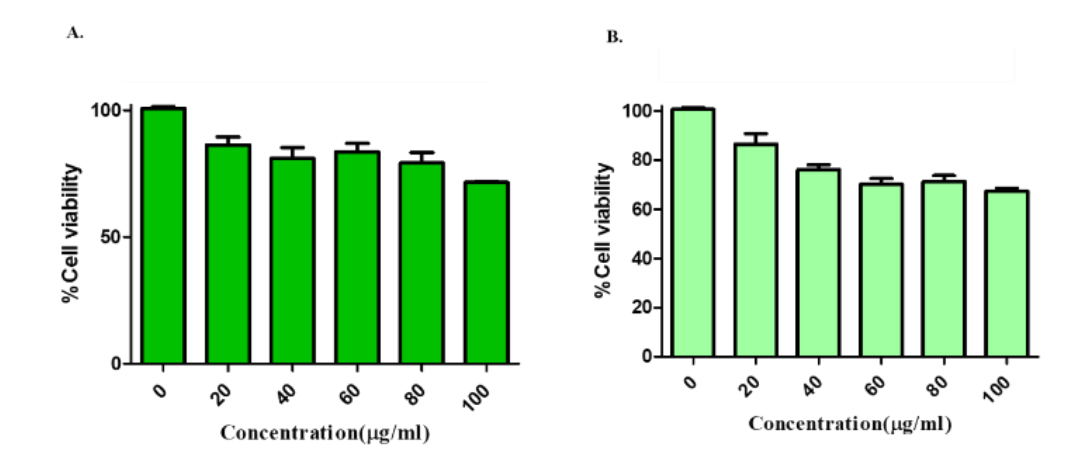


Figure 4.8. Biocompatibility of A) sf-AgBiS2 and B) PEG-AgBiS2 nanoparticles.

4.3.4. In-vitro cytotoxicity in 2D and 3D cell culture

Cancer cell killing activity of **sf-AgBiS2** and **PEG-AgBiS2** against HeLa was studied using the same MTT assay. A remarkable decline in the viable cell % of HeLa was observed when cultured in the presence of **sf-AgBiS2** (20 μ g/ml) and **PEG-AgBiS2** (20 μ g/ml) and irradiated with NIR laser (Figure 4.9). For **sf-AgBiS2**, the cell viability was 80 \pm 3% without NIR laser and 51 \pm 4% with NIR laser. For **PEG-AgBiS2**, the cell viability without the NIR laser was 85 \pm 5%, and with the NIR laser was 72 \pm 6% (Table 4.2). These observations show that **sf-AgBiS2** has more cell-killing efficiency than **PEG-AgBiS2**. The results indicate that the synergic effect of the availability of free active surface and the photothermal efficiency of **sf-AgBiS2** results in more cancer cell death than **PEG-AgBiS2**, where the presence of surfactant hinders the PTT active AgBiS2 activity. Since both **sf-AgBiS2** and **PEG-AgBiS2** have the same morphology, the difference in the anticancer activity exhibited by these nanoparticles can be attributed to the presence and absence of the stabilising agent.

In-vitro 3D tumor spheroids can mimic the microenvironment of live tumours present in-vivo. We observed that sf-AgBiS₂ with NIR irradiation has better cell-killing efficacy than PEG-AgBiS₂ (Figure 4.10) and without NIR irradiation (Figure 4.11). Figure 4.10 shows that sf-AgBiS₂ has significantly damaged tumour cells from the edge to the core compared to PEG-AgBiS₂. In cancer treatment, it is important to target the hypoxic core of tumour cells to avoid metastasis and angiogenesis. When NIR light is absorbed by nanoparticles, it gets excited and undergoes vibrational relaxation and leads to lattice vibration and results in temperature rise. The increased temperature eventually destroys the membrane and proteins which covers the cancer cells resulting in the penetration of nanoparticles into the cell and leads to cell death (Figure 4.12). The possible reason for the cancer cell death could be the good penetration

capability of **sf-AgBiS**₂ in the hypoxic core of the tumour than **PEG-AgBiS**₂. In addition to that, the decreased size (16.5 nm) and increased SPR response of nanorod morphology in the case of capping agent free **sf-AgBiS**₂ will also pave the way for its enhanced activity. In conjunction with that, capping agents will cover the active sites on the surface of nanoparticles. Therefore, the adsorption of nanoparticles to the cell surface is hindered, whereas the **sf-AgBiS**₂, with a greater number of active sites, is able to get adsorbed on cell surface easily, which results in easy and more penetration of nanoparticles inside cancer cells [4, 52].

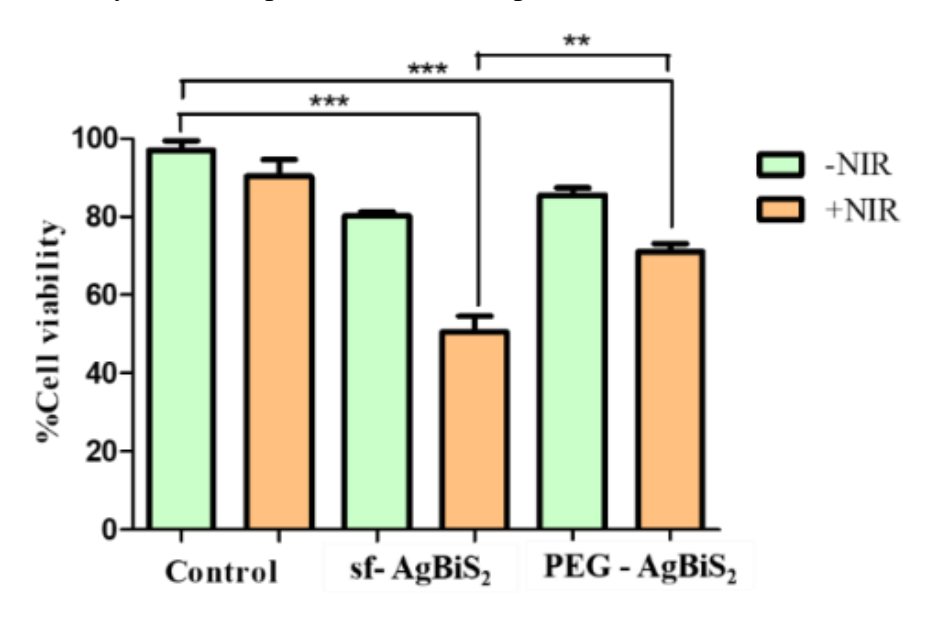


Figure 4.9. NIR laser mediated cell cytotoxicity of **sf-AgBiS₂** and **PEG-AgBiS₂** nanoparticles in HeLa cell line (P < 0.05).

Table 4.2. The cell viability of sf-AgBiS2 and PEG-AgBiS2 against HeLa cells

Sample	Cell viability (%)		
Sample	without NIR irradiation	with NIR irradiation	
sf-AgBiS ₂	80 ± 3	51 ± 4	
PEG- AgBiS ₂	85 ± 5	72 ± 6	

+NIR

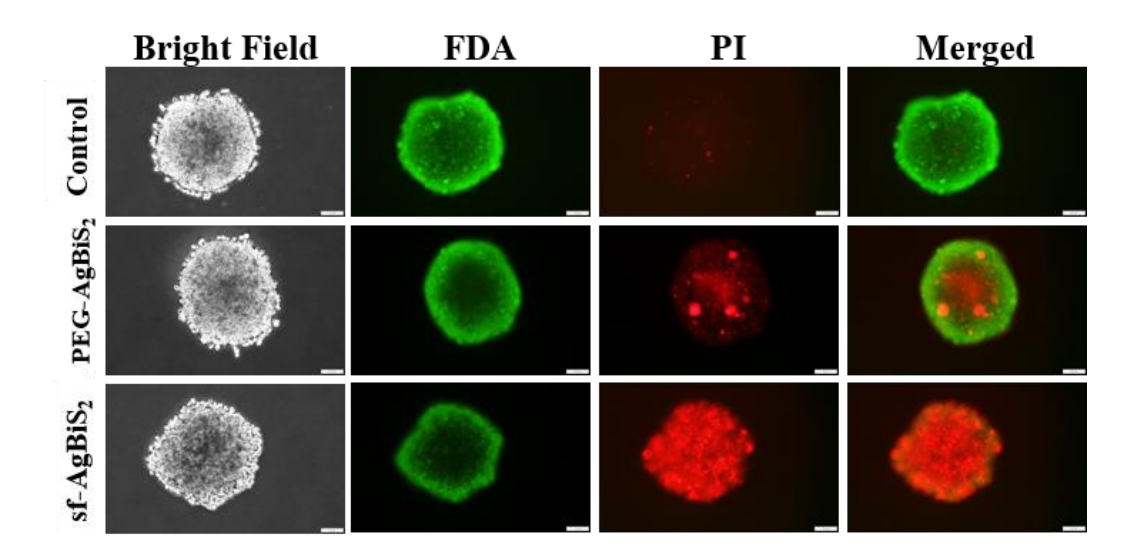


Figure 4.10. *In vitro* NIR-laser-mediated cell cytotoxicity of **sf-AgBiS2** and **PEG-AgBiS2** by the live/dead assay (FDA stains live cells (green) and PI stains dead cells (red).

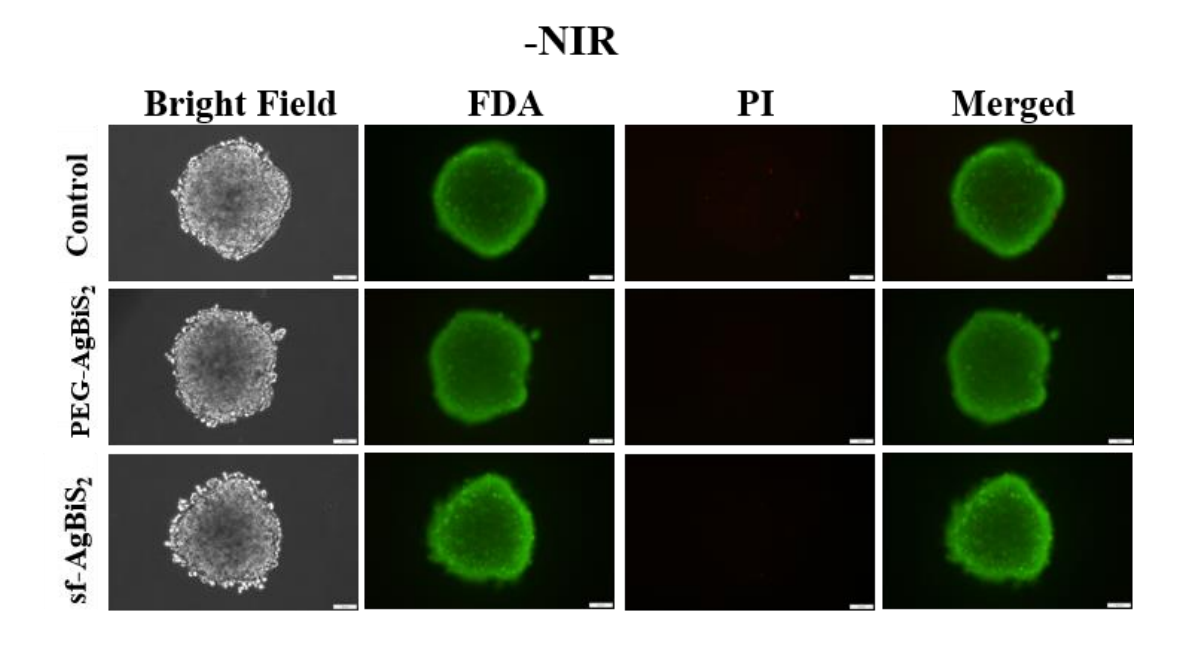


Figure 4.11. *In-vitro* cell killing efficacy of **sf-AgBiS₂** and **PEG-AgBiS₂** against 3D tumor spheroids without NIR irradiation.

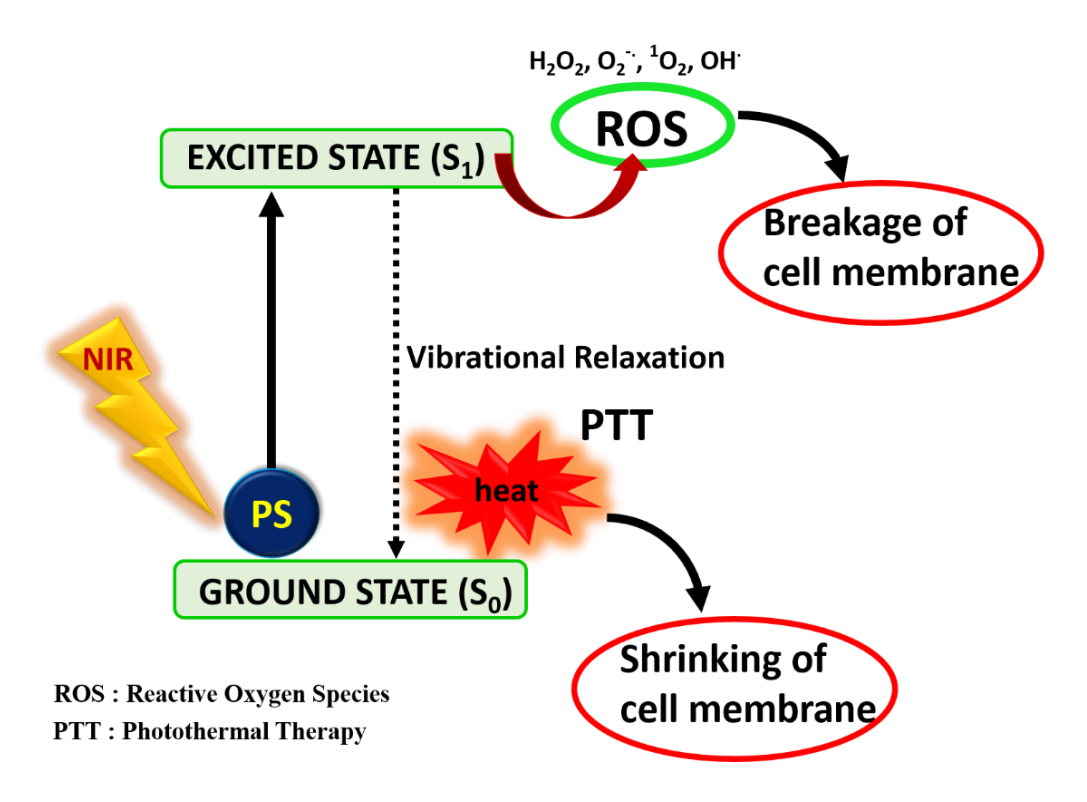
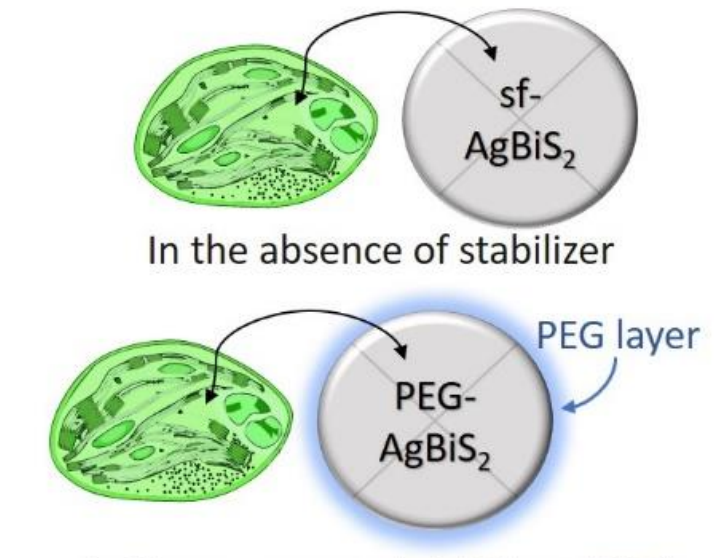


Figure 4.12. Schematic illustration of cell killing mechanism in Photothermal therapy.

4.3.5. Reactive Oxygen Species (ROS) Analysis

The Anticancer and Antibacterial Activity of AgBiS₂ is usually from the photothermal therapy (PTT) and the photocatalytic activity (deriving from photo-excited ·OH, holes, O₂ · or other active radicals). As reported earlier, [27] the capping agents or stabilizer molecules cover the active sites on the photocatalyst and hinder the transfer of excitons to dye molecules retarding the photocatalytic activity of nanoparticles [27, 33-38]. Similarly, antibacterial and anticancer activities involve the adsorption of nanoparticles on the cell surface. The stabilizers may impede the interaction between cancer cell/bacterial and active radicals (Figure 4.13). Since sf-AgBiS₂ is not covered with the capping agent, it can directly interact with the cell surface than coated nanoparticles

INTERACTION OF BIOLOGICAL CELL WITH NANOPARTICLES



In the presence of stabilizer (PEG) sf = stabilizer free; PEG= polyethylene glycol

PEG act as a barrier for interaction

Figure 4.13. Schematic diagram showing the possible interaction of sf-AgBiS₂ and PEG-AgBiS₂ with bacteria or cells.

Reactive oxygen species (ROS) or free-radical generation in the presence of NIR light is one of the cell-killing mechanisms where excessive production of ROS can trigger DNA damage or programmed cancer cell death [4, 53]. 2',7'-Dichlorodihydrofluorescein diacetate (DCFDA) is an indicator to analyse the generation of ROS. Our analysis using DCFDA showed the generation of ROS in both **sf-AgBiS2** and **PEG-AgBiS2** treated cells in the presence of NIR light. The cell death is more with NIR light when **sf-AgBiS2** is used (Figure 4.14). The possible reason for the enhanced activity of **sf-AgBiS2** can be because the excitons produced are available for the production of ROS, whereas, in the case of **PEG-AgBiS2**, the excitons are trapped within the nanoparticle due to the presence of PEG, resulting in decreased ROS production. Also, the free active surface on the **sf-AgBiS2** makes adsorption easier for these nanoparticles than the **PEG-AgBiS2**. The **sf-AgBiS2** may also trigger other cell death mechanisms, which we will check in future.

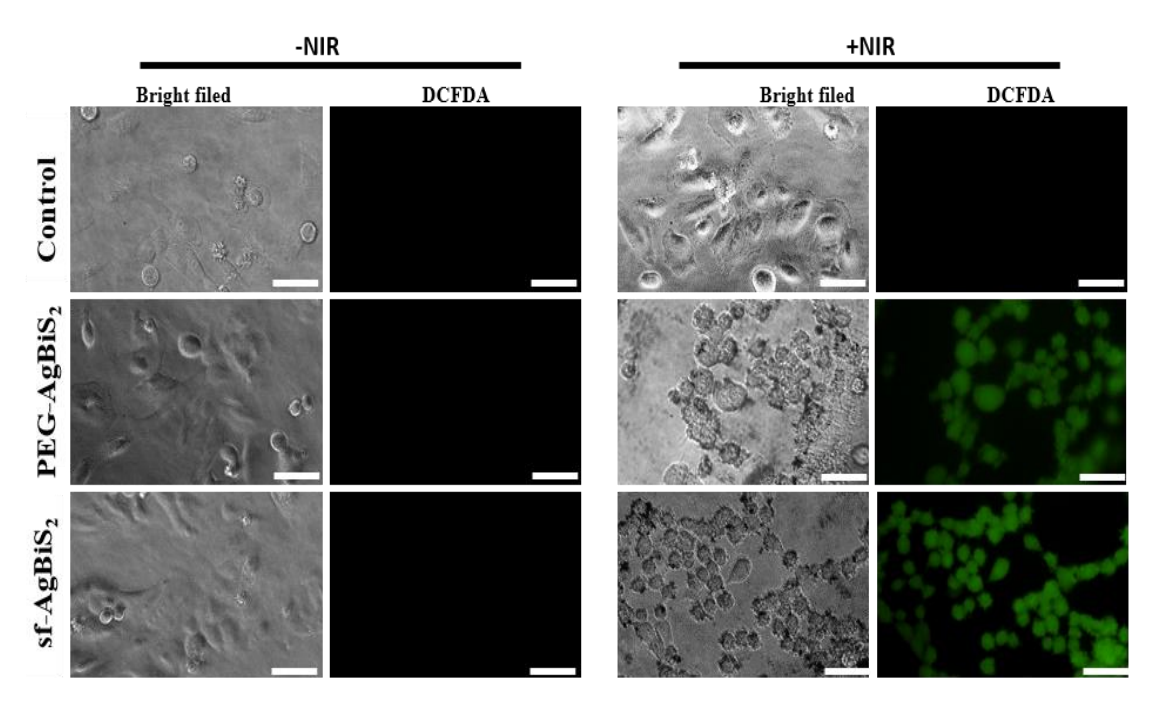


Figure 4.14. DCFDA analysis for reactive oxygen species (ROS) generation of **sf-AgBiS**² and **PEG-AgBiS**² nanoparticles with and without NIR irradiation.

4.3.6. Antibacterial activity

The antibacterial activity of sf-AgBiS₂ and PEG-AgBiS₂ against Gram (+) S. aureus was investigated using the disc diffusion method and MTT assay method (Figures 4.15 and 4.16). Clinically derived S. aureus due to immunosuppression by chemotherapy is a significant cause of infection in tumour treatment. Silver has proven to be one of the best antibacterial agents [28-32]. The area of the zone of inhibition visible around the disc indicates the activity of nanoparticles as an antibacterial agent. According to the earlier studies [31, 54, 55] the sharp edges of AgBiS₂ rods pierce the cell membrane and thus release ROS, which damages DNA and oxidises proteins, ultimately leading to cell death. From Figure 4.15, it is clear that sf-AgBiS₂ has a higher antibacterial effect against S. aureus than PEG-AgBiS₂. This observation depicts that the surfactant-free AgBiS2 nanoparticles synthesised using HMDS assisted method improve the chances of getting S. aureus bacteria directly in contact with nanoparticles (improves the cling between S. aureus bacteria with the bare surface of nanoparticle) by exposing more active sites than the nanoparticles covered with polyethylene glycol (PEG) as surfactant. The antibacterial activity of sf-AgBiS₂ and PEG-AgBiS₂ was also confirmed using the MTT assay method (Figure 4.16). Accordingly, the results indicate that sf-AgBiS₂ nanoparticles could be an excellent antibacterial agent and can prevent the infection caused during cancer therapy.

We have studied the antibacterial activity of **sf-AgBiS2** and **PEG-AgBiS2** against *S. aureus* with NIR irradiation by MTT assay method. Since these materials showed lowest antibacterial activity with 150 µg/mL concentration (Figure 4.15) without NIR, we have checked the antibacterial activity at this lowest concentration (Figure 4.17) with NIR irradiation. As shown in Figure 4.17, the instant antibacterial activity without NIR irradiation was insignificant, whereas, with NIR irradiation, these materials showed effective bacterial inactivation. As expected, **sf-AgBiS2** is better compared to **PEG-AgBiS2**. The photothermal antibacterial activity under NIR irradiation results from lattice vibration caused by the non-radioactive de-excitation process. This vibration results in photothermia, eventually leading to the degradation of the bacterial cell membrane, helping the penetration of nanoparticles inside the cell and leading to cell death. As discussed earlier, the nanorod morphology of materials described here shows good light absorption and scattering cross-section [47]. However, thermal absorption by **PEG-AgBiS2** diminished its activity compared to **sf-AgBiS2**.

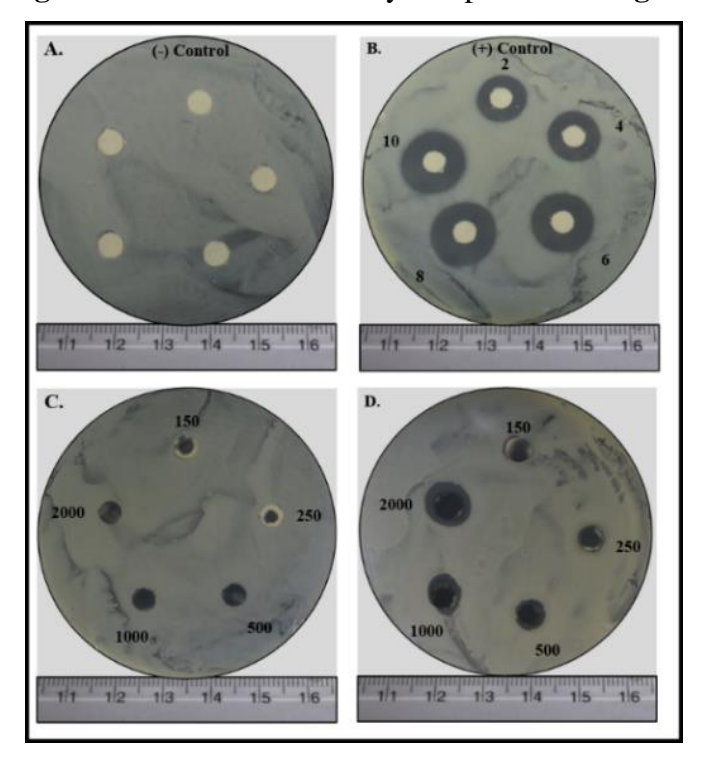


Figure 4.15. Antibacterial activity by disk diffusion method against *S.aureus*, A) Negative control, B) Negative control (with antibiotic Gentamicin), C) **PEG-AgBiS2** and D) **sf-AgBiS2** nanoparticles.

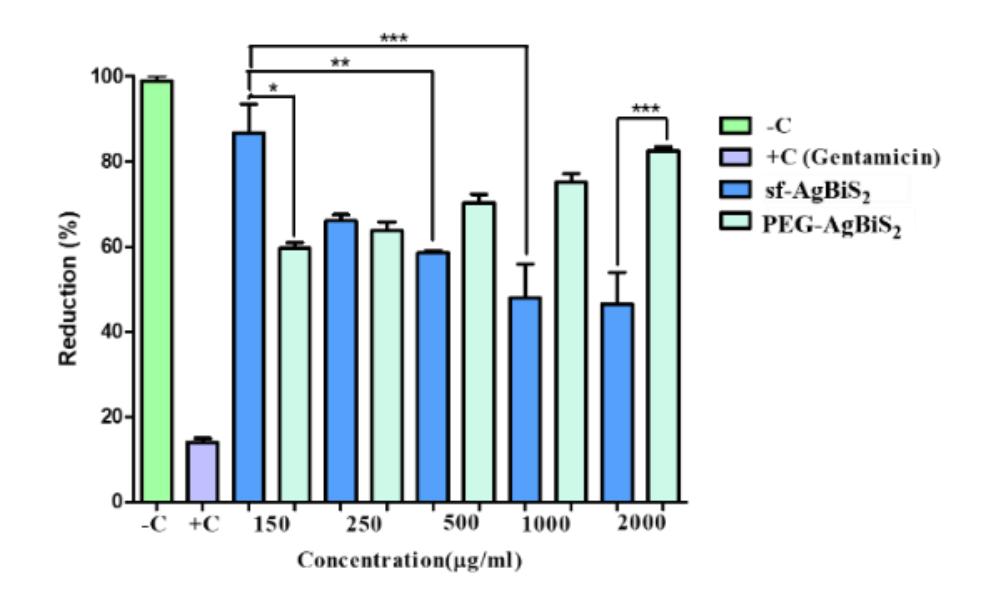


Figure 4.16. Antibacterial activity of **sf-AgBiS**₂ and **PEG-AgBiS**₂ nanoparticles by MTT assay against *S.aureus* (P < 0.05).

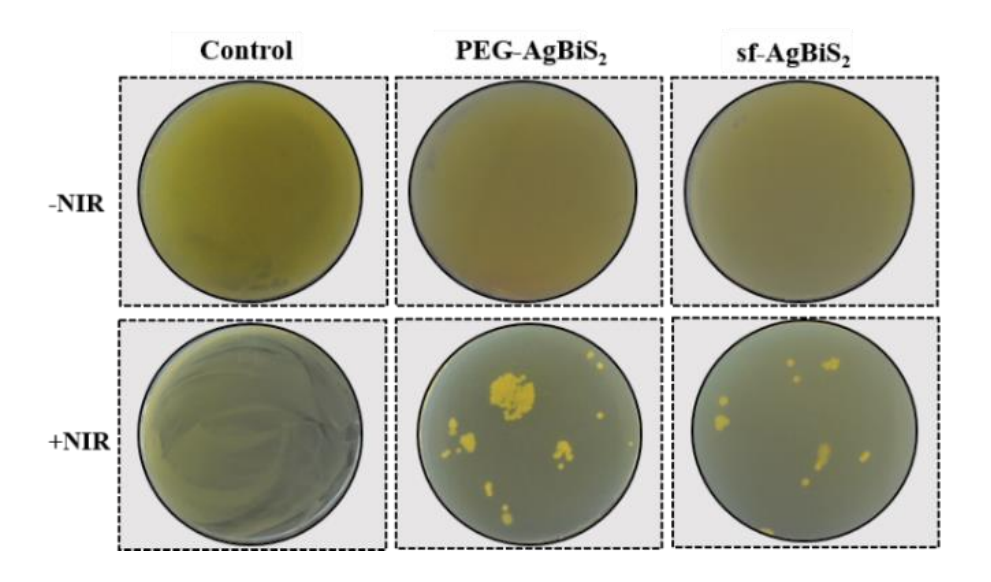


Figure 4.17. Antibacterial activity of sf-AgBiS₂ and PEG-AgBiS₂ against S. *aureus* with and without NIR irradiation.

4.4. Conclusion

In summary, $\mathbf{sf-AgBiS_2}$ and $\mathbf{PEG-AgBiS_2}$ nanoparticles were prepared successfully employing the HMDS-assisted synthesis. The X-ray diffraction and SAED patterns revealed the cubic phase formation of crystalline $AgBiS_2$ nanoparticles. The maximum temperature attained for 20 μ g/ml of $\mathbf{sf-AgBiS_2}$ when irradiated with 808 nm NIR laser (power = 650 mW) is much higher than the earlier reported temperatures for $AgBiS_2$ nanoparticles. The as-synthesised $\mathbf{sf-higher}$

AgBiS² nanoparticles performed as an excellent photothermal (PPT) agent against HeLa cells, live 3-D tumour spheroids and an antibacterial agent against *Staphylococcus aureus* than **PEG-AgBiS**² nanoparticles with and without NIR irradiation. The study showed that **sf-AgBiS**² has more cell-killing efficiency than **PEG-AgBiS**². This chapter highlights and the importance of surfactant-free surfaces of nanoparticles to pave the way for effective nanomedicine and, perhaps, justifies the utility of HMDS-assisted method.

4.5. References

- 1. Lei, P., An, R., Zheng, X., Zhang, P., Du, K., Zhang, M., Dong, L., Gao, X., Feng, J. and Zhang, H. Ultrafast synthesis of ultrasmall polyethylenimine-protected AgBiS₂ nanodots by "rookie method" for in vivo dual-modal CT/PA imaging and simultaneous photothermal therapy. *Nanoscale*. **2018**, 10, 16765-16774.
- 2. Vines, J.B., Yoon, J.H., Ryu, N.E., Lim, D.J. and Park, H. Gold nanoparticles for photothermal cancer therapy. *Front. Chem.* **2019**, 7, 167.
- 3. Chen, B., Zhang, C., Wang, W., Chu, Z., Zha, Z., He, X., Zhou, W., Liu, T., Wang, H. and Qian, H. Ultrastable AgBiS₂ hollow nanospheres with cancer cell-specific cytotoxicity for multimodal tumor therapy. *ACS Nano.* **2020**, 14, 14919-14928.
- 4. PS, Rajalakshmi., Alvi, S.B., Begum, N., Veeresh, B. and Rengan, A.K. Self-Assembled Fluorosome–Polydopamine Complex for Efficient Tumor Targeting and Commingled Photodynamic/Photothermal Therapy of Triple-Negative Breast Cancer. *Biomacromolecules*. **2021**, 22, 3926-3940.
- 5. Gayathri, R., Rajalakshmi, P.S., Thomas, A. and Rengan, A.K. Doxorubicin loaded polyvinylpyrrolidone-copper sulfide nanoparticles enabling mucoadhesiveness and chemo-photothermal synergism for effective killing of breast cancer cells. *Materialia*. **2021**, 19, 101195.
- 6. Cheng, J., Wang, W., Xu, X., Lin, Z., Xie, C., Zhang, Y., Zhang, T., Li, L., Lu, Y. and Li, Q. AgBiS₂ nanoparticles with synergistic photodynamic and bioimaging properties for enhanced malignant tumor phototherapy. *Mater. Sci. Eng. C.* **2020**, 107, 110324.
- 7. Zou, L., Wang, H., He, B., Zeng, L., Tan, T., Cao, H., He, X., Zhang, Z., Guo, S. and Li, Y. Current approaches of photothermal therapy in treating cancer metastasis with nanotherapeutics. *Theranostics*. **2016**, 6, 762–772.
- 8. Cheng, K., Zhang, R.Y., Yang, X.Q., Zhang, X.S., Zhang, F., An, J., Wang, Z.Y., Dong, Y., Liu, B., Zhao, Y.D. and Liu, T.C. One-for-all nanoplatform for synergistic mild cascade-potentiated ultrasound therapy induced with targeting imaging-guided photothermal therapy. *ACS Appl. Mater. Interfaces.* **2020**, 12, 40052-40066.
- 9. Khan, M.D., Aamir, M., Sohail, M., Bhoyate, S., Hyatt, M., Gupta, R.K., Sher, M. and Revaprasadu, N. Electrochemical investigation of uncapped AgBiS₂ (schapbachite) synthesized using in situ melts of xanthate precursors. *Dalton Trans.* **2019**, 48, 3714-3722.

- 10. Chen, C., Qiu, X., Ji, S., Jia, C. and Ye, C. The synthesis of monodispersed AgBiS₂ quantum dots with a giant dielectric constant. *CrystEngComm*, **2013**, 15, pp.7644-7648.
- 11. Wang, J., Yang, X., Hu, W., Li, B., Yan, J. and Hu, J. Synthesis of AgBiS₂ microspheres by a templating method and their catalytic polymerization of alkylsilanes. *Chem. Commun.* **2017**, 4931-4933.
- 12. Nakazawa, T., Kim, D., Oshima, Y., Sato, H., Park, J. and Kim, H. Synthesis and Application of AgBiS₂ and Ag₂S Nanoinks for the Production of IR Photodetectors. *ACS Omega.* **2021**, 6, 20710-20718.
- 13. Wen, S., Wu, T., Long, H., Ke, L., Deng, S., Huang, L., Zhang, J. and Tan, S. Mechanism insight into rapid photo-driven sterilization based on silver bismuth sulfide quantum dots. *ACS Appl. Mater. Interfaces.* **2021**, 13, 21979-21993.
- 14. Paul, S., Dalal, B., Jana, R., Shit, A., Datta, A. and De, S.K. Enhanced Photophysical Properties of Bi₂S₃/AgBiS₂ Nanoheterostructures Synthesised via Ag (I) Cation Exchange-Mediated Transformation of Binary Bi₂S₃. *J. Phys. Chem. C.* **2020**, 124, 12824-12833.
- 15. Ganguly, P., Mathew, S., Clarizia, L., Akande, A., Hinder, S., Breen, A. and Pillai, S.C. Theoretical and experimental investigation of visible light responsive AgBiS₂-TiO₂ heterojunctions for enhanced photocatalytic applications. *Appl. Catal.*, *B.* **2019**, 253, 401-418.
- Sugarthi, S., Bakiyaraj, G., Abinaya, R., Navaneethan, M., Archana, J. and Shimomura,
 M. Effect of different growth temperature on the formation of ternary metal chalcogenides AgBiS₂. *Mater. Sci. Semicond. Process.* 2020, 107, 104781.
- 17. Wang, J., Li, L., Yu, H., Guan, F. and Wang, D. Binary–Ternary Bi₂S₃–AgBiS₂ Rod-to-Rod Transformation via Anisotropic Partial Cation Exchange Reaction. *Inorg. Chem.* **2019**, 58, 12998-13006.
- 18. Chen, D., Shen, G., Tang, K., Jiang, X., Huang, L., Jin, Y. and Qian, Y. Microwave synthesis of AgBiS₂ dendrites in aqueous solution. *Inorg. Chem. Commun.* **2003**, 6, 710-712.
- 19. Calva-Yáñez, J.C., Pérez-Valdovinos, O., Reynoso-Soto, E.A., Alvarado-Tenorio, G., Jaramillo-Quintero, O.A. and Rincón, M. Interfacial evolution of AgBiS₂ absorber layer obtained by SILAR method in hybrid solar cells. *J. Phys. D.* **2019**, 52, 125502.

- 20. Xiao-Xue, S.H.I., Xiu-Qi, L.I., Xiao-Ping, W.E.I. and Jian-Ping, L.I. Molecularly imprinted photoelectrochemical sensor based on AgBiS₂/Bi₂S₃ for determination of propoxur. *Chinese J. Anal. Chem.* **2020**, 48, 396-404.
- 21. Cates, N. and Bernechea, M. Research Update: Bismuth-based materials for photovoltaics. *APL Mater.* **2018**, 6, 084503.
- 22. Le Ouay, B. and Stellacci, F. Antibacterial activity of silver nanoparticles: A surface science insight. *Nano Today*, **2015**, 10, 339-354.
- 23. a) Huang, R., Carney, R.P., Stellacci, F. and Lau, B.L. Protein–nanoparticle interactions: the effects of surface compositional and structural heterogeneity are scale dependent. *Nanoscale*. **2013**, 5, 6928-6935. b) Huang, R., Carney, R.P., Ikuma, K., Stellacci, F. and Lau, B.L. Effects of surface compositional and structural heterogeneity on nanoparticle–protein interactions: different protein configurations. *ACS Nano*. **2014**, 8, 5402-5412.
- 24. Eigenheer, R., Castellanos, E.R., Nakamoto, M.Y., Gerner, K.T., Lampe, A.M. and Wheeler, K.E. Silver nanoparticle protein corona composition compared across engineered particle properties and environmentally relevant reaction conditions. *Environ. Sci. Nano.* **2014**, 1, 238-247.
- 25. Lundqvist, M., Stigler, J., Elia, G., Lynch, I., Cedervall, T. and Dawson, K.A. Nanoparticle size and surface properties determine the protein corona with possible implications for biological impacts. *Proc. Natl. Acad. Sci.* **2008**, 105, 14265-14270.
- 26. a) Lara, S., Alnasser, F., Polo, E., Garry, D., Lo Giudice, M.C., Hristov, D.R., Rocks, L., Salvati, A., Yan, Y. and Dawson, K.A. Identification of receptor binding to the biomolecular corona of nanoparticles. *ACS Nano*, 2017, 11, 1884-1893. b) Herda, L.M., Hristov, D.R., Lo Giudice, M.C., Polo, E. and Dawson, K.A. Mapping of molecular structure of the nanoscale surface in bio nanoparticles. *J. Am. Chem. Soc.* 2017, 139, 111-114. c) Lo Giudice, M.C., Herda, L.M., Polo, E. and Dawson, K.A. In situ characterisation of nanoparticle biomolecular interactions in complex biological media by flow cytometry. *Nat. Commun.* 2016, 7, 13475.
- 27. a) Joseph, A., Billakanti, S., Pandit, M.A., Khatun, S., Rengan, A.K. and Muralidharan, K. Impact of bandgap tuning on ZnS for degradation of environmental pollutants and disinfection. *Environ. Sci. Pollut. Res.* 2022, 29, 56863-56875. b) Srinivas, B., Pandit, M.A. and Muralidharan, K. Importance of clean surfaces on the catalyst: SnS₂ nanorings for environmental remediation. *ACS Omega.* 2019, 4, 14970-14980. c) Kumar, B.G. and Muralidharan, K. Hexamethyldisilazane-assisted synthesis of indium

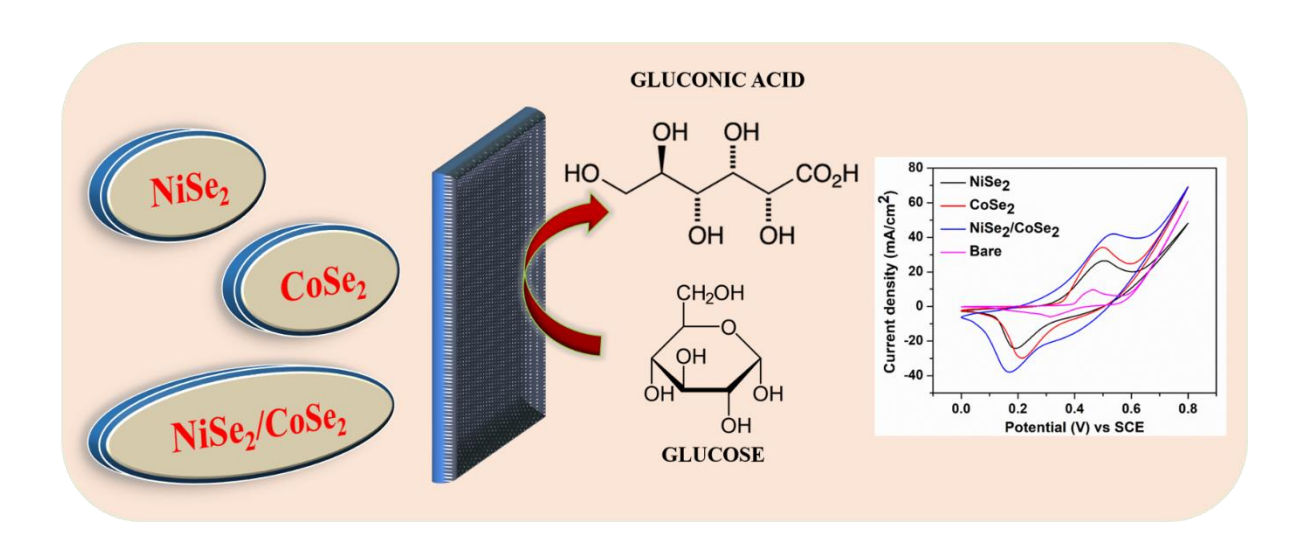
- sulfide nanoparticles. *J. Mater. Chem.* **2011**, 21, 11271-11275. d) Kumar, B.G. and Muralidharan, K. Organic-Free Self-Assembled Copper Sulfide Microflowers. *Eur. J. Inorg. Chem.* **2013**, 2013, 2102-2108.
- 28. Wang, L., Hu, C. and Shao, L. The antimicrobial activity of nanoparticles: present situation and prospects for the future. *Int. J. Nanomedicine*. **2017**, 12, 1227–1249.
- 29. Seil, J.T. and Webster, T.J. Antimicrobial applications of nanotechnology: methods and literature. *Int. J. Nanomedicine*. **2012**, 7, 2767–2781.
- 30. Feng, Q.L., Wu, J., Chen, G.Q., Cui, F.Z., Kim, T.N. and Kim, J.O. A mechanistic study of the antibacterial effect of silver ions on Escherichia coli and Staphylococcus aureus. *J. Biomed. Mater. Res.* **2000**, 52, 662-668.
- 31. Pal, S., Tak, Y.K. and Song, J.M. Does the antibacterial activity of silver nanoparticles depend on the shape of the nanoparticle? A study of the gram-negative bacterium Escherichia coli. *Appl. Environ. Microbiol.* **2007**, 73, 1712-1720.
- 32. Cheon, J.Y., Kim, S.J., Rhee, Y.H., Kwon, O.H. and Park, W.H. Shape-dependent antimicrobial activities of silver nanoparticles. *Int J Nanomedicine*. **2019**, 14, 2773–2780.
- 33. a) Sudha, M. and Rajarajan, M. Deactivation of photocatalytically active ZnO nanoparticle by surface capping with polyvinyl pyrrolidone. *J. Appl. Chem.* **2013**, 3, 45-53. b) Sudha, M., Senthilkumar, S., Hariharan, R., Suganthi, A. and Rajarajan, M. Controlled reduction of the deleterious effects of photocatalytic activity of ZnO nanoparticles by PVA capping. *J. Sol-Gel Sci. Technol.* **2011**, 61, 14-22. c) Sudha, M., Senthilkumar, S., Hariharan, R., Suganthi, A. and Rajarajan, M. Synthesis, characterisation and study of photocatalytic activity of surface modified ZnO nanoparticles by PEG capping. *J. Sol-Gel Sci. Technol.* **2013**, 65, 301-310.
- 34. Cao, Z. and Zhang, Z. Deactivation of photocatalytically active ZnO nanoparticle and enhancement of its compatibility with organic compounds by surface-capping with organically modified silica. *Appl. Surf. Sci.* **2011**, 257, 4151-4158.
- 35. Chandran, P., Netha, S. and Khan, S.S. Effect of humic acid on photocatalytic activity of ZnO nanoparticles. *J. Photochem. Photobiol. B, Biol.* **2014**, 138, 155-159.
- 36. Akhil, K., Jayakumar, J., Gayathri, G. and Khan, S.S. Effect of various capping agents on photocatalytic, antibacterial and antibiofilm activities of ZnO nanoparticles. *J. Photochem. Photobiol. B, Biol.* **2016**, 160, 32-42.
- 37. Singla, M.L. and Kumar, M. Optical characterisation of ZnO nanoparticles capped with various surfactants. *J. Lumin.* **2009**, 129, 434-438.

- 38. Hong, R.Y., Li, J.H., Chen, L.L., Liu, D.Q., Li, H.Z., Zheng, Y. and Ding, J.J.P.T. Synthesis, surface modification and photocatalytic property of ZnO nanoparticles. *Powder Technol.* **2009**, 189, 426-432.
- 39. Yao, F., Jiang, L., Qi, Y., Li, R., Li, Y., Xu, Y., Liu, H. and Lin, Q. Chemical bath deposition of AgBiS₂ films for visible and X-ray detection. *Appl. Mater. Today.* **2022**, 26, 101262.
- 40. Mandal, A., Meda, V., Zhang, W.J., Farhan, K.M. and Gnanamani, A. Synthesis, characterisation and comparison of antimicrobial activity of PEG/TritonX-100 capped silver nanoparticles on collagen scaffold. *Colloids Surf. B: Biointerfaces.* **2012**, 90, 191-196.
- 41. Jose, A., Devi, K.S., Pinheiro, D. and Narayana, S.L. Electrochemical synthesis, photodegradation and antibacterial properties of PEG capped zinc oxide nanoparticles. *J. Photochem. Photobiol. B, Biol.* **2018**, 187, 25-34.
- 42. Catauro, M., Renella, R.A., Papale, F. and Ciprioti, S.V. Investigation of bioactivity, biocompatibility and thermal behaviour of sol–gel silica glass containing a high PEG percentage. *Mater. Sci. Eng. C.* **2016**, 61, 51-55.
- 43. Chirife, J., Herszage, L., Joseph, A., Bozzini, J.P., Leardini, N. and Kohn, E.S. In vitro antibacterial activity of concentrated polyethylene glycol 400 solutions. *Antimicrob. Agents Chemother.* **1983**, 24, 409-412.
- 44. Javed, R., Sajjad, A., Naz, S., Sajjad, H. and Ao, Q. Significance of capping agents of colloidal nanoparticles from the perspective of drug and gene delivery, bioimaging, and biosensing: an insight. *Int. J. Mol. Sci.* **2022**, 23, 10521.
- 45. Bastos, V., de Oliveira, J.F., Brown, D., Jonhston, H., Malheiro, E., Daniel-da-Silva, A.L., Duarte, I.F., Santos, C. and Oliveira, H. The influence of Citrate or PEG coating on silver nanoparticle toxicity to a human keratinocyte cell line. *Toxicol. Lett.* **2016**, 249, 29-41.
- 46. Cabral, R.M. and Baptista, P.V. The chemistry and biology of gold nanoparticle-mediated photothermal therapy: promises and challenges. *Nano Life*. **2013**, 3, 1330001.
- 47. Zhang, Y., Zhan, X., Xiong, J., Peng, S., Huang, W., Joshi, R., Cai, Y., Liu, Y., Li, R., Yuan, K. and Zhou, N. Temperature-dependent cell death patterns induced by functionalized gold nanoparticle photothermal therapy in melanoma cells. *Sci. Rep.* **2018**, 8, 8720.

- 48. Li, X., Lovell, J.F., Yoon, J. and Chen, X. Clinical development and potential of photothermal and photodynamic therapies for cancer. *Nat. Rev. Clin. Oncol.* **2020**, 17, 657-674.
- 49. Yeshchenko, O.A., Dmitruk, I.M., Alexeenko, A.A., Kotko, A.V., Verdal, J. and Pinchuk, A.O. Size and temperature effects on the surface plasmon resonance in silver nanoparticles. *Plasmonics*, **2012**, 7, 685-694.
- 50. Pattani, V.P. and Tunnell, J.W. Nanoparticle-mediated photothermal therapy: A comparative study of heating for different particle types. *Lasers Surg Med.* **2012**, 44, 675-684.
- 51. Sánchez López de Pablo, C., Olmedo, J.J.S., Rosales, A.M., Ramírez Hernández, N. and del Pozo Guerrero, F. A method to obtain the thermal parameters and the photothermal transduction efficiency in an optical hyperthermia device based on laser irradiation of gold nanoparticles. *Nanoscale Res. Lett.* **2014**, 9, 1-7.
- 52. Brüningk, S.C., Rivens, I., Box, C., Oelfke, U. and Ter Haar, G. 3D tumour spheroids for the prediction of the effects of radiation and hyperthermia treatments. *Sci. Rep.* **2020**, 10, 1653.
- 53. Appidi, T., Pemmaraju, D.B., Khan, R.A., Alvi, S.B., Srivastava, R., Pal, M., Khan, N. and Rengan, A.K. Light-triggered selective ROS-dependent autophagy by bioactive nanoliposomes for efficient cancer theranostics. *Nanoscale*. **2020**, 12, 2028-2039.
- 54. Iftekhar Hossain, M., Edwards, J., Tyler, J., Anderson, J. and Bandyopadhyay, S. Antimicrobial properties of nanorods: killing bacteria via impalement. *IET Nanobiotechnol.* **2017**, 11,501-505.
- 55. Morones, J.R., Elechiguerra, J.L., Camacho, A., Holt, K., Kouri, J.B., Ramírez, J.T. and Yacaman, M.J. The bactericidal effect of silver nanoparticles. *Nanotechnology*, **2005**, 16, 2346.

Chapter 5

Synthesis of surfactant free NiSe₂, CoSe₂ and NiSe₂/CoSe₂ for Non-Enzymatic Glucose Sensing



Abstract

A stable, sensitive, and efficient material is indispensable for measuring glucose content precisely. This chapter describes the synthesis of surfactant-free NiSe₂ (sf-NiSe₂), CoSe₂ (sf-CoSe₂), and composite NiSe₂/CoSe₂ (sf-NiSe₂/CoSe₂) using hexamethyldisilazane (HMDS) - assisted method and their utility as non-enzymatic glucose sensors. Detailed structural and morphological characterization was performed using the X-ray diffraction technique, UV-Visible spectroscopy, Scanning Electron Microscopy (SEM), and Transmission Electron Microscope (TEM). We have investigated the electrocatalytic oxidation abilities of synthesised materials for non-enzymatic glucose sensing. The findings demonstrated the efficacy and sensing capabilities of the synthesised materials for the electrochemical detection of glucose. The composite sf-NiSe₂/CoSe₂ showed a higher electrochemical response with long-term stability and good anti-interference ability than individual materials. This material showed a limit of detection of 0.0588 mM, a sensitivity of 0.0576 mAmM⁻¹cm⁻² and a quick response time of 0.603 s. This observation showed the great potential of sf-NiSe₂/CoSe₂ electrode material as non-enzymatic glucose sensors. This work could introduce a new material for realizing an affordable and dependable electrochemical glucose sensor platform.

5.1. Introduction

According to World Health Organization and International Diabetes Federation, 53.7 crore people have diabetes and expect 64.3 crore by 2030. Diabetes is a severe chronic disease and a major cause of impairment and fatalities, along with its long-term complications brought on by high blood glucose levels, including cardiovascular disease, retinopathy, neuropathy, nephropathy, amputation, hypertension, and hyperlipidemia. Therefore, evaluation and treatment of glucose levels is essential. The two methods involved in glucose detection are electrochemical and analytical detection methods. Compared to analytical detection methods such as optical, chromatographic, colourimetric etc., electrochemical detection methods dominate by their low cost, high sensitivity, accuracy, portable and easy fabrication advantages. The electrochemical methods for detecting glucose are categorized into enzymatic and non-enzymatic techniques [1, 2]. Enzymatic glucose sensors rely on the catalytic process of an immobilized enzyme in which the methodical and rapid renaissance of the enzyme is the primary criterion [3]. These methods have limitations due to the vulnerability of enzymes towards temperature, pH, humidity, and chemical substances, their high cost, and low stability. In contrast, non-enzymatic glucose sensors with advantages such as easy fabrication, high chemical and thermal stability, reproducibility, and low cost are well-studied these days [1, 2, 31.

Metals including Pd, Pt, Au, oxides, sulphides, and selenides of Mn, Fe, Co, Ni, Cu, and Zn, bimetallic systems have been widely investigated for glucose oxidation. Further, carbon materials and polymers have also been tested. Among all these materials, NiSe₂ is an effective candidate for electron transfer-assisted sensing applications owing to its unique physical, optical, and electrochemical features such as excellent carrier mobility and large surface-to-volume ratio, its low toxicity, narrow bandgap, inherent electrical conductivity and resistance to chloride poisoning [4]. Also, CoSe₂ has attracted attention due to its fast electron transfer ability, which makes it advantageous material for sensing applications [5, 6]. Many methods, such as hydrothermal or solvothermal, solution chemical process, electrodeposition, pyrolysis etc., are employed to prepare NiSe₂ and CoSe₂. Most of which involve the use of organic surfactants, multistep procedures, higher temperatures and time-consuming [7, 8]. Furthermore, using capping materials lower the electrochemical properties due to their insulating properties.

As discussed in previous chapters, we are using hexamethyldisilazane (HMDS) assisted methods to avoid the complexities and synthesise surfactant-free nanoparticles with benefits such as a high level of purity, good uniformity, high crystallinity, and low processing temperature [9]. Ni foam is frequently used as a conductive substrate because of its wide electrochemical active surface area and porous structure [10]. Therefore, we have synthesised surfactant-free NiSe₂ (sf-NiSe₂), (sf-CoSe₂), and NiSe₂/CoSe₂ (sf-NiSe₂/CoSe₂) composite and employed them for non-enzymatic glucose sensing by coating it on Ni foam. Therefore, the combined properties of both materials can be used for constructing an enhanced sensitive non-enzymatic glucose sensor. This method helped increase material conductivity, offered excellent electrochemical activity, and avoided structural collapse. The results highlighted that the synthesised materials could perform excellently in electrochemical glucose sensing. This study provides a new approach to enhance the performance of sf-NiSe₂, sf-CoSe₂ and sf-NiSe₂/CoSe₂ materials and is also expected to affect diagnosis positively.

5.2. Experimental

5.2.1. Materials required

Nickel chloride (NiCl₂), Cobalt chloride (CoCl₂), Selenium powder, Sodium hydroxide (NaOH), Sodium borohydride (NaBH₄), hexamethyldisilazane (HMDS) were purchased from Sigma Aldrich. The characterisation of samples is done as described in Chapter 2.

5.2.2. Preparation of Selenide solution

Selenium powder (200 mg, 2.53 mmol) was added slowly and carefully to the mixture containing sodium hydroxide (50 mg, 1.25 mmol) and sodium borohydride (100 mg, 1.25 mmol) in 2 ml DI water. This solution was stirred for 1 h under nitrogen atmosphere.

5.2.3. Preparation of sf-NiSe₂, sf-CoSe₂ and sf-NiSe₂/CoSe₂ composite by HMDS-assisted method

NiCl₂ (200 mg, 1.54 mmol) was mixed with excess hexamethyldisilazane (HMDS) in a pressure tube under a nitrogen atmosphere. The selenide solution was injected into this mixture and heated to 180 °C for 12 h. At the end of the reaction, a high vacuum was applied to eliminate excess HMDS and other gaseous side products. The residue was washed repeatedly with acetone and ethanol. The obtained product (sf-NiSe₂) was dried in an oven at 70 °C for 24 h. We followed the same procedure to prepare sf-CoSe₂ using CoCl₂ (200 mg, 1.54 mmol) as the metal source. To prepare sf-NiSe₂/CoSe₂, 100 mg each of sf-NiSe₂ and sf-CoSe₂ were

taken and pulverized for 5 min in mortar. The reaction condition and work-up procedures were the same as above.

5.2.4. Electrochemical measurements

Electrochemical measurements were performed in CHI6112E electrochemical workstation at room temperature using a three-electrode system using synthesised nanoparticles coated Ni foam, saturated calomel electrode and platinum spiral wire as working, reference and counter electrode, respectively. To prepare the working electrode, 5 mg of synthesised catalyst was added into 1 ml of ethanol and sonicated for 30 min to get a homogenous solution. This solution was then drop-casted on purified Ni foam 2-3 times and dried in an oven at 80 °C overnight. Electrochemical analyses like Cyclic Voltammetry (CV), Electrochemical impedance spectroscopy (EIS), and Chronoamperometry techniques were performed at room temperature in 0.5 M KOH solution.

5.3. Results and Discussion

5.3.1. Preparation and characterisation of sf-NiSe2, sf-CoSe2 and sf-NiSe2/CoSe2

The non-enzymatic glucose sensors work based on the electrochemical principles where electron movement is essential. The presence of insulating organic molecules as capping agents is expected to influence the sensing ability of the materials. As discussed in the previous chapters, to take advantage of surfactant-free surfaces on the catalyst, we have prepared sf-NiSe2, sf-CoSe2 (Scheme 5.1) and sf-NiSe2/CoSe2 composites via HMDS-assisted synthetic method (Scheme 5.2). As expected, this method yielded pure metal selenides and composite material in simple procedures. Though sf-NiSe2 and sf-CoSe2 were reported earlier, the glucose sensing application of sf-NiSe2/CoSe2 composite is unknown until now.

$$MCl_2$$
 + Se powder MSe_2
 $M = Ni, Co$

MSe₂

Scheme 5.1. Preparation of sf-NiSe₂, sf-CoSe₂.

$$\begin{array}{ccc} NiCl_2 + CoCl_2 & \xrightarrow{\quad Pulverization \quad \\ \quad 1 & : \quad 1 & \\ \end{array} \qquad \begin{array}{c} Pulverization \\ \hline \qquad R.T & \\ \end{array}$$

Scheme 5.2. Preparation of sf-NiSe₂/CoSe₂ composite

The prepared samples were analysed by powder X-ray diffraction pattern (PXRD). The PXRD spectrum of **sf-NiSe**² (figure 5.1) confirmed the formation of NiSe² (JCPDS-88-1711) with peaks at 29.9°, 33.6°, 36.9°, 42.8°, 50.7°, 55.5°, 57.8°, 62.2°, 72.6°, 74.6°, 84.3°, and 88.2° indicating (200), (210), (211), (220), (311), (023), (321), (400), (421), (332), (511), and (234) planes [11, 12]. The PXRD of CoSe² (JCPDS-09-234) showed peaks 33.7°, 45.2°, 51.5°, 63.1°, and 72.0° indicating (210), (221), (311), (400), and (024) planes [13]. The major peaks and SAED pattern of NiSe² indicated the formation of cubic pyrite-phase [14]. The PXRD peaks and SAED pattern of CoSe² confirmed the formation of the cubic phase [15]. These findings illustrate that NiSe² and CoSe² were successfully prepared. In the PXRD pattern of the NiSe²/CoSe² composite, we observed the diminishing of peaks at 36.9°; otherwise, all other peaks were a combination of **sf-NiSe²** and **sf-CoSe²** peaks.

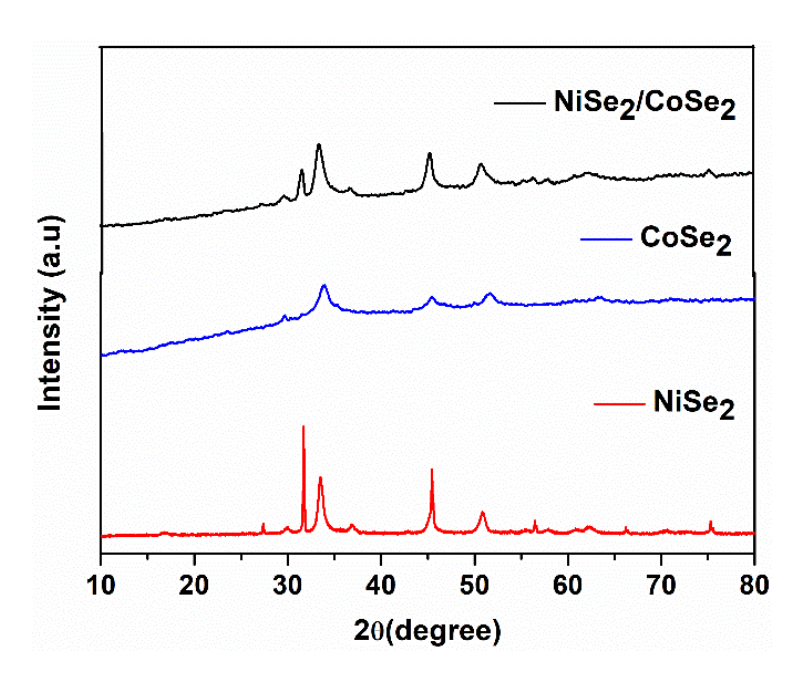


Figure 5.1. PXRD pattern of sf-NiSe₂, sf-CoSe₂, sf-NiSe₂/CoSe₂ nanoparticles.

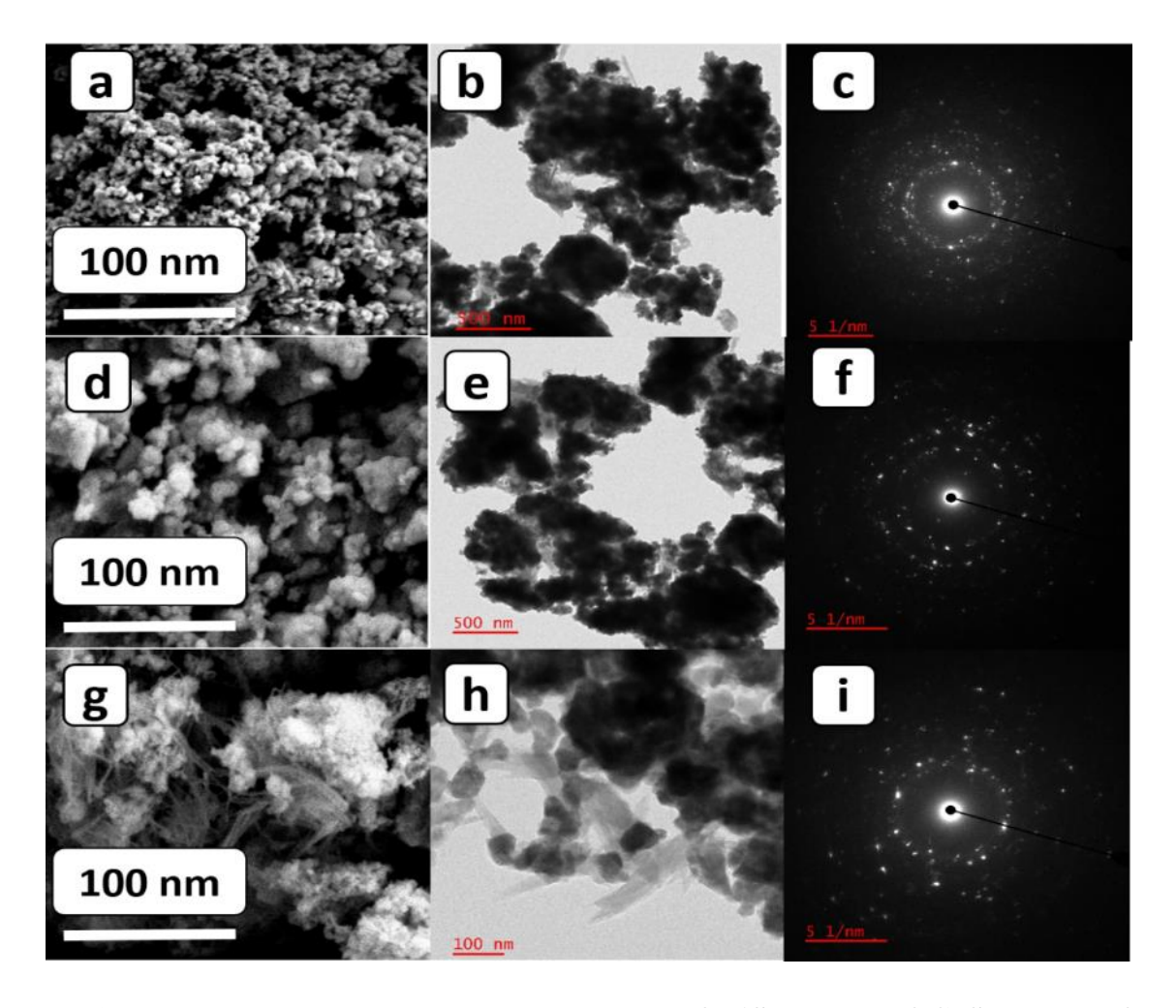


Figure 5.2. FE-SEM, TEM image and SAED pattern of **sf-NiSe**₂ (a,b,c), **sf-CoSe**₂ (d,e,f), **sf-NiSe**₂/**CoSe**₂ (g, h, i) nanoparticles, respectively.

Figure 5.2. shows the morphologies of **sf-NiSe**₂, **sf-CoSe**₂ and **sf-NiSe**₂/**CoSe**₂, where **sf-NiSe**₂ and **sf-CoSe**₂ exhibited spherical morphologies whereas **sf-NiSe**₂/**CoSe**₂ composite material have fibrous structure connecting the spheres. The elemental mapping is shown in Figure 5.3 and confirmed the presence of Ni, Co, Se and combination in **sf-NiSe**₂/**CoSe**₂ composite. The bandgap of each material was calculated from the absorption spectra as shown in Figure 5.4 and found to be 0.807 eV,0.77 eV, and 0.729 eV for **sf-NiSe**₂, **sf-CoSe**₂ and **sf-NiSe**₂/**CoSe**₂ respectively.

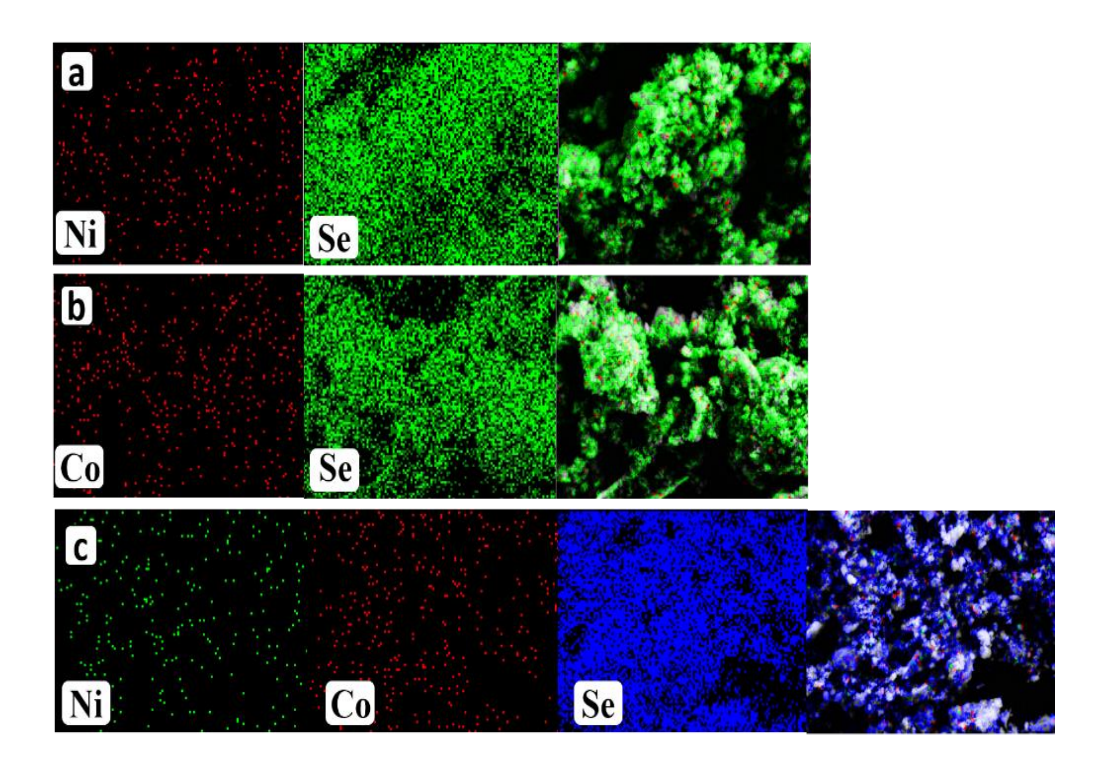


Figure 5.3. EDS elemental mapping of a) sf-NiSe₂, b) sf-CoSe₂ and c) sf-NiSe₂/CoSe₂, respectively.

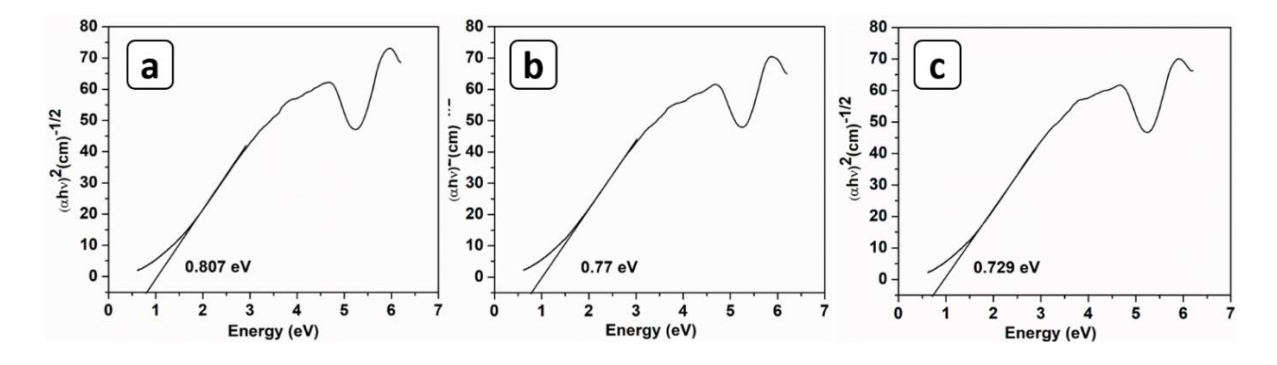


Figure 5.4. Bandgap calculations of a) sf-NiSe₂, b) sf-CoSe₂ and c) sf-NiSe₂/CoSe₂ respectively.

5.3.2 Surface area of sf-NiSe₂, sf-CoSe₂ and sf-NiSe₂/CoSe₂ composite materials

The most important factor in assessing the catalytic ability of catalysts is their active surface area. It is well-known that the larger the surface area better the catalytic activity. The rationale is that a substance with a large surface area will have an adequate number of active sites that will result in maximal adsorption, leading to enhanced catalytic activity. The N₂ adsorption-desorption isotherm curves in Figure 5.5 (a, b, c) showed that all materials followed type III isotherm. The isotherm displayed an exquisite interface between the adsorbent and the adsorbed layer, indicating an effective interaction and demonstrating multilayer adsorption. sf-

NiSe2, **sf-CoSe2** and **sf-NiSe2/CoSe2** had a specific surface area of 17.65 m²/g, 21.24 m²/g, and 26.29 m²/g respectively. According to BJH pore size distributions (Figure 5.5. d, e, f), the average pore sizes of **sf-NiSe2**, **sf-CoSe2** and **sf-NiSe2/CoSe2** were around 1.7 nm, 1.95 nm, 1.56 nm. It is evident from the values that the samples were microporous. The whole surface area of materials was available for catalytic action because no other organic surfactant molecules were in their immediate vicinity [9d].

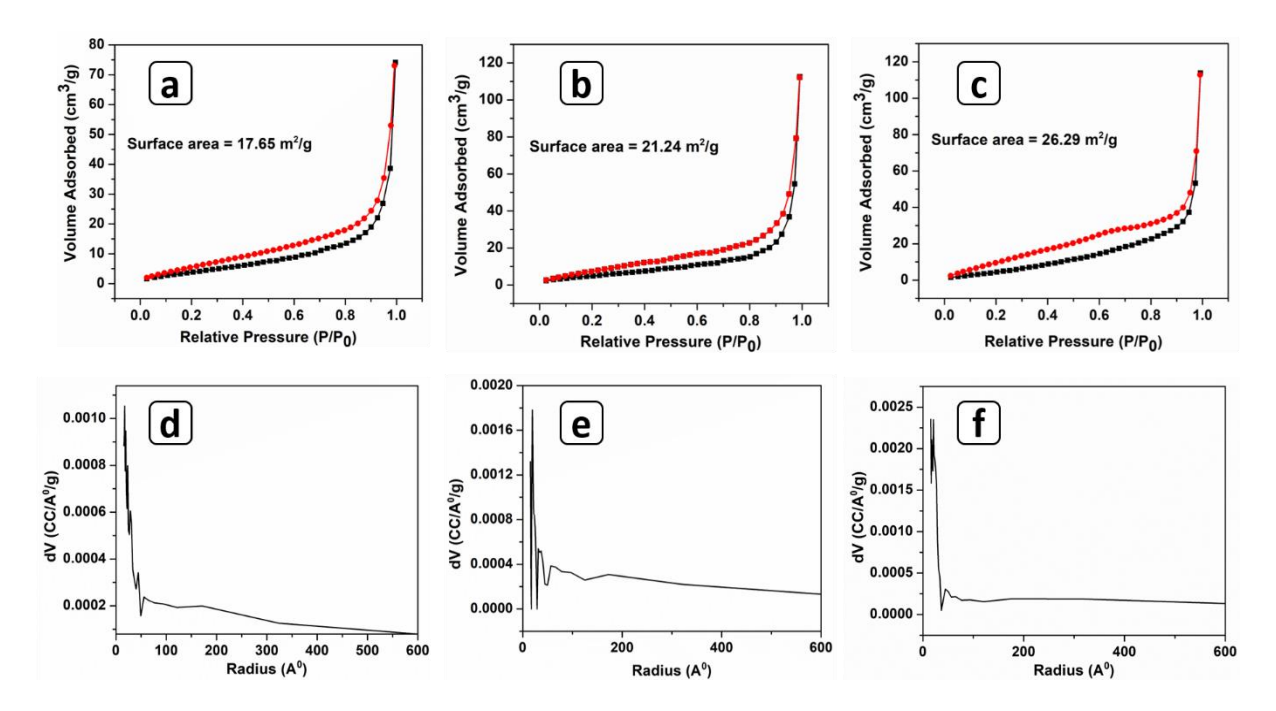


Figure 5.5. Nitrogen adsorption—desorption curves (a,b, and c) of a) sf-NiSe₂, b) sf-CoSe₂ and c) sf-NiSe₂/CoSe₂ and BJH pore size distribution plot of d) sf-NiSe₂, e) sf-CoSe₂ and f) sf-NiSe₂/CoSe₂ respectively.

5.3.3. Electrochemical non-enzymatic detection of glucose using sf-NiSe₂, sf-CoSe₂ and sf-NiSe₂/CoSe₂

Electrochemical activities of the modified electrocatalyst were investigated in 0.1 M KCl solution containing 5 mM potassium ferricyanide (K₃[Fe(CN)₆]). In Cyclic voltammetry (Figure 5.6 a), a well-defined pair of redox peaks with an anodic peak at 0.24 V and cathodic peak at 0.16 V with a peak-to-peak separation of 0.08 V observed for **sf-NiSe₂/CoSe₂** composite material indicating the quasi-reversible redox reaction. While for **sf-NiSe₂** and **sf-CoSe₂** materials, no proper redox peaks or higher peak-to-peak separations were observed. These observations demonstrated the better catalytic activity of the **sf-NiSe₂/CoSe₂** composite material. EIS measurements were also performed in the frequency range of 100 KHz to 100 mHz with an amplitude of 10 mV (Figure 5.6 b). The Nyquist plots showed that **sf-NiSe₂/CoSe₂**

composite has a lower semicircle diameter than **sf-NiSe**₂ and **sf-CoSe**₂ materials, implying a lower electron transfer resistance at the electrolyte/electrode surface. Furthermore, **sf-NiSe**₂/**CoSe**₂ composite material exhibits characteristics spectra in the high-frequency region due to its electron transfer controlled process [2].

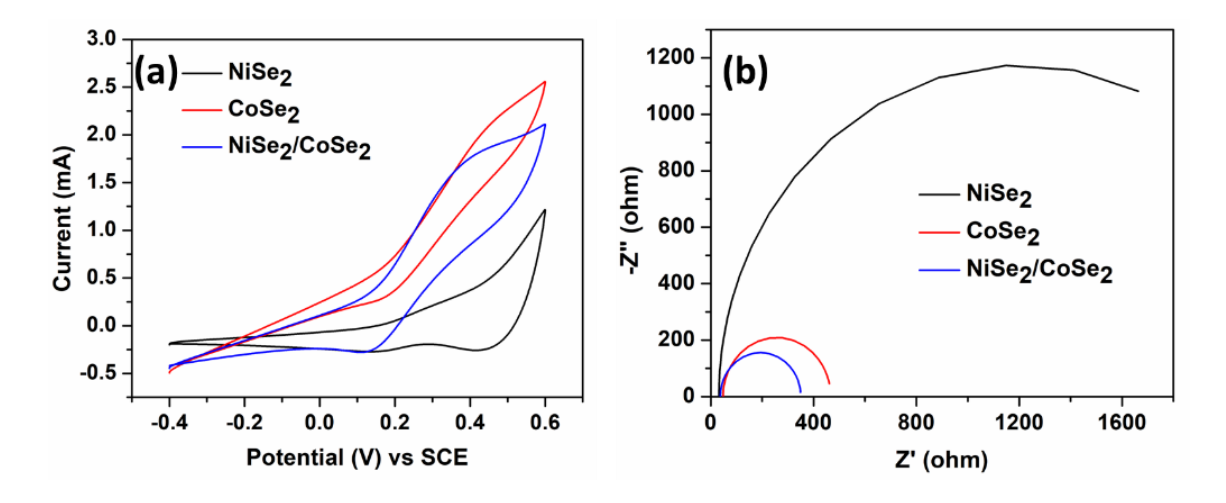


Figure 5.6. (a) Cyclic voltammograms and (b) EIS spectra of **sf-NiSe₂**, **sf-CoSe₂**, **sf-NiSe₂/CoSe₂**, in 0.10 M KCl containing 5.0 mM K₃[Fe (CN)₆] at a scan rate of 50 mV s⁻¹.

Cyclic voltammetry was performed to demonstrate the response of electrodes in glucose sensing. Figure 5.7 illustrates the current response of each electrode with and without 0.1 mM glucose addition in 0.5 M KOH within the potential range of 0 to 0.8 V at a scan rate of 50 mV/s. In Figure 5.7 a, b and c, it can be seen that all three electrodes showed redox peaks even in the absence of glucose. These peaks were due to the oxidation and reduction of electrode materials (catalyst coated on Ni sponge). The shift in the oxidation peak in the voltammogram of the catalyst in pure KOH solution and solution where glucose is added represents the current response with respect to the oxidation of glucose. This observation means that quick and complete oxidation of glucose would be responded to as more change in the oxidation peak, i.e., good sensing ability. From Figure 5.7d, it can be clearly noted that sf-NiSe2/CoSe2 showed a higher current response compared to sf-NiSe2 and sf-CoSe2, explaining the good electrochemical sensing capability of sf-NiSe2/CoSe2 composite material towards electro-oxidation of glucose. This increased response might be due to the higher surface area (ref: Section 5.3.2) of composite materials, which increased the chances of adsorption and oxidation.

The whole mechanism can be explained according to Incipient Hydrous Oxide Adatom Mediator (IHOAM) Model, as depicted below.

$$MSe_2 + OH_{medium}^- \rightleftharpoons MSe_2OH + e^-$$
, where $M^{2+} \rightleftharpoons M^{3+} + e^-$,

Here the oxidation and reduction of metal centres happen in which the oxidation peak current is due to the oxidation of metal and reduction peaks due to the reduction of metals. After the addition of glucose, there is an enhancement in the current response, which can be explained as:

$$MSe_2OH$$
 + $C_6H_{12}O_6$ \rightarrow $C_6H_{12}O_7$ + MSe_2 + $2H_2O$ glucose gluconic acid

The MSe₂OH species formed by the oxidation of metal centres will act as an oxidizing species (oxidizing agent) and helps in the oxidation of glucose to Gluconic acid, where the species itself will undergo reduction to form MSe₂ material back. This species again undergoes oxidation and releases electrons, which increases the oxidation current. And this cycle continues [10, 16].

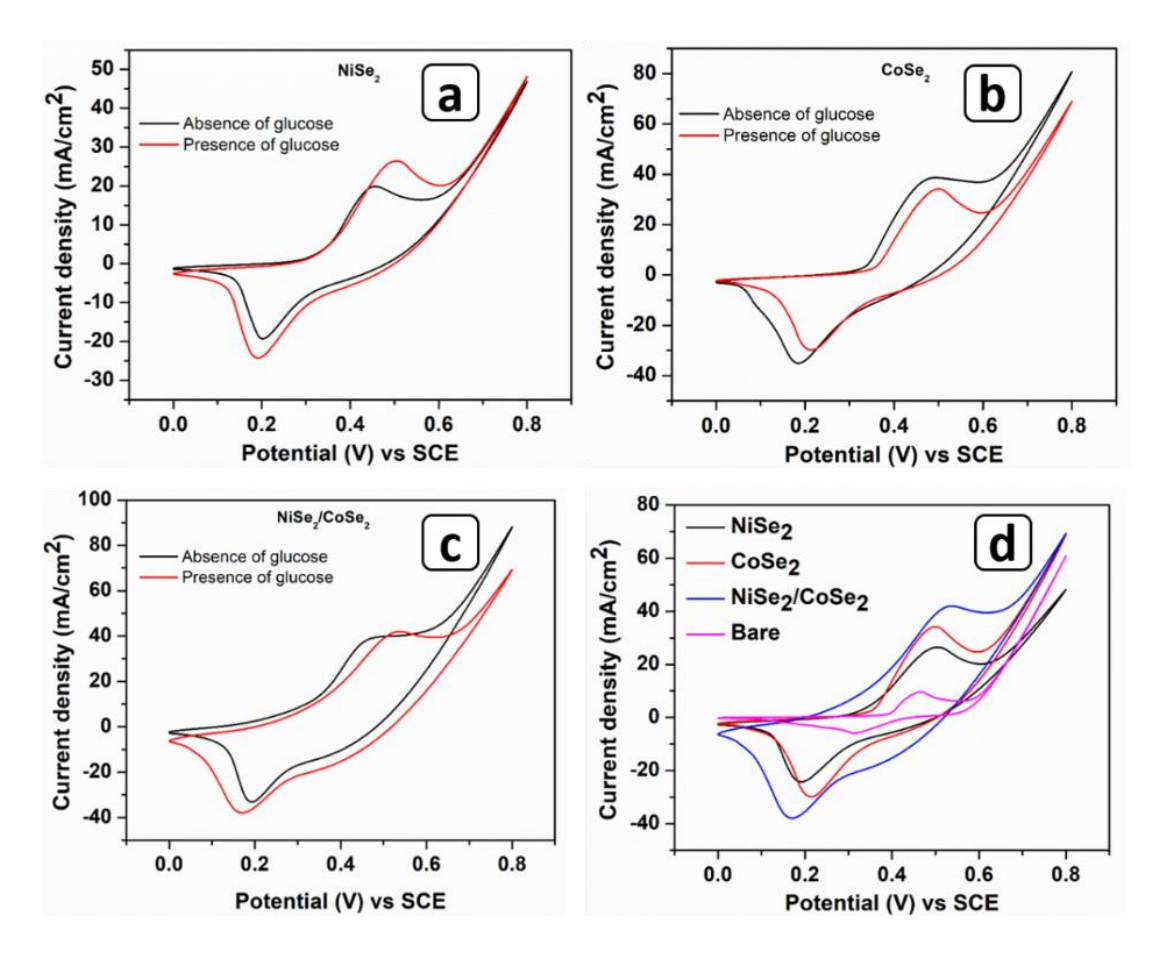


Figure 5.7. Cyclic voltammograms of a) **sf-NiSe₂**, b) **sf-CoSe₂**, c) **sf-NiSe₂/CoSe₂**, before and after 0.1 mM glucose addition and d) merged responses of each electrode and bare after the addition of 0.1 mM glucose in 0.5 M KOH solution, scan rate: 50 mV/s.

The dependence of anodic peak current on scan rate for sf-NiSe₂, sf-CoSe₂, and sf-NiSe₂/CoSe₂ was studied by recording the CV at different scan rates in 0.5 M KOH solution with 0.1 mM glucose (Figure 5.8 a, b and c). The study showed that as the scan rate increased, the oxidation peak current shifted towards the positive region while the reduction peak shifted in the negative direction. This shift demonstrated the quick and reversible redox reactions at the electrode-electrolyte interface, referring to the low resistance of electrode materials. The shape of the voltammograms was consistent across all scanning rates, indicating that the reaction was reversible and further established the reversibility of the catalytic oxidation of glucose by sf-NiSe₂, sf-CoSe₂, and sf-NiSe₂/CoSe₂ [10]. In addition to that, the peak current was directly proportional to the scan rate (figure 5.8 d, e, f) with correlation coefficients of 0.9873, 0.9906, and 0.9958 for sf-NiSe₂, sf-CoSe₂, and sf-NiSe₂/CoSe₂ respectively [17], This observation established that the electro-oxidation of glucose was diffusion controlled, which is preferred for an ideal detection of glucose [3, 16].

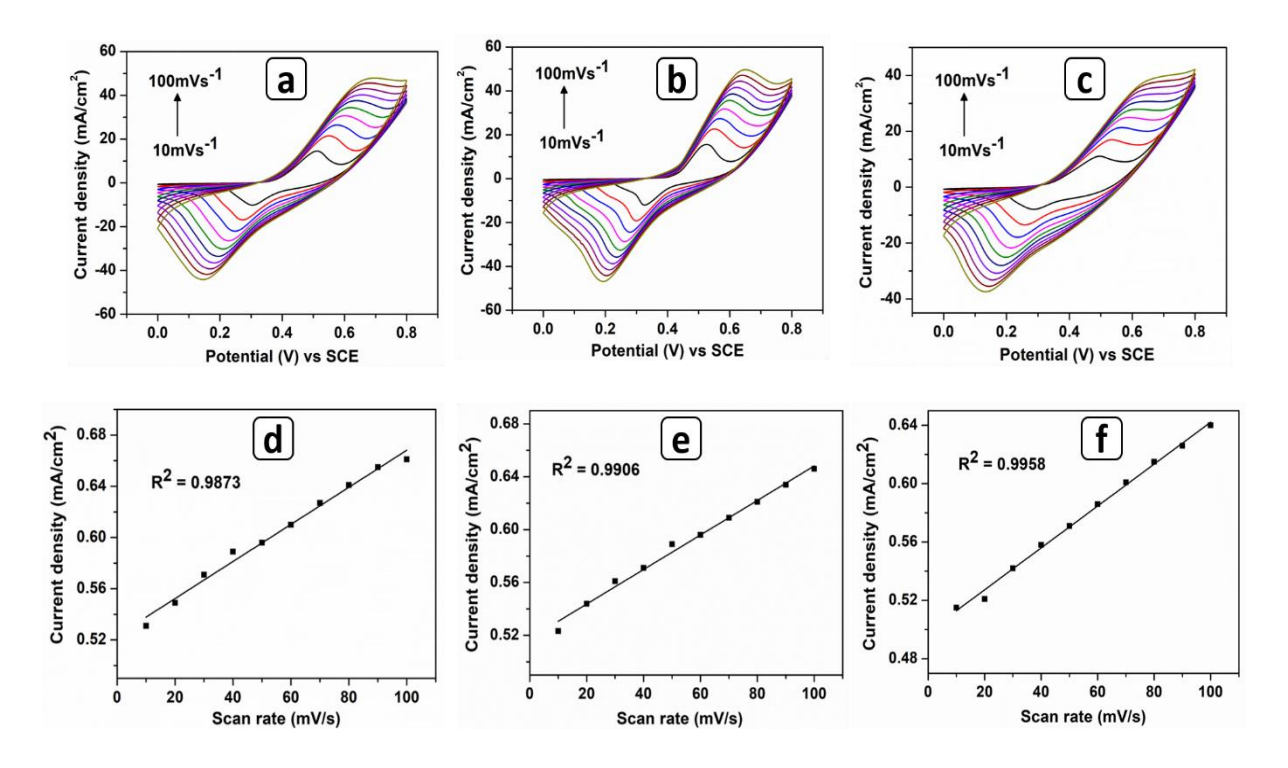


Figure 5.8. CV of a) **sf-NiSe**₂, b) **sf-CoSe**₂, c) **sf-NiSe**₂/**CoSe**₂ electrodes at different scan rate from 10 to 100 mVs⁻¹ and plot of peak current versus scan rate for d) **sf-NiSe**₂, e) **sf-CoSe**₂, f) **sf-NiSe**₂/**CoSe**₂ electrodes with 1 mM glucose in 0.5 M KOH.

The effect of glucose concentration on performance by sf-NiSe₂, sf-CoSe₂, and sf-NiSe₂/CoSe₂ electrodes was studied by CV measurements (figure 5.9). There was a rise in anodic and cathodic peak currents with an increase in the glucose concentration from 0.1 mM

to 1 mM. This rise proved that all three electrodes favored glucose oxidation with a correlation coefficient of 0.9948, 0.9964, and 0.9970 for **sf-NiSe₂**, **sf-CoSe₂**, and **sf-NiSe₂/CoSe₂**. The limit of detection and sensitivity was calculated from the linear plots of Figure 5.9. (d, e, f) and the results are tabulated in Table 5.1. The data (Table 5.1) established that **sf-NiSe₂/CoSe₂** showed higher sensitivity and lower detection limits than **sf-NiSe₂** and **sf-CoSe₂**. Also, the Ni foam on which the materials were coated increased the conductivity due to its charge transfer ability [2, 16].

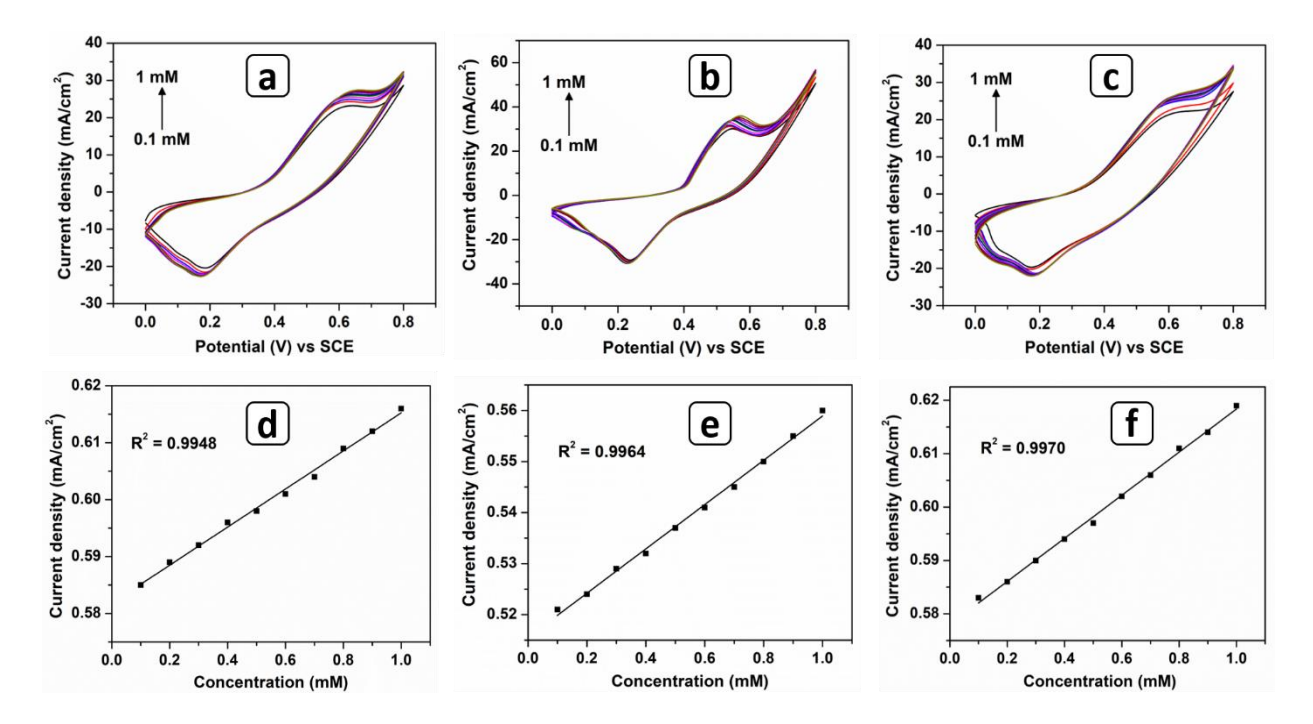


Figure 5.9. CV of a) **sf-NiSe₂**, b) **sf-CoSe₂**, c) **sf-NiSe₂/CoSe₂** electrodes at different glucose concentrations and plot of peak current versus concentration for d) **sf-NiSe₂**, e) **sf-CoSe₂**, f) **sf-NiSe₂/CoSe₂** electrodes in 0.5 M KOH at a scan rate of 50 mVs⁻¹.

Material	Limit of Detection	Sensitivity
Wateriai	(mM)	(mA/mM cm ²)
NiSe ₂	0.08716	0.0495
CoSe ₂	0.0655	0.0619
NiSe ₂ /CoSe ₂	0.0588	0.0896

Table 5.1. Limit of detection and Sensitivity of sf-NiSe2, sf-CoSe2, and sf-NiSe2/CoSe2 as calculated.

Long-term stability is crucial for sensors, which was examined by measuring up to 200 cycles of **sf-NiSe₂**, **sf-CoSe₂** and **sf-NiSe₂/CoSe₂** electrodes in 0.1 mM glucose in 0.5 M KOH solution. As illustrated in Figure 5.12, all electrodes showed good stability up to 200 cycles. Higher stability was shown by the **sf-NiSe₂/CoSe₂** composite electrode, which again confirmed its increased applicability for practical use. Therefore, it can be utilized as a reliable glucose sensor.

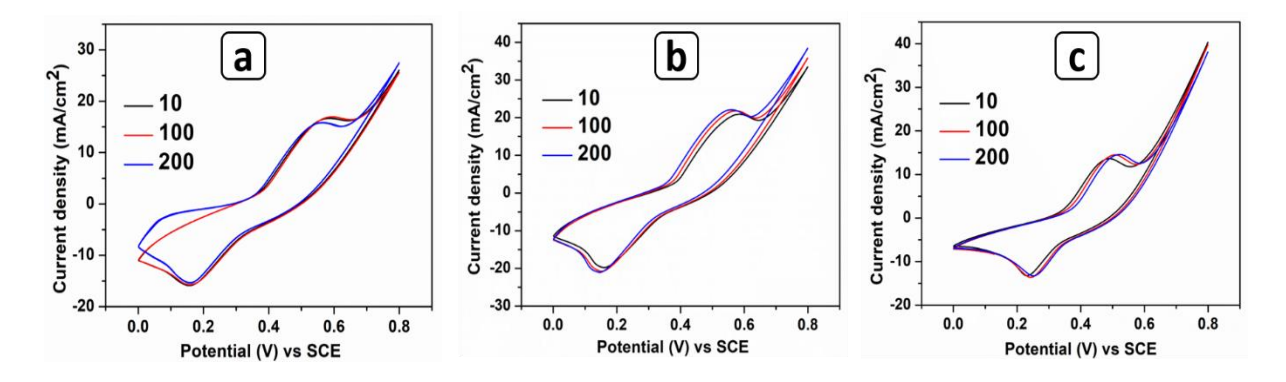


Figure 5.12. CV of a) sf-NiSe₂, b) sf-CoSe₂ and c) sf-NiSe₂/CoSe₂ electrodes for 200 cycles for showing the stability.

5.3.4. Glucose sensing via chronoamperometric using sf-NiSe₂, sf-CoSe₂ and sf-NiSe₂/CoSe₂

The amperometry technique is a well-known quick detection technique due to its higher sensitivity and lower signal-to-noise ratio characteristics, which is paramount for sensing applications. We performed chronoamperometric measurements to assess the operating range and sensitivity of sf-NiSe2, sf-CoSe2, and sf-NiSe2/CoSe2 electrodes [3]. Figure 5.10. a, b, and c show the chronoamperometric measurement for successive addition of glucose per minute in 0.5 M KOH with stirring conditions under 0.517 V, 0.496 V and 0.487 V for sf-NiSe2, sf-CoSe2, and sf-NiSe2/CoSe2 respectively. It can be clearly seen that, as the concentration of glucose increased, the current response also increased step-wise, which validated the efficient catalytic performance of sf-NiSe2, sf-CoSe2, and sf-NiSe2/CoSe2 electrode for electrochemical glucose oxidation. After adding glucose, all electrodes responded and reached a steady state current. Among which sf-NiSe2/CoSe2 composite was responding within a short time of 0.603 s when compared to sf-NiSe2 (0.73 s) and sf-CoSe2 (0.668 s), which illustrated the higher efficiency of sf-NiSe2/CoSe2 composite electrodes for glucose sensing than individual ones. The high efficiency of composite material is due to the synergistic effect of both sf-NiSe2 and sf-CoSe2 and the availability of more active sites for adsorption. As can be seen in

Figure 5.10. (d, e, f), electrocatalytic activity had a strong linear dependence with different glucose concentrations with correlation coefficients of 0.9905, 0.9941 and 0.9964 for sf-NiSe₂, sf-CoSe₂, and sf-NiSe₂/CoSe₂, respectively.

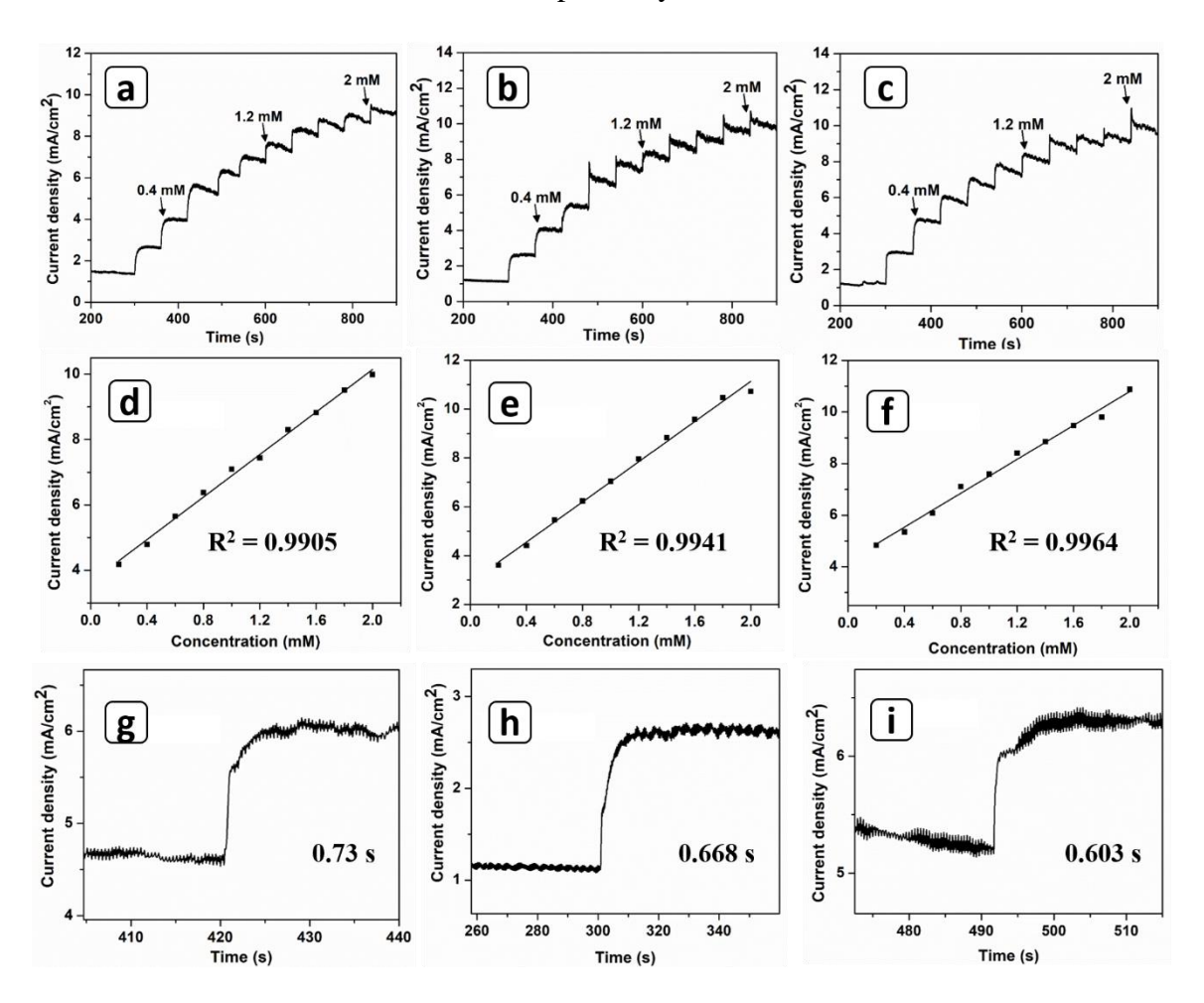


Figure 5.10. Chronoamperometric response for successive glucose addition in 0.5 M KOH (a,b,c), corresponding calibration plot (d,e,f) and response time of **sf-NiSe₂**, **sf-CoSe₂**, and **sf-NiSe₂/CoSe₂** respectively.

The average glucose level is 4-7 mM but varies from person to person [3]. The selectivity of a non-enzymatic glucose sensor must be evaluated since the presence of interference-causing substances affects glucose detection. Because clinical and biological specimens contain a significant amount of co-existing and iso-structural species that could interfere with the target analyte, the ability of the suggested sensing platform for the selective measurements of glucose was assessed using interference analysis. In this context, the impact of species such as ascorbic acid (AA), urea, potassium chloride (KCl), potassium nitrate (KNO₃), and sodium nitrite (NaNO₂) were studied. Interfering substances are often quickly oxidized in human blood. However, the glucose level in the blood is typically at least ten times

higher than the interfering substances [18]. The amperometric current response after the continuous addition of 500 µM glucose solution followed by 100 µM interfering compounds in 0.5 M KOH with stirring conditions is as shown in Figure 5.11. The current response of each interfering ion was negligible compared to the response for glucose molecules. This observation indicated that interfering molecules in the clinical analysis would not affect the glucose signal, which showed the selectivity of synthesized materials. Among the three electrodes sf-NiSe₂/CoSe₂ composite electrode showed a higher current response when compared to individual electrodes, which again highlights the higher sensitivity and future applicability of this material in glucose sensors.

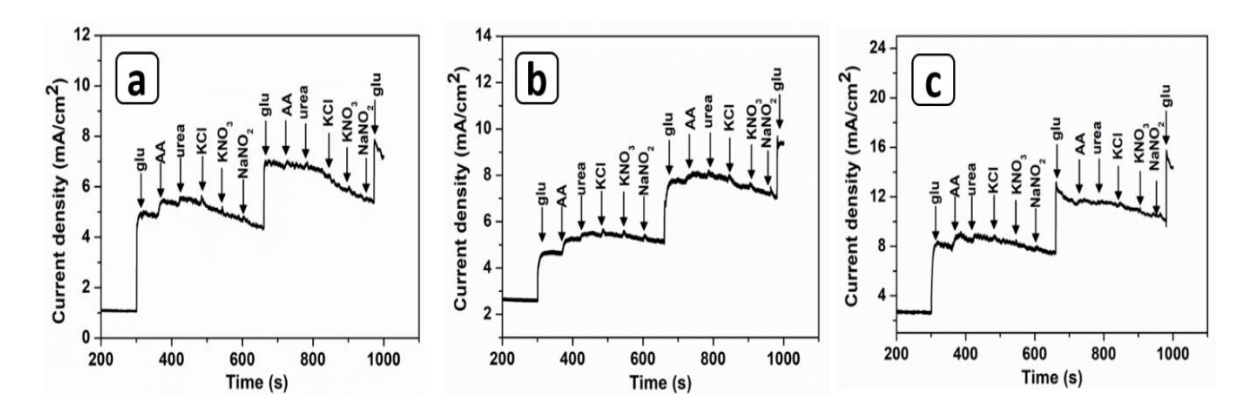


Figure 5.11. Amperometric response of a) **sf-NiSe**₂, b) **sf-CoSe**₂ and c) **sf-NiSe**₂/**CoSe**₂ electrodes towards sequential addition of 500 μM glucose, 100 μM of Ascorbic acid (AA), urea, potassium chloride (KCl), potassium nitrate (KNO₃), sodium nitrite (NaNO₂) in 0.5 M KOH solution.

5.4. Conclusion

In conclusion, we were able to synthesize surfactant free-NiSe₂ (**sf-NiSe₂**), CoSe₂ (**sf-CoSe₂**), and NiSe₂/CoSe₂ (**sf-NiSe₂/CoSe₂**) composite materials using HMDS-assisted method. PXRD and SAED patterns confirmed the formation and crystalline nature of products. In the non-enzymatic glucose sensing experiments, all materials showed good performance, whereas **sf-NiSe₂/CoSe₂** composite material showed better electrochemical oxidation of glucose with a sensitivity of 0.0896 mA/mMcm² and limit of detection (LOD) value of 0.0588 mM and a quick response time of 0.603 s. **sf-NiSe₂/CoSe₂** composite also exhibits enhanced anti-interference and stability at the same time. Therefore, **sf-NiSe₂/CoSe₂** offers a new option for non-enzymatic glucose sensor materials due to its high performance, making it a promising candidate for accurately detecting glucose in real-world clinical samples.

5.5. References

- 1. Venkadesh, A., Mathiyarasu, J., Dave, S. and Radhakrishnan, S. Amine mediated synthesis of nickel oxide nanoparticles and their superior electrochemical sensing performance for glucose detection. *Inorg. Chem. Commun.* **2021**, 131, 108779.
- 2. Phetsang, S., Kidkhunthod, P., Chanlek, N., Jakmunee, J., Mungkornasawakul, P. and Ounnunkad, K. Copper/reduced graphene oxide film modified electrode for non-enzymatic glucose sensing application. *Sci. Rep.* **2021**, 11, 9302.
- 3. Arif, D., Hussain, Z., Sohail, M., Liaqat, M.A., Khan, M.A. and Noor, T. A non-enzymatic electrochemical sensor for glucose detection based on Ag@ TiO₂@ metalorganic framework (ZIF-67) nanocomposite. *Front. Chem.* **2020**, 8, 573510.
- 4. Umapathi, S., Singh, H., Masud, J. and Nath, M. Nanostructured copper selenide as an ultrasensitive and selective non-enzymatic glucose sensor. *Mater. Adv.* **2021**, 2, 927-932.
- 5. Wang, L., Li, S., Zhang, X. and Huang, Y. CoSe₂ hollow microspheres with superior oxidase-like activity for ultrasensitive colorimetric biosensing. *Talanta*, **2020**, 216, 121009.
- 6. He, B. and Yan, X. Ultrasensitive electrochemical aptasensor based on CoSe₂/AuNRs and 3D structured DNA-PtNi@Co-MOF networks for the detection of zearalenone. *Sens. Actuators B: Chem.* **2020**, 306, 127558.
- 7. Franceschini, F. and Taurino, I. Nickel-based catalysts for non-enzymatic electrochemical sensing of glucose: A review. *Phys. Med.* **2022**, 14, 100054.
- 8. Wang, D. and Chang, Y. The Construct CoSe₂ on Carbon Nanosheets as High Sensitivity Catalysts for Electro-Catalytic Oxidation of Glucose. *Nanomater*. **2022**, 12, 572.
- 9. a) Joseph, A., Billakanti, S., Pandit, M.A., Khatun, S., Rengan, A.K. and Muralidharan, K. Impact of bandgap tuning on ZnS for degradation of environmental pollutants and disinfection. Environ Sci Pollut Res. 2022, 29, 56863-56875. b) Joseph, A., Khatun, S., Sai Hemanth Kumar, D., Rengan, A.K. and Muralidharan, K. Insight into the Effect of Stabilizers on Anticancer and Antibacterial Activity of AgBiS₂ Nanomaterial. Chem. Eur. J. 2023, e202203796. c) Srinivas, B., Pandit, M.A. and Muralidharan, K., 2019. Importance of clean surfaces on the catalyst: SnS₂ nanorings for environmental remediation. ACS omega. 2019, 4, 14970-14980. d) Pandit, M.A., Sai Hemanth Kumar, D., Billakanti, S., Ramadoss, M. and Muralidharan, K.

- Chalcopyrite with magnetic and dielectric properties: an introductory catalyst for 4-nitrophenol reduction. *J. Phys. Chem. C.* **2020**, 124, 18010-18019.
- 10. Peng, S., Lai, T., Kong, Y., Ran, Y., Su, L., Ma, D., Xiao, X. and Wang, Y. A novel non-enzymatic glucose electrochemical sensor with high sensitivity and selectivity based on CdIn₂O₄ nanoparticles on 3D Ni foam substrate. *Nanotechnol.* **2021**, *32*, 405502.
- 11. Cho, J.S., Lee, S.Y. and Kang, Y.C. First introduction of NiSe₂ to anode material for sodium-ion batteries: a hybrid of graphene-wrapped NiSe₂/C porous nanofiber. *Sci. Rep.* **2016**, 6, 1-10.
- 12. Wang, T., Gao, D., Xiao, W., Xi, P., Xue, D. and Wang, J. Transition-metal-doped NiSe₂ nanosheets towards efficient hydrogen evolution reactions. *Nano Res.* **2018**, 11, 6051-6061.
- 13. Wu, H., Shi, L., Feng, C. and Ding, Y. Synthesis of MoS₂/CoSe_{2-x} hybrids as electrocatalysts for hydrogen evolution reaction. *Ionics*. **2022**, 28, 1337-1345.
- 14. Nai, J., Lu, Y., Yu, L., Wang, X. and Lou, X.W. Formation of Ni–Fe mixed diselenide nanocages as a superior oxygen evolution electrocatalyst. *Adv. Mater.* **2017**, 29, 1703870.
- 15. Zhou, Q.S., Peng, X.W., Zhong, L.X. and Sun, R.C. CoSe₂ nanobelt coupled with CoMoO4 nanosheet as efficient electrocatalysts for hydrogen and oxygen evolution reaction. *Environ. Sci. Ecotechnology.* **2020**, 1, 100004.
- 16. Farid, A., Pan, L., Usman, M., Khan, I.A., Khan, A.S., ul Ahmad, A. and Javid, M. Insitu growth of porous CoTe₂ nanosheets array on 3D nickel foam for highly sensitive binder-free non-enzymatic glucose sensor. *J. Alloys Compd.* **2021**, 861, 158642.
- 17. Kang, X., Wang, J., Wu, H., Aksay, I.A., Liu, J. and Lin, Y. Glucose oxidase—graphene—chitosan modified electrode for direct electrochemistry and glucose sensing. *Biosensors and Bioelectronics*. **2009**, 25, 901-905.
- 18. Kachouei, M.A., Shahrokhian, S. and Ezzati, M. Bimetallic CoZn-MOFs easily derived from CoZn-LDHs, as a suitable platform in fabrication of a non-enzymatic electrochemical sensor for detecting glucose in human fluids. *Sens. Actuators B: Chem.* **2021**, 344, 130254.

CHAPTER 6

SUMMARY AND CONCLUSION

Organic surfactants have been used in most reactions to synthesise nanomaterials to date. Additionally, the majority of them involve lengthy, multistep reactions. Surfactants typically control morphology, cap the surface, and avoid nanoparticle aggregation by forming micelles surrounding the nanoparticles. However, the prominent involvement of surfactants has the drawback of lowering the efficiency of materials in various applications, specifically catalysts. The disadvantage is caused by the fact that surfactants block active sites of materials and create a barrier that prevents substrates from accessing the surface of the catalysts. Further, these surfactants can be toxic to the environment. However, the work presented here is an entirely one-step, surfactant-free synthesis.

Our group developed a novel hexamethyldisilazane (HMDS)-assisted synthetic method to produce nanoparticles without organic surfactants or polymers. HMDS serves as a reaction initiator, reducing agent, and stabilizer in this simplest chemical method to produce different nanomaterials. Using this method, we produced various nanomaterials, including binary, ternary, and composite metal chalcogenide materials, using our ground-breaking method. As previously discussed in their respective chapters, we were successful in synthesising different metal doped surfactant free ZnS, AgBiS₂ nanoparticles with and without surfactant, SnS₂ with and without surfactant, surfactant-free NiSe₂, CoSe₂, NiSe₂/CoSe₂ nanoparticles. All chalcogenides were produced without the aid of an external surfactant under inert conditions.

In the first study, we synthesised ZnS nanoparticles and metal-doped ZnS nanoparticles (sf-m-ZnS; m = Cu, Ni, Cd, Bi, or Mn) and correlated their activity with bandgap changes. Without using surfactants, polymers, or template molecules, we synthesised all of these compounds using hexamethyldisilazane (HMDS), and we comprehensively characterized them using various methods. The photocatalytic and antibacterial properties exhibited by the materials have demonstrated their dual usefulness. We have shown how doping has an impact on the expansion of the absorption band into the visible spectrum and the improvement of photocatalytic activity under visible light. Thus, we found that the bandgap variation has altered the material's performance as photocatalysts. While degrading two organic contaminants, Rhodamine B (RhB) and Methylene blue (MB), in water, sf-Cd-ZnS outperformed all other materials synthesised. The antibacterial activity of sf-ZnS and sf-m-ZnS against Staphylococcus aureus (S. aureus) was evaluated using the Zone of Inhibition method. The

material sf-Ni-ZnS exhibited the highest activity. The increased activity of materials can be attributed to the availability of the free surface of the nanoparticles, which allowed for close contact between the inorganic semiconductor material and organic and biomolecules. Therefore, we have explained that the properties can be improved by modifying the bandgap of the materials and enabling close contact between the materials and substrates.

Intending to check the efficiency of surfactant-free materials in degrading the organic contaminants in water, we have studied the quality of water obtained before and after the degradation of pollutant Rhodamine B by SnS₂ with (PEG-SnS₂) and without surfactant (sf-SnS₂) under sunlight illumination. Similarly, we have tested AgBiS₂ with (OLA/OA-AgBiS₂) and without surfactant (sf-AgBiS₂). Also, we have compared the efficiency of materials prepared using the HMDS and literature methods. The qualitative analysis was done by measuring Chemical Oxygen Demand (COD). The results demonstrated that the materials without capping agents (sf-SnS₂ and sf-AgBiS₂) had the highest Rhodamine B dye solution degradation and the lowest COD value. Therefore, this work emphasizes the significance of the Hexamethyldisilazane (HMDS) method for nanoparticle synthesis. This procedure ensured free active surface availability, resulting in close contact with the substrate.

As an initiatory step, nanoparticles synthesised using the HMDS-assisted method are subjected to therapeutic study. Long-chain organic surfactants or polymers are invariably needed for the chemical production of nanomaterials to stabilize them in the nano regime. These stabilizing compounds prevent nanomaterials from interacting with biological cells. In order to investigate the impact of stabilizers, we synthesised AgBiS₂ nanoparticles with and without polymer coatings (sf-AgBiS₂ and PEG-AgBiS₂) using the HMDS method and tested their NIR-mediated anticancer and antibacterial activities. The key feature of a photoresponsive system is the ability to get excited by a single wavelength. The near-infrared (NIR) light-absorbing AgBiS₂ exhibit this characteristic feature. This work demonstrated the superior anticancer activity and biocompatibility of sf-AgBiS₂ against HeLa cells and live 3-D tumour spheroids and showed excellent antibacterial activity against Gram-positive Staphylococcus aureus (S. aureus) in both the presence and absence of NIR radiation of over PEG-AgBiS₂. The photothermal treatment (PTT) outcomes demonstrated the capacity of sf-AgBiS₂ by raising the temperature of cancer cells to 53.3 °C under NIR illumination leading to the destruction of cancer cells. The significance of synthesising stabilizer-free nanoparticles to synthesise safe and potent PTT agents is illustrated by this work.

We have employed the HMDS method to synthesise NiSe₂, CoSe₂ and NiSe₂/CoSe₂ composite materials. These materials exhibited their usefulness in effective glucose oxidation, highlighting the usage of these materials for non-enzymatic electrochemical detection of glucose. sf-NiSe₂/CoSe₂ showed a higher response. When compared to individual materials, sf-NiSe₂/CoSe₂ exhibited more excellent electrochemical response with a lower limit of detection of 0.0588 mM, good sensitivity of 0.0576 mAmM⁻¹cm⁻², and a short response time of 0.603 s as well as long-term stability and good anti-interference capabilities. Thus, this work demonstrates the enormous potential of sf-NiSe₂/CoSe₂ electrode material as non-enzymatic glucose sensors, making it possible to be employed as a practical glucose detector.

The HMDS-assisted method, when compared to intricate or multistep approaches published in various works of literature, was capable of producing nanomaterials in a single step. Materials with excellent phase purity and good crystallinity could be produced employing this HMDS-assisted method. The synthesised nanoparticles, however, were weakly soluble in organic solutions. Interestingly, the heterogeneous catalysts made using the HMDS-assisted method outperformed the identical materials synthesised using already-known methods in various catalytic applications. The current work offers novel insights into preparing materials with clean surfaces for the efficient degradation of contaminants in wastewater, biocompatible and potent PTT agents, and non-enzymatic glucose sensors.

LIST OF PUBLICATIONS

Publication from thesis

- Anju Joseph, Srinivas Billakanti, Manzoor Ahmad Pandit, Sajmina Khatun, Aravind Kumar Rengan, Krishnamurthi Muralidharan. "Impact of bandgap tuning on ZnS for degradation of environmental pollutants and disinfection." *Environmental* Science and Pollution Research, 29, 56863-56875.
- 2. **Anju Joseph**, Sajmina Khatun, Dasari Sai Hemanth Kumar, Aravind K. Rengan, and Krishnamurthi Muralidharan. "Insight into the Effect of Stabilizers on Anticancer and Antibacterial Activity of AgBiS₂ Nanomaterial." *Chemistry–A European Journal*, p.e202203796.
- 3. **Anju Joseph**, Dasari Sai Hemanth Kumar, Ahsan Zohaib, Srinivas Billikanti^c, Manzoor Ahmad Pandit, Krishnamurthi Muralidharan. "Study on Effect of Capping Agent on Chemical Oxygen Demand of Water Bodies" (Manuscript under preparation).
- 4. **Anju Joseph**, Dasari Sai Hemanth Kumar, Manigandan Ramadoss, Krishnamurthi Muralidharan. "Synthesis of surfactant free-NiSe₂, CoSe₂, NiSe₂/CoSe₂ for non-enzymatic glucose sensing" (Manuscript under preparation).

ORAL AND POSTER PESENTATIONS

- Presented Poster entitled as "Bandgap Tuning on ZnS for Effective Degradation of Organic Pollutants and Antibacterial Activity" at CHEMFEST-2019 Annual inhouse Symposium of School of Chemistry, 22-23 February at University of Hyderabad.
- Presented Poster and delivered Oral talk entitled as "Impact of Bandgap tuning on ZnS for Degradation of Environmental Pollutants and Disinfection" at CHEMFEST-2022, Annual in-house symposium of School of Chemistry, 19-20 March at University of Hyderabad.
- 3. Presented Poster entitled as "Effective degradation of organic molecules and increased antibacterial activity by bandgap tuning of ZnS" in 29th CRSI National Symposium in Chemistry (NCS-29), 7-9 July 2022 at IISER, Mohali.
- 4. Presented Poster entitled as "Bandgap Tuning on ZnS for Effective Degradation of Organic Pollutants and Antibacterial Activity" in "International Conference on Chemistry and Applications of Soft Materials (CASM 2022)", 25-27 July 2022 at CSIR- NIIST, Thiruvananthapuram.

RESEARCH ARTICLE



Impact of bandgap tuning on ZnS for degradation of environmental pollutants and disinfection

Anju Joseph¹ · Srinivas Billakanti^{1,2} · Manzoor Ahmad Pandit¹ · Sajmina Khatun³ · Aravind Kumar Rengan³ · Krishnamurthi Muralidharan^{1,2}

Received: 13 January 2022 / Accepted: 8 March 2022 © The Author(s), under exclusive licence to Springer-Verlag GmbH Germany, part of Springer Nature 2022

Abstract

The materials showing multiple applications are appealing for their practical use and industrial production. To realize the suitable property for various applications, we have produced ZnS (sf-ZnS) and metal-doped ZnS nanoflakes (sf-m-ZnS) where m = Cu, Ni, Cd, Bi, or Mn) and correlated their activity with bandgap variation. We obtained all these materials via hexamethyldisilazane (HMDS)-assisted synthetic method without using any surfactants, polymers, or template molecules and characterized them thoroughly using various techniques. Photocatalytic, as well as antibacterial, activities of these materials showed their bifunctional utility. We have demonstrated the effect of doping and consequent extension of absorption band to the visible region and resultant improved photocatalytic activity under sunlight. Thus, the change in bandgap influenced their performance as photocatalysts. Among all materials produced, sf-Cd-ZnS provided superior results as a photocatalyst while degrading two organic pollutants—rhodamine B (RhB) and methylene blue (MB) in water. The antibacterial activity of sf-ZnS and sf-m-ZnS against Gram-positive bacteria, i.e., Staphylococcus aureus (S. aureus), was examined by the zone of inhibition method, wherein sf-Ni-ZnS showed maximum activity. The enhanced activity of these ZnS materials can be attributed to the free surface of nanoparticles without any capping by organic molecules, which provided an intimate interaction of inorganic semiconductor material with organic and biomolecules. Thus, we have demonstrated modification of properties both by bandgap tuning of materials and providing the opportunity for intimate interaction of materials with substrates. The photocatalytic activity and antibacterial action of metal-doped ZnS produced by our method exhibited their potential for environmental remediation, specifically water purification.

Keywords Zinc sulfide · Transition metal dopants · Surfactant free · Photocatalysts · Antibacterial action

Introduction

Rapid growth in population and industrialization have resulted in vast pollution to the environment and water, leading to a severe threat to the endurance of human beings (Zhang et al. 2019; Ferreira-Neto et al. 2020). Photocatalysis

Responsible Editor: Sami Rtimi

Krishnamurthi Muralidharan murali@uohyd.ac.in

Published online: 27 March 2022

- School of Chemistry, University of Hyderabad, Hyderabad, India
- Advanced Centre of Research in High Energy Materials, University of Hyderabad, Hyderabad, India
- ³ Biomedical Engineering, Indian Institute of Technology, Hyderabad, Kandi, India

is a light-driven chemical process and is a much-needed process for our society's well-being in terms of water purification, water splitting, and other photocatalytic applications. The photocatalysis process is helpful for the degradation of contaminants on the surface of the photocatalyst. There is an increasing need to control chemical and bacterial contaminations in water that originate mainly from chemical, textile, printing, plastics, papers, food, cosmetic, drugs, and healthcare industries. Photocatalysts play a crucial role in the degradation of water pollutants that have fatal effects on humans. Though many methods such as coagulation, biodegradation, and photocatalysis have been used for water purification, photocatalysis is proved to be lethal for the degradation of pollutants like organic dyes (RhB and MB) (Poormohammadi-Ahandani et al. 2014; Velanganni et al. 2018). Several semiconductor photocatalysts such as metal oxides, metal hydroxides, sulfides, and metal-free



semiconductors have been used for water purification. Many of them worked well because of their high surface to volume ratio and quantum confinement effect (Wang et al. 2006; Corrado et al. 2009; Naofumiuekawa et al. 2015).

After the pioneering work of using the environmentally friendly and economical process of photocatalytic splitting of water on TiO₂ electrodes by Honda and Fujishima, the focus on preparing II-VI semiconductor nanomaterials received widespread attention for their application in phosphors, electroluminescence devices, light-emitting displays, and optical sensors. Among many semiconductors, zinc sulfide (ZnS) is studied extensively by researchers for (Yang et al. 2002; Peng et al. 2006; Wang et al. 2006; Cadis et al. 2011; Kole and Kumbhakar 2012; Ummartyotin et al. 2012; Zhang and Guo 2013; Poormohammadi-Ahandani et al. 2014; Sahraei and Darafarin 2014; Singh et al. 2014; Naofumiuekawa et al. 2015; Harish et al. 2017; Prasad and Balasubramanian 2017) versatile applications in many fields like photonics, electroluminescence, nonlinear optical devices, infrared windows, and as sensors. ZnS is an II-VI semiconductor material at room temperature with a wide direct bandgap (3.5–3.8 eV), and it possesses high exciton binding energy (40 meV) and is less toxic. Therefore, it can be used in the short wavelength region (UV, blue, green) of the electromagnetic spectrum for optoelectronic applications (Kole and Kumbhakar 2012). It is also a phosphor material with electroluminescent and photoluminescent properties and shows size-dependent electrical and photoluminescent properties, which are useful in the fields of sensors, displays, and lasers (Wang et al. 2006; Naofumiuekawa et al. 2015; Song et al. 2018).

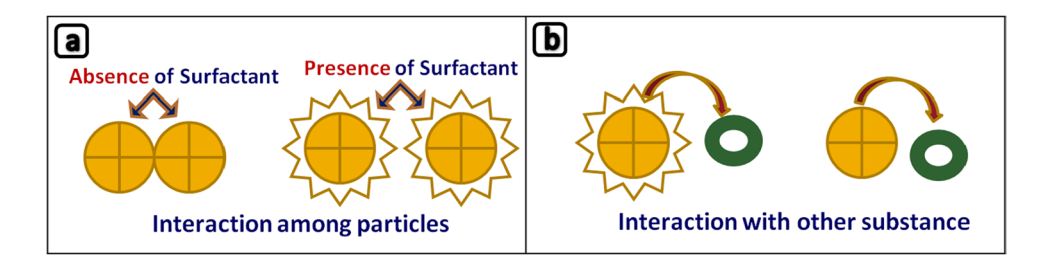
Theoretically, ZnS possess a much higher capability of photo-carrier generation than TiO₂ due to the direct bandgap. However, its wide bandgap energy restricts the absorption of the visible light reducing its usability as a photocatalyst. At the same time, the large bandgap favors it to host any metal ions. By incorporating the transition metal dopants on the ZnS material with different loadings, it is possible to tune the absorption capacity from the UV region to the visible region. Therefore, many studies were directed on improving its properties by doping process where the transition metal–doped ZnS are prominent (Wang et al. 2006; Peng et al. 2006; Cadis et al. 2011; Kole and Kumbhakar 2012; Ummartyotin et al. 2012; Poormohammadi-Ahandani et al. 2014; Singh et al. 2014;

Fig. 1 a, b Schematic representation of interaction of surfactant-free and stabilized nanoparticles

Naofumiuekawa et al. 2015; Dilpazir et al. 2015; Prasad and Balasubramanian 2017; Jung et al. 2017; Velanganni et al. 2018; Song et al. 2018; Suganthi and Pushpanathan 2019a, 2019b). Since these materials have comparable surface atoms to those in the crystal lattice, their chemical and physical properties differ from bulk. In addition, luminescent centers are formed by doping ions, resulting in their luminescent property (Yang et al. 2002; Wang et al. 2006). The role of these dopants is to create charge carrier traps which result in enhanced photocatalytic activities (Poormohammadi-Ahandani et al. 2014; Prasad and Balasubramanian 2017).

While acting as a photocatalyst, ZnS has also shown potent biological applicability, particularly the antibacterial activity. According to the Infectious Disease Society of America (IDSA), the threatening bacterial species exhibiting rapid growth of antibiotic resistance include Staphylococcus aureus (S. aureus), Pseudomonas aeruginosa (P. aeruginosa), and Enterobacter species. The methicillin-resistant Staphylococcus aureus caused a large number of deaths worldwide (Qumar et al. 2020). Therefore, more effective antibiotics are to be developed to overcome the resistance of S. aureus. The effect of doping ZnS in its antibacterial activity against Gram-positive bacteria S. aureus has also been studied and evaluated by the zone of inhibition method (Singh et al. 2014; Arun Kumar et al. 2017; Song et al. 2018). These materials are popularly used in medical diagnostics since they are non-toxic, biocompatible, and biosafe (Rose et al. 2020; Hussain et al. 2020).

Different transition metals have been doped into ZnS through different methods of preparation for potential applications. While the unhindered mobility of charge is an essential characteristic, the toxicity of materials used is the deciding factor for biological activity. The intimate contact of active catalytic materials with polluting molecules for their degradation and inhibition of bacterial growth is much needed for efficient catalytic activities. Many synthetic methods of ZnS and its doping processes involve using long-chain organic molecules as surfactants to assist in controlling the growth process of nanoparticles. These molecules form a layer between the active materials and the substrates, such as dye needing decomposition or bacteria required to be inactivated (Fig. 1). Sometimes these surfactant molecules may be toxic to humans and also inhibit charge mobility. There





are few reports on stripping these surfactants by postsynthetic methods such as ligand exchange reactions and annulation. Though these methods are somewhat effective, they do leave some impurities, and many of them involve multistep preparation processes.

This work aims to tune the absorption capacity of pure zinc sulfide (UV region) to visible region by having transition metal ions as dopants and providing unhindered movement to the charge carriers. In this work, the high pure surfactant-free ZnS nanoparticles (sf-ZnS) and surfactant-free metal-doped ZnS nanoparticles (sf-m-ZnS; where m = Cu, Ni, Cd, Bi, or Mn) were prepared with the tuneable bandgap, which showed excellent photocatalytic and antibacterial properties. The materials were synthesized by a simple one-pot reaction utilizing the hexamethyldisilazane (HMDS)-assisted synthesis method, wherein HMDS played a multi-role such as a solvent and a capping agent (Srinivas et al. 2015; Kumar et al. 2017; Srinivas and Muralidharan 2018; Ahmad Pandit et al. 2019, 2020). There are no previous reports on the preparation of metal-doped ZnS using this method. The reactions yielded high pure materials without any organic molecules in their surroundings. Various analytical and spectroscopic techniques are used to characterize the sf-**ZnS** and **sf-m-ZnS** nanoparticles. The materials were tested for the photocatalytic degradation of organic dyes (RhB and MB) to explain clearly the impact of doping on ZnS nanoparticles. Besides photocatalysis, the effect of doping was studied through its action against the Grampositive bacteria S. aureus. This work, therefore, provides a way of tuning the properties of wide bandgap semiconductors and their impact on the degradation of environmental pollutants and health hygiene.

Experimental

Materials required

Zinc chloride (ZnCl₂), thiourea, hexamethyldisilazane (HMDS), copper chloride (CuCl₂), nickel chloride (NiCl₂), cadmium chloride (CdCl₂), bismuth chloride (BiCl₂), and manganese chloride (MnCl₂) were purchased from Sigma-Aldrich. All chemicals were used without any further purification.

Synthesis of ZnS by the HMDS-assisted method

The hexamethyldisilazane (HMDS)-assisted method (Scheme 1) was utilized to synthesize ZnS nanoparticles. Zinc chloride (200 mg, 1.4 mmol), thiourea (106 mg, 1.4 mmol) (1:1 stoichiometric ratio), and excess HMDS (5 ml) were taken in a flask, and the mixture was heated

$$ZnCl_2 + SC(NH_2)_2 + excess HNSi(Me_3)_2 \rightarrow$$

$$\rightarrow [-S - N(SiMe_3) -] \cdots ZnCl_2 \rightarrow$$

$$\rightarrow ZnS + (Me_3)SiCl + N_2 + H_2$$

Scheme 1 Formation of zinc sulfide via HMDS-assisted reaction

to about 140 °C for 6 h under nitrogen (flow) atmosphere. After the reaction was completed, high vacuum was applied to remove excess HMDS and other gaseous side products. The residue was washed repeatedly with distilled water and acetone. The collected product (sf-ZnS) was dried in an oven at 70 °C for 24 h.

Preparation of metal doping of ZnS (sf-m-ZnS)

To prepare metal-doped ZnS, metal chloride (5% loading) was added to the reaction mixture of zinc chloride, thiourea, and HMDS. The rest of the reaction conditions and workup were similar to the one discussed for ZnS. Likewise, the other metal-doped zinc sulfides (**sf-m-ZnS**; where m = Cu, Ni, Cd, Bi, or Mn) (9 mg of CuCl₂; 9 mg of NiCl₂; 14 mg of CdCl₂; 24 mg of BiCl₃; and 9 mg of MnCl₂) were also prepared following the above prescribed procedure.

Instrumentation

XRD patterns of sf-ZnS and sf-m-ZnS were collected at room temperature using a Bruker D8 X-ray diffractometer (XRD) at a scan rate of 1 min⁻¹ (CuK α = 1.54 Å; operating voltage = 40 kV; operating current = 30 mA) measurements with Cu Kα radiation in a 2θ range from 10° to 80°. The synthesized sf-ZnS and sf-m-ZnS materials were made into suspension in ethanol by sonicating for 2-3 min. The suspension was drop cast on carboncoated copper grids (200 mesh) for the TEM analyses. FEI Technai G2 20 STEM with a 200-kV acceleration voltage was used to capture TEM images of sf-ZnS and sf-m-ZnS particles. The morphology (FESEM) of sf-ZnS and sf-m-ZnS materials and energy-dispersive spectroscopy (EDS) were studied using an Ultra 55 Carl Zeiss instrument at an operating voltage of 10 kV. A JASCO 5300 spectrophotometer was used to record the Fourier transform infrared (FT-IR) spectra (KBr pellet) of sf-ZnS and sf-m-ZnS materials. The optical properties of sf-ZnS and sf-m-ZnS materials were confirmed by studying the UV/Vis absorption spectra of samples in the solid and liquid states (for photocatalysis) using a JASCO-V770 UV/Vis spectrometer, wherein barium sulfate was used as the filler. The lifetime studies were



performed using a MicroTime 200 resolved confocal fluorescence setup from PicoQuant equipped with an inverted microscope, a 485-nm pulsed laser source used for excitation.

Photocatalytic degradation of organic dyes

Rhodamine B and methylene blue are the dyes chosen as pollutants in our study. The corresponding wavelengths used for rhodamine B and methylene blue are 554 nm and 663 nm, respectively. Stock solutions of dyes (rhodamine B (RhB) and methylene blue (MB)) were prepared by adding 10 mgl⁻¹ of dye in deionized water for the study of catalytic activity. From this stock solution, 60 ml was taken in a beaker. For the photocatalyst powders (doped and undoped ZnS), 30 mg was added to the solution, and 3 ml of solution was taken in a specific interval of time. The sample was centrifuged at 2500 rpm for 5 min, and its UV-Vis spectrum was recorded to identify the degradation of dye. The observed decrease in intensity of absorption peak represented the degradation. The rate of decolorization of the solution was measured as the decrease in absorbance. The decolorization efficiency is calculated using the formula given below.

Decolorization efficiency =
$$\left(\frac{C_0 - C_t}{C_0}\right) \times 100$$
,

where C_0 is the amount of dye at 0 time, and C_t is the amount of dye at time t.

Antibacterial activity test

The antibacterial activity of ZnS and metal-doped ZnS has been evaluated through the zone of inhibition method in agar medium. The liquid agar medium was sterile at a temperature of 121 °C. It was poured into a petri dish, 20 ml/plate, and was allowed to solidify. Filter papers of 0.5–0.6 cm in diameter were cut using a sterile borer. Nanoparticle solutions with concentration 2, 5, 10, 15, and 20 mg/ml were delivered to the filter paper discs leaving 5-10 min for semi-dry. As a positive-standard control, gentamicin discs consisting of the concentration of 2, 4, 8, and 10 µl (from the stock solution of 2 mg/4 ml) were used to determine the sensitivity of microbial species. One hundred microliters of bacterial inoculums (1 O.D. at 600-nm wavelength of Staphylococcus aureus containing 8.3×10^8 CFU/ml) was used to spread for each solidified agar plate. The inoculated plates were incubated at 37 °C for 12 and 24 h. To evaluate the antibacterial activity, the diameter of the inhibition zone of tested bacteria was measured in centimeters. After 12 h and 24 h, the inhibition zone was examined.



Synthesis and characterization of ZnS and metal-doped ZnS

We have chosen the HMDS-assisted synthetic method to produce ZnS without organic surfactants (sf-ZnS) and metal-doped ZnS (sf-m-ZnS) to obtain high pure materials. When ZnCl₂ was reacted with thiourea in an excess amount of HMDS, we obtained sf-ZnS. When the same reaction was conducted in the presence of other metal sources (Zn: metal ratio = 0.95:0.05), metal-doped ZnS were obtained. The possibility of getting a series of metal-doped ZnS by systematically changing the metal sources showcased the control and the versatility of the synthetic method. Earlier, we postulated the mechanism of this HMDS-assisted reaction as occurring via the formation of a polymetric intermediate. The intermediate formation was confirmed earlier by time-dependent ³¹Si NMR spectral studies and GPC data of partially purified air and moisture-sensitive intermediate. This intermediate would form on the interaction of thiourea and HMDS and then surround the metal chloride. The interaction of this intermediate with chloride would produce trimethylsilyl chloride. When we monitored the pH of the reaction every 1 h, it remained around 7 and did not change considerably as the reaction progressed even after 6 h. This observation indicates the leaving of hydrogen gas rather than H⁺ ions from HMDS and thus rule out the formation of H₂S gas as an intermediate. Also, since pH was not increasing towards basic, the formation of NH₃ in this reaction is ruled out. All these observations suggested that hydrogen and nitrogen from HMDS are leaving as H2 and N2 gases. Scheme 1 depicts the overall reaction. In all these reactions, HMDS played a dual role as a solvent and a surfactant during synthesis, but not a part of the product. Therefore, these reactions are termed HMDS-assisted reactions.

The crystalline structure and grain size are obtained from powder X-ray diffraction. The PXRD pattern (Fig. 2) shows the Bragg's reflection peaks at 2θ of 28.68° , 47.70° , and 56.47° analogous to the planes (111), (220), and (311), which are the planes of cubic phase zinc blende (ZnS) (JCPDS-05-0566) (Peng et al. 2006). We have noticed the shift in the peak positions in the PXRD pattern of doped ZnS due to the small dissimilitude in ionic radii of doped ions (Sahraei and Darafarin 2014). However, the peak pattern remains the same for all samples, indicating no crystal structure disturbances, showing that the metal ions are inside the lattice. Also, no impurity phases were observed within the resolution limits of the diffractometer (Peng et al. 2006). The small changes in full width at half maximum (FWHM) are due to the changes in the radius of metal atoms doped (Harish et al. 2017).



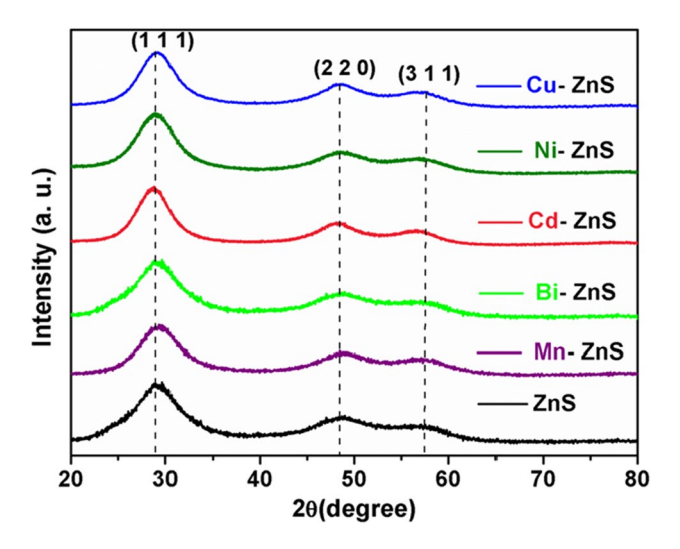


Fig. 2 PXRD patterns of as synthesized **sf-ZnS** and **sf-m-ZnS** (m = Cu, Ni, Cd, Bi, and Mn) nanoparticles

Effect of doping on morphology and optical property

The effect of doping on the size and shape of ZnS nanoparticles can be observed in electron microscopic images (Fig. 3 (SEM) and Fig. 4 (TEM)). The SEM and TEM images revealed that all the synthesized particles exhibited a nanoflake morphology. There was a variation in thickness of nanoflakes as seen in SEM images attributed to doping.

The average particle size of nanoparticles has been calculated (Fig. 3). The analysis revealed the average particle size as 119 nm for sf-ZnS, 115 nm for Cu-sf-ZnS, 124 nm for Ni-sf-ZnS, 98 nm for Cd-sf-ZnS, 112 nm for Bi-sf-ZnS, and 137 nm for Mn-sf-ZnS. Recorded elemental mapping (Fig. S1) of doped and undoped samples confirmed the homogeneous distribution of doped elements. The SAED patterns (Fig. 4 inset) show three broad diffused rings for ZnS due to the smaller size of particles, whereas the spots in the SAED pattern for the doped sample show a crystalline nature. The three rings in the SAED pattern are corresponding to planes (111), (220), and (311) (Wang et al. 2006; Kuppayee et al. 2011; Vijai Anand et al. 2013; Murugadoss 2013; Kumar et al. 2019; Bindu and Anila 2021; Mostafa et al. 2021). The PXRD pattern supports these observations as well.

Optical properties of the synthesized sf-ZnS and transition metal-doped sf-ZnS nanoflakes were examined by UV-Vis spectroscopy. Solid-state spectra were recorded to understand the optical properties, which showed a broad absorption. E-gap spectra (Fig. 5) calculated from DRS spectra (Fig. S2) for undoped and cadmium-doped zinc sulfide nanoparticles showed a blue shift in absorption after doping. For an efficient photocatalyst, the conduction band should be more negative, which zinc sulfide fulfills. However, ZnS has a wide bandgap that helps to absorb only UV light and not the visible light where doping becomes necessary. When zinc sulfide is doped with transition metal ions, it creates a dopant level that acts as an electron-hole trap

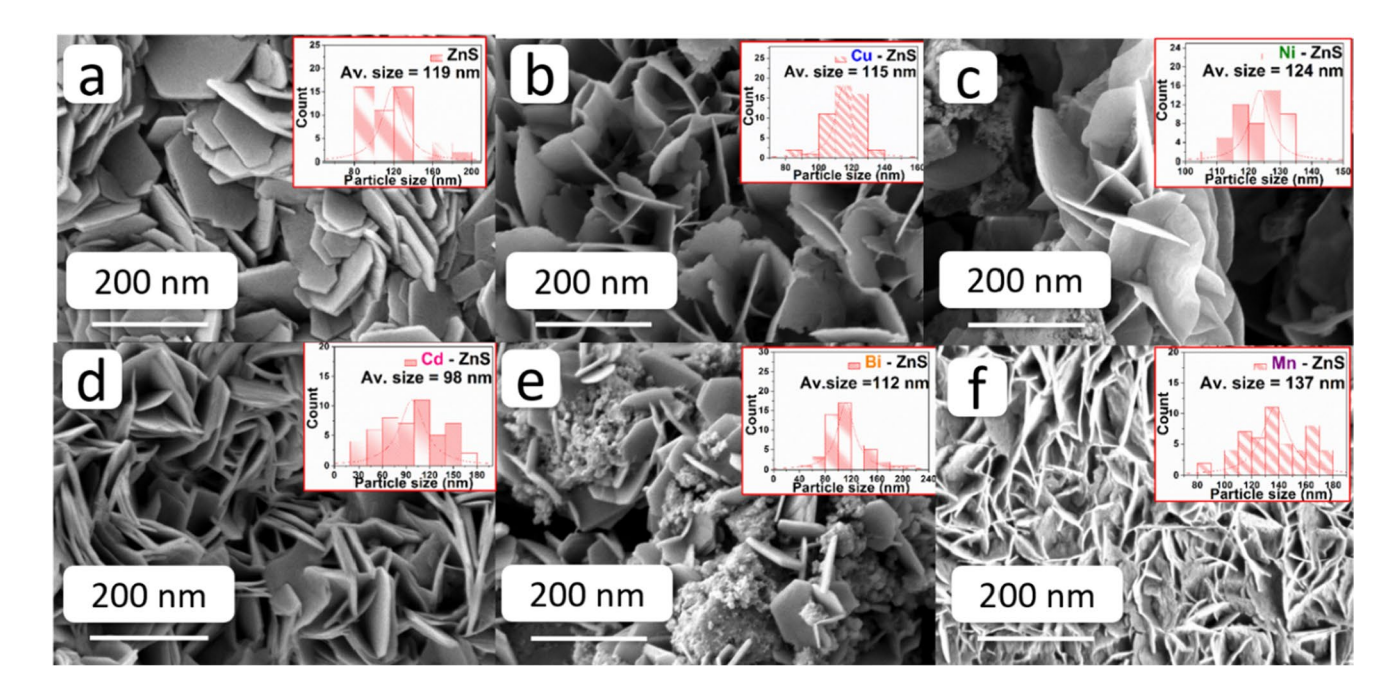


Fig. 3 FESEM images of as synthesized surfactant-free ZnS and transition metal—doped ZnS nanoflakes and also the calculated average particle size distribution of nanoflakes (inset). a sf-ZnS, b sf-Cu-ZnS, c sf-Ni-ZnS, d sf-Cd-ZnS, e sf-Bi-ZnS, and f sf-Mn-ZnS



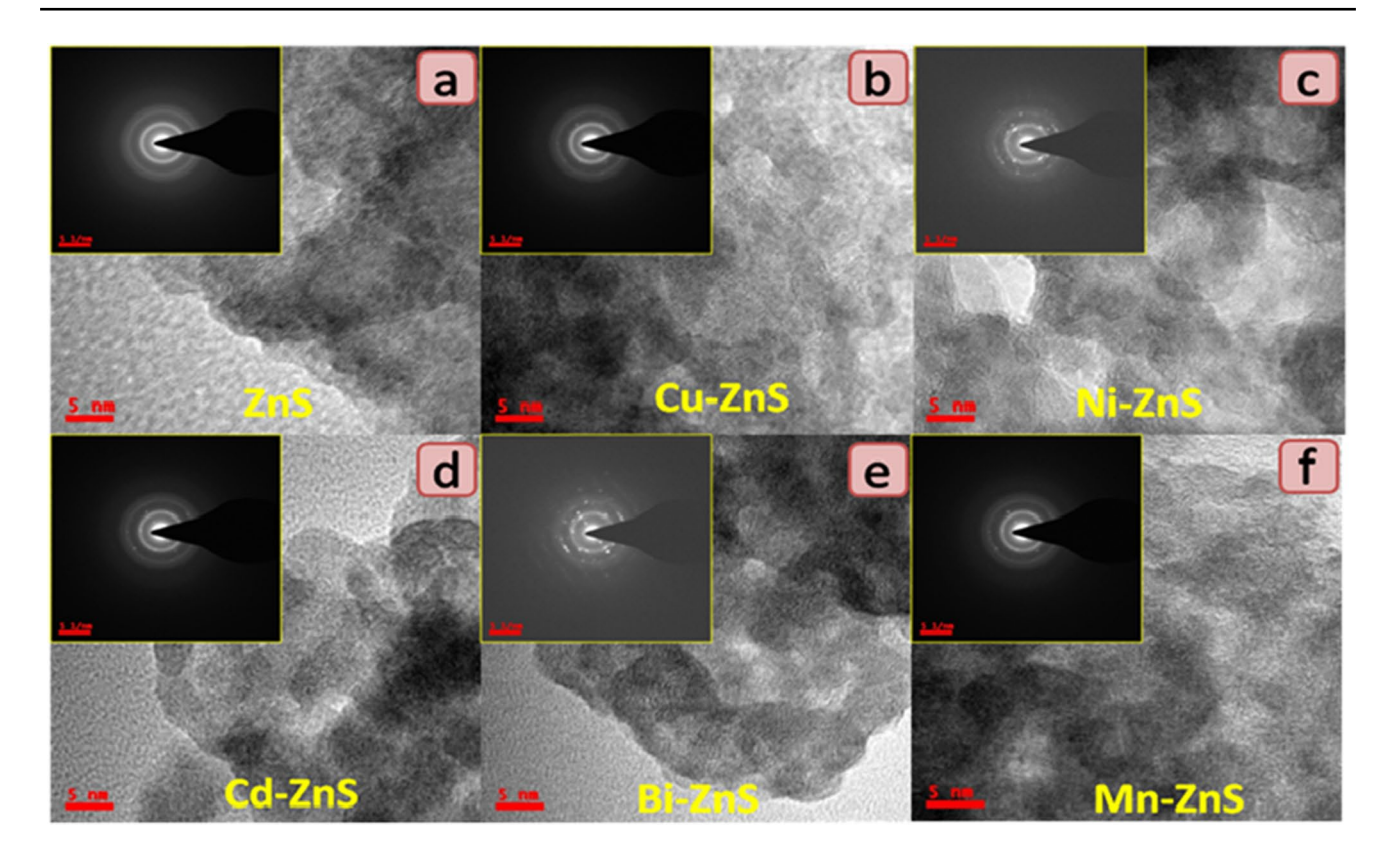
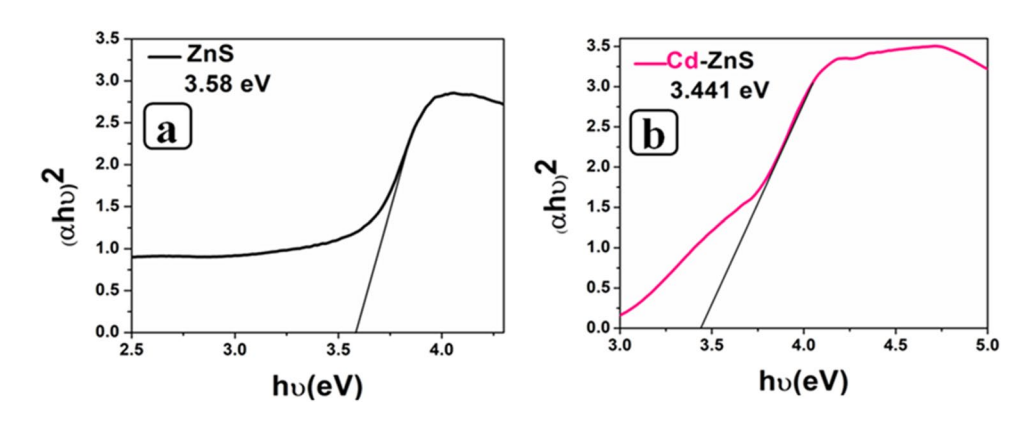


Fig. 4 TEM and SAED patterns (inset) of a sf-ZnS, b sf-Cu-ZnS, c sf-Ni-ZnS, d sf-Cd-ZnS, e sf-Bi-ZnS, and f sf-Mn-ZnS

Fig. 5 Bandgap calculations of a sf-ZnS and b sf-Cd-ZnS



site between the fundamental energy level and thus helps decrease the HOMO–LUMO gap than that of undoped zinc sulfide. While doping, an exchange interaction occurs between valence band sp electrons and localized d electrons of doped ions (Harish et al. 2017) as observed in UV–Vis spectra and bandgap spectra. Among the doped metal ions, sf-Cd-ZnS has the lowest bandgap (3.441 eV), the lowest among the reported works. This observation highlights the effect of doping on ZnS nanoparticles and the efficiency of the HMDS-assisted method, which helped to synthesize capping agent-free nanoparticles with control in size. Similarly, in the bandgap calculated for Cu-, Ni-, Bi-, and Mn-doped ZnS (Fig. S3, Table 1), a variation is displayed compared

to pure ZnS. A fine-tuning in the bandgap resulted in the change in absorption capacitance from UV to the visible region, enhancing the overall photocatalytic activity.

Effect of metal doping on photochemical degradation of dyes using zinc sulfides

Photocatalysis is a well-established technology for environmental remediation. The doped ZnS photocatalysts exhibited excellent photocatalytic efficiencies since the high conduction band of ZnS is maintained even after doping (Michael et al. 2015). Apart from the bandgap tuning, the HMDS-assisted method provided metal-doped



Table 1 Bandgap and rate constant determined for the photocatalytic degradation of dyes

Substance	Bandgap	Lifetime	Rate constant value (min ⁻¹)	
	(eV)	(ns)	Rhodamine B	Methylene blue
ZnS	3.58	2.47	-2.345×10^{-2}	-6.23×10^{-2}
sf-Cu-ZnS	3.56	2.66	-7.254×10^{-2}	-7.066×10^{-2}
sf-Ni-ZnS	3.53	2.68	-8.888×10^{-2}	-10.01×10^{-2}
sf-Cd-ZnS	3.44	3.27	-18.6×10^{-2}	-28.23×10^{-2}
sf-Bi-ZnS	3.49	2.90	-10.405×10^{-2}	-14.69×10^{-2}
sf-Mn-ZnS	3.45	3.05	-12.584×10^{-2}	-20.61×10^{-2}

ZnS without any organic insulating agent at the immediate surroundings of the particles. We tested the degrading abilities of these materials by measuring the absorbance dye solutions (RhB and MB) (Fig. S4 and S5) and calculating the rate constants of degradation reactions (Table 1). The plots of change in concentration of dyes versus time (Figs. 6, 7, S6, S7, and S8) in the presence of various catalysts showed that the dye degradation followed first-order kinetics. The rate of dye degradation reaction was low $(-2.345 \times 10^{-2} \text{ min}^{-1} \text{ for RhB and } -6.23 \times 10^{-2} \text{ min}^{-1}$ for MB) in undoped ZnS nanoparticle catalyst, whereas the rate increased considerably with doping. While using sf-Cd-ZnS nanoparticles as the catalyst, an approximately

eightfold increase of reaction rate was observed $(-18.6 \times 10^{-2} \text{ min}^{-1} \text{ for RhB and} - 28.23 \times 10^{-2} \text{ min}^{-1}$ for MB). We have performed few controlled experiments to highlight the importance of the photocatalysis. In the first reaction, the degradation of dyes (RhB and MB) was monitored in the absence of catalyst but in the presence of light (photolysis), while the second degradation reaction was conducted in the presence of catalyst in dark condition (catalysis). From the results (Fig. S9), it was clear that to degrade the chosen pollutants, the catalyst shows its efficiency only in the presence of sunlight (photocatalysis). To know the morphological stability of the used catalyst, we have performed the FESEM analysis for the recycled catalyst and noted that the morphology of the catalyst has been deformed after the fifth cycle, which might be the reason for the decrease in the activity (Fig. S10).

The metal doping creates impurity levels in the forbidden band, accommodating charge carriers and thereby increasing photocatalytic activity. Presumably, while doping with Cd, it maintained a relatively high conduction band compared to others, resulting in the best catalytic activity. The photocatalytic efficiency is related to the efficient separation of photo-induced electrons and holes. It appeared that the charge separation was effective in the case of Cd, which showed excellent catalytic behavior. This explanation is supported by the lifetime of charge

Fig. 6 a (C/C_0) and b $\ln(C/C_0)$ vs time for degradation of rhodamine B dve solution by sf-ZnS and sf-Cd-ZnS nanoflakes

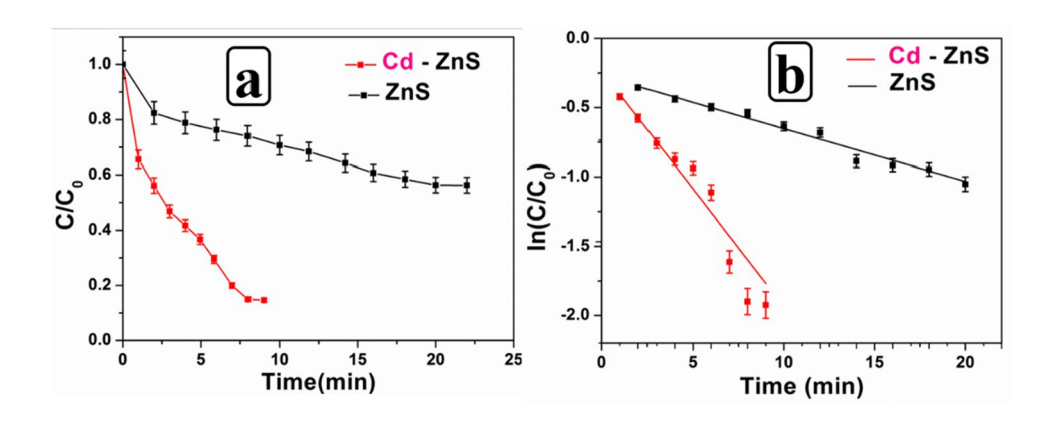


Fig. 7 a (C/C_0) and b $\ln(C/C_0)$ vs time for degradation of methylene blue dye solution by sf-ZnS and sf-Cd-ZnS nanoflakes

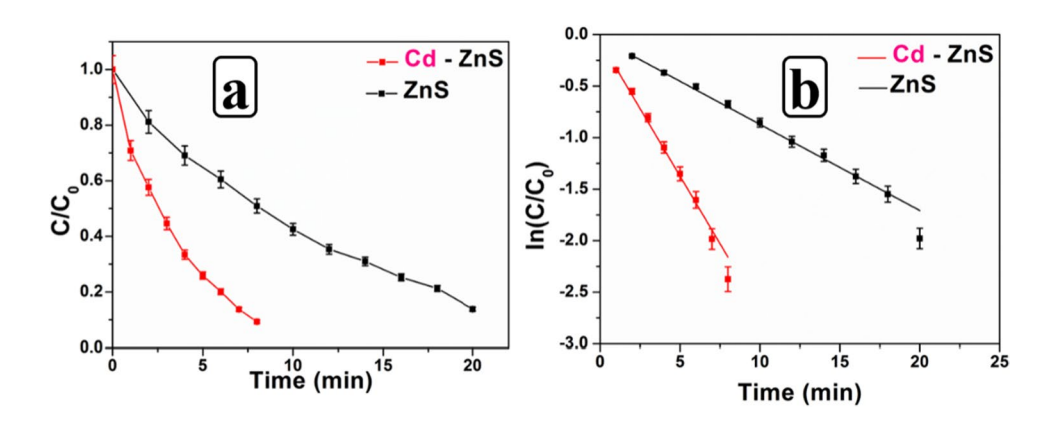
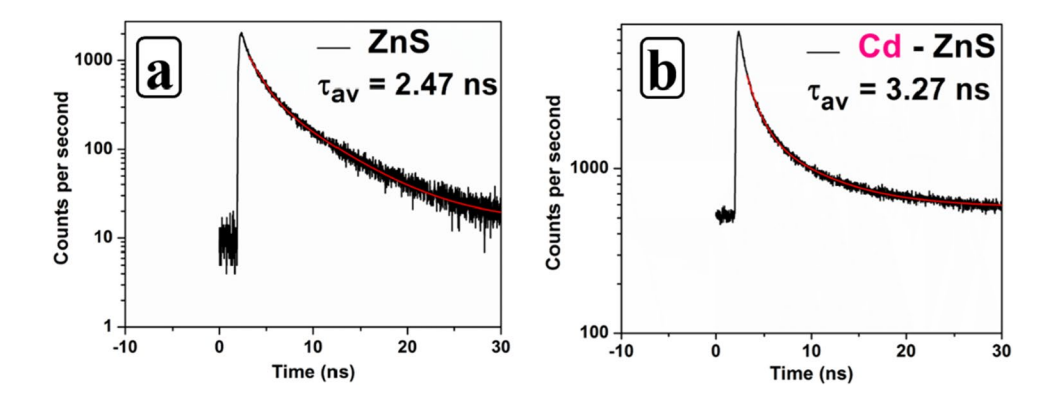




Fig. 8 Plot of lifetime of a sf-ZnS, b sf-Cd-ZnS nanoflakes



separation (Fig. 8), where Cd-doped ZnS showed a higher lifetime than other nanoparticles synthesized (Fig. S11).

Table 2 depicts the comparison of literature data on the photocatalytic performances of ZnS and doped ZnS-based photocatalysts to purify wastewater. To endorse our study, the results were compared with standard TiO₂-P25 nanoparticles (Ren et al. 2006; Natarajan et al. 2011). Interestingly, **sf-Cd-ZnS** was repeatedly used, and it showed good activity even after five cycles of degradation of both RhB and MB (Fig. S12 and S13 for RhB and MB, respectively).

The mechanism of degradation reaction is well-known in the literature. When sunlight falls on the semiconductor, the electrons from the valence band get excited to the conduction band. While doping with metal ions, it creates intermediate trap states decreasing the bandgap. More electrons get excited to these states since less energy is needed

for the excitation of electrons (Mageswari et al. 2013; Mote et al. 2013; Dilpazir et al. 2015; Kurnia and Hart 2015; Madkour et al. 2016; Pricilla Jeyakumari et al. 2017; Mosavi and Kafashan 2019; Kumar et al. 2019; Gbashi and Hussein 2020; Ramki et al. 2020; Bindu and Anila 2021; Mostafa et al. 2021; Das et al. 2021; Samba Vall et al. 2021) and this will increase the number of charge carriers available for dye degradation, which results in increasing photocatalytic activity (Poormohammadi-Ahandani et al. 2014; Prasad and Balasubramanian 2017). As soon as electrons are excited to the conduction bands or trap states, holes are created in the valence band. These holes are taken immediately by water adsorbed on the catalyst surface to undergo oxidation and produce hydroxyl radical, OH. These hydroxyl radicals so produced oxidize the organic species (dyes) adsorbed on the surface of catalysts to simpler molecules, CO₂, H₂O. The

Table 2 Photocatalytic performances of ZnS and metal-doped ZnS-based photocatalysts for the waste water treatment

Type of catalyst	Pollutant concentration	Amount of catalyst	Time (min)	Efficiency (%)	References
ZnS	RhB 10 mg/l	1000 mg/l	30	_	Luo et al. 2012
PVP-ZnS	MB 10 mg/l	100 mg/l	360	65	Soltani et al. 2013
$Zn_{0.2}Cd_{0.8}S$	MB 10 mg/l	1600 mg/l	60	96	Song et al. 2010
ZnS	MB 10 mg/l	300 mg/l	60	93	Zhang 2014
ZnS	RhB 10 mg/l	750 mg/l	210	82	La Porta et al. 2017
ZnS	RhB 20 mg/l	200 mg/l	180	70	Ayodhya and Veerabhadram 2016
ZnS	MB 50 mg/l	500 mg/l	120	78	Ye et al. 2010
Ni-ZnS	MB 10 mg/l	500 mg/l	120	52	Othman et al. 2019
Ni-ZnS	RhB 10 mg/l	500 mg/l	180	87	Zhao et al. 2019
Mn-ZnS	MB 5 mg/l	Film in 20 ml	180	99	Kannan et al. 2020
Cu-ZnS	MB 10 mg/l	1000 mg/l in 50 ml	300	100	Chauhan et al. 2014
Cu-ZnS	MB 10 μM	250 mg/l in 100 ml	60	74	Prasad and Balasubramanian 2017
Sn-ZnS	MB 20 ppm	1000 mg/l	180	93	Ramki et al. 2020
TiO ₂ -P25	RhB 5 mg/l	1000 mg/l	300	22	Ren et al. 2006
TiO ₂ -P25	RhB 2.8×10^{-5} M	1600 mg/l	180	96	Natarajan et al. 2011
sf-ZnS	RhB 10 mg/l	500 mg/l	22	40	Present work
	MB 10 mg/l	500 mg/l	20	74	
sf-Cd-ZnS	RhB 10 mg/l	500 mg/l	9	98	Present work
	MB 10 mg/l	500 mg/l	8	99	



electrons in the conduction band react with oxygen to produce anionic superoxide radical species $O_2^{-\bullet}$, which produces hydroperoxyl radicals, which in turn leads to the formation of H_2O_2 and undergo dissociation to form OH^{\bullet} , which degrades the organic dyes present on the surface (Fig. 9). In the case of Cd, this process is happening at a faster rate and thus enhances the photocatalytic activity. In contrast, there is a decrease in activity in other cases due to the recombination of charge carriers, resulting in the unavailability of charge carriers for the dye to participate in photocatalysis.

The retarding effect of capping agents on photocatalysis

The purpose of capping agents aimed for controlling the particle size in nano region, but impact, necessity, and further consequences of those capping agents were decided based on targeted applications. Adverse effects of capping agents were elaborated in the "Introduction" (Fig. 1). The presence of capping agents decreases the communication between the particles, which hinders the mobility of charge carrier. As we discussed in previous sections, capping agents hide the active centers of absorption which leads to reduced surface area and simultaneously affects the catalytic activity and finally reduces device efficiency and catalyst activity.

Photocatalysis is a surface phenomenon. In this area of research, capping agents play a major role in the photodegradation of organic dyes, since they are at interface between dye molecules and catalyst surface. A reduction of visible emission spectra was observed for ZnO nanoparticles capped with capping agents such as polyvinylpyrrolidone (PVP), hexamine, tetraethylammonium bromide (TEAB), tetraoctlyammonium bromide (TOAB), and cetyltrimethylammonium bromide (CTAB) (Singla et al. 2009; Sudha et al. 2012; Sudha and Rajarajan 2013). In support, the increase

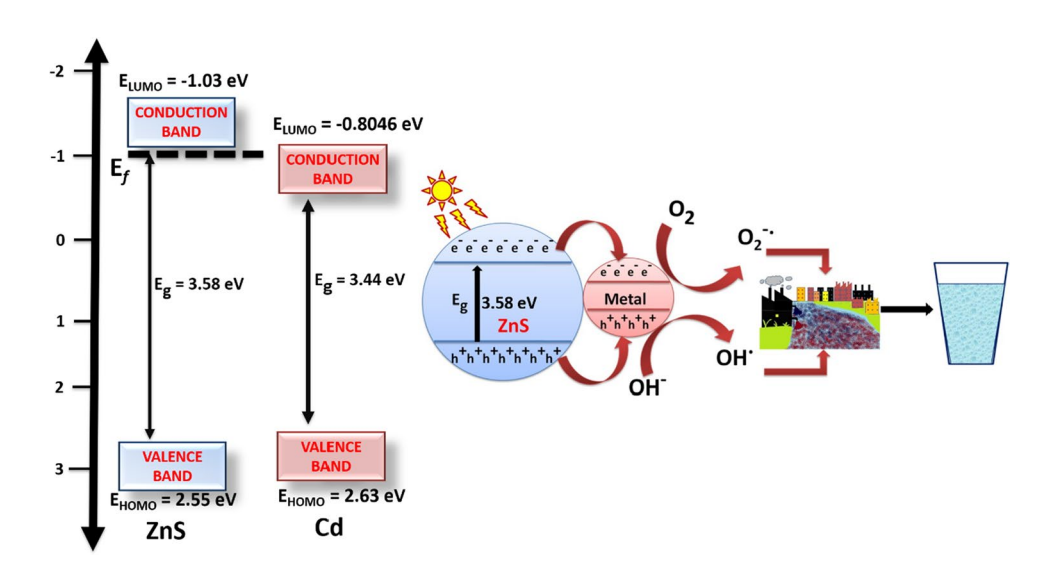
decreased the photocatalytic efficiency of the catalyst, by trapping the electron generated by excitation of photocatalyst by humic acid (Cao and Zhang 2011; Chandran et al. 2014). From our group, Srinivas et al. (2019) endorsed the surfactant-free approach over the PVP-stabilized SnS₂ nanostructures for the organic dye degradation and reduction of toxic heavy metals. The electrons and holes created by the excitation of photocatalysts are not able to reach the surface due to the covering created by capping agent, which restricts the formation of superoxide radical anion and hydroxide radicals, which are the active species required for dye degradation. This ineptitude of active species formation decreases the photocatalytic activity of the photocatalyst.

in concentration of humic acid as capping agent on ZnO

Antibacterial activity of metal-doped zinc sulfides

An earlier report (Song et al. 2018) suggested that the sharp edges and corners of nanoflakes can cause breakage of the bacterial cell membrane, which releases the oxidation products to cause oxidation of protein and eventually leads to cell death (Singh et al. 2014; Chu et al. 2014; Gnanamozhi et al. 2020). The organic-free exposed surface of nanoflakes produced in our HMDS-assisted method could help to improve the adhesion between Staphylococcus aureus (S. aureus) bacteria and the nanoparticles. The antibacterial activity of ZnS and metal-doped ZnS against Gram-positive S. aureus was studied by the zone of inhibition method. Figure 10 depicts the results of the antibacterial study at different concentrations of each nanoparticle produced in this work. In these pictures of agar–agar plates, the zone of inhibition is visible around the ZnS materials. The results illustrate that as the concentration of materials increased, the zone of inhibition also increased (Figs. S14 and S15) and thus,

Fig. 9 Schematic illustration of energy band mechanism of photocatalysis by doped ZnS nanoparticles





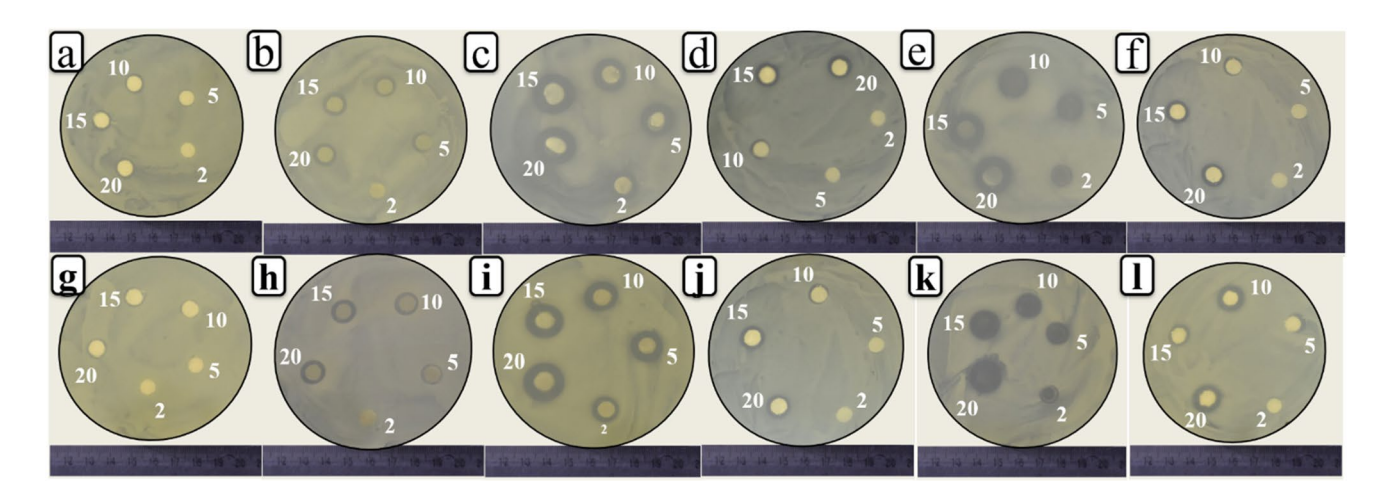


Fig. 10 Agar-agar plates showing the zone of inhibition test results using the concentrations 2, 5, 10, 15, and 20 mg/ml of a sf-ZnS, b sf-Cu-ZnS, c sf-Ni-ZnS, d sf-Cd-ZnS, e sf-Bi-ZnS, and f sf-Mn-ZnS

for 12 h, and g sf-ZnS, h sf-Cu-ZnS, i sf-Ni-ZnS, j sf-Cd-ZnS, k sf-Bi-ZnS. and l sf-Mn-ZnS for 24 h

the nanoparticle synthesized was effective against Grampositive bacteria (S. aureus).

It is clear that the metal-doped ZnS showed higher activity than the undoped ZnS. The Ni-doped ZnS showed the highest activity among all doped ZnS. As explained in the existing reports, the nanoparticles like ZnS attack the cytoplasmic and extra-cytoplasmic targets when they enter through the bacterial membrane. This interaction results in the production of biologically reactive oxygen species (R.O.S) like superoxide anion (O₂), hydroxyl ion (OH⁻), and hydroxyl radicals (OH[•]). In addition to this, the metal ions do have an affinity towards carboxyl (-COOH), amino (-NH2), thiol (R-SH), and imidazole (C₃H₄N₂) groups present in the microbial membrane proteins, which cause a change in protein functions and nucleic acids of the targeted organism. These changes enhance the cell permeability, which in turn cause DNA damage and oxidation of protein, eventually causing cell death (Singh et al. 2014; Chu et al. 2014; Harish et al. 2017; Gnanamozhi et al. 2020). The results of the present study limn the efficiency of Ni-doped ZnS as an antibacterial agent.

Conclusion

In summary, we have successfully produced surfactant-free ZnS (\mathbf{sf} - \mathbf{ZnS}) and metal-doped ZnS (\mathbf{sf} - \mathbf{m} - \mathbf{ZnS}): m = Cu, Ni, Cd, Bi, Mn) nanoparticles using the HMDS-assisted method. The X-ray diffraction and SAED patterns confirmed the formation of the cubical phase of crystal-line ZnS nanoparticles. The bandgap tuning of ZnS was achieved by doping with transition metals as confirmed through measurements of the optical property. The \mathbf{sf} - \mathbf{Cd} - \mathbf{ZnS} exhibited higher photocatalytic activity among the

other doped and undoped ZnS nanoparticles in degrading organic dyes (RhB and MB) under visible light. In the case of antibacterial activity, **sf-Ni-ZnS** showed higher activity against Gram-positive bacteria, *Staphylococcus aureus*. The absorption edge of the doped ZnS materials shifts to the lower energy region compared to pure ZnS. Simultaneously, the activity of the doped ZnS nanoparticles has increased a maximum of eightfold for the photodegradation of organic dyes in comparison to undoped ZnS nanoparticles. Thus, this work highlights the impact of tuning the bandgap of wide bandgap semiconductor photocatalyst, ZnS, and its application in industrial wastewater treatment and its role as an antibacterial agent.

Supplementary Information The online version contains supplementary material available at https://doi.org/10.1007/s11356-022-19677-y.

Acknowledgements The project is funded partially by IOE grants of University of Hyderabad. The authors thank the Centre for Nanotechnology at the University of Hyderabad for the TEM facility. A. J. thanks UGC-JRF for the fellowship.

Author contribution Anju Joseph performed the experiment and wrote the manuscript. Srinivas Billakanti contributed significantly to data analysis and manuscript preparation. Manzoor Ahmad Pandit contributed in data collection. Sajmina Khatun and Aravind Kumar Rengan performed and analyzed the antibacterial study. Conception of the study, manuscript correction, supervision, and validation by Krishnamurthi Muralidharan.

Funding The authors highly appreciate the financial support from the Ministry of Human Resource Development (MHRD-IN) for Institute of Eminence (IOE) grants.

Data availability All data generated or analyzed during this study are included in this published article.



Declarations

Ethics approval The manuscripts reporting studies are not applicable for human participants, human data, or human tissue. The manuscript does not contain any individual person's data in any form.

Consent to participate Not applicable.

Consent for publication Not applicable.

Competing interests The authors declare no competing interests.

References

- Ahmad Pandit M, Billakanti S, Muralidharan K (2019) A simplistic approach for the synthesis of CuS-CdS heterostructure: a novel photo catalyst for oxidative dye degradation. J Environ Chem Eng 8:103542. https://doi.org/10.1016/j.jece.2019.103542
- Ahmad Pandit M, Srinivas B, Kumar DSH, Manigandan R, Muralidharan K (2020) Chalcopyrite with magnetic and dielectric properties: an introductory catalyst for 4-nitrophenol reduction. J Phys Chem C 124:18010–18019. https://doi.org/10.1021/acs.jpcc.0c02697
- Arun Kumar G, Bhojya Naik HS, Viswanath R, Suresh Gowda IK, Santhosh KN (2017) Tunable emission property of biotin capped Gd:ZnS nanoparticles and their antibacterial activity. Mater Sci Semicond Process 58:22–29. https://doi.org/10.1016/j.mssp.2016. 11.002
- Ayodhya D, Veerabhadram G (2016) Green synthesis, optical, structural, photocatalytic, fluorescence quenching and degradation studies of ZnS nanoparticles. J Fluoresc 26:2165–2175. https://doi.org/10.1007/s10895-016-1912-2
- Bindu KR, Anila EI (2021) Optimized synthesis temperature and doping concentration of copper in zinc sulphide nanoparticles for green emission. Mater Sci Semicond Process 121:105317. https:// doi.org/10.1016/j.mssp.2020.105317
- Cadis AI, Popovici EJ, Bica E, Perhaita I, BarbuTudoran L, Indrea E, SilaghiDumitrescu L (2011) Synthesis of manganese doped zinc sulphide nanocrystalline powders by wet-chemical synthesis route. Dig J Nanomater Biostructures 6:1479–1489. https://doi.org/10.13140rg.2.1.2242.2249
- Cao Z, Zhang Z (2011) Deactivation of photocatalytically active ZnO nanoparticle and enhancement of its compatibility with organic compounds by surface-capping with organically modified silica. Appl Surf Sci 257:4151–4158. https://doi.org/10.1016/j.apsusc. 2010.11.188
- Chandran P, Netha S, Sudheer Khan S (2014) Effect of humic acid on photocatalytic activity of ZnO nanoparticles. J Photochem Photobiol. B 138:155–159. https://doi.org/10.1016/j.jphotobiol. 2014.05.013
- Chauhan R, Kumar A, Chaudhary RP (2014) Photocatalytic degradation of methylene blue with Cu doped ZnS nanoparticles. J Lumin 145:6–12. All rights reserved. https://doi.org/10.1016/j.jlumin.2013.07.005
- Chu Z, Zhang S, Zhang B, Zhang C, Fang C-Y, Rehor I, Cigler P, Chang H-C, Lin Ge, Liu R, Li Q (2014) Unambiguous observation of shape effects on cellular fate of nanoparticles. Sci Rep 4:4495. https://doi.org/10.1038/srep04495
- Corrado C, Jiang Y, Oba F, Kozina M, Bridges F, Zhang JZ (2009) Synthesis, structural, and optical properties of stable ZnS:Cu, Cl, nanocrystals. J Phys Chem A 113:3830–3839. https://doi.org/10.1021/jp809666t

- Das P, Tantubay K, Ghosh R, Dam S, Moni Baskey (Sen) (2021) Transformation of CuS/ZnS nanomaterials to an efficient visible light photocatalyst by 'photosensitizer' graphene and the potential antimicrobial activities of the nanocomposites. Environ Sci Pollut Res 35:49125–49138. https://doi.org/10.1007/s11356-021-14068-1
- Dilpazir S, Siddiq M, Iqbal A (2015) Synthesis of zinc sulphide nanostructures by co-precipitation: effects of doping on electro-optical properties. Kenk Nanotec Nanosci 1:34–39. https://doi.org/10. 13140/rg.2.1.1087.8887
- Ferreira-Neto EP, Ullah S, da Silva TCA, Domeneguetti RR, Perissinotto AP, de Vicente FS, Rodrigues-Filho UP, Ribeiro SJL (2020) Bacterial nanocellulose/MoS₂ hybrid aerogels as bifunctional adsorbent/photocatalyst membranes for in-flow water decontamination. ACS Appl Mater Interfaces 12:41627–41643. https://doi.org/10.1021/acsami.0c14137
- Gbashi KR, Hussein AK (2020) Cu-doped ZnS coatings for optoelectronics with enhanced protection for UV radiations. J Mater Sci: Mater Electron 31:17258–21726. https://doi.org/10.1007/ s10854-020-04280-z
- Gnanamozhi P, VengudusamyRenganathan S-M, Pandiyan V, Antony Arockiaraj M, Alharbi NS, Kadaikunnan S, Khaled JM, Alanzi KF (2020) Influence of nickel concentration on the photocatalytic dye degradation (methylene blue and reactive red 120) and antibacterial activity of ZnO nanoparticle. Ceram Int 46:18322–18330. https://doi.org/10.1016/j.ceramint.2020.05.054
- Harish S, Archana J, Navaneethan M, Ponnusamy S, Singh A, Gupta V, Aswal DK, Ikeda H, Hayakawa Y (2017) Synergetic effect of CuS@ZnS nanostructures on photocatalytic degradation of organic pollutant under visible light irradiation. RSC Adv 7:34366–34375. https://doi.org/10.1039/c7ra04250g
- Hussain I, Mohapatra D, Dhakal G, Lamiel C, Mohamed SG, Sayed MS, Shim J-J (2020) Different controlled nanostructures of Mndoped ZnS for high-performance supercapacitor applications. J Energy Storage 32:101767. https://doi.org/10.1016/j.est.2020. 101767
- Jung HJ, Koutavarapu R, Lee S, Kim JH, Choi HC, Choi MY (2017) Enhanced photocatalytic activity of Au-doped Au@ZnO coreshell flower-like nanocomposites. J Alloys Compd. https://doi. org/10.1016/j.jallcom.2017.11.378
- Kannan S, Subiramaniyam NP, Sathishkumar M (2020) Effect of annealing temperature and Mn doping on the structural and optical properties of ZnS thin films for enhanced photocatalytic degradation under visible light irradiation. Inorg Chem Commun 119:108068. https://doi.org/10.1016/j.inoche.2020.108068
- Kole AK, Kumbhakar P (2012) Effect of manganese doping on the photoluminescence characteristics of chemically synthesized zinc sulfide nanoparticles. Appl Nanosci 2:15–23. https://doi.org/10. 1007/s13204-011-0036-x
- Kumar BG, Srinivas B, Muralidharan K (2017) Photo-responsive Bi₂S₃ nanoflakes: synthesis and device fabrication at ambient conditions. Mater Res Bull 89:108–115. https://doi.org/10.1016/j.mater resbull.2017.01.029
- Kumar V, Rawal I, Kumar V, Goyal PK (2019) Efficient UV photodetectors based on Ni-doped ZnS nanoparticles prepared by facial chemical reduction method. Phys b: Condens Matter 575:411690. https://doi.org/10.1016/j.physb.2019.411690
- Kuppayee M, Vanathi Nachiyar GK, Ramasamy V (2011) Synthesis and characterization of Cu²⁺ doped ZnS nanoparticles using TOPO and SHMP as capping agents Appl. Surf Sci 257:6779–6786. https://doi.org/10.1016/j.apsusc.2011.02.124
- Kurnia F, Hart JN (2015) Band-gap control of zinc sulfide: towards an efficient visible-light-sensitive photocatalyst. ChemPhysChem 16:2397–2402. https://doi.org/10.1002/cphc.201500264
- La Porta FA, Nogueira AE, Gracia L, Pereira WS, Botelho G, Mulinari TA, Andres J, Longo E (2017) An experimental and theoretical investigation on the optical and photocatalytic properties



- of ZnS nanoparticles. J Phys Chem Solids 103:179–189. https://doi.org/10.1016/j.jpcs.2016.12.025
- Luo M, Liu Y, Juncheng Hu, Li J, Liu J, Richards RM (2012) General strategy for one-pot synthesis of metal sulfide hollow spheres with enhanced photocatalytic activity. Appl Catal B 125:180–188. https://doi.org/10.1016/j.apcatb.2012.05.041
- Madkour M, Salih T, Al-Sagheer F, Bumajdad A (2016) Nano-heterostructured photo-stable Cd_xZn_{1-x}S heterojunction as a non-photocorrosive visible light active photocatalyst. Opt Mater Express 6:2857–2870. https://doi.org/10.1364/OME.6.002857
- Mageswari S, Dhivya L, Palanivel B, Murugan R (2013) Influence of bismuth doping on the structural and optical properties of ZnS thin films and nanopowders. Phys Scr 88:65703. https://doi.org/ 10.1088/0031-8949/88/06/065703
- Michael RJV, Theerthagiri J, Madhavan J, Umapathy MJ, Manoharan PT (2015) Cu₂S-incorporated ZnS nanocomposites for photocatalytic hydrogen evolution. RSC Adv 5:30175–30186. https://doi.org/10.1039/c5ra03621f
- Mosavi SM, Kafashan H (2019) Physical properties of Cd-doped ZnS thin films. Superlattices Microstruct 126:139–149. https://doi.org/10.1016/j.spmi.2018.12.002
- Mostafa M, El Nady J, Ebrahim SM, Elshaer AM (2021) Synthesis, structural, and optical properties of Mn²⁺ doped ZnS quantum dots for biosensor application. Opt Mater 112:110732. https://doi.org/10.1016/j.optmat.2020.110732
- Mote VD, Purushotham Y, Dole BN (2013) Structural, morphological and optical properties of Mn doped ZnS nanocrystals. Cerâmica 59:395–400. https://doi.org/10.1590/S0366-69132013000300008
- Murugadoss G (2013) Luminescence properties of co-doped ZnS:Ni, Mn and ZnS:Cu, Cd nanoparticles. J Lumin 132:2043–2048. https://doi.org/10.1016/j.jlumin.2012.02.011
- Naofumiuekawa, Mayumi ouchi, Chun Ming wen, Takaakimatsumoto, Takashi kojima (2015) Synthesis of copper ion doped ZnS phosphor sols by peptization process of sulfide-citrate complex precipitates. J Ceram Soc Jpn Suppl 123: 924-928.https://doi.org/10.2109/jcersj2.123.924
- Natarajan TS, Thomas M, Natarajan K, Bajaj HC, Tayade RJ (2011) Study on UV-LED/TiO₂ process for degradation of Rhodamine B dye. Chem Eng J 169:126–134. https://doi.org/10.1016/j.cej. 2011.02.066
- Othman AA, Osman MA, Ali MA, Mohamed WS, Ibrahim EMM (2019) Sonochemically synthesized Ni-doped ZnS nanoparticles: structural, optical, and photocatalytic properties. J Mater Sci Mater Electron 31:1752–1767. https://doi.org/10.1007/s10854-019-02693-z
- Peng WQ, Cong GW, Qu SC, Wang ZG (2006) Synthesis and photoluminescence of ZnS: Cu nanoparticles. Opt Mater 29:313–317. https://doi.org/10.1016/j.optmat.2005.10.003
- Poormohammadi-Ahandani Z, Habibi-Yangjeh A, Pirhashemi M (2014) Ultrasonic-assisted method for preparation of Cu-doped ZnS nanoparticles in water as a highly efficient visible light photocatalyst. Phys Chem Res 2:76–89. https://doi.org/10.22036/PCR. 2014.4012
- Prasad N, Balasubramanian K (2017) Optical phonon and efficient visible and infrared photocatalytic activity of Cu doped ZnS micro crystals. Spectrochim Acta A Mol Biomol Spectrosc 173:687–694. https://doi.org/10.1016/j.saa.2016.10.014
- Pricilla Jeyakumari A, Sumathi M, Thirumagal N, Uthaya Kumar M (2017) Chemical precipitation synthesis of Fe, Ni, and Co doped zinc sulphide nanoparticles. J Appl Phys 1:64–70. https://doi.org/10.9790/4861-17002016470
- Qumar U, Ikram M, Imran M, Haider A, Ul-Hamid A, Haider J, Riaz KN, Ali S (2020) Synergistic effect of Bi-doped exfoliated MoS₂ nanosheets on their bactericidal and dye degradation potential. Dalton Trans 49:5362–5371. https://doi.org/10.1039/d0dt00924e

- Ramki K, RajaPriya A, Sakthivel P, Murugadoss G, Thangamuthu R, Rajesh Kumar M (2020) Rapid degradation of organic dyes under sunlight using tin-doped ZnS nanoparticles. J Mater Sci Mater Electron 31:8750–8760. https://doi.org/10.1007/s10854-020-03410-x
- Ren W, Ai Z, Jia F, Zhang L, Fan X, Zou Z (2006) Low temperature preparation and visible light photocatalytic activity of mesoporous carbon-doped crystalline TiO₂. Appl Catal b: Environ 69:138– 144. https://doi.org/10.1016/j.apcatb.2006.06.015
- Rose A, Shunmugapriya B, Maiyalagan T, Vijayakumar T (2020) Investigation on the electrochemical properties of hydrothermally synthesized pure and nickel doped zinc sulfide microspheres for supercapacitor electrode applications. J Mater Sci: Mater Electron 31:19204–19212. https://doi.org/10.1007/s10854-020-04456-7
- Sahraei R, Darafarin S (2014) Preparation of nanocrystalline Ni doped ZnS thin films by ammonia-free chemical bath deposition method and optical properties. J Lumin 149:170–175. https://doi.org/10.1016/j.jlumin.2014.01.040
- Samba Vall CM, Chaik M, Tchenka A, Hnawi S, Mellalou A, El kissani A, Aggour M, Outzourhit A (2021) Effect of chromium percentage doping on the optical, structural, morphological and electrical properties of ZnS: Cr thin films. Phys e: Low-Dimens Syst Nanostructures 130:114694. https://doi.org/10.1016/j.physe.2021. 114694
- Singh PK, Sharma PK, Kumar M, Dutta R, Sundaram S, Pandey AC (2014) Red luminescent manganese-doped zinc sulphide nanocrystals and their antibacterial study. J Mater Chem B 2:522– 528. https://doi.org/10.1039/c3tb21363c
- Singla ML, Muhamed Shafeeq M, Kumar M (2009) Optical characterization of ZnO nanoparticles capped with various surfactants. J Lumin 129:434–438. https://doi.org/10.1016/j.jlumin.2008.11.021
- Soltani N, Saion E, Mahmood Mat Yunus W, Navasery M, Bahmanrokh G, Erfani M, Zare M R, Gharibshahi E (2013) Photocatalytic degradation of methylene blue under visible light using PVP-capped ZnS and CdS nanoparticles. Sol Energy 97:147–154. https://doi.org/10.1016/j.solener.2013.08.023
- Song L, Zhang S, Chen B, Ge J, Jia X (2010) Fabrication of ternary zinc cadmium sulfide photocatalysts with highly visible-light photocatalytic activity. Catal Commun 11:387–390. https://doi.org/ 10.1016/j.catcom.2009.11.007
- Song J, Zhang F, Huang Y, Keller AA, Tang X, Zhang W, Jia W, Santos J (2018) Highly efficient bacterial removal and disinfection by magnetic barium phosphate nanoflakes with embedded iron oxide nanoparticles. Environ Sci: Nano 5:1341–1349. https://doi.org/10.1039/c8en00403j
- Srinivas B, Muralidharan K (2018) Facile preparation of surfactant or support material free CdS nanoparticles with enhanced photocatalytic activity. J Environ Chem Eng 6:1250–1256. https://doi.org/ 10.1016/j.jece.2018.01.041
- Srinivas B, Kumar BG, Muralidharan K (2015) Stabilizer free copper sulphide nanostructures for rapid photocatalytic decomposition of rhodamine B. J Mol Catal A Chem 410:8–18. https://doi.org/10. 1016/j.molcata.2015.08.028
- Srinivas B, Ahmad Pandit M, Muralidharan K (2019) Importance of clean surfaces on the catalyst: SnS₂nanorings for environmental remediation. ACS Omega 4:14970–14980. https://doi.org/10.1021/acsomega.9b01766
- Sudha M, Rajarajan M (2013) Deactivation of photocatalytically active ZnO nanoparticle by surface capping with poly vinyl pyrrolidone. J Appl Chem 3:45–53. https://doi.org/10.9790/5736-0334553
- Sudha M, Senthilkumar S, Hariharan R, Suganthi A, Rajarajan M (2012) Controlled reduction of the deleterious effects of photocatalytic activity of ZnO nanoparticles by PVA capping. J Sol-Gel Sci Technol 61:14–22
- Suganthi N, Pushpanathan K (2019a) Cerium doped ZnS nanorods for photocatalytic degradation of turquoise blue H5G dye. J Inorg



- Organomet Polym Mater 29:1141–1153. https://doi.org/10.1007/s10904-019-01077-4
- Suganthi N, Pushpanathan K (2019b) Photocatalytic degradation and antimicrobial activity of transition metal doped mesoporous ZnS nanoparticles. Int J Environ Sci Technol 16:3375–3388. https://doi.org/10.1007/s13762-018-1811-y
- Ummartyotin S, Bunnak N, Juntaro J, Sain M, Manuspiya H (2012) Synthesis and luminescence properties of ZnS and metal (Mn, Cu)-doped-ZnS ceramic powder. Solid State Sci 14:299–304. https://doi.org/10.1016/j.solidstatesciences.2011.12.005
- Velanganni S, Pravinraj S, Immanuel P, Thiruneelakandan R (2018) Nanostructure CdS/ZnO heterojunction configuration for photocatalytic degradation of methylene blue. Phys b: Condens Matter 534:56–62. https://doi.org/10.1016/j.physb.2018.01.027
- Vijai Anand K, Mohan R, Mohan Kumar R, Karl Chinnu M, Jayavel R (2013) Structural and optical properties of high-purity cubic phase ZnS nanoparticles prepared by thermal decomposition route for optoelectronic applications. Proc Indian Natn Sci Acad 79:395– 399. https://doi.org/10.1016/j.molliq.2019.01.121
- Wang W, Chen L, Wang S, Xi B, Xiong S, Qian Y, Zhang Z (2006) Low-temperature synthesis of nearly monodisperse ZnS nanospheres using a facile solution-phase approach. Aust J Chem 59:791–795. https://doi.org/10.1071/CH06170
- Yang P, Song C, Mengkai Lu, Zhou G, Yang Z, Dong Xu, Yuan D (2002) Photoluminescence of Cu⁺ doped and Cu²⁺- doped ZnS

- nanocrystallites. J Phys Chem Solids 63:639–643. https://doi.org/ 10.1016/S0022-3697(01)00206-2
- Ye Z, Kong L, Chen F, Chen Z, Lin Y, Liu C (2010) A comparative study of photocatalytic activity of ZnS photocatalyst for degradation of various dyes. Optik (Stuttg.) 164: 345–354. https://doi.org/10.1016/j.ijleo.2018.03.030
- Zhang S (2014) Preparation of controlled-shape ZnS microcrystals and photocatalytic property. Ceram Int 40:4553–4557. https://doi.org/ 10.1016/j.ceramint.2013.08.131
- Zhang K, Guo L (2013) Metal sulphide semiconductors for photocatalytic hydrogen production. Catal Sci Technol 3:1672–1690. https://doi.org/10.1039/c3cy00018d
- Zhang F, Li Y-H, Li J-Y, Tang Z-R, Yi-Jun Xu (2019) 3D graphene-based gel photocatalysts for environmental pollutants degradation. Environ Pollut 253:365–376. https://doi.org/10.1016/j.envpol. 2019.06.089
- Zhao W-H, Wei Z-Q, Xiao-juan Wu, Zhang X-D, Zhang Li, Wang X (2019) Microstructure and photocatalytic activity of Ni-doped ZnS nanorods prepared by hydrothermal method. Trans Nonferrous Met Soc China 29:157–164. https://doi.org/10.1016/S1003-6326(18)64924-6

Publisher's note Springer Nature remains neutral with regard to jurisdictional claims in published maps and institutional affiliations.





www.chemeurj.org

Insight into the Effect of Stabilizers on Anticancer and Antibacterial Activity of AgBiS₂ Nanomaterial

Anju Joseph⁺,^[a] Sajmina Khatun⁺,^[b] Dasari Sai Hemanth Kumar,^[a] Aravind K. Rengan,^{*[b]} and Krishnamurthi Muralidharan^{*[a]}

Abstract: The near-infrared (NIR) light-absorbing AgBiS₂ nanoparticles can be excited by single-wavelength light, which is the primary characteristic of a photo responsive platform. Chemical synthesis of nanomaterials inevitably requires long-chain organic surfactants or polymers to stabilize them in the nano regime. These stabilizing molecules barricade the interaction of nanomaterials with biological cells. We have produced stabilizer-free (sf-AgBiS₂) and polymer-coated (PEG-AgBiS₂) nanoparticles; and assessed their NIR mediated anticancer and antibacterial activity to evaluate the effect of

stabilizers. **sf-AgBiS**₂ showed better antibacterial activity against Gram-positive Staphylococcus aureus (S. *aureus*) and displayed excellent cytotoxicity against HeLa cells and live 3-D tumour spheroids compared to **PEG-AgBiS**₂ both in presence and absence of NIR radiation. The photothermal therapy (PTT) results illustrated the tumour ablation ability of **sf-AgBiS**₂, which converted light into heat effectively up to 53.3 °C under NIR irradiation. This work demonstrates the importance of synthesizing stabilizer-free nanoparticles to produce safe and highly active PTT agents.

Introduction

The organizations for disease control and prevention reported cancer is the major reason for death worldwide with 22.5% death rate. The standard treatments practiced are surgery, chemotherapy, and radiotherapy.^[1] The usage of these methods is limited due to their adverse effects on healthy cells and the immune system. Further, there exist chances of the generation of secondary cancers.^[2] There are enormous efforts by scientists to develop efficient cancer treatments, among which the NIR-mediated photothermal therapy (PTT) is more attractive owing to its high specificity to tumour cells, non-invasive nature, and minimal side effects. It also helps prevent metastasis by stimulating immune-mediated abscopal phenomenon.^[1-8] NIR light possesses safety advantages like temperature-controlled localized therapy, deep penetration, cancer cell cytotoxicity, and minimal damage to healthy cells.

A good photothermal agent can inhibit the growth of cancer cells effectively. In PTT, photothermal agents absorb NIR light and translate it to heat energy, killing cancer cells.^[1,5] Various researchers have introduced different photothermal

agents, including noble metals like platinum (Pt), palladium (Pd), gold (Au), metal sulphides, and metal selenides. A good photothermal agent is anticipated to have high photothermal conversion efficiency and good photo stability. Bismuth-based materials are significantly attractive due to their broad NIR absorption, in vivo and in vitro photothermal effect, and low cost. Specifically, AgBiS₂ is known for various applications as they are non-toxic, in vivo, and in vitro biocompatible. Again and most prominently as good photothermal agents as they are non-toxic, in vivo, and in vitro biocompatible.

Many methods are available to synthesize AgBiS₂ nanoparticles, including microwave, solvothermal, and solid-state chemical reaction methods. [1,3,6,9-21] These methods involve complicated preparation procedures, high temperatures, and using surfactant or polymer molecules to stabilize the particle size in nano regimes. Nanoparticles interact with various cell biopolymers in the biological environment. The physicochemical interactions between nanoparticles and proteins have a crucial impact on their potency. [22-25] The surface properties of the nanoparticles influence physical and chemical phenomena such as aggregation, an affinity for bacterial membranes, and dissolution. Therefore, it is necessary to understand the stabilizer molecule's impact on the interaction with biological cells.

The stabilizers (long-chain surfactant or polymer molecules) used during the synthesis of nanoparticles stay with particles. They can sometimes be cytotoxic to the healthy cells during treatment and encounter compatibility issues. Lao and coworkers^[23] studied the effects of surface compositional and structural heterogeneity on protein adsorption on gold nanoparticles. Wheeler and co-workers^[24] discussed the engineered silver nanoparticle's mediation in protein corona formation, while Lundqvist et al. studied^[25] the surface implications of polystyrene nanoparticles in a biological fluid. Dawson and co-

E-mail: aravind@bme.iith.ac.in

 [[]a] A. Joseph, D. Sai Hemanth Kumar, Prof. K. Muralidharan School of Chemistry
 University of Hyderabad
 Gachibowli, Hyderabad 500046, Telangana (India)
 E-mail: murali@uohyd.ac.in

[[]b] S. Khatun,⁺ Prof. A. K. Rengan
Department of Biomedical Engineering
Indian Institute of Technology
Kandi-502284, Sangareddy, Telangana (India)

^[+] These authors contributed equally to the manuscript

Supporting information for this article is available on the WWW under https://doi.org/10.1002/chem.202203796



workers explained, through in vitro or in vivo experiments, the key protein recognition motifs that bind with SiO_2 nanoparticle's surface when they adsorb proteins. Though the surface effect has been studied to some extent by varying protein environments, a comparative study on stabilizer's effects by modifying the surface of nanoparticles on their biological activity has been largely overlooked. In order to minimize the complexity and adverse impact of surfactants, we need a simple and effective way to synthesize AgBiS_2 nanoparticles.

Herein, we adapted the hexamethyldisilazane (HMDS) assisted method^[27] to synthesize surfactant-free AgBiS₂ (**sf-AgBiS**₂) and polyethylene glycol decorated AgBiS₂ (**PEG-AgBiS**₂) nanoparticles. A comparative study of anticancer activity against HeLa cells using **sf-AgBiS**₂ and **PEG-AgBiS**₂ reveals the importance of a surfactant-free surface. In tumour treatments, the immunosuppression from chemotherapy is always accompanied by bacterial infection.^[6] Since silver has been known as an antibacterial agent for years,^[28-32] a comparative study of the antibacterial activity of **sf-AgBiS**₂ and **PEG-AgBiS**₂ against clinically derived Gram-positive bacteria, S. *aureus* was also performed. In this work, we have highlighted the importance and advantage of using surfactant-free AgBiS₂ nanoparticles as an effective photothermal and antibacterial agent.

Results and Discussion

Synthesis and characterization

Numerous attempts have been made to identify photo responsive material for simultaneous photothermal and photodynamic therapy. Silver bismuth sulphide (AgBiS₂) is studied well for light-activated sterilization techniques as it can be excited by a single-wavelength light in the NIR region. However, many reported synthetic procedures of AgBiS₂ are tedious and inevitably require stabilizers like surfactants or polymers. In this work, we prepared stabilizer-free nanoparticles sf-AgBiS2 and polyethylene glycol wrapped PEG-AgBiS2, then compared their antibacterial and photothermal anticancer abilities. These materials were prepared successfully by a versatile hexamethyldisilazane (HMDS)-assisted synthetic method. [27a] In this method, thiourea reacts with HMDS to form a polymeric molecule, which then reacts with metal chloride to form metal sulphides and trimethylsilyl chloride as a by-product. The pH monitoring throughout the reaction showed no change indicating the absence of formation of both NH₃ and H₂S, and these reactions are believed to occur via the formation of S-N polymeric intermediate.[27]

HMDS acts as a reducing agent, solvent, and surfactant in the synthesis by forming S–N polymeric intermediate. The advantage of this method is all side products are volatile and can be removed simply by vacuum. Since HMDS or any intermediate in this reaction is removed after nanoparticle formation, the purity of sf-AgBiS₂ is very high. Further, the active sites on the surface of sf-AgBiS₂ are readily available for interactions resulting in higher activity in multiple applications.

In comparison, many other reported methods use long-chain surfactant molecules in the synthesis, which covers the surface and prevents interactions. The presence of these surfactants mostly retards the activity of nanoparticle by forming an intermediate layer between the active surface and substrates. Some surfactants are toxic to human beings also. This sophisticated HMDS-assisted method has been used to produce various surfactant-free metal sulphides, and those results demonstrated increased performance in terms of conductivity, photoresponsivity and catalytic activity. [27,33-38]

The powder X-ray diffraction pattern of **sf-AgBiS**₂ and **PEG-AgBiS**₂ (Figure 1) implies the formation of cubic AgBiS₂ (JCPDS-89-2046).^[10] The major peaks found at 27.451, 31.751, 45.531, 53.931, 56.621 and 66.281 corresponding to (111), (200), (220), (311), (222), and (400) planes of cubic AgBiS₂ respectively can be clearly observed in Figure 1. Both **sf-AgBiS**₂ and **PEG-AgBiS**₂ nanoparticles shows the same crystal structure which can be identified from the PXRD pattern. Moreover, the absence of Bi₂S₃ and Ag₂S peaks in PXRD shows the purity of samples prepared using HMDS assisted method. The absence of peaks in the IR spectrum (Figure 2A) of **sf-AgBiS**₂ related to HMDS indicates the absence of HMDS, whereas the peaks in IR spectrum (Figure 2B) corresponding to PEG in **PEG-AgBiS**₂, confirm the formation of it. As discussed in the literature, ^[27] the

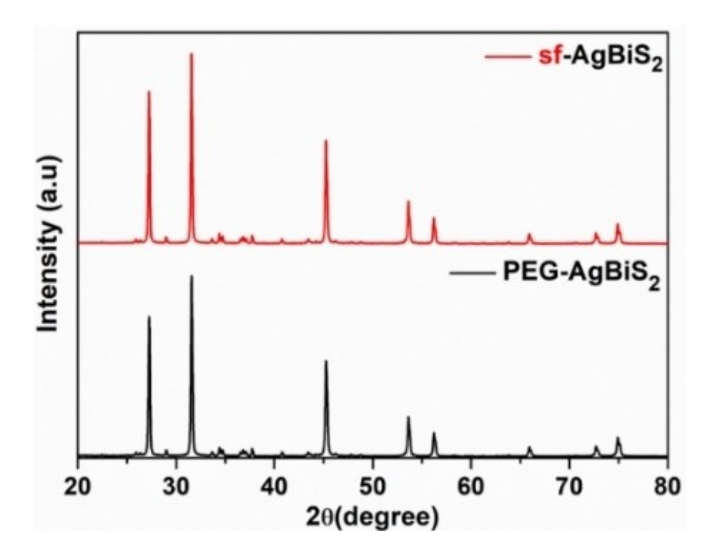


Figure 1. PXRD pattern of sf-AgBiS₂ and PEG-AgBiS₂ nanoparticles.

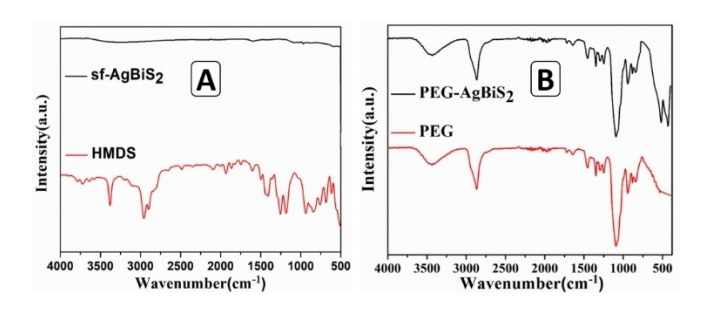


Figure 2. FTIR spectra. A) sf-AgBiS₂ and hexamethyldisilazane (HMDS), B) PEG-AgBiS₂ and polyethylene glycol (PEG).



presence of surfactant or stabilizer molecules on the surface of nanoparticles receded its activity as most of their active sites were covered.

The calculated absorption coefficient spectra (Figure 3) of AgBiS₂ shows the broad and strong absorption spectra near the NIR region for both the samples indicating their utilization as PTT agents.^[3,6,39] The SEM and TEM images (Figure 4) showed a nanorod-like morphology of both **sf-AgBiS**₂ and **PEG-AgBiS**₂ particles, while the SAED pattern confirmed the crystalline nature of the samples. The average particle size of **sf-AgBiS**₂ and **PEG-AgBiS**₂ and **PEG-AgBiS**₂ nanoparticles was 16.5 nm and 19 nm respectively (Figure S1). Interestingly, both **sf-AgBiS**₂ and **PEG-AgBiS**₂ exhibited similar morphology and formed an excellent dyad for a comparative study vis-à-vis presence and absence of stabilizers on the biological activity of AgBiS₂. It appears that **PEG-AgBiS**₂ was agglomerated, probably due to the adhesive nature of surfactants.

Capping agents are generally used to control the growth of particles and prevent agglomeration. The surface modification of nanoparticles is acquired using these capping agents. We have chosen PEG as a capping agent in the current study because of its biocompatibility for biomedical applications. This non-ionic, hydrophilic, low molecular weight polymer with antioxidant properties and high solubility in the buffer has a high adsorption rate. It helps the nanoparticle penetrate through the mucous membrane. PEG also helps nanoparticles from non-specific protein binding and macrophages. PEG also

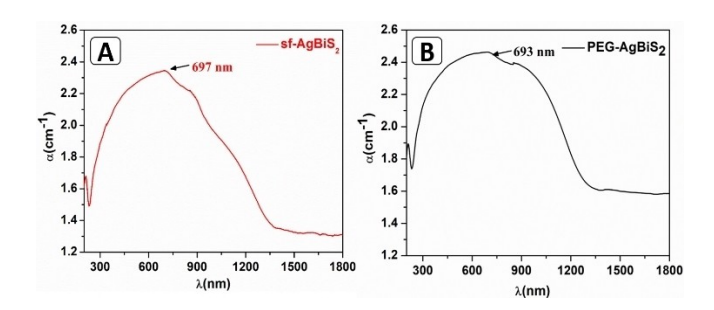


Figure 3. Calculated absorption coefficient of sf-AgBiS₂ and PEG-AgBiS₂ nanoparticles.

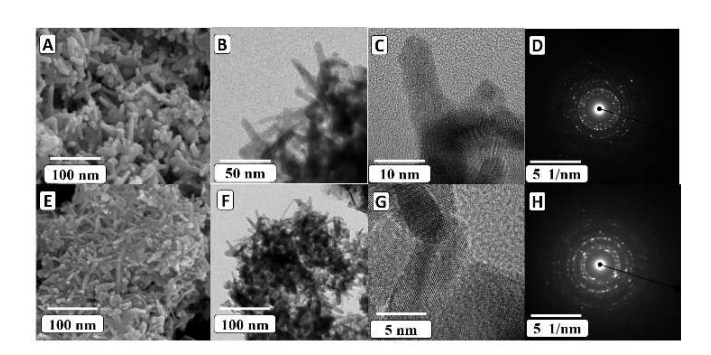


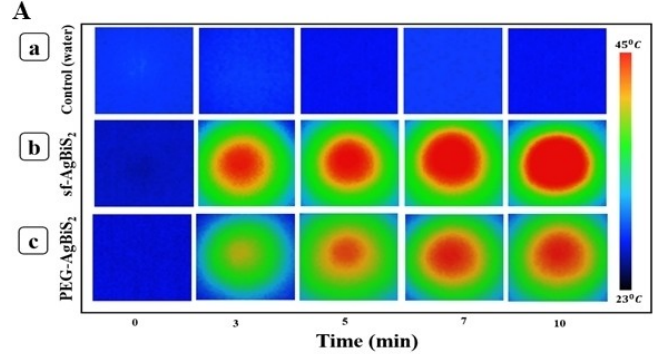
Figure 4. A) FESEM image, B) TEM image, C) High resolution TEM image, and D) SAED pattern of **sf-AgBiS**₂ nanoparticles. E) FESEM image, F) TEM image, G) High resolution TEM image, and H) SAED pattern of **PEG-AgBiS**₂ nanoparticles.

has antibacterial activity against various pathogens and is used in biomedical applications.^[40–45]

Photothermal effect

A good PTT agent can absorb at NIR regime. They get excited when the PTT agent accumulated on cancer cells is irradiated with the external light source. The excited PTT agent undergoes vibrational relaxation through non-radiative decay, releasing the energy as heat, which is transferred to the cancer cells. The cells die when the temperature of the tissue is increased above 46°C due to protein denaturation and plasma membrane destruction. $^{[5,46-51]}$ The photothermal effect of $sf\text{-}AgBiS_2$ and PEG-AgBiS₂ (20 μg/ml each) was measured at various time using an 808 nm NIR laser (power=650 mW) for 3-10 min (Figure 5). It was found that the temperature of sf-AgBiS₂ reached to a maximum 53.3 °C after 10 min of radiation and 43.9°C with 3 min exposure was. Similarly, the maximum temperature obtained for PEG-AgBiS₂ was 44.9 °C at 10 min and 38.9 °C for 3 min exposure. The temperature of DI water (control) was only 25.9 °C (Table 1). The thermal stability of compounds was studied as shown in Figure 6.

Generally, a temperature above 41 °C makes cell inactivation for a definite time, while a temperature above 48 °C results in irreversible cell inactivation. These results demonstrate the efficiency of sf-AgBiS₂ and PEG-AgBiS₂ as effective photothermal agents by converting NIR light to heat efficiently. Interestingly, sf-AgBiS₂ act as a more powerful photothermal



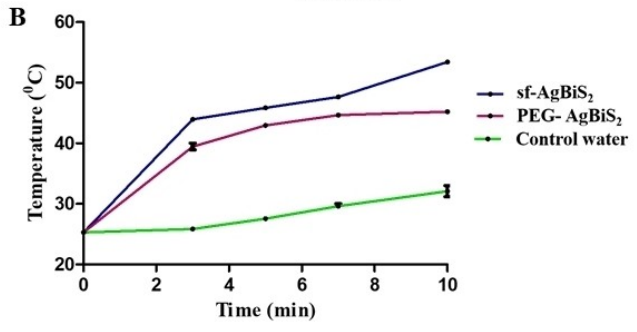
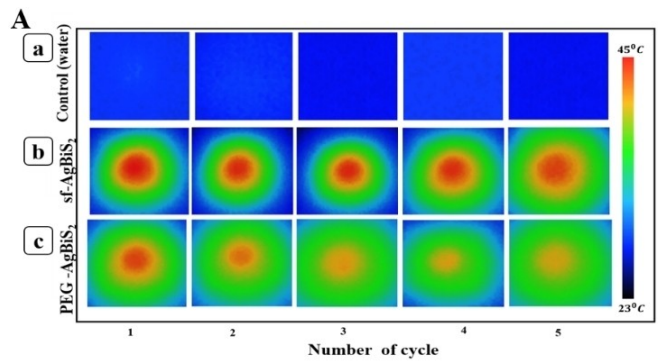


Figure 5. A) Photothermal transduction efficiency thermal images of (a) control (water), (b) **sf-AgBiS**₂, and (c) **PEG- AgBiS**₂ nanoparticles irradiated with 808 nm NIR laser. B) PTT transduction efficiency graph of control (water), **sf-AgBiS**₂ and **PEG-AgBiS**₂ nanoparticles.



Table 1. Photothermal transduction temperatures were obtained for control (water), sf-AgBiS ₂ , and PEG- AgBiS ₂ nanoparticles.				
Time [min]	Temperature of Control (water)	Temperature of sf-AgBiS2	Temperature of PEG-AgBiS2	
0	25.4	25.1	25.2	
3	25.9	43.9	38.9	
5	27.6	45.8	42.9	
7	28.0	47.4	44.6	
10	29.0	53.3	44.9	



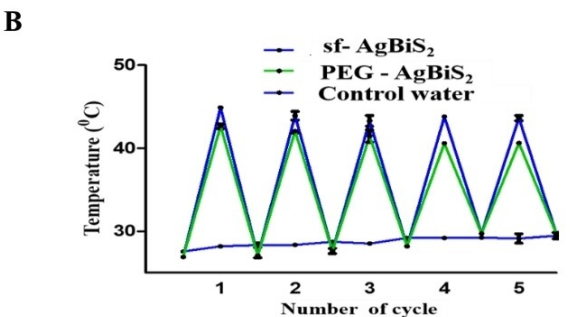


Figure 6. A) Thermal stability (on/ off cycle) images irradiated with an 808 nm Laser of (a) control (water), (b) sf-AgBiS₂, and (c) PEG- AgBiS₂ NPs for 5 min (five cycles), B) Thermal stability (on/off cycle) graph of water, sf-AgBiS₂ and PEG-AgBiS₂ nanoparticles irradiated with a 808 nm laser for 5 min (five cycles).

agent compared with **PEG-AgBiS** $_2$. ^[3,6] The maximum temperature obtained for even 20 µg/ml of **sf-AgBiS** $_2$ when irradiated with 808 nm NIR laser (power = 650 mW) is much higher than the earlier reported temperatures for AgBiS $_2$ nanoparticles prepared using different methods. In many reported works, researchers have used a higher concentration of 150 µg/ml, 1000 µg/ml 125 µg/ml to obtain 60 °C, 62 °C, and 49 °C, respectively, with NIR 808 radiation of 1 W for 10 min irradiation and 200 µg/ml with 0.4 W NIR radiation to obtain 46.7 °C. ^[1,3,6] Interestingly, we can bring a temperature as high as 53.3 °C even at a lower concentration of **sf-AgBiS** $_2$.

The difference in photothermal transduction temperature can be explained based on the low thermal conductivity of polyethylene glycol (PEG) in **PEG-AgBiS**₂. In the case of **PEG-AgBiS**₂, the heat generated is trapped within the nanoparticle and is not transferred to cancer cells. Whereas in the case of **sf-AgBiS**₂ the heat generated is wholly transferred to the cancer cells as these nanoparticles are not covered with capping agents, making it a good PTT agent. These can also exhibit SPR, a phenomenon in which conductive free electrons resonate

jointly with the incoming electromagnetic radiation, which results in increased light absorption and scattering. This observation indirectly reveals that more free surface electrons are available for sf-AgBiS₂ than PEG-AgBiS₂, where the surface electrons are unavailable due to the coverage by the capping agent polyethylene glycol (PEG). Thus, more NIR light absorption is observed in the case of sf-AgBiS₂, leading to higher temperature generation.

Due to their large light absorption and scattering cross section, nanorods usually give high SPR frequency. Therefore, nanorods can generally increase the temperature in tumour cells more than other morphologies. Since both sf-AgBiS₂ and PEG-AgBiS₂ exhibit nanorods morphology, the difference in photothermal transduction temperature can be due to the absence of the capping agent in sf-AgBiS₂. sf-AgBiS₂ prepared using the HMDS-assisted method is crystalline. Albeit crystalline nature, it exhibited a good PTT. It is worth mentioning that few crystalline nanoparticles reported in the literature exhibited a good PTT effect. These results also demonstrate the importance of HMDS-assisted method to obtain surfactant-free nanoparticles to acquire a more active photothermal agent. St. 46-51]

In vitro biocompatibility

In vitro biocompatibility for 20, 40, 60, 80, 100 μ g/ml of sf-AgBiS₂ and PEG-AgBiS₂ to normal cell line L929 was measured using MTT assay. The results (Figure 7) reveal that both exhibited no significant toxicity. Even at the high concentration of 100 μ g/ml, sf-AgBiS₂ shows a cell viability 86.29% to 71.63 \pm 5% with 20, 40, 60, 80 and 100 μ g/ml and PEG-AgBiS₂ shows a cell viability of cell viability 86.29% to 67.3 \pm 3% with 20, 40, 60, 80 and 100 μ g/ml. Among these, sf-AgBiS₂ showed slightly greater biocompatibility to normal fibroblast cell lines L929

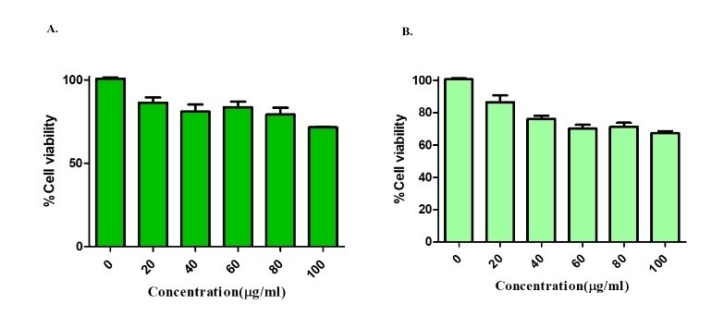


Figure 7. Biocompatibility of A) $sf-AgBiS_2$ and B) $PEG-AgBiS_2$ nanoparticles.



than PEG-AgBiS₂. The good biocompatibility of sf-AgBiS₂ may attribute to their more active sites available on the surface than PEG-AgBiS₂, where most of the active sites are covered, resulting in less interaction with the cells.^[33]

In vitro cytotoxicity in 2D and 3D cell culture

Cancer cell killing activity of sf-AgBiS2 and PEG-AgBiS2 against HeLa was studied using the same MTT assay. A remarkable decline in the viable cell % of HeLa was observed when cultured in the presence of sf-AgBiS₂ (20 µg/ml) and PEG-AgBiS₂ (20 μg/ml) and irradiated with NIR laser (Figure 8). For sf-AgBiS₂, the cell viability was $80\pm3\%$ without NIR laser and $51\pm4\%$ with NIR laser. For **PEG-AgBiS**₂, the cell viability without the NIR laser was $85\pm5\%$ and with the NIR laser was $72\pm6\%$ (Table 2). These observations show that sf-AgBiS₂ has more cell-killing efficiency than PEG-AgBiS₂. The results indicate that the synergic effect of the availability of free active surface and the photothermal efficiency of sf-AgBiS₂ results in more cancer cell death than $PEG-AgBiS_2$, where the presence of surfactant hinders the PTT active AgBiS₂ activity. Since both sf-AgBiS₂ and PEG-AgBiS₂ have the same morphology, the difference in the anticancer activity exhibited by these nanoparticles can be attributed to the presence and absence of the stabilizing agent.

In vitro 3D tumor spheroids can mimic the microenvironment of live tumours present in vivo. We observed that sf-AgBiS₂ with NIR irradiation has better cell-killing efficacy than PEG-AgBiS₂ (Figure 9) and without NIR irradiation (Figure S2). Figure 9 shows that sf-AgBiS₂ has significantly damaged tumour cells from the edge to the core compared to PEG-

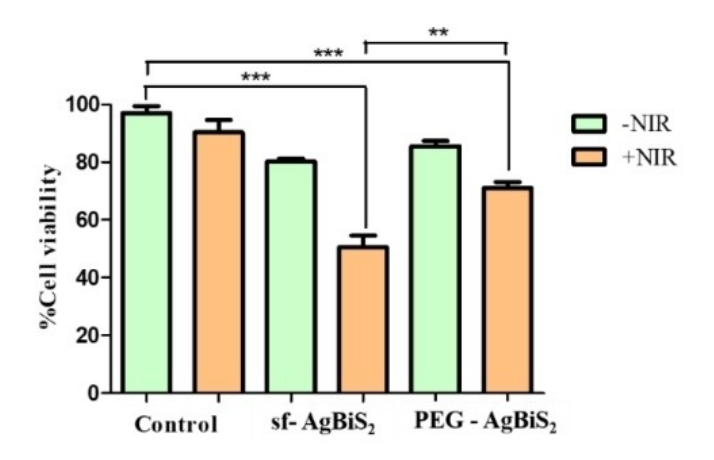


Figure 8. NIR laser mediated cell cytotoxicity of sf-AgBiS₂ and PEG-AgBiS₂ nanoparticles in HeLa cell line (P < 0.05).

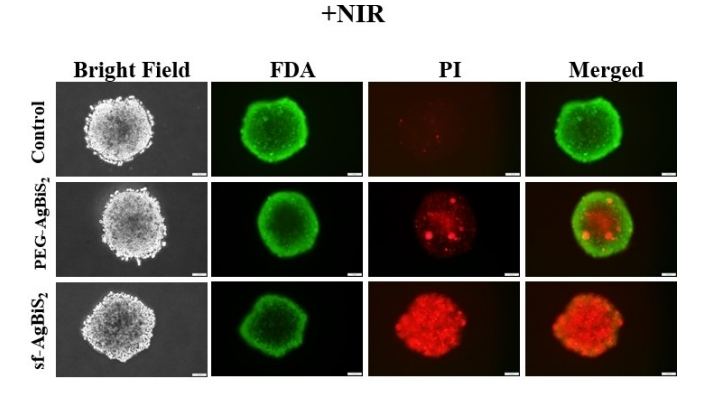


Figure 9. In vitro NIR-laser-mediated cell cytotoxicity of sf-AgBiS₂ and PEG-AgBiS₂ by the live/dead assay (FDA stains live cells (green) and PI stains dead cells (red).

AgBiS₂. In cancer treatment it is important to target the hypoxic core of tumour cells to avoid metastasis, angiogenesis. When NIR light is absorbed by nanoparticles, it gets excited and undergo vibrational relaxation and leads to lattice vibration and results in temperature rise. The increased temperature eventually destroys the membrane and proteins which covers the cancer cells resulting in the penetration of nanoparticles into the cell and leads to cell death. The possible reason for the cancer cell death could be the good penetration capability of sf-AgBiS₂ in the hypoxic core of the tumour than PEG-AgBiS₂. In addition to that the decreased size (16.5 nm) and increased SPR response of nanorod morphology in the case of capping agent free sf-AgBiS₂ will also pave the way for its enhanced activity. In conjunction with that, capping agents will cover the active sites on the surface of nanoparticles. Therefore, the adsorption of nanoparticles to the cell surface is hindered, whereas the sf-AgBiS2, with a greater number of active sites is able to get adsorbed on cell surface easily which results in easy and more penetration of nanoparticles inside cancer cells. [4,52]

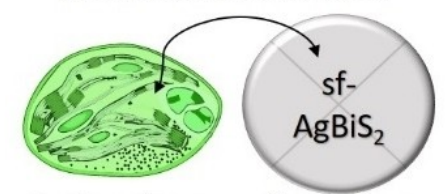
Reactive Oxygen Species (ROS) Analysis

The Anticancer and Antibacterial Activity of AgBiS₂ is usually from the photothermal therapy (PTT) and the photocatalytic activity (deriving from photo-excited ·OH, holes, O₂ · or other active radicals). As reported earlier, ^[27] the capping agents or stabilizer molecules cover the active sites on the photocatalyst and hinder the transfer of excitons to dye molecules retarding the photocatalytic activity of nanoparticles. ^[27,33–38] Similarly, antibacterial and anticancer activities involve the adsorption of nanoparticles on the cell surface. The stabilizers may impede

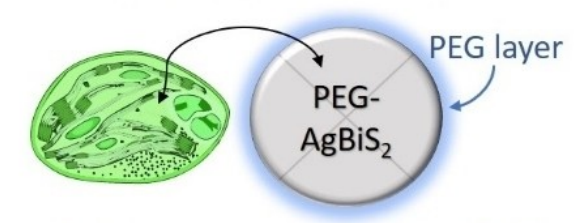
Table 2. The cell viability of sf-AgBiS ₂ and PEG-AgBiS ₂ against HeLa cells.			
Sample	Cell viability [%] without NIR irradiation	with NIR irradiation	
sf-AgBiS2 PEG-AgBiS2	80±3 85±5	51±4 72±6	



INTERACTION OF BIOLOGICAL CELL WITH NANOPARTICLES



In the absence of stabilizer



In the presence of stabilizer (PEG) sf = stabilizer free; PEG= polyethylene glycol

PEG act as a barrier for interaction

Figure 10. Schematic diagram showing the possible interaction of sf-AgBiS $_2$ and PEG-AgBiS $_2$ with bacteria or cell.

the interaction between cancer cell/ bacterial and active radicals (Figure 10). Since **sf-AgBiS₂** is not covered with the capping agent, it can directly interact with the cell surface than coated nanoparticles.

Reactive oxygen species (ROS) or free-radical generation in the presence of NIR light is one of the cell-killing mechanisms where excessive production of ROS can trigger DNA damage or programmed cancer cell death. [4,53] 2',7'-Dichlorodihydrofluorescein diacetate (DCFDA) is an indicator to analyse the generation of ROS. Our analysis using DCFDA showed the generation of ROS in both sf-AqBiS₂, and PEG-AqBiS₂ treated cells in the presence of NIR light. The cell death is more with NIR light when sf-AgBiS₂ is used (Figure S3). The possible reason for the enhanced activity of sf-AgBiS₂ can be because the excitons produced are available for the production of ROS, whereas, in the case of PEG-AgBiS₂, the excitons are trapped within the nanoparticle due to the presence of PEG resulting in decreased ROS production. Also, the free active surface on the sf-AgBiS₂ makes adsorption easier for these nanoparticles than the PEG-AgBiS₂. The sf-AgBiS₂ may also trigger other cell death mechanisms, which we will check on in future work.

Antibacterial activity

The antibacterial activity of sf-AgBiS₂ and PEG-AgBiS₂ against Gram (+) S. *aureus* was investigated using the disc diffusion method and MTT assay method (Figures 11 and 12). Clinically derived S. *aureus* due to immunosuppression by chemotherapy is a significant cause of infection in tumour treatment. Silver

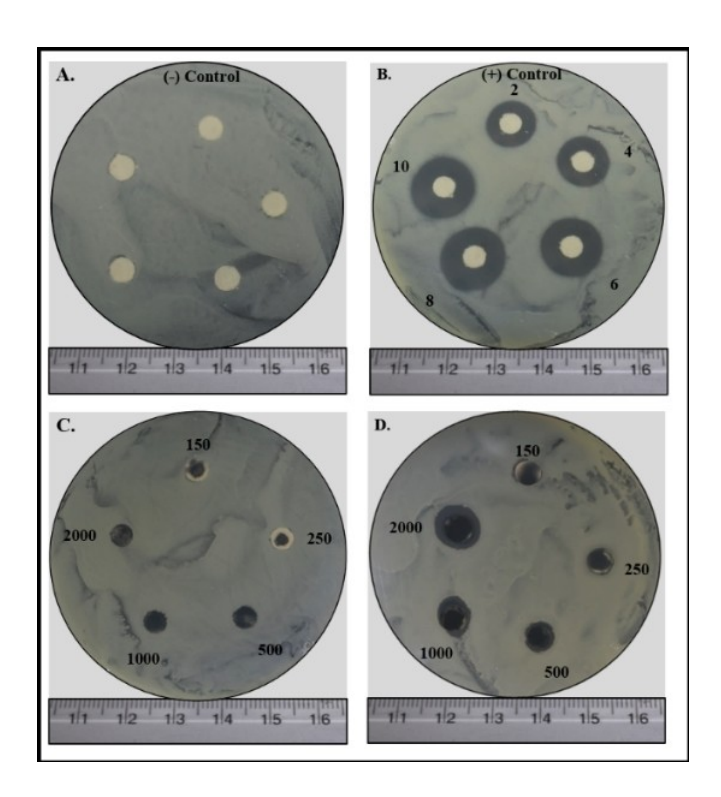


Figure 11. Antibacterial activity by disk diffusion method against *S.aureus*, A) Negative control, B) Negative control (with antibiotic Gentamicin), C) **PEG-AgBiS₂** and D) **sf-AgBiS₂** nanoparticles.

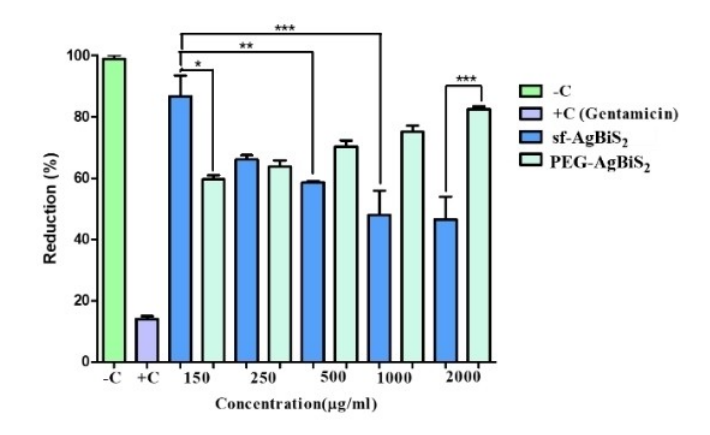


Figure 12. Antibacterial activity of $sf-AgBiS_2$ and $PEG-AgBiS_2$ nanoparticles by MTT assay against *S.aureus* (P < 0.05).

has proven to be one of the best antibacterial agents. [28-32] The area of the zone of inhibition visible around the disc indicates the activity of nanoparticles as an antibacterial agent. According to the earlier studies, [31,54,55] the sharp edges of AgBiS₂ rods pierce the cell membrane and thus release ROS, which damages DNA and oxidises proteins, ultimately leading to cell death. From Figure 11, it is clear that sf-AgBiS₂ has a higher antibacterial effect against S. aureus than PEG-AgBiS₂. This observation depicts that the surfactant-free AgBiS₂ nanoparticles synthesized using HMDS assisted method improve the chances of getting S. aureus bacteria directly in contact with

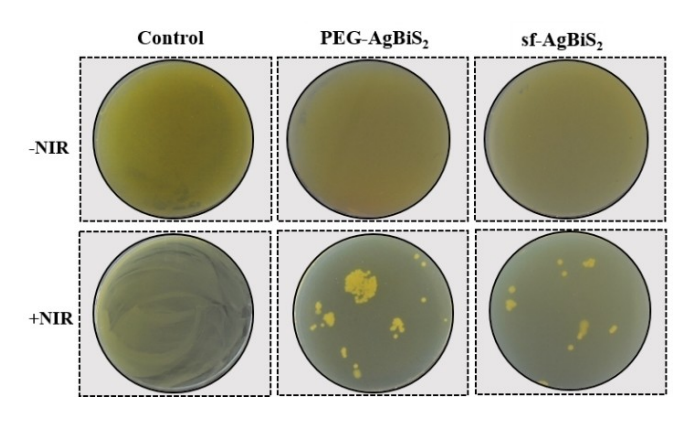


Figure 13. Antibacterial activity of $sf-AgBiS_2$ and $PEG-AgBiS_2$ against S. *aureus* with and without NIR irradiation.

nanoparticles (improves the cling between S. *aureus* bacteria with the bare surface of nanoparticle) by exposing more active sites than the nanoparticles covered with polyethylene glycol (PEG) as surfactant. The antibacterial activity of **sf-AgBiS**₂ and **PEG-AgBiS**₂ was also confirmed using the MTT assay method (Figure 12). Accordingly, the results indicate that **sf-AgBiS**₂ nanoparticles could be an excellent antibacterial agent and can prevent the infection caused during cancer therapy.

We have studied the antibacterial activity of sf-AgBiS₂ and PEG-AgBiS₂ against S. aureus with NIR irradiation by MTT assay method. Since these materials showed lowest antibacterial activity with 150 µg/mL concentration (Figure 11) without NIR, we have checked the antibacterial activity at this lowest concentration (Figure 13) with NIR irradiation. As shown in Figure 13, the instant antibacterial activity without NIR irradiation was insignificant, whereas, with NIR irradiation, these materials showed effective bacterial inactivation. As expected, sf-AgBiS₂ is better compared to PEG-AgBiS₂. The photothermal antibacterial activity under NIR irradiation results from lattice vibration caused by the non-radioactive deexcitation process. This vibration results in photothermia, eventually leading to the degradation of the bacterial cell membrane, helping the penetration of nanoparticles inside the cell and leading to cell death. As discussed earlier, the nanorod morphology of materials described here shows good light absorption and scattering cross-section. [47] However, thermal absorption by PEG-AgBiS₂ diminished its activity compared to sf-AgBiS₂.

Conclusion

In summary, **sf-AgBiS**₂ and **PEG-AgBiS**₂ nanoparticles were prepared successfully employing the HMDS-assisted synthesis. The X-ray diffraction and SAED patterns revealed the cubic phase formation of crystalline AgBiS₂ nanoparticles. The maximum temperature attained for 20 µg/ml of **sf-AgBiS**₂ when irradiated with 808 nm NIR laser (power=650 mW) is much higher than the earlier reported temperatures for AgBiS₂ nanoparticles. The as-synthesized **sf-AgBiS**₂ nanoparticles performed as an excellent photothermal (PPT) agent against HeLa cells,

live 3-D tumour spheroids and an antibacterial agent against *Staphylococcus aureus* than **PEG-AgBiS**₂ nanoparticles with and without NIR irradiation. The study showed that **sf-AgBiS**₂ has more cell-killing efficiency than **PEG-AgBiS**₂. This work highlights and the importance of surfactant-free surfaces of nanoparticles to pave the way for effective nanomedicine and, perhaps justifies the utility of HMDS-assisted method.

Acknowledgements

The project is funded partially by IOE grants (No UoH-IoE-RC3-21-043) of University of Hyderabad. A.J. thanks UGC-JRF for fellowship.

Conflict of Interest

The authors declare no conflict of interest.

Data Availability Statement

The data that support the findings of this study are available in the supplementary material of this article.

Keywords: antibacterial agent \cdot anticancer agent \cdot nanoparticle surface \cdot silver bismuth sulphide \cdot stabilizer free

- [1] P. Lei, R. An, X. Zheng, P. Zhang, K. Du, M. Zhang, L. Dong, X. Gao, J. Feng, H. Zhang, *Nanoscale* 2018, 10, 16765.
- [2] J. B. Vines, J. H. Yoon, N. E. Ryu, D. J. Lim, H. Park, Front. Chem. 2019, 7, 167
- [3] B. Chen, C. Zhang, W. Wang, Z. Chu, Z. Zha, X. He, W. Zhou, T. Liu, H. Wang, H. Qian, ACS Nano 2020, 14, 14919–14928.
- [4] P. S. Rajalakshmi, S. B. Alvi, N. Begum, B. Veeresh, A. K. Rengan *Biomacromolecules* **2021**, *22*, 3926.
- [5] R. Gayathri, P. S. Rajalakshmi, A. Thomas, A. K. Rengan, *Materialia* 2021, 19, 101195.
- [6] J. Cheng, W. Wang, X. Xu, Z. Lin, C. Xie, Y. Zhang, T. Zhang, L. Li, Y. Lu, Q. Li, Mater. Sci. Eng. C. 2020, 107, 110324.
- [7] L. Zou, H. Wang, B. He, L. Zeng, T. Tan, H. Cao, X. He, Z. Zhang, S. Guo, Y. Li, *Theranostics* 2016, 6, 762.
- [8] K. Cheng, R. Y. Zhang, X. Q. Yang, X. S. Zhang, F. Zhang, J. An, Z. Y. Wang, Y. Dong, B. Liu, Y. D. Zhao, T. C. Liu, ACS Appl. Mater. Interfaces 2020, 12, 40052.
- [9] M. D. Khan, M. Aamir, M. Sohail, S. Bhoyate, M. Hyatt, R. K. Gupta, M. Sher, N. Revaprasadu 2019, 48, 3714.
- [10] C. Chen, X. Qiu, S. Ji, C. Jia, C. Ye, CrystEngComm 2013, 15, 7644.
- [11] J. Wang, X. Yang, W. Hu, B. Li, J. Yan, J. Hu, Chem. Commun. 2007, 931.
- [12] T. Nakazawa, D. Kim, Y. Oshima, H. Sato, J. Park, H. Kim, ACS Omega 2021, 6, 20710.
- [13] S. Wen, T. Wu, H. Long, L. Ke, S. Deng, L. Huang, J. Zhang, S. Tan, ACS Appl. Mater. Interfaces 2021, 13, 21979.
- [14] S. Paul, B. Dalal, R. Jana, A. Shit, A. Datta, S. K. De, J. Phys. Chem. C. 2020, 124, 12824.
- [15] P. Ganguly, S. Mathew, L. Clarizia, A. Akande, S. Hinder, A. Breen, S. C. Pillai, Appl. Catal. B 2019, 253, 401.
- [16] S. Sugarthi, G. Bakiyaraj, R. Abinaya, M. Navaneethan, J. Archana, M. Shimomura, Mater. Sci. Semicond. Process. 2020, 107, 104781.
- [17] J. Wang, L. Li, H. Yu, F. Guan, D. Wang, *Inorg. Chem.* **2019**, *58*, 12998.
- [18] D. Chen, G. Shen, K. Tang, X. Jiang, L. Huang, Y. Jin, Y. Qian, *Inorg. Chem. Commun.* **2003**, *6*, 710.
- [19] J. C. Calva-Yáñez, O. Pérez-Valdovinos, E. A. Reynoso-Soto, G. Alvarado-Tenorio, O. A. Jaramillo-Quintero, M. Rincón, J. Phys. D 2019, 52, 125502.



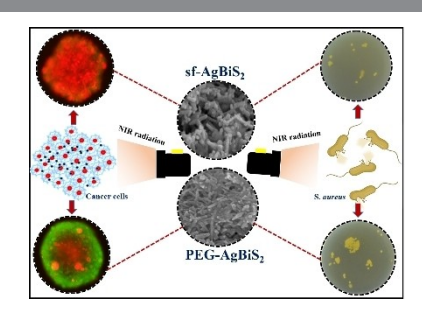
- [20] S. H. I. Xiao-Xue, L. I. Xiu-Qi, W. E. I. Xiao-Ping, L. I. Jian-Ping, Chin. J. Anal. Chem. 2020, 48, pp.396–404.
- [21] N. Cates, M. Bernechea, APL Materials 2018, 6, 084503.
- [22] a) B. Le Ouay, F. Stellacci, Nano Today 2015, 10, 339.
- [23] a) R. Huang, R. P. Carney, F. Stellacci, B. L. T. Lau, Nanoscale 2013, 5, 6928; b) R. Huang, R. P. Carney, K. Ikuma, F. Stellacci, B. L. T. Lau, ACS Nano 2014, 8, 5402.
- [24] R. Eigenheer, E. R. Castellanos, M. Y. Nakamoto, K. T. Gerner, A. M. Lampe, K. E. Wheeler, Environ. Sci.-Nano 2014, 1, 238.
- [25] a) M. Lundqvist, J. Stigler, G. Elia, I. Lynch, T. Cedervall, K. A. Dawson, PNAS 2008, 105, 14265.
- [26] a) S. Lara, F. Alnasser, E. Polo, D. Garry, M. C. Lo Giudice, D. R. Hristov, L. Rocks, A. Salvati, Y. Yan, K. A. Dawson, ACS Nano 2017, 11, 1884; b) L. M. Herda, D. R. Hristov, M. C. Lo Giudice, E. Polo, K. A. Dawson, J. Am. Chem. Soc. 2017, 139, 111–114; c) M. C. Lo Giudice, L. M. Herda, E. Polo, K. A. Dawson, Nat. Commun. 2016, 7, 13475.
- [27] a) A. Joseph, S. Billakanti, M. A. Pandit, S. Khatun, A. K. Rengan, K. Muralidharan, Environ Sci Pollut Res. 2022, 29, 56863; b) B. Srinivas, M. A. Pandit, K. Muralidharan, ACS Omega 2019, 4, 14970; c) B. Ganesh Kumar, K. Muralidharan, J. Mater. Chem. 2011, 21, 11271; d) B. Ganesh Kumar, K. Muralidharan, Eur. J. Inorg. Chem. 2013, 2102.
- [28] L. Wang, C. Hu, L. Shao, Int. J. Nanomed. 2017, 12, 1227.
- [29] J. T. Seil, T. J. Webster, Int. J. Nanomed. 2012, 7, 2767.
- [30] Q. L. Feng, J. Wu, G. Q. Chen, F. Z. Cui, T. N. Kim, J. O. Kim, J. Biomed. Mater. Res. 2000, 52, 662.
- [31] S. Pal, Y. K. Tak, J. M. Song, Appl. Environ. Microbiol. 2007. 73, 1712.
- [32] J. Y. Cheon, S. J. Kim, Y. H. Rhee, O. H. Kwon, W. H. Park, Int. J. Nanomed. 2019, 14, 2773.
- [33] a) M. Sudha, M. Rajarajan, J. Appl. Chem. 2013, 3, 45; b) M. Sudha, S. Senthilkumar, R. Hariharan, A. Suganthi, M. Rajarajan, J. Sol-Gel Sci. Technol. 2011, 61, 14; c) M. Sudha, S. Senthilkumar, R. Hariharan, A. Suganthi, M. Rajarajan, J. Sol-Gel Sci. Technol. 2013, 65, 301.
- [34] Z. Cao, Z. Zhang, Appl. Surf. Sci. 2011, 257, 4151.
- [35] P. Chandran, S. Netha, S. S. Khan, J. Photochem. Photobiol. B 2014, 138, 155.
- [36] K. Akhil, J. Jayakumar, G. Gayathri, S. S. Khan, J. Photochem. Photobiol. B 2016, 160, 32.
- [37] M. L. Singla, M. Shafeeq, M. Kumar, J. Lumin. 2009, 129, 434.
- [38] R. Y. Hong, J. H. Li, L. L. Chen, D. Q. Liu, H. Z. Li, Y. Zheng, J. Ding, Powder Technol. 2009, 189, 426.

- [39] F. Yao, L. Jiang, Y. Qi, R. Li, Y. Li, Y. Xu, H. Liu, Q. Lin, Appl. Mater. Today. 2022, 26, 101262.
- [40] A. Mandal, V. Meda, W. J. Zhang, K. M. Farhan, A. Gnanamani, Colloids Surf. B 2012, 90, 191.
- [41] A. Jose, K. R. S. Devi, D. Pinheiroa, S. L. Narayana J. Photochem. Photobiol. B 2018, 187, 25.
- [42] M. Catauro, R. A. Renella, F. Papale, S. V. Ciprioti, *Mater. Sci. Eng. C* 2016, 61, 51.
- [43] J. Chirife, L. Herszage, A. Joseph, J. P. Bozzini, N. Leardini, E. S Kohn, Antimicrob. Agents Chemother. 1983, 24, 409.
- [44] R. Javed, A. Sajjad, S. Naz, H. Sajjad, Q. Ao, Int. J. Mol. Sci. 2022, 23, 10521.
- [45] V. Bastos, J. M. P. Ferreira de Oliveira, D. Brown, H. Jonhston, E. Malheiro, A. L. Daniel-da-Silva, I. F. Duarte, C. Santos, H. Oliveira, *Toxicol. Lett.* 2016, 249, 29.
- [46] R. M. Cabral, P. V. Baptista, Nano Life. 2013, 3, 1330001.
- [47] Y. Zhang, X. Zhan, J. Xiong, S. Peng, W. Huang, R. Joshi, Y. Cai, Y. Liu, R. Li, K. Yuan, N. Zhou, Sci. Rep. 2018, 8, 8720.
- [48] X. Li, J. F. Lovell, J. Yoon, X. Chen, Nat. Rev. Clin. Oncol. 2020, 17, 657.
- [49] O. A. Yeshchenko, I. M. Dmitruk, A. A. Alexeenko, A. V. Kotko, J. Verdal, A. O. Pinchuk, *Plasmonics* 2012, 7, 685.
- [50] V. P. Pattani, J. W. Tunnell, Lasers Surg. Med. 2012, 44, 675.
- [51] C. Sánchez López de Pablo, J. J. S. Olmedo, A. M. Rosales, N. Ramírez Hernández, F. del Pozo Guerrero, Nanoscale Res. Lett. 2014, 9, 1.
- [52] S. C. Brüningk, I. Rivens, C. Box, U. Oelfke, G. Ter Haar, Sci. Rep. 2020, 10, 1653.
- [53] T. Appidi, D. B. Pemmaraju, R. A. Khan, S. B. Alvi, R. Srivastava, M. Pal, N. Khan, A. K. Rengan, *Nanoscale* 2020, 12, 2028.
- [54] M. D. Iftekhar Hossain, J. Edwards, J. Tyler, J. Anderson, S. Bandyopadhyay, IET Nanobiotechnol. 2017, 11, 501.
- [55] J. R. Morones, J. L. Elechiguerra, A. Camacho, K. Holt, J. B. Kouri, J. T. Ramírez, M. J. Yacaman, *Nanotechnology* 2005, 16, 2346.

Manuscript received: December 5, 2022 Accepted manuscript online: March 9, 2023 Version of record online: ■■, ■■

RESEARCH ARTICLE

The physicochemical interaction of nanoparticles with biological systems differs in the presence and absence of stabilizers (surfactant or polymer molecules) used during their synthesis. In this study, the AgBiS₂ nanoparticles produced without stabilizing molecules demonstrated better anticancer activity than the polymer-coated nanoparticles. This work provides insight into the importance of the clean surface of nanoparticles in nanomedicine.



A. Joseph, S. Khatun, D. Sai Hemanth Kumar, Prof. A. K. Rengan*, Prof. K. Muralidharan*

1 – 9

Insight into the Effect of Stabilizers on Anticancer and Antibacterial Activity of AgBiS₂ Nanomaterial



A Comparative Study on Applications of Surfactant-Free Metal Chalcogenides

by Anju Joseph

Submission date: 21-Jul-2023 11:03AM (UTC+0530)

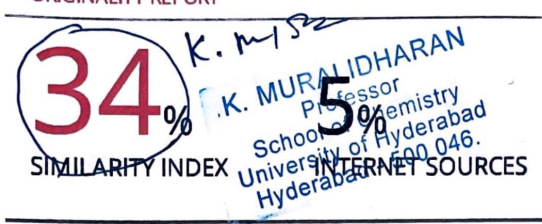
Submission ID: 2134417874

File name: Anju_Joseph.pdf (875.58K)

Word count: 22490 Character count: 131721

A Comparative Study on Applications of Surfactant-Free Metal Chalcogenides

ORIGINALITY REPORT



33% PUBLICATIONS 1% STUDENT PAPERS

PRIMARY SOURCES

Anju Joseph, Srinivas Billakanti, Manzoor Ahmad Pandit, Sajmina Khatun, Aravind Kumar Rengan, Krishnamurthi Muralidharan. "Impact of bandgap tuning on ZnS for degradation of environmental pollutants and disinfection", Environmental Science and Pollution Research, 2022 Self pleglarion

K. MURALIDHARAN
Professor
School of Chemistry
University of Hyderabad
Hyderabad - 500 046.

Publication

Anju Joseph, Sajmina Khatun, Dasari Sai Hemanth Kumar, Aravind K. Rengan, Krisnamurthi Muralidharan. "Insight into the Effect of Stabilizers on Anticancer and Antibacterial Activity of AgBiS2 Nanomaterial", Chemistry – A European Journal, 2023

Self plegaring
K. M.?2

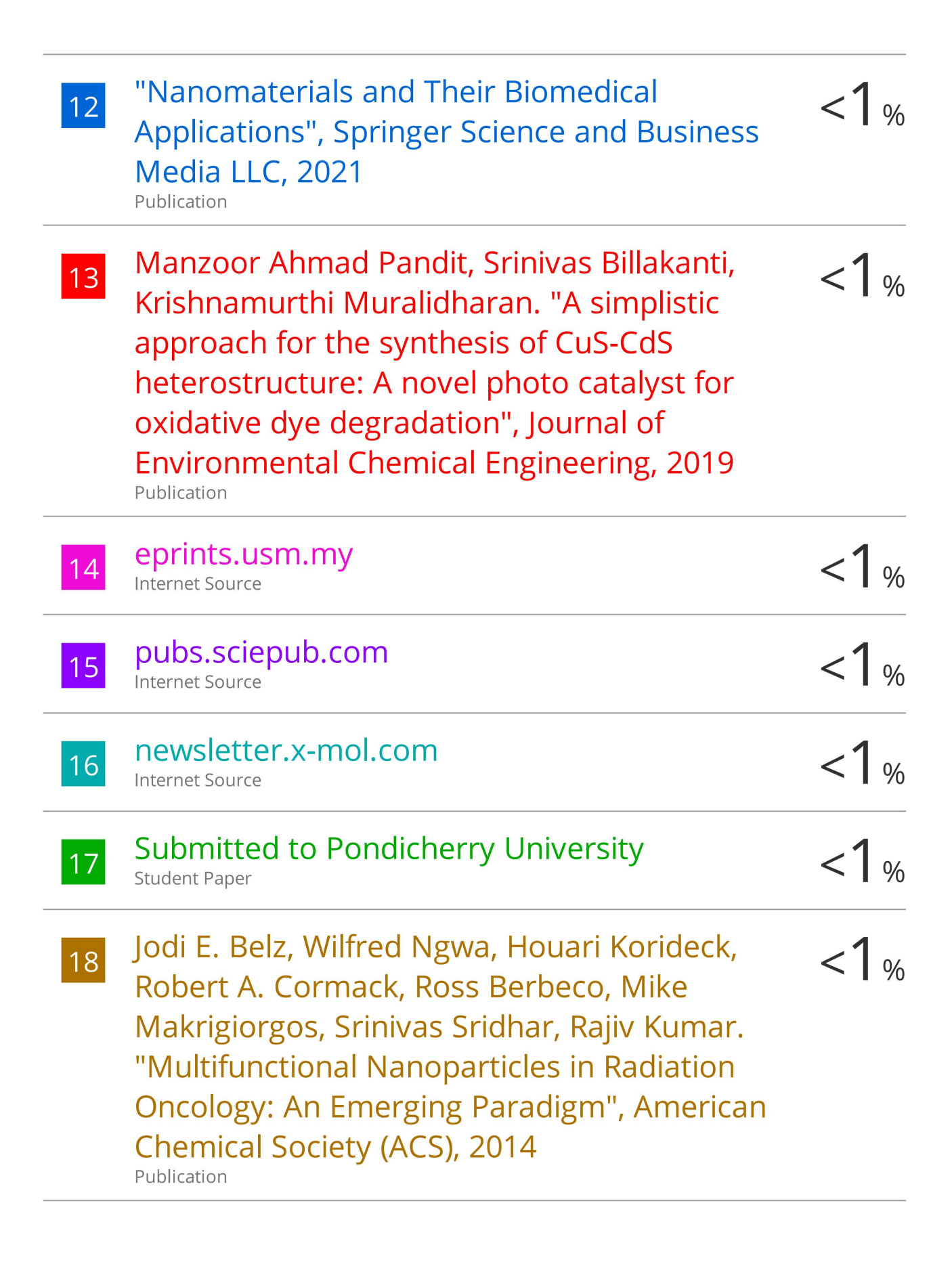
K. MURALIDHARAN
Professor
School of Chemistry
University of Hyderabad
Hyderabad - 500 046.

Anju Joseph, Sajmina Khatun, Dasari Sai Hemanth Kumar, Aravind K. Rengan, Krishnamurthi Muralidharan. "Insight into the Effect of Stabilizers on Anticancer and Antibacterial Activity of AgBiS Nanomaterial "," Chemistry – A European Journal, 2023

TE K. MURALIDHARAN

Professor School of Chemistry University of Hyderabad Hyderabad - 500 046.

4	pubmed.ncbi.nlm.nih.gov Internet Source	1 %
5	www.researchgate.net Internet Source	<1%
6	Submitted to University of Hyderabad, Hyderabad Student Paper	<1%
7	www.science.gov Internet Source	<1%
8	www.mdpi.com Internet Source	<1%
9	Claudia Coughlan, Maria Ibáñez, Oleksandr Dobrozhan, Ajay Singh, Andreu Cabot, Kevin M. Ryan. "Compound Copper Chalcogenide Nanocrystals", Chemical Reviews, 2017	<1%
10	Tshimangadzo S. Munonde, Philiswa Nosizo Nomngongo. "Review on Metal Chalcogenides and Metal Chalcogenide-Based Nanocomposites in Photocatalytic Applications", Chemistry Africa, 2023	<1%
11	"Nanoparticles Reinforced Metal Nanocomposites", Springer Science and Business Media LLC, 2023	<1%



19	researchwith.njit.edu Internet Source	<1%
20	Janani Balasubramanian, Jack Lemere, S. Sudheer Khan, Nisha Rani Agarwal. "Plasmonic nanosensors and their spectroscopic applications—current trends and future perspectives", Elsevier BV, 2022 Publication	<1%
21	Submitted to Symbiosis International University Student Paper	<1%
22	mafiadoc.com Internet Source	<1%
23	Submitted to University of Macau Student Paper	<1%
24	Manzoor Ahmad Pandit, Dasari Sai Hemanth Kumar, Srinivas Billakanti, Manigandan Ramadoss, Krishnamurthi Muralidharan. "Chalcopyrite with Magnetic and Dielectric Properties: An Introductory Catalyst for 4- Nitrophenol Reduction", The Journal of Physical Chemistry C, 2020 Publication	<1%
25	Submitted to Runshaw College, Lancashire Student Paper	<1%
26	Submitted to University of British Columbia Student Paper	

		<1%
27	Billakanti Srinivas, Manzoor Ahmad Pandit, Krishnamurthi Muralidharan. "Importance of Clean Surfaces on the Catalyst: SnS Nanorings for Environmental Remediation ", ACS Omega, 2019 Publication	<1%
28	Sushmitha Veeralingam, Sushmee Badhulika. "Two-Dimensional Metallic NiSe2 Nanoclusters-Based Low-Cost, Flexible, Amperometric Sensor for Detection of Neurological Drug Carbamazepine in Human Sweat Samples", Frontiers in Chemistry, 2020 Publication	<1%
29	Submitted to University of Pune Student Paper	<1%
30	real.mtak.hu Internet Source	<1%
31	www.energy-xprt.com	<1 ov

Internet Source

31